High resolution measurements of quasi-static biomagnetic fields

Thesis

High resolution measurements of quasi-static biomagnetic fields

Ian Thomas BSc ARCS MSc

December 1990

Date of submission : 21st December 1990

Date of award : 18th March 1991

Abstract

This thesis addresses the problem of making high resolution magnetic measurements. The design and development of a new instrument, optimized for this type of investigation, are described and experiments utilizing this instrument to measure slowly changing fields are reported.

The biological system studied was the chick *in ovo*, from which strong (10–100 pT), slowly changing magnetic fields were measured during the first few days of incubation. Two independent sources were modelled. Using a novel extended source algorithm, a continuous current density distribution in the extra-embryonic membranes was imaged and, by greatly refining the experiment, a localized generator was discovered. There is evidence that this source may be associated with the morphological development of the chick embryo.

Acknowledgements

Without the assistance of many people, the production of this thesis would not have been possible. I shall mention the most notable contributions.

Firstly, I wish to thank Jean and Jeff Thomas, whose support and encouragement carried me through several difficult times.

I am very grateful to Stuart Freake, my co-supervisor, who constantly provided valuable advice throughout my stay at the Open University and spent many long hours in the laboratory. Krish Singh (graphics programs), Robert Hasson (analysis), Kathia Fiaschi (experimentation), Marilyn Moffat (computing advice) and Roger Bence (building apparatus) made vital contributions and I thank them all.

I am particularly indebted to John Wikswo for making possible the series of experiments carried out in his laboratory at Vanderbilt University, Nashville, Tennessee, USA. He and his colleagues, Jan van Egeraat and Danny Staton worked extremely hard on my behalf during my visit in January 1990.

Finally, I shall mention Steve Swithenby. Over the last four years, I have benefited enormously from his criticism, experience, approachability and friendship in the laboratory, in the office and on the cricket field. Thankyou, Steve.

Contents

1 Introduction 1

1.1 The state of biomagnetism 1

1.2 Issues addressed by this thesis 3

1.2.1 Instrumental issues 3

1.2.2 Experimental issues 5

1.2.3 Modelling issues 7

1.3 A biological system: the chick *in ovo* 9

1.4 Overview of the thesis 9

2 Resolving magnetic fields in space and time 11

2.1 General considerations 11

2.2 Practical aspects of measuring static fields 13

2.2.1 Relative motion between source and detector 13

2.2.2 Eliminating spurious signals 14

2.2.3 Phase distortion 16

2.3 The spatial resolution of magnetic fields 18

2.3.1 Resolving field patterns: a simulation 18

2.3.2 The effect of coil size 22

2.3.3 Practical considerations 27

2.3.4 Summary 28

3 SQUIDLET: a high resolution magnetometer 30

3.1 The dewar 31

3.2 Gradiometers 33

3.2.1 Discrimination against distant sources 34

3.2.2 A high resolution gradiometer 37

3.2.3 Balancing the coils 41

3.3 The operating SQUIDLET probe 51

3.3.1 Noise 51

3.3.2 Hysteretic behaviour 55

3.3.3 High resolution performance of SQUIDLET 57

3.4 Measurements of ionic currents from *Acetabularia* 60

4 Modelling discrete and extended sources 63
4.1 Introduction . . . 63
4.2 Discrete source models . . . 64
4.3 Extended sources . . . 65
4.3.1 Mathematical framework . . . 65
4.3.2 Implementation . . . 67

5 Electrophysiology of developing systems 70
5.1 Introduction to electrophysiology . . . 71
5.1.1 Bioelectricity and regeneration . . . 72
5.1.2 Developmental bioelectric effects . . . 74
5.2 Chick embryology . . . 76
5.2.1 The embryo . . . 77
5.2.2 The extra-embryonic membranes . . . 79
5.3 Electrophysiology of the egg . . . 83
5.4 Low resolution measurements . . . 84
5.4.1 Procedure and typical results . . . 85
5.4.2 Auxiliary experiments . . . 86
5.4.3 Improvements to the experiment . . . 87

6 High resolution measurements of chick eggs 89
6.1 General protocols . . . 89
6.1.1 Treatment of the eggs . . . 89
6.1.2 Data acquisition software . . . 90
6.1.3 Experimental procedure . . . 93
6.1.4 Preprocessing the data . . . 94
6.2 Measurements of intact eggs . . . 94
6.2.1 The effect of cooling . . . 94
6.2.2 Serial measurements . . . 97
6.3 Serial measurements of windowed eggs . . . 98
6.3.1 Protocol for windowed eggs . . . 98
6.3.2 Results . . . 100
6.4 The 'snapshot' measurements . . . 104
6.5 Modelling the source as a distributed current density . . . 106
6.5.1 A physiological model . . . 106
6.5.2 Using the distributed source model . . . 108
6.5.3 Results . . . 109
6.6 Discussion and implications . . . 109
6.6.1 The distributed source . . . 109
6.6.2 A localized source? . . . 113

7 Very high resolution measurements 115
7.1 Acquiring the data . . . 115
7.1.1 MicroSQUID: a very high resolution magnetometer . . . 115
7.1.2 Auxiliary apparatus . . . 118
7.1.3 Experimental protocol . . . 121
7.2 Analyzing the data . . . 123
7.2.1 Noise and initial measurements . . . 124
7.2.2 Constancy of the source . . . 125
7.2.3 Isofield contour plots . . . 127
7.2.4 Baseline corrections . . . 128
7.2.5 Summary of results . . . 130
7.2.6 An interpretation . . . 132
7.3 Modelling the data . . . 133
7.3.1 The distributed current source . . . 133
7.3.2 The smoothed V3 transformation . . . 137
7.3.3 Subtraction of the large-scale field . . . 139
7.4 Discussion . . . 140
7.5 The state of chick egg magnetometry . . . 141

Chapter 1

Introduction

"It is a pleasure to welcome our guests from many countries to the 7th International Conference on Biomagnetism held at New York University, in the great city of New York. This conference includes virtually all of the research areas dealing with magnetic fields accompanying biological processes ..." [67]

1.1 The state of biomagnetism

Lloyd Kaufman and Sam Williamson's introduction to the 1989 conference digest previewed an exhibition of posters, presentations and workshops covering a diversity of topics which impinged, more or less, upon the domain of biomagnetism. That domain, however, is difficult to define. "Magnetic fields accompanying biological processes" is a reasonable description, but it is neither exclusive nor all-embracing (consider magnetic resonance imaging and *in vitro* magnetopneumography, respectively).

Prior to embarking upon a scientific research project, it is desirable to have an understanding of the scope of that science, its interactions with other subjects and the particular areas where problems are to be addressed. I shall remark briefly on these topics.

Biomagnetism is certainly *concerned* with magnetic fields and living systems and it has carved its own niche, infiltrating both the physical and life sciences. It is frequently referred to as an interdisciplinary science and this is apparent in both the practice of biomagnetism and the backgrounds of the researchers it has attracted.

In biomagnetism, the electrical phenomena ubiquitous amongst living systems (biology) are studied via their associated magnetic fields (physics), most often using sensitive instruments which rely on superconductivity and cryogenics (also physics). Figure 1.1 shows the other disciplines which are making increasingly important contributions. As the instrumentation becomes more sensitive, biomagnetism relies more heavily on electronics. As more ambitious clinical problems are tackled, greater insights from medical scientists and psychologists are required. As data becomes more detailed and comprehensive, so the necessary techniques of mathematics and computing grow in complexity. Additionally, if high temperature superconducting ceramics prove viable as magnetic sensors or shields, then chemistry and materials science will be drawn in from the periphery.

Practitioners in biomagnetism contribute in a variety of ways and, by classifying the subject, the distribution of their endeavour can be examined. Any classification is neces-

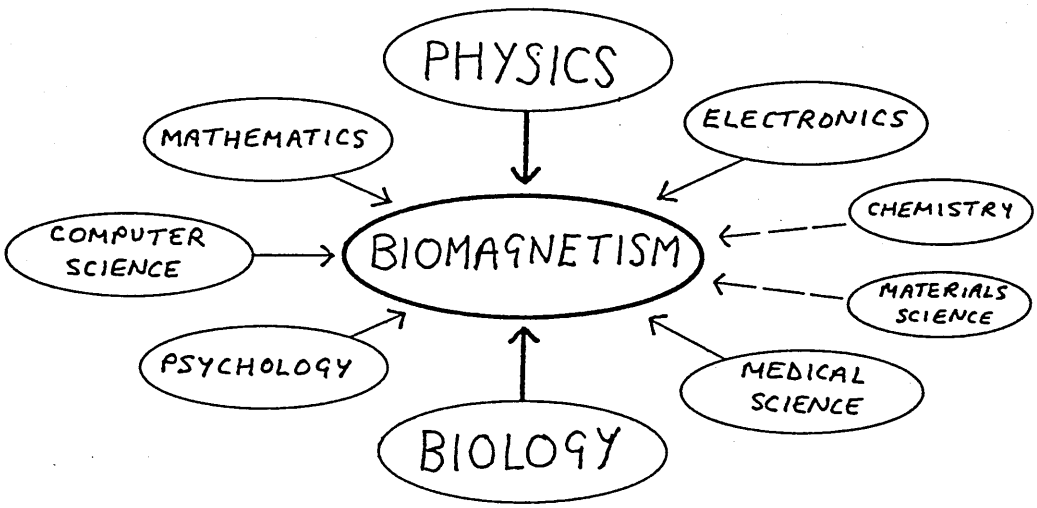

Figure 1.1 An interdisciplinary science

sarily somewhat arbitrary, but the six activities listed in table 1.1 cover all of the subject without overlapping too substantially. Each of the 169 submitted papers at the 7th International Conference on Biomagnetism was allocated to one or more of these categories. The papers were classified according to the area or areas that were deemed to have benefited from the reported work. For example, methods of magnetic shielding were considered to be 'experimentation' and multi-channel instruments to be either 'instrumentation' or 'theory' depending upon whether the paper reported an actual instrument or a theoretical analysis. Many contributors reported magnetocardiography (MCG) or magnetoencephalography (MEG) experiments within a specific medical context: each of these was split between 'applications' and 'interpretation'. Other papers discussed modelling techniques relevant to particular types of experiment and they were shared by 'modelling' and 'applications'.

Applications	36 %
Instrumentation	9 %
Experimentation	14 %
Theory	7 %
Modelling	15 %
Interpretation	19 %
(Sample: 169)	

Table 1.1 Distribution of current research effort

This survey indicates that there is a considerable emphasis on using the techniques of biomagnetic investigation in a diversity of applications and attempting to interpret the results of such studies. Relatively little effort is apparently being invested in theoretical analyses of the subject or in the development of instrumentation and experimental techniques[1]. As

[1]The impact of this result is somewhat diluted by considering that it is now 27 years since Baule and McFee's pioneering measurement of a magnetic component of the human heartbeat using induction coils of several million turns [6] and that substantial work has been done in all areas in the interim. There is, nevertheless, a lingering feeling that, in biomagnetism, everyone is ploughing ahead with complicated experiments generating vast quantities of data without taking proper account of the sensitivities and limitations of the technique.

described below, these are precisely the areas of activity of this project.

There are fundamental limits to the precision with which a spatially varying magnetic field distribution can be measured by any given magnetometer. These in turn limit the spatial precision with which a possible source can be specified and, if no account of this effect is taken, the interpretation of results can be misleading. The main theme of this thesis, then, will be the spatial resolution of measurements and, in particular, the drive towards high spatial resolution.

There is a second theme. Different biological functions proceed at very different rates and, consequently, biomagnetic signals can contain a wide range of frequencies. Because of the considerable interest in the human heart and brain, most studies have concentrated on these relatively high ($\gtrsim$ 1 Hz) frequency sources. However, there are a number of important applications of biomagnetism, such as the growth, development and regeneration of tissue, which involve much more slowly changing fields and this type of measurement has its own special sensitivites and difficulties. In this thesis, I shall be concerned with these areas and I shall therefore be discussing quasi-static (very slowly changing) fields.

Combining the themes of high spatial frequencies and low temporal frequencies produces an investigation into 'High resolution measurements of quasi-static biomagnetic fields'.

1.2 Issues addressed by this thesis

In this section I shall develop the main themes outlined in section 1.1 and introduce a third and subsidiary topic: the modelling of experimental data. The usual aim of analyzing biomagnetic data is to elucidate the electric current or magnetization configuration responsible for the measured magnetic field and, in general, this is only possible if a source model is used. In section 1.2.3, I shall discuss why modelling is necessary and contrast discrete and continuous models.

Before data can be analyzed, however, an instrument and an experiment are required. In sections 1.2.1 and 1.2.2, I shall describe the popular approaches to these issues and this will lead to considerations of the difficulties associated with making high resolution and quasi-static measurements, respectively.

1.2.1 Instrumental issues

At the heart of the most sensitive type of magnetometer system is a superconducting quantum interference device, usually referred to as a SQUID. The operation of SQUIDs and their control electronics has been extensively reviewed (for example [24], [91] and [49]). In this thesis, they will be considered simply as linear flux transducers which output a voltage change, ΔV_{out}, in direct proportion to the magnetic flux change, $\Delta\Phi_{in}$, at the SQUID:

$$\Delta V_{out} \propto \Delta\Phi_{in}. \tag{1.1}$$

Although a SQUID could be used directly to measure magnetic field changes, this is not generally done. In practice, it is isolated from the environment and a 'gradiometer', which is connected to it, actually detects the field. The gradiometer, which is also superconducting,

usually consists of a 'sensing coil' and one or more 'compensating coils' as shown in figure 1.2. The function and design of gradiometers will be described in detail in section 3.2.

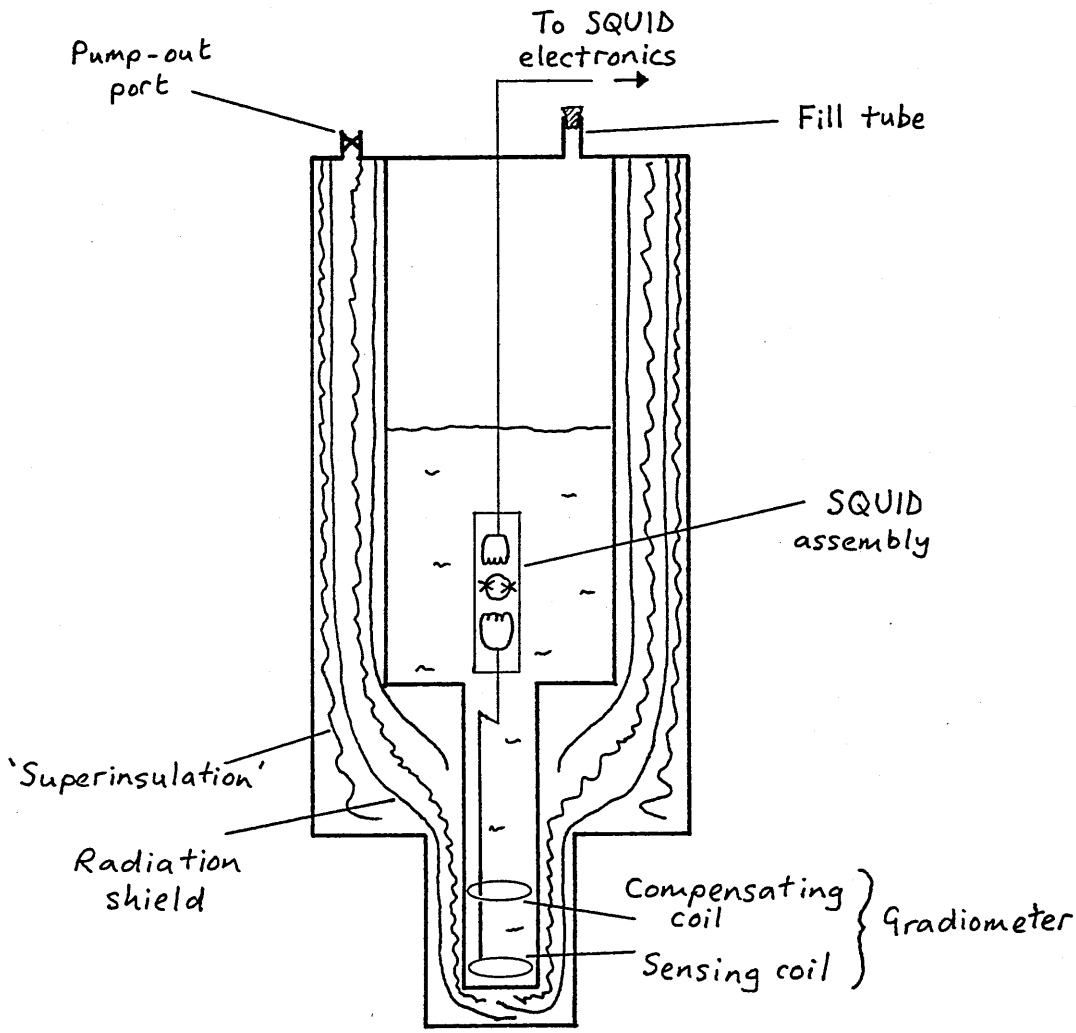

Figure 1.2 Schematic diagram of a SQUID system

The first stage in the mechanism of magnetic field detection is a time-varying supercurrent which is induced in the sensing coil by the time-varying flux through it. Thus, the coil is sensitive to the magnetic field component perpendicular to its plane. However, it is not sensitive to the fine structure of the magnetic field within the coil because any instantaneous measurement effectively *spatially averages* the field over the area of the coil. For static fields it is possible to obtain some information about this fine structure by scanning, and this technique will be considered in section 2.2. As a rough guide, though, the sensing coil diameter represents the best spatial resolution of the field which can be achieved, and minimizing the coil size improves the resolution.

The trade-off suffered by reducing the coil size is reduced overall sensitivity since a smaller coil intercepts less flux and consequently generates a weaker signal. The compromise struck for conventional systems has been to adopt coil diameters of 20–30 mm and these have proved to be well-suited to measurements of the human heart and brain.

Until recently there has been no effort to improve spatial resolution by reducing coil size, largely because, for most applications, very little extra information about the sources would be forthcoming. The electrical activity underlying MEG and MCG signals occurs several centimetres from the sensing coil beneath the skull and rib cage respectively and, as will be shown in section 2.3, it is not possible to resolve features of the magnetic field to much greater accuracy than the depth of the source. Thus, it would only be worthwhile to reduce the coil size if the source to detector distance could also be reduced.

Contributing to this separation, in addition to the interjacent body tissue, is the helium dewar which is required in order to maintain the superconducting state of the coils and SQUID. A conventional dewar design consists of two concentric fibreglass vessels separated by an evacuated space. Inside this space radiation shields and sheets of 'superinsulation' are mounted, to minimize the influx of heat (see figure 1.2). Although reducing the overall thickness at the tail is desirable for sensitivity and resolution, it increases the rate of helium boil-off and, hence, running costs. A typical biomagnetic dewar has a liquid helium to room temperature separation of about 12–15 mm.

Although these standard designs are fine for neuromagnetic and cardiomagnetic studies, they are not suitable for studying small biological systems in which the electrical activity involves one or a few cells rather than thousands or millions [103]. Investigations of biomagnetic sources such as single nerve or muscle cells, embryonic organisms and regenerating tissue require a magnetometer with a much better spatial resolution [104]. Chapter 3 describes just such an instrument.

1.2.2 Experimental issues

SQUIDs are excellent measuring devices because, in addition to their great sensitivity to tiny magnetic fields, they have a wideband frequency response from dc to tens of kilohertz. Figure 1.3 shows typical noise power spectra, which were measured by an unshielded SQUID magnetometer. The mains spike at 50 Hz and its third harmonic at 150 Hz are almost always present and there may be other isolated spikes due to local noise sources such as electric motors, switches or fans. There is always noise at very low frequencies, which can be caused by slow variations in the background field and drift in the SQUID electronics.

The mains interference and its harmonics are generally dealt with using filters[2]. A common arrangement is to remove frequencies of 100 Hz and higher with a low-pass filter and to suppress the line frequency with a notch filter centred at 50 Hz. This leaves a low-noise bandwidth between about 0.1 Hz and 100 Hz, which is ideal for cardiac signals, evoked MEG signals and spontaneous brain activity such as alpha and delta waves. To record these signals, the magnetometer coil set is simply positioned close to the source.

Slower waves, changing over timescales of minutes, hours or days are very difficult to measure directly because of drift[3]. Examples include brain activity connected with spreading cortical depression [75], fields associated with the development and regeneration of tissue

[2]Care must always be taken with filtered data because phase shifts (for instance, from a 50 Hz notch filter) may complicate interpretation.

[3]Running a magnetometry experiment permanently for several hours or days may also prove inconvenient for other reasons.

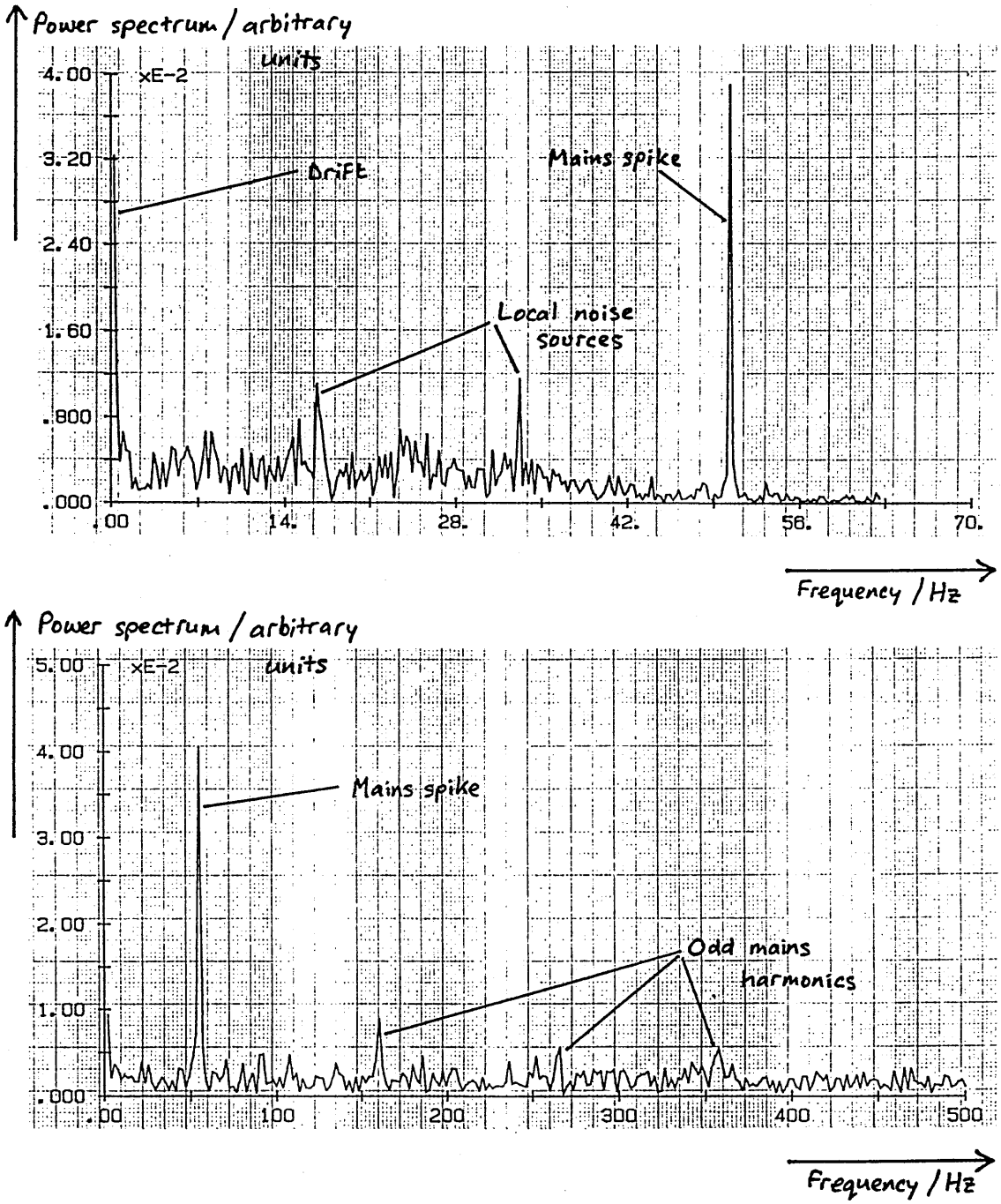

Figure 1.3 Typical SQUID magnetometer power spectra

[92] and the effectively static signals of interest in biosusceptometry [80]. In the last case, a dipole moment is induced into a tissue sample, and so the only time development is due to magnetization relaxation. In order to measure signals from all these sources, their frequency can be artificially increased to bring them into the suitable bandwidth.

This is done by introducing relative motion between the source and detector (scanning). In this way, the detector becomes sensitive to the *spatial* frequency of the field. For instance, if the spatial variation of the field has a component of 40 m^{-1}, and the scanning speed is 0.2 ms^{-1}, the SQUID will record a signal at 8 Hz, at which frequency there is little interference from other sources. A convenient experimental geometry is to measure the field in a horizontal plane above the specimen. For several reasons it is impractical to move the magnetometer and so measurements are usually made by passing the specimen beneath the fixed detector. However, when analyzing data, it is intuitively easier to think of the source as

stationary, and so the magnetometer is perceived to move in the specimen's reference frame.

Because it may take several minutes to record a field map, it is important that the field pattern does not change (significantly) during this time. If this condition is met, the map can serve as a 'snapshot' in the slow evolution of the pattern, and a sequence of snapshots can be produced by repeating the mapping at suitable intervals.

There are a number of specific features of dc measurements that must be considered.

The spatial analogue of signal averaging may be used to improve the signal-to-noise ratio by repeating scans, but the signal must remain (effectively) constant. Also, the extent of the map should be wide enough that the biomagnetic field becomes negligible at the edges to ensure a knowledge of the zero field level. Scanning speed and sampling rate must be carefully chosen, otherwise the signal profile can be distorted. Furthermore, the ambient dc field in the region of measurement should be maintained close to zero to avoid inadvertently recording diamagnetic or paramagnetic signals from the sample. Finally, the most serious difficulty is often created by ferromagnetic contamination.

Problematic though this type of measurement may be, it is the only way to study quasi-static fields and all the difficulties *can* be overcome. I shall discuss these problems in more detail in section 2.2.

1.2.3 Modelling issues

The primary objective in biomagnetism experiments is to understand the mechanism which generated the measured field. This is usually an electric current configuration and, although analytical expressions based on the Biot-Savart law,

$$d\mathrm{B} = \frac{\mu_0 I}{4\pi}\left(\frac{d\mathrm{l}\times\mathrm{r}}{r^3}\right), \tag{1.2}$$

exist for calculating the magnetic field due to a given current configuration, the converse is not true. These two calculations (current to field and field to current) are termed the forward and inverse problems respectively.

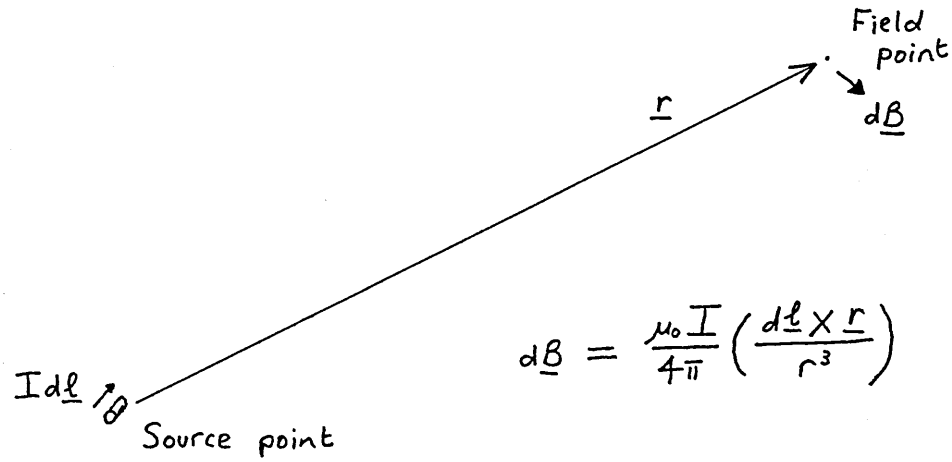

Figure 1.4 The Biot-Savart law

The forward problem can be solved by applying the Biot-Savart law (equation 1.2 and

figure 1.4) to every current element. The inverse problem, on the other hand, has no unique solution. Nevertheless, helpful solutions to the inverse problem *can* be found by assuming a source model with a limited number of parameters [84].

The simplest source model is a current dipole: an infinitesimal current element which can be fully described by the magnitude (in Am) and direction of its dipole moment $\mathbf{Q}$ and its position vector $\mathbf{r}'$. A current dipole produces an azimuthally directed magnetic field $\mathbf{B}(\mathbf{r})$ which decreases in strength with the square of the distance,

$$\mathbf{B}(\mathbf{r}) = \left(\frac{\mu_0}{4\pi}\right) \frac{\mathbf{Q} \times (\mathbf{r} - \mathbf{r}')}{|\mathbf{r} - \mathbf{r}'|^3}, \tag{1.3}$$

where primed coordinates represent the source space and unprimed coordinates represent field points. When the normal component of the field associated with a current dipole is mapped in a plane (see figure 1.5), the separation of the field extrema Δ is related to the depth of the dipole d by

$$\Delta = d\sqrt{2}. \tag{1.4}$$

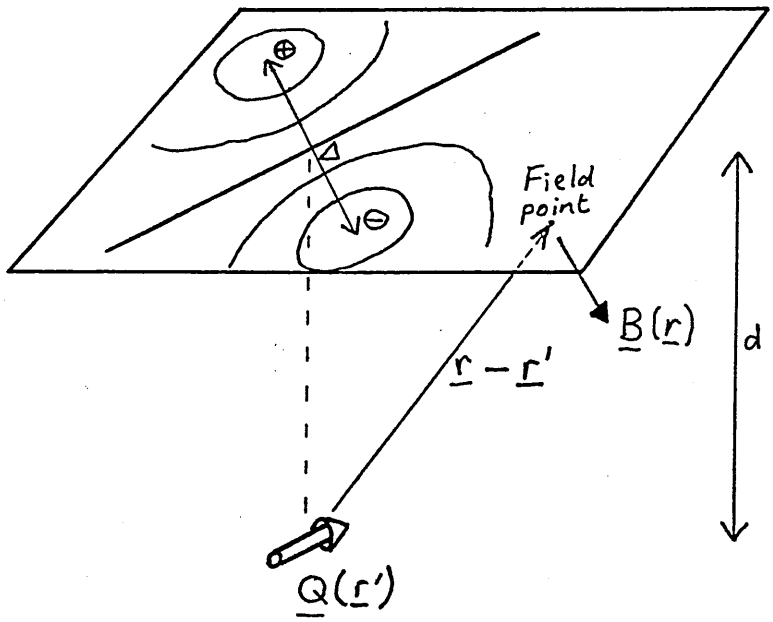

Figure 1.5 Isofield contour map due to a current dipole

Largely because of the mathematical intractability of other models, the current dipole model was studied in detail. The magnetic fields due to current dipoles within spherical conducting spaces were calculated [26] as a step towards a more realistic model of the magnetoencephalogram. This type of model utilizes modified forms of equations 1.3 and 1.4 to compute the location, orientation and strength of the *effective* dipole from the magnetic field data. Its reliability can be tested, in a certain sense, by calculating a 'quality of fit' parameter that depends on the correlation between the data and the computed field due to the effective dipole.

However, the assumption that the electrical activity of the brain, in response to a sensory stimulus, is similar to a point current dipole is a highly questionable one. There are up to a

hundred thousand million neurons in the human brain, whose interconnections are numerous and complex.

There is another problem concerning the use of an effective dipole, which is more subtle. As will be demonstrated in section 2.3, it is easy to find configurations of several current dipoles or even continuous current distributions that produce field patterns superficially similar to that of a single current dipole. Any field pattern can be expanded as a series of terms due to a dipole, a quadrupole, an octupole, etc [89] and, as the distance from the source is increased, the dipole term progressively dominates the signal. Consequently, any current distribution appears dipolar when the magnetic field is mapped sufficiently far away.

The current dipole can be considered as a special case (a delta function) of the fully general current density distribution. However, this is a very much more difficult model to apply. An approach that has gained popularity recently is to treat the problem probabilistically. The basis for this method and the development of a sophisticated and general algorithm for solving the biomagnetic inverse problem that has been implemented at the Open University [56] will be the subject of chapter 4.

1.3 A biological system: the chick *in ovo*

Steady ionic currents have been observed to accompany the development and regeneration of living tissue [62], [10] in many species. The embryo of the chick, *Gallus domesticus*, has been widely studied as a model developing system, and developmental currents have been observed [63]. In a preliminary magnetometer investigation, Lennard [71] measured large ($\sim$10 pT) signals around fertilized chick eggs.

Peak signals were recorded on the third or fourth day of incubation when the living contents of the egg comprise a 5 mm embryo and an area of extra-embryonic membranes about 20 mm in diameter [79]. Since unfertilized eggs were found to be magnetically silent, the measured signals were presumed to be generated within these small vital structures. These and later measurements [64] were made with a conventional magnetometer system which had a sensing coil diameter of 24 mm.

In order to elucidate more precisely which structures and ionic processes are responsible for the fields, it was necessary to make measurements with much higher resolution. The field patterns do not change noticeably over a period of up to ten minutes and so they can be treated as quasi-static fields. Chapters 6 and 7 describe high resolution dc measurements of these fields, and the results of applying both localized and extended source models to the data.

1.4 Overview of the thesis

In chapter 2, I shall discuss the measurement of magnetic fields that vary in time and space, concentrating on theoretical aspects of making high resolution measurements and practical aspects of recording dc fields. The design and development of SQUIDLET, a magnetometer destined specifically for high resolution quasi-static measurements, will be

described in chapter 3. Modelling of biomagnetic data will be the subject of chapter 4, and I shall concentrate on the development and implementation of the extended source model that was used in the analysis of data in the later chapters. In chapter 5, I shall preface the chick experiments with a review of developmental electrophysiology and a summary of previous magnetometer measurements of chick eggs. The final two chapters will contain details of high resolution measurements of chick eggs, firstly using SQUIDLET (chapter 6), and secondly using a magnetometer with even better spatial resolution (chapter 7).

Chapter 2

Resolving magnetic fields in space and time

There is a gate in Japan, a gate in Neiko, which is sometimes called by the Japanese the most beautiful gate in all Japan; it was built in a time when there was great influence from Chinese art. The gate is very elaborate, with lots of gables and beautiful carving and lots of columns and dragon heads and princes carved into the pillars, and so on. But when one looks closely he sees that in the elaborate and complex design along one of the pillars, one of the small design elements is carved upside down; otherwise the thing is completely symmetrical. If one asks why this is, the story is that it was carved upside down so that the gods will not be jealous of the perfection of man. Richard Feynman [33]

There is symmetry between space and time that can be illustrated by considering the nature of fields. For instance, magnetic fields are continuous in both space and time. Hence, it is not possible to map a field completely with a finite number of measurements in any region of space during any particular time interval. However, that state of affairs can be approached by making higher resolution measurements more frequently.

In this chapter, I shall discuss the measurement of spatially and temporally varying magnetic fields. After introducing the topics in section 2.1, I shall consider separately two limiting cases. Section 2.2 will concentrate on practical aspects of the measurement of static fields. Then, in section 2.3, I shall discuss the measurement of fields containing high spatial frequencies and demonstrate that, in general, two improvements need to be made to a magnetometer system so that it can measure a particular field pattern with higher resolution.

2.1 General considerations

Classical electromagnetism is founded upon the semi-empirical equations written down by Maxwell in 1865:

$$\int_s \mathrm{E}.d\mathrm{A} = \frac{Q_T}{\varepsilon_0} \tag{2.1}$$

$$\int_s \mathrm{B}.d\mathrm{A} = 0 \tag{2.2}$$

$$\oint_c \mathrm{E}.d\mathrm{l} = -\frac{d}{dt}\Phi \tag{2.3}$$

$$\oint_c \mathrm{B}.d\mathrm{l} = \mu_0 I_T. \tag{2.4}$$

In these equations, respectively, E and B represent the electric and magnetic field vectors, dA is an elemental area of the closed surface S and dl is an elemental length of the closed circuit C, Q_T and I_T are the total enclosed charge and current[1], ε_0 and μ_0 represent free space permittivity and permeability, and Φ is the total magnetic flux threading C.

Electric and magnetic fields are smoothly varying functions of space and time. They are also continuous in the sense that they possess a value in the interval between any two arbitrarily close points in space or time. These are examples of a symmetry which is revealed when considering these fields: space and time are linked via Maxwell's equations and neither is more fundamental than the other. This idea will be a theme of this chapter.

Experiments in biomagnetism rely on measurements of a component of the magnetic field vector, and subsequent analysis of those measurements. Because numerical analysis requires that the data be in the form of a finite number of discrete values, the field must be *sampled*, both spatially and temporally, and the higher the frequency of sampling, the more accurately will the recorded data represent the actual field. Ideally, a close-spaced multiple-channel magnetometer would be placed close to the source and sampled at high frequency. The spatial and temporal resolution could be improved by introducing extra, more closely spaced channels and by sampling them more frequently. In practice, however, these factors are limited by engineering and data storage constraints, and ultimately by cost. For instance, the latest multichannel instruments [7], [53] monitor thirty or more sites over a two-dimensional space simultaneously and are available for a few million dollars: inevitably, compromises must be struck.

If the available instrumentation consists of a single-channel magnetometer and a standard laboratory data acquisition computer, there are two types of biomagnetic source which can be investigated by different techniques, and in each case a criterion of acceptability needs to be satisfied.

If the signal is reproducible, such as the magnetoencephalogram of a primary cortical response, the magnetometer may be positioned successively at different sites close to the source and allowed to record data as a function of time at each. The signal must be evoked again (by re-presenting the stimulus) at each new position; in fact, the signal may be evoked many times at each recording site so that random noise in the waveforms can be reduced by signal averaging. The data can then be collated to allow examination of the spatial distribution of the signal at any particular latency. This is an example of recording as a function of time first and space second, and the method is legitimate only if the evoked signal is genuinely reproducible. I shall refer to this type of measurement as a 'dynamical' measurement.

Conversely, the field may be measured as a function of space first and time second. This is the only method for a single-channel instrument to obtain temporal *and* spatial information about an innate biomagnetic source (ie a spontaneous, rather than an evoked, process). Because it takes time to measure a field pattern over a region of space, this type of recording is restricted to quasi-static fields. It is critical that the field pattern does not change (significantly) during the time taken to record a complete map, and this condition

[1] I_T includes the displacement current as well as the free current.

can be tested by comparing subsets of the data recorded at the start and at the end of the measurement.

The measurements can then be repeated every few minutes, hours or days to investigate the time development of the field pattern. The remainder of this thesis will be concerned with quasi-static fields unless I explicitly state that I am reporting a dynamical measurement.

2.2 Practical aspects of measuring static fields

2.2.1 Relative motion between source and detector

As described in section 1.2.2, scanning a quasi-static magnetic field artificially raises its frequency into a low-noise region of the SQUID's power spectrum. Because an operational SQUID magnetometer is housed in a bulky fluid-filled container it is usually more convenient to move the source than the detector, although it is intuitively simpler to imagine the opposite arrangement. When interpreting results, therefore, care must be taken with reference frames.

The sensing coil in a standard SQUID magnetometer (see figure 1.2) is at the bottom and the simplest scanning mechanism is a two-dimensional moving stage beneath the dewar with vertical adjustment of the specimen platform (see figure 2.1). This is relatively straightforward from an engineering viewpoint and data recorded in this way are easily interpreted with a Cartesian coordinate system.

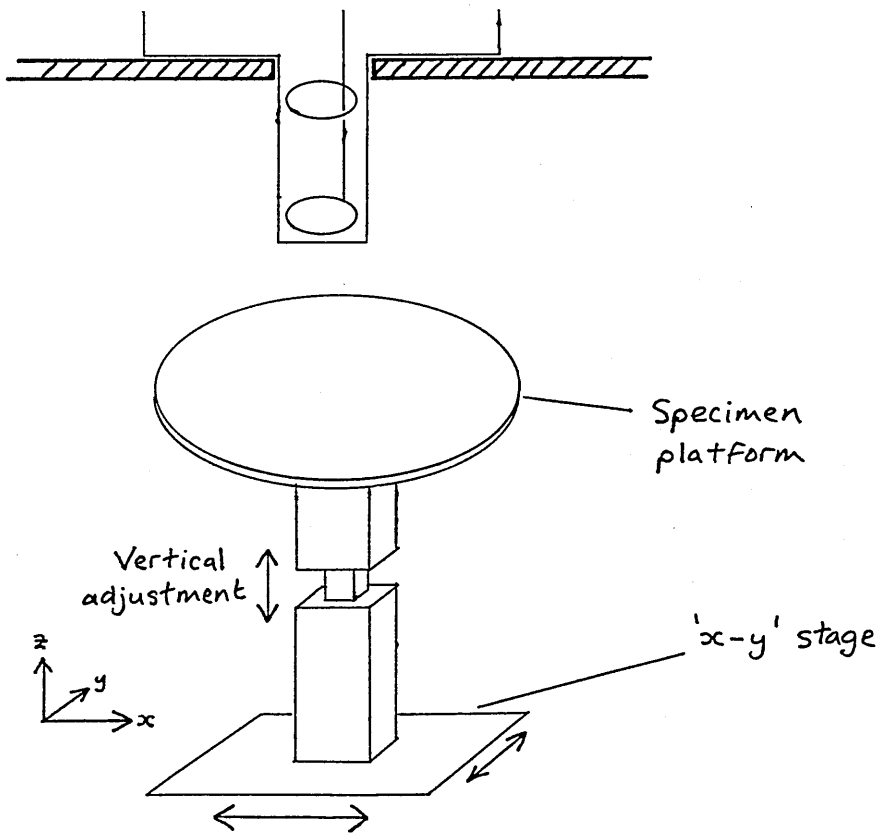

Figure 2.1 Axial measurement in a plane with an x-y stage

An alternative design could measure the field on the surface of a sphere, by rotating the

source about the vertical axis while the dewar is tilted to various latitudes. This may be more appropriate when the source has spherical geometry (eg a head or an egg). It would then be possible (with different coil geometries) to measure either the radial or tangential components.

I shall only consider the arrangement illustrated in figure 2.1: the measurement of the vertical component of the field in a horizontal plane. Data recorded with this technique can be conveniently displayed as 'isofield contour maps' in which points of equal magnitude of the normal field component are linked by a contour line. Figure 1.5 shows the contour map obtained by scanning the field of a current dipole.

The simplest procedure for mapping a rectangular area is to perform a series of parallel scans while recording the SQUID output. Although the output of a SQUID gives an accurately calibrated measure of relative field strengths, it provides no information about the *absolute* field. One method of locating the zero-field baseline would be to make control measurements with no source present. However, there is a danger that the flux-locked SQUID, which can operate close to any one of a number of quantized flux levels, may 'jump' to another level, or that there will be significant drift due to noise sources, between the two sets of measurements. The safest strategy is to ensure that the area mapped is large enough to allow the field due to the source to become negligible at the edges; the values obtained in these peripheral regions can then be assumed to be the baseline.

As with dynamical measurements, it is possible to improve the signal-to-noise ratio by signal averaging. For static measurements, this involves repeating the same scan[2] several times and then, at each coordinate along the scan, averaging all the measured field values. The signal must not change (significantly) between these scans, but the more stringent condition, that the signal does not change (significantly) whilst recording the entire map, must be satisfied in any case.

2.2.2 Eliminating spurious signals

The major difficulty associated with the measurement of static magnetic fields is the identification and elimination of magnetic contamination of the signal. Such contamination is encountered in two forms: permanently magnetized particles which adhere to the sample or scanning apparatus, and the magnetization of constituents of the sample due to a net ambient field. I shall discuss them separately.

Ferromagnetic particles are commonly found in many conventional construction materials (such as laminated wood, glass, plastics and metals) and in dust, particularly near areas where machine tools are used. There is typically a strong local field around each particle, and if the particle is within or becomes attached to the sample which is being scanned, or part of the scanning apparatus, its field will be measured along with that of the sample.

Fortunately, it is relatively easy to identify this situation in experiments in which a current distribution is being studied. If it is suspected that ferromagnetic contamination is responsible for a particular feature on a scan, the hypothesis can be tested by passing

[2] I shall use the noun 'scan' specifically to mean a single one-dimensional pass of the source beneath the detector, whereas 'scanning' will more loosely refer to the whole process of recording static field maps.

a permanent magnet close to the sample and the scanning apparatus. If ferromagnetic contamination *was* the source, its dipole moment will be affected and a repeat scan will, in general, have an altered field profile. On the other hand, if the feature is genuinely due to the current source, the magnet will have no effect and the repeat scan will be identical.

Removing contamination relies on trial and error procedures. Wooden surfaces can be sandpapered and biological samples can be washed (with distilled or filtered water), but if the measured signal continues to be modifiable by a permanent magnet, then the contaminated component or sample must be replaced.

This technique will not identify contamination in experiments to study a magnetization distribution since waving a magnet around will also alter the signal of interest. In this case, prevention is better than cure, and extra care should be taken to avoid contamination during preparation and measurement.

A related artefact which can contaminate the measured signal is due to the magnetization of the sample or scanning apparatus in an ambient field. The susceptibility of all materials is either predominantly paramagnetic, in which case the material becomes magnetized in the same direction as the ambient field, or diamagnetic — producing an opposite magnetization. Water is the major constituent of all biological material and so most tissues have a susceptibility close to that of water. In biomagnetism, then, we are concerned primarily with the magnetization of water in the Earth's magnetic field.

To illustrate the seriousness of this problem, I shall calculate the magnetization field due to 10 cm^3 of water. Water is a diamagnet with a susceptibility[3] of $\chi_B = -9.1 \times 10^{-6}$ and the Earth's magnetic field at its surface in Milton Keynes, UK is $\mathrm{B}_{earth} = 4.8 \times 10^{-5}$ T directed downwards at 24° to the vertical. Magnetization M is given by

$$\mathrm{M} = \chi_B \frac{\mathrm{B}_{earth}}{\mu_0} \tag{2.5}$$

and so the magnetization of water is about 3.5×10^{-4} Am^{-1} in the opposite direction to the geomagnetic field. The magnetic dipole moment (the magnetization multiplied by the volume of material) is thus about 3.5×10^{-9} Am^2.

The peak vertical field magnitude due to a magnetic dipole at a distance z is given by

$$B_{z,peak}(z) = \frac{\mu_0 m_z}{2\pi z^3}. \tag{2.6}$$

Taking account of the angle of the geomagnetic field lines, then, the magnetic field 2 cm above 10 cm^3 of water due to its magnetization has a magnitude of about 80 pT.

This is much greater than most biomagnetic fields and to remove this interference, the ambient field needs to be cancelled. A set of Helmholtz coils can reduce the net field to 10–100 parts per million of the Earth's field in the central region, thus reducing the magnetization field to a few femtoTesla.

[3] I have chosen to use χ_B (where $\chi_B = \chi_M/\{\chi_M + 1\}$) for susceptibility instead of the more conventional χ_M (although the difference is only 1 part in 10^5 in this case) because B is more commonly quoted for laboratory magnetic fields than field strength H. The vector B is properly called the flux density and it is measured in Tesla. However, this terminology can be misleading and I intend to refer to B in this thesis simply as the magnetic field.

Neither magnetization fields nor ferromagnetic contamination cause difficulties when making dynamical measurements because there is no relative motion between the source and the detector.

2.2.3 Phase distortion

In this section, I shall describe another problem inherent in measurements of static fields: a distortion of the true signal caused by low-pass filtering. After estimating a typical magnitude of the effect, I shall explain the precautions which can be taken to ensure that the error introduced is not significant.

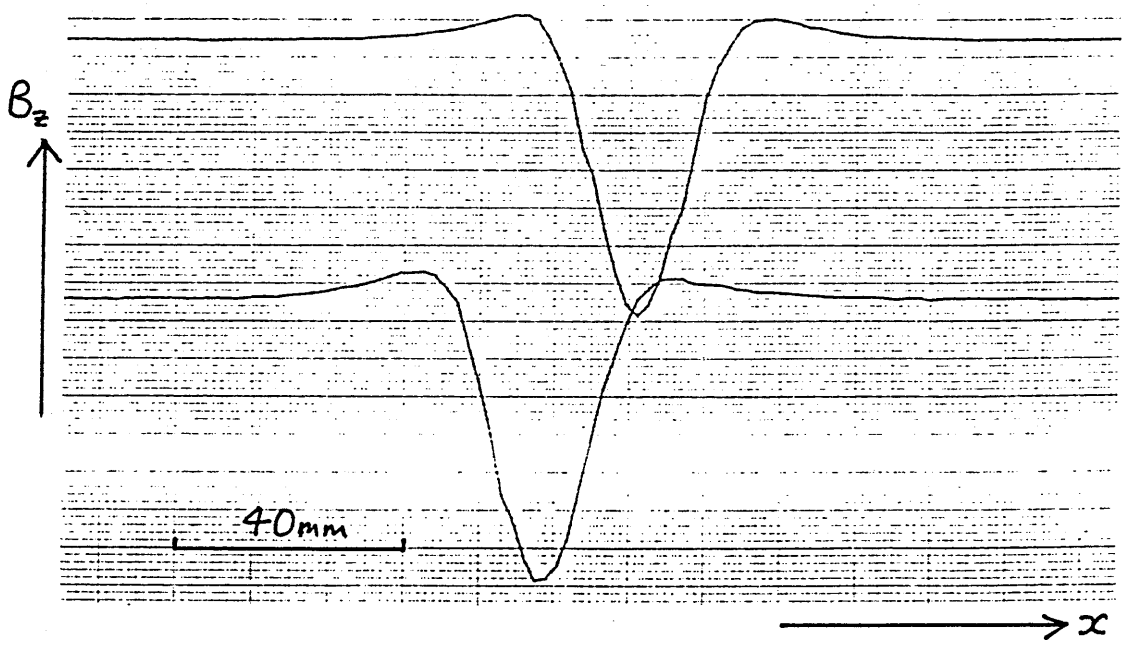

Figure 2.2 Phase distortion of a signal

Figure 2.2 illustrates the problem. It shows two scans over a loop of current-carrying wire. In the upper scan, the loop was travelling from right to left, and vice-versa in the lower one. Although the shape of the field profile is qualitatively correct in both cases, there is a large offset between the two traces. A distortion of the true signal has been introduced, which depends on the direction of relative motion of the magnetometer with respect to the source.

The offset is greatest at high scanning speeds and approaches zero as the speed is reduced. It also depends on the cut-off frequency of the low-pass filter: the lower it is, the greater is the offset and vice-versa, as shown below.

Taking a simplified example (see figure 2.3) the transfer characteristic of a first-order low-pass filter (containing a single resistor-capacitor section) is given [66] by

$$A = \frac{V_{out}}{V_{in}} = \frac{\frac{1}{j2\pi fC}}{\frac{1}{j2\pi fC} + R} = \frac{1}{1 + j\frac{f}{f_c}} = \frac{1 - j\frac{f}{f_c}}{1 + \frac{f^2}{f_c^2}}. \qquad (2.7)$$

V_{out} and V_{in} are, respectively, the output and input signals, f is the frequency, $f_c = \{2\pi RC\}^{-1}$ is the filter's cut-off frequency (the -3 dB point) and $j = \sqrt{-1}$.

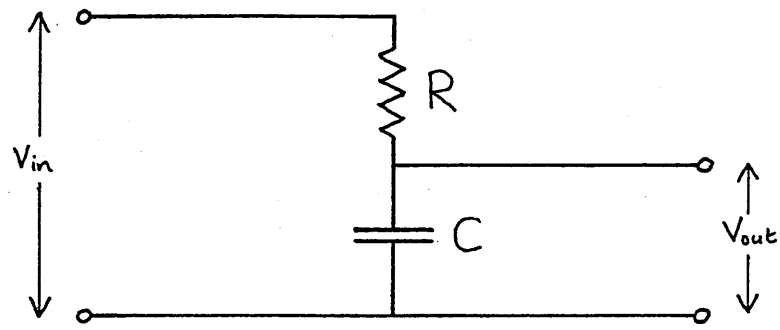

Figure 2.3 A first-order low-pass filter

There will be a phase shift ϕ between the output and input signals which is given by

$$\tan\phi = \frac{Im(A)}{Re(A)} = -\frac{f}{f_c}. \tag{2.8}$$

Now, this phase shift depends on the signal frequency, and any real signal contains a range of frequencies. To further simplify the analysis, I shall consider the field profile measured above a single long current-carrying wire (see figure 2.4 in which the direction of current is into the page). This signal clearly has one dominant spatial frequency, which depends on the depth d of the wire below the scanning plane.

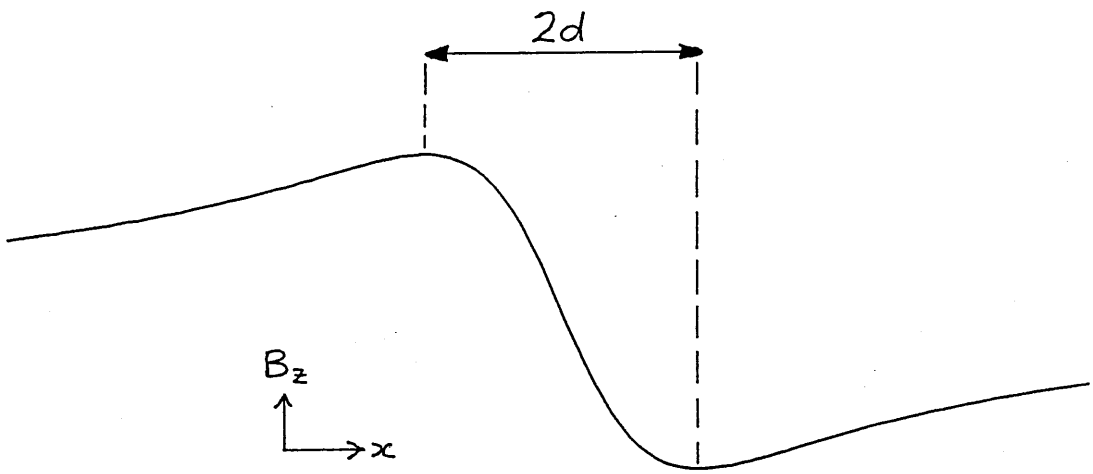

Figure 2.4 Field profile measured a distance d above a single long current-carrying wire

The extrema separation in this field profile is $2d$ (compare this with equation 1.4 for an infinitessimal current dipole: $\Delta = d\sqrt{2}$) and so the equivalent wavelength of this dominant spatial frequency component is $4d$. Now, by incorporating the speed of scanning v, it is possible to translate this spatial frequency component into the temporal frequency component that would be recorded:

$$f = \frac{v}{4d}. \tag{2.9}$$

Thus, using equation 2.8, the phase shift ϕ can be determined in the time domain and this

must be equal to the spatial phase shift:

$$\phi = \arctan\left(-\frac{v}{4df_c}\right) = 2\pi\frac{\delta x}{4d}. \tag{2.10}$$

Thus, the shift of the signal along the x-axis δx is given by

$$\delta x = \frac{4d}{2\pi}\arctan\left(-\frac{v}{4df_c}\right). \tag{2.11}$$

This equation is almost insensitive to d for small shifts and so, choosing an arbitrary depth of 20 mm, the effect of varying the scanning speed and cut-off frequency can be investigated. Scanning at 5 cms^{-1}, the shift is 0.08 mm ($f_c = 100\text{Hz}$), 0.20 mm ($f_c = 40\text{Hz}$) and 0.79 mm ($f_c = 10\text{Hz}$). However, scanning at 100 cms^{-1} (which is not ridiculously fast), the shift is 1.6 mm ($f_c = 100\text{Hz}$), 3.9 mm ($f_c = 40\text{Hz}$) and 11.4 mm ($f_c = 10\text{Hz}$). Because v may be positive or negative depending on the direction of travel, the actual offset between two scans in opposite directions is $2\delta x$.

This analysis ignores the effect of the gradiometer's compensating coils and the spatial averaging of the sensing coil, and greatly simplifies the configuration of the low-pass filter. In practice, these effects tend to increase the calculated offset further, making it imperative that any experimental protocol take account of this phenomenon. Ideally, a slow scanning speed and a high cut-off frequency are required. 5 cms^{-1} is about the slowest rate at which a platform can be moved smoothly by hand, but this can be reduced with a motor and suitable gearing. The higher the cut-off frequency is, the greater is the noise in the signal and so a compromise must be struck. Most importantly, for high resolution measurements, the maximum position error must be known as this may limit the accuracy of the overall measurement.

2.3 The spatial resolution of magnetic fields

In this section I shall discuss how higher resolution can be achieved and what extra source information might be obtained in this way. In section 2.3.1, I shall examine the field patterns due to various simple model source configurations and deduce that *two* modifications need to be made to a magnetometer system in order to improve its resolving power. Section 2.3.2 is a study of the effect of coil size on the spatial resolution of a magnetometer. Finally, in section 2.3.3, I shall review attempts to improve spatial resolution and discuss the likely effect on practical aspects of biomagnetic measurements (such as helium cost, system noise and sensitivity) of making a high resolution system.

2.3.1 Resolving field patterns: a simulation

In section 1.2.1, I asserted that the best achievable spatial resolution of a magnetometer system was roughly equal to the diameter of its sensing coil. That hypothesis will be examined more closely in section 2.3.2. I wish here, however, to go back one stage further and consider field patterns themselves, without worrying about the practicalities of measuring them. I shall calculate field components due to certain current configurations *at points in space.*

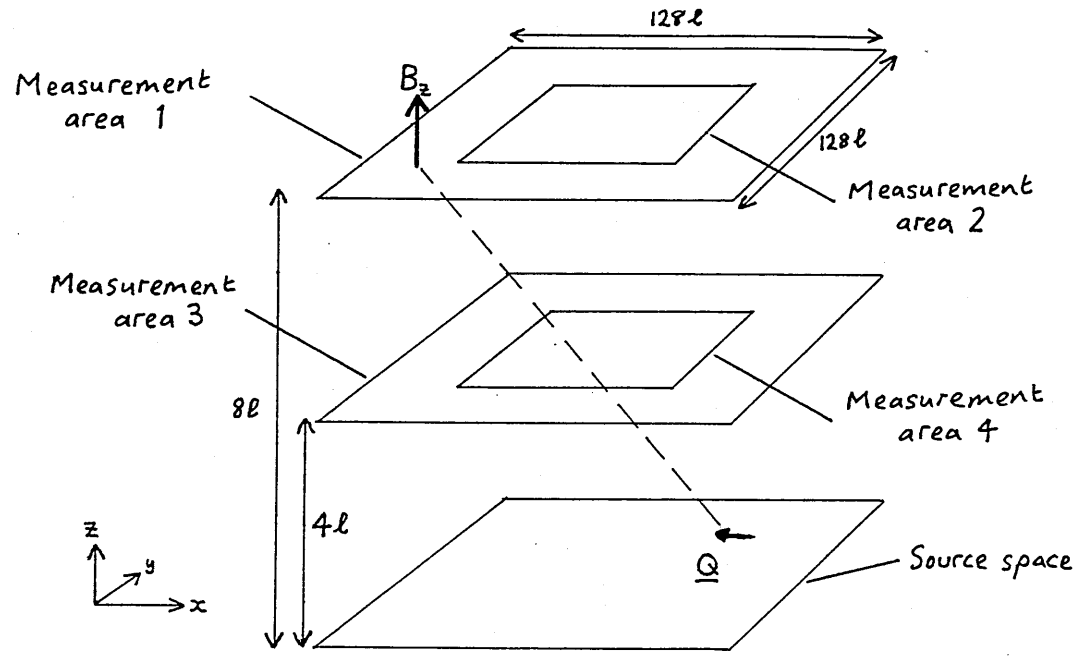

Figure 2.5 Experimental geometry for generating the simulated data

Figure 2.5 shows the geometrical arrangement which is used in the simulations. Note that the vertical scale has been greatly expanded for clarity. The source space is two-dimensional and coplanar with the x-y plane. It contains the coordinate origin at its centre. All the source configurations consist of a number of current dipoles whose position and orientation lie within this space. In each of a number of square 'measurement areas', the perpendicular component of the magnetic field B_z is then calculated at 16,384 (128×128) sites and a contour map is plotted. The measurement areas differ from each other in their z-coordinates and their sizes (and hence the sampling interval β), but they are all parallel with the source space.

The field due to a current dipole was given by equation 1.3. The field at any point due to a collection of current dipoles is simply equal to the vector sum of the contributions from each one. The first source configuration I wish to consider consists of nine current dipoles arranged in a line along the x-axis, and all oriented in the +y-direction. The central one lies at the origin and they are each separated by a distance, l.

It is not surprising that the individual dipoles are not resolved using measurement area 1 which is $8l$ above the source plane ($z = 8l$) and has a sampling interval of l ($\beta = l$) (see figure 2.6 in which the axes are calibrated in units of l). In this and all following isofield contour maps, positive contours are represented by solid lines and negative contours by broken lines.

I shall now present three sequences of four field maps each. In the first sequence (figure 2.7), the sampling interval in both x- and y-directions is successively halved while maintaining a constant $z = 8l$. In the second sequence (figure 2.8), the original sampling interval is maintained at $\beta = l$ while successively halving the distance between the source space and the measurement area. The final sequence (figure 2.9) combines these two approaches by simultaneously halving the sampling interval *and* the separation between source space and

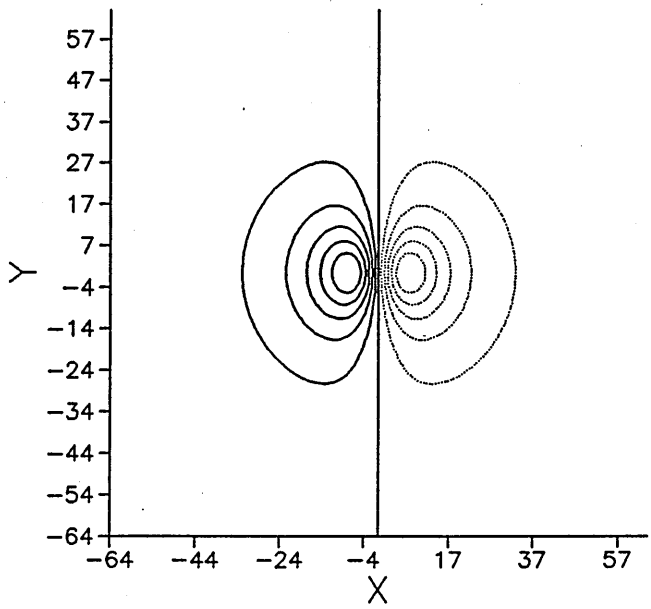

Figure 2.6 Field calculated in measurement area 1 ($z = 8l, \beta = l$)

measurement area.

I shall now discuss these simulations in more detail.

1. Reducing sampling interval (figure 2.7)

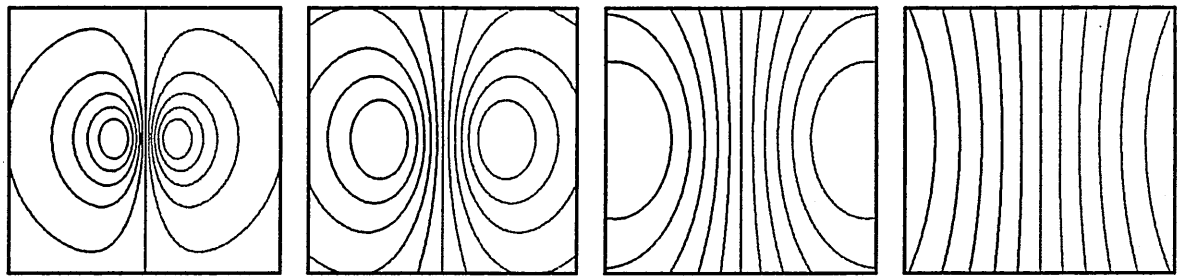

Figure 2.7 Reducing the sampling interval at constant $z = 8l$

The first magnetic field map in this sequence (figure 2.7a) is calculated in measurement area 2 in figure 2.5. Subsequent measurement areas are coplanar with it and centred at the same point, but their sides are successively reduced by a factor of two. Increasing the sampling frequency (reducing β) might be expected to reveal some fine structure in the field pattern, but as can be seen from figure 2.7, this is not the case. Making higher frequency measurements on a smaller central area simply reproduces the original pattern in greater detail. Note that figures 2.7b–d have been expanded to the same size as figure. 2.7a even though they represent smaller areas.

2 Reducing separation between source space and measurement area (figure 2.8)

Figure 2.8a represents measurement area 3 in figure 2.5, and subsequent measurement

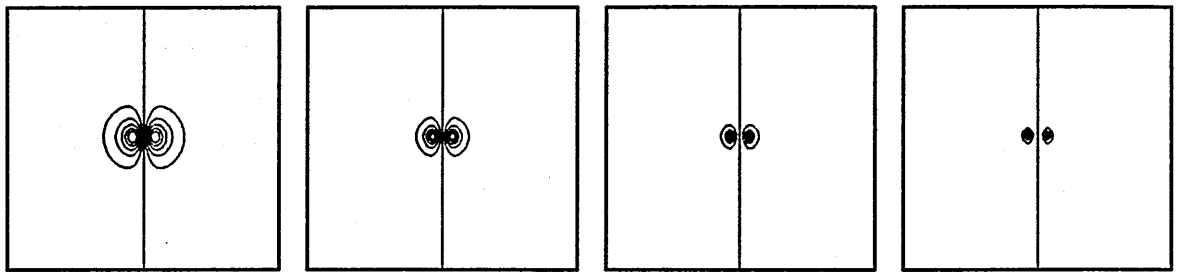

(a) $z = 4l$ (b) $z = 2l$ (c) $z = l$ (d) $z = \frac{1}{2}l$

Figure 2.8 Moving closer to the source with constant $\beta = l$

areas are all of the same size, but successively closer to the source space by a factor of two. This alternative approach also fails to elucidate the multiple sources. In this case, the pattern becomes more sharply peaked at the two extrema (as shown by the closeness of the contours) but there is still no fine structure. Note that the plots are individually normalized and that the contours in figure 2.8d represent much higher field values than those in figure 2.8a–c.

3. Reducing both sampling interval and separation between source space and measurement area (figure 2.9)

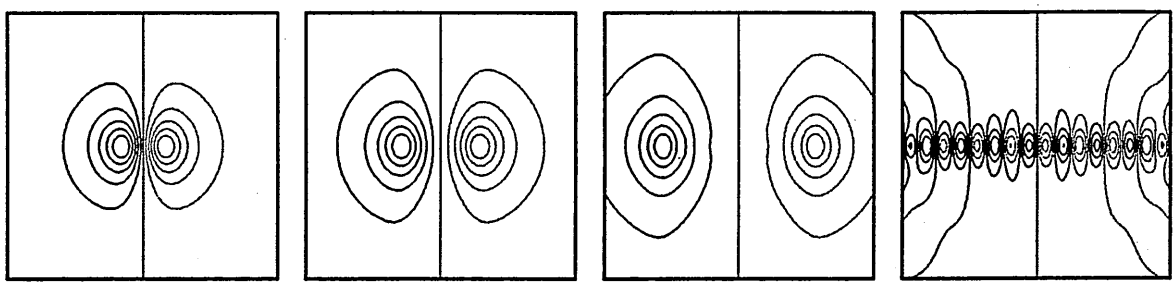

(a) $\beta = \frac{1}{2}l, z = 4l$ (b) $\beta = \frac{1}{4}l, z = 2l$ (c) $\beta = \frac{1}{8}l, z = l$ (d) $\beta = \frac{1}{16}l, z = \frac{1}{2}l$

Figure 2.9 Reducing the sampling interval and moving closer to the source

In this sequence, the field is calculated in measurement area 4 (figure 2.9a) and, then, in successively smaller areas, successively closer to the source space. This procedure eventually reveals the field patterns due to the individual sources (see figure 2.9d).

The general conclusion from this analysis (including data not shown here) is that parallel dipoles can only be resolved when the source–detector distance is less than the separation of the dipoles *and* the sampling frequency is greater than the spatial frequency of the dipoles.

Another important fact which emerges from this analysis is that it is quite easy to misinterpret a field pattern. Figure 2.6 certainly *looks* dipolar and so do the contour plots in figure 2.9a–c. Equation 1.4 was used to estimate the depth of the effective *single* current dipole for these four sets of data. As can be seen from table 2.1 the results are not always reliable, and the error is greatest at small depths.

This behaviour was investigated by Okada [74] who found that a single dipole adequately

Sampling interval (β)	l	$\frac{1}{2}l$	$\frac{1}{4}l$	$\frac{1}{8}l$
Actual depth of source plane (z)	$8l$	$4l$	$2l$	l
Estimated depth of effective dipole	$9l$	$7l$	$6l$	$6l$

Table 2.1 Comparison of actual source depth and estimated single dipole depth

models a line or sheet of dipoles as long as the spatial extent of the source is not too large relative to its depth. However, outside of these limits, the depth of the current generator can be seriously overestimated. Errors in depth estimation are also introduced if the finite size of the measuring coils is not taken into account [27]. Consequently, there is considerable danger in recklessly applying a current dipole model to data.

The dipole term in any current distribution tends to dominate the field pattern at sufficiently large distances [89] and to conclude this section, I shall demonstrate this. Figures 2.10–2.12 are the computed field maps of four different configurations of dipoles (a–d). All appear dipolar in the figure 2.10, but, as β and z are reduced, the patterns of the individual generators become apparent.

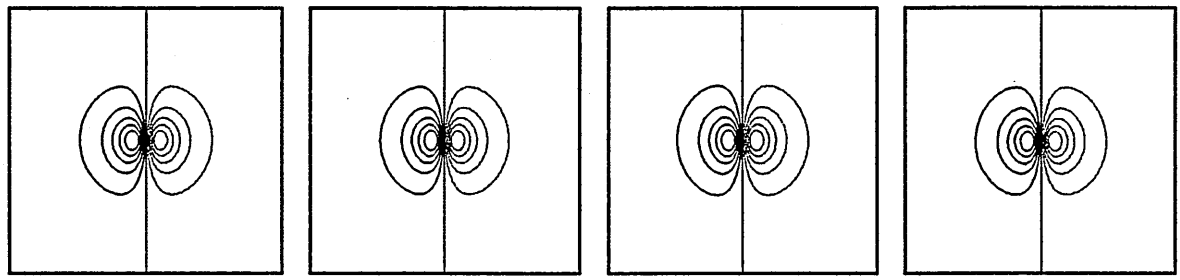

Figure 2.10 Field patterns due to four source configurations ($\beta = l, z = 8l$)

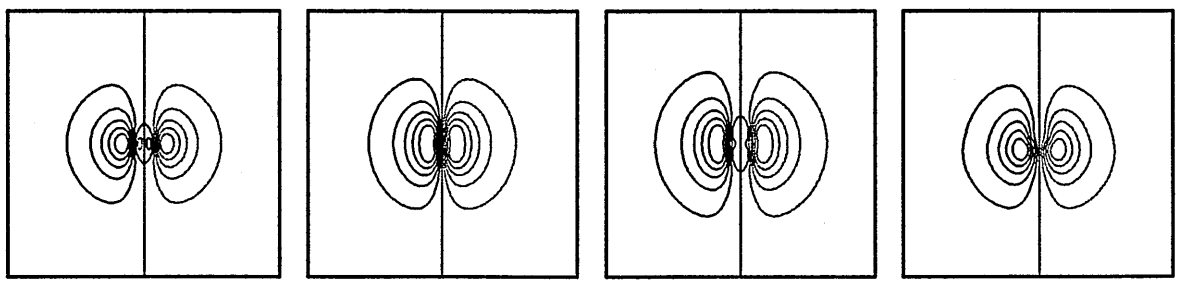

Figure 2.11 Field patterns due to four source configurations ($\beta = \frac{1}{4}l, z = 2l$)

It is important to mention that there may be methods of discriminating current dipole generators under much less strict conditions. In this section, my criterion for discrimination has relied entirely on *visual* inspection of isofield contour maps.

2.3.2 The effect of coil size

In the previous section, I demonstrated that, in order to discriminate close parallel current dipoles, the field must be measured close to the source and with a high sampling frequency.

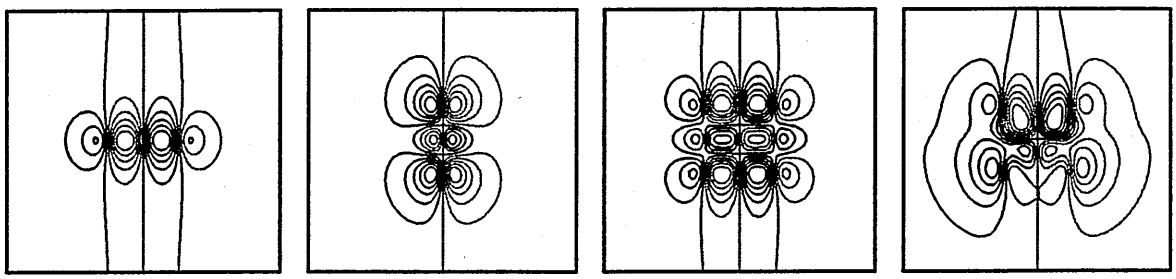

Figure 2.12 Field patterns due to four source configurations ($\beta = \frac{1}{16}l, z = \frac{1}{2}l$)

It may appear initially, from a practical point of view, that the first requirement is the more stringent as any arbitrarily high sampling frequency can be used. However, the relationship between the sampling frequency and the coil diameter is quite subtle.

In this section, I shall investigate this relationship in three ways: intuitively with the aid of diagrams, by taking the spatial Fourier transform of a detector and, finally, by integrating the signal over a detector. I shall not be concerned with resolving sources as I was in section 2.3.1, but instead, with the accuracy of imaging the magnetic field variation in the measurement plane.

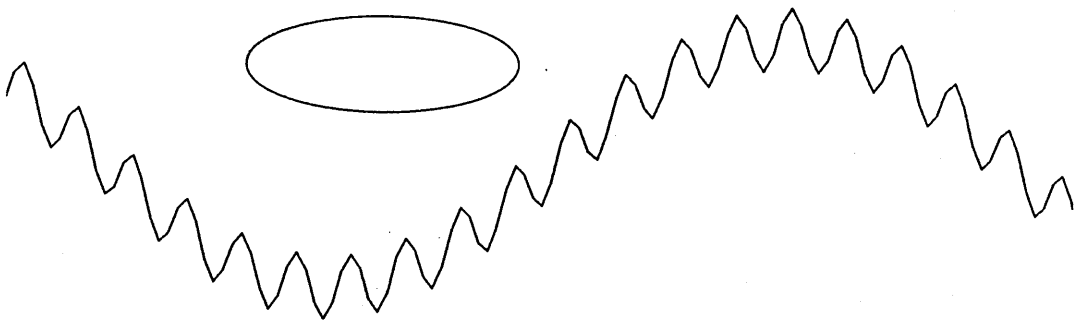

Figure 2.13 The resolution of spatial frequencies

Figure 2.13 shows a spatially varying field consisting of two frequency components and a sensing coil whose diameter is greater than the wavelength of one and less than the wavelength of the other. Examination of this figure suggests that, by scanning, the coil will measure the low frequency component quite accurately, whilst being almost insensitive to the other one, even if the sampling frequency is very high. With reference to figure 2.14, I shall now study the relative sensitivity of a coil to various single-component sinusoidal signals, with spatial frequencies s_{sig}, in one dimension. In this model, which is simplified for didactic purposes, the 'coil' is also considered to be one-dimensional and the 'coil frequency' (s_{coil}) is defined as the reciprocal of the coil diameter.

In figure 2.14a, the high frequency field may be detected if the scan is sampled at an even higher frequency. However, the magnetometer sensitivity will be extremely weak because many complete cycles will be averaged by the coil. The sensitivity remains weak as s_{sig} is reduced until it is equal to s_{coil} (b). In this special case, the coil is completely insensitive

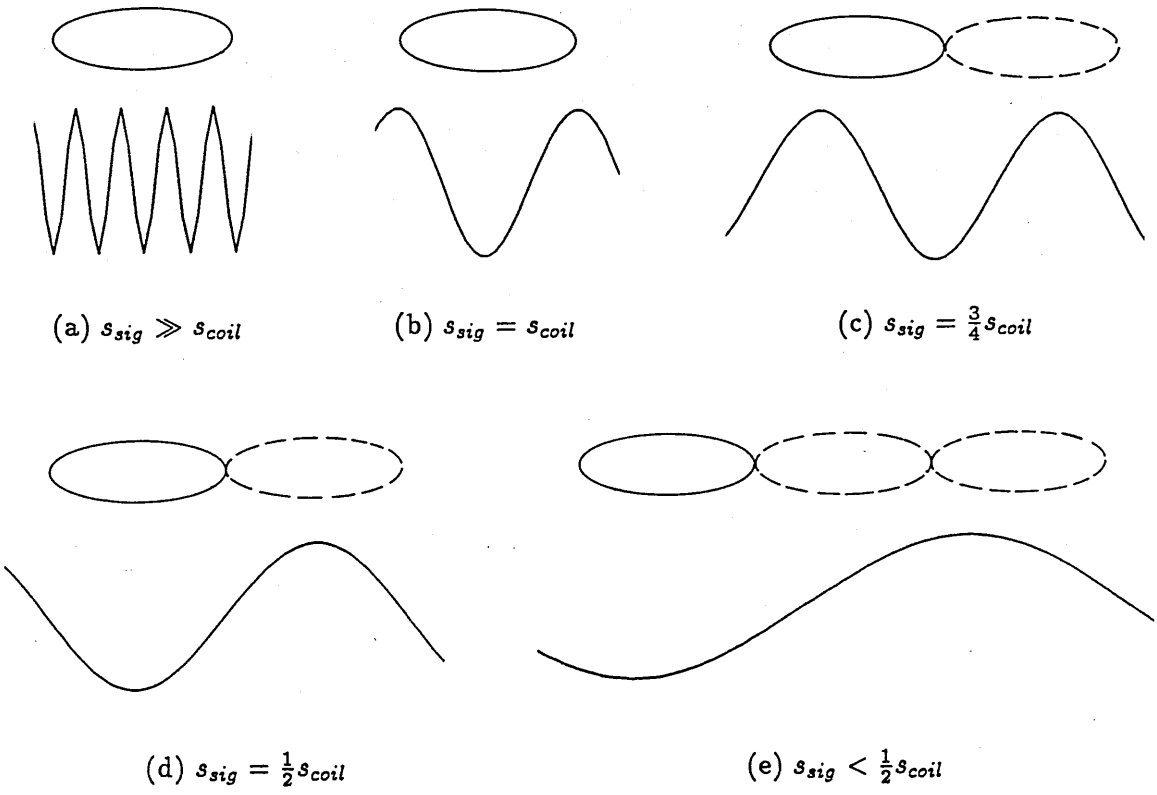

Figure 2.14 Sensitivity of a sensing coil to various spatial frequencies

to the signal during scanning, because whatever the relative phase, the coil will average a single complete cycle. This rather surprising result is also true for signal frequencies equal to any integer multiple of the coil frequency.

With frequencies lower than s_{coil} but greater than $\frac{1}{2}s_{coil}$ (c), sensitivity is improved, but there is still the unavoidable averaging of positive and negative segments of the signal. This is no longer the case with $s_{sig} = \frac{1}{2}s_{coil}$ (d) and lower frequencies (e). It is now always possible (with appropriate choice of phase) to include just a single polarity in the average. I conclude, therefore, that only frequencies less than or approximately equal to half the coil frequency should be trusted (although there is still *some* smoothing of the signal), unless additional information about the field is available:

$$s \lesssim \frac{1}{2}s_{coil} = \frac{1}{4r_{coil}}, \tag{2.12}$$

where r_{coil} is equal to half the coil dimension.

When this approach is extrapolated to a two-dimensional circular coil, the sensitivity 'zeroes' do not occur at simple multiples of the coil frequency. Instead, they correspond to the zeroes of a Bessel function, which are not uniformly separated.

An alternative method for determining a coil's sensitivity to spatial frequencies uses the spatial Fourier transform. This approach has been used by Bruno, Costa Ribeiro and others to characterize axial [14] and planar [16] gradiometers and for calibrating gradiometer arrays [15]. My objective here is less ambitious than theirs, considering only finite size one-dimensional detectors.

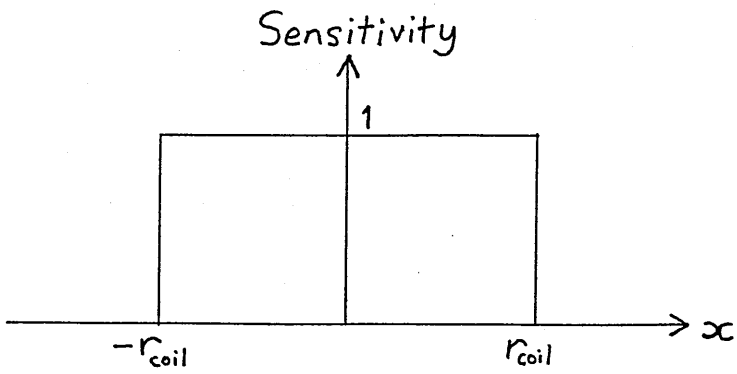

(a) Spatial sensitivity function

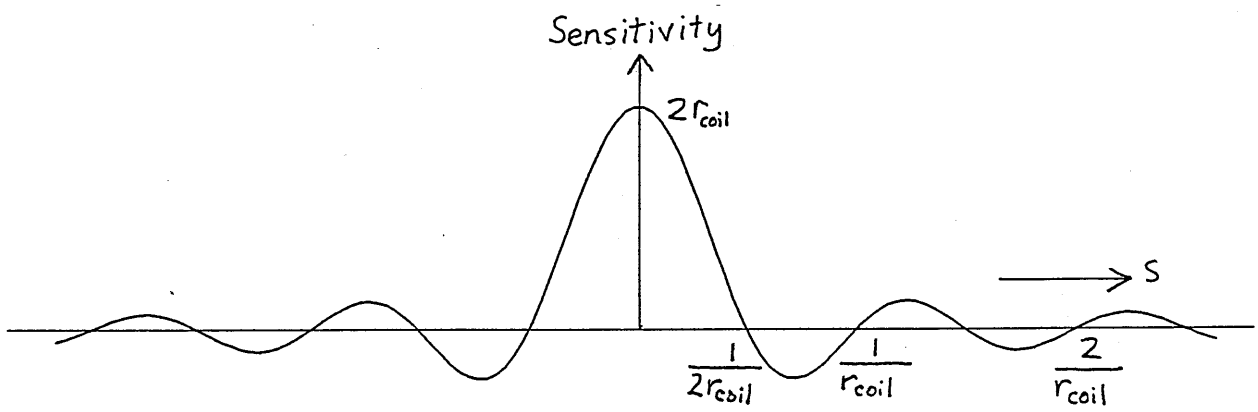

(b) Frequency spectrum of (a)

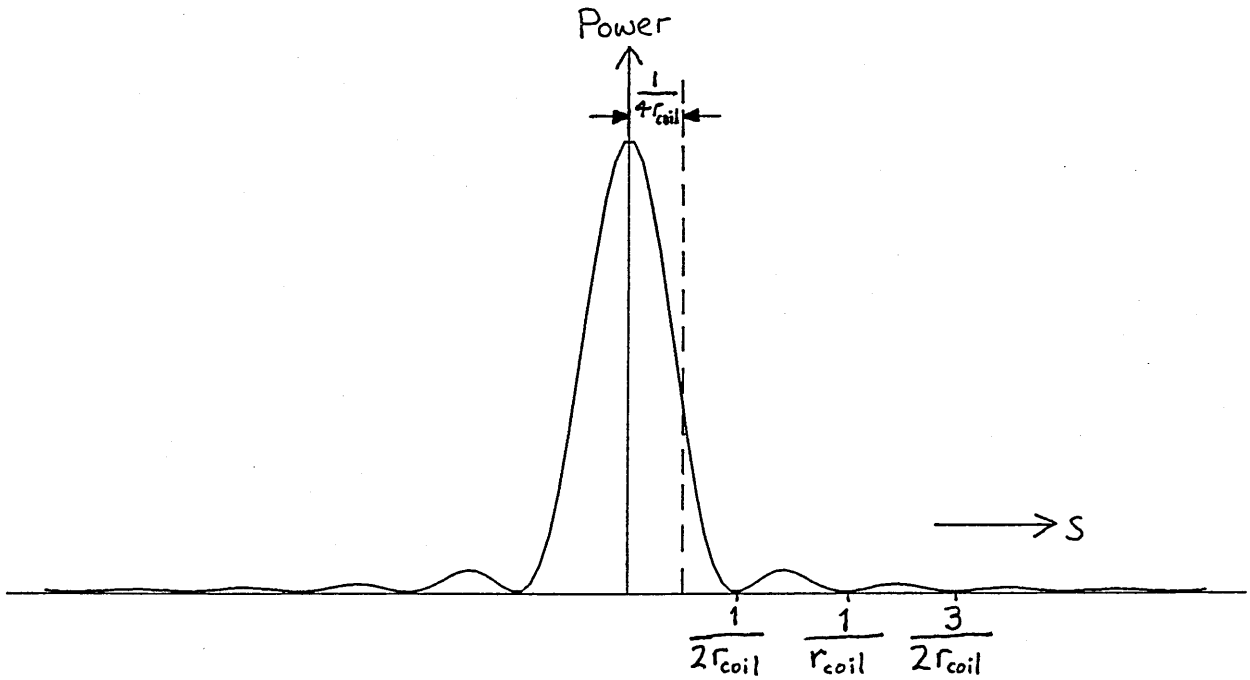

(c) Power spectrum of (a)

Figure 2.15 Fourier transform of a one-dimensional detector

The Fourier transform of a single pulse (rectangular waveform) is a 'sinc' function, which defines the relative strengths of the signal's frequency components. A single pulse can be used to model the sensitivity of a detector which is switched on and then switched off again, with negligible ramping time in both cases. In this case, the Fourier transform defines the frequency sensitivity function of the detector. If it is used to measure a complex time-varying signal, the relative strength with which signal frequencies will be represented can then be calculated by multiplying the frequency spectrum of the signal by the sensitivity function of the detector.

There is an analogous argument for spatial transforms. The spatial sensitivity function of a coil (in one dimension) is a unit pulse of width $2r_{coil}$ (figure 2.15a) and its Fourier transform is

$$2r_{coil}\frac{\sin\{2\pi s_{sig}r_{coil}\}}{2\pi s_{sig}r_{coil}}$$

(figure 2.15b). This function is zero when the signal spatial frequency s_{sig} is equal to integer multiples of $1/(2r_{coil})$ and hence the coil is insensitive to all these frequencies. Squaring the sensitivity spectrum gives the coil's power spectrum (c).

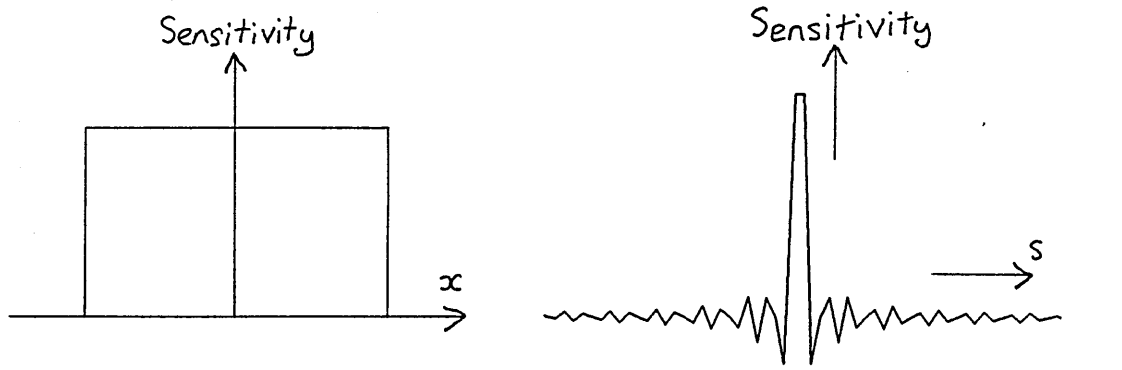

(a)Large coil

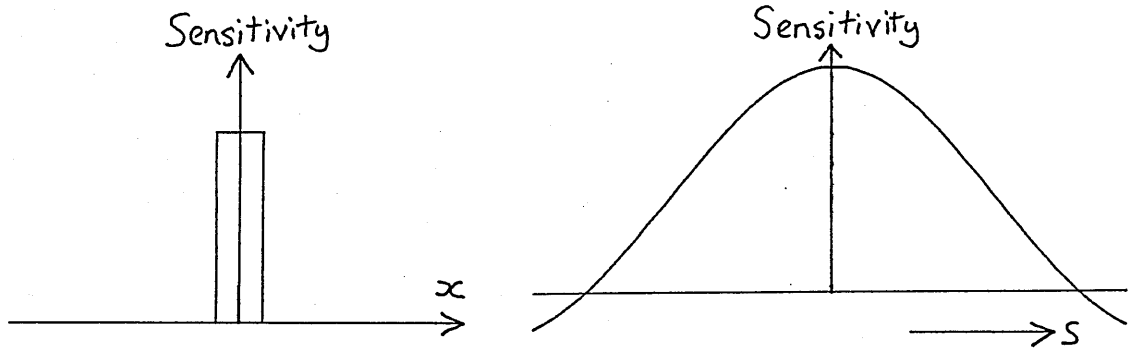

(b)Small coil

Figure 2.16 Spatial sensitivities and spectra for two coils

As illustrated by figure 2.16a, the sensitivity spectrum of a large coil is compressed in the low frequency region. However, the periodic peak amplitude of the sinc function approaches

zero very slowly (for instance, the tenth peak at $s_{sig} = 10.25/r_{coil}$ has an amplitude equal to 12% of that of the first peak at $s_{sig} = 1.25/r_{coil}$). Hence, high frequency components *are* represented in the coil signal. A small coil (b), on the other hand, has an expanded spectrum so that the 'reliable' fairly flat region extends to higher frequencies.

Finally, I shall derive an analytical expression [93] for the coil sensitivity as a function of spatial frequency and consider the amplitude and phase responses. Integration of the general sinusoidal magnetic field

$$B(x) = B\sin(\omega x + \phi)$$

over a one-dimensional coil of dimension l eventually yields equation 2.13:

$$\begin{aligned}\int_x^{x+l} B(x)dx &= -\frac{B}{\omega}\Big[\cos(\omega x + \phi)\Big]_x^{x+l} \\ &= -\frac{B}{\omega}\left[\cos(\omega x + \omega l + \phi) - \cos(\omega x + \phi)\right] \\ &= \frac{2B}{\omega}\sin\frac{\omega l}{2}\sin\left(\omega x + \phi + \frac{\omega l}{2}\right). \end{aligned} \tag{2.13}$$

In these and following equations, $\omega = 2\pi s_{sig}$ is the (spatial) angular frequency, ϕ is the phase angle and $\lambda = \frac{2\pi}{\omega} = \frac{1}{s_{sig}}$ is the wavelength. From equation 2.13, it is now possible to write down the amplitude $A(\omega)$ and phase $P(\omega)$ responses:

$$A(\omega) = \frac{2B}{\omega}\sin\left(\frac{\omega l}{2}\right) = \frac{B\lambda}{\pi}\sin\left(\frac{\pi l}{\lambda}\right), \tag{2.14}$$

$$P(\omega) = \left(\phi + \frac{\omega l}{2}\right) = \left(\phi + \frac{\pi l}{\lambda}\right). \tag{2.15}$$

Analysis of these equations confirms that there is zero amplitude response for $l = n\lambda$ where $n = 0, 1, 2\ldots$. Setting $l = (n + \frac{1}{2})\lambda$ gives the periodic amplitude peaks of the sinc function $(\frac{2}{\pi}Bl, -\frac{2}{3\pi}Bl, \frac{2}{5\pi}Bl\ldots)$ with alternating phase shifts $\pm\frac{\pi}{2}$. The optimum transfer characteristic of $A = Bl$ and $P_{shift} = 0$ corresponds to the regime of validity of the small angle approximation ($\sin\frac{\pi l}{\lambda} \approx \frac{\pi l}{\lambda}$). For instance, the approximation is in error by 0.4 % for an angle of 0.157 radians, which corresponds to $l \leq 0.05\lambda$.

2.3.3 Practical considerations

It is not possible to quote, for a particular magnetometer system, a single parameter defining its spatial resolution since this depends on the form of the current distribution and also on whether there is any prior knowledge of that form. However, in general terms, individual sources separated by a distance r can be resolved if r is greater than both the source—detector distance and the sensing coil diameter [95]. Whether any actual configuration of sources will be resolved by a real magnetometer depends on many other factors including the ambient and intrinsic magnetic noise, the complete gradiometer geometry and the model which is applied.

The practical limit to spatial resolution is usually determined by the source–detector distance. Wikswo *et al* [106] used an innovative experimental arrangement to reduce this. They measured the action potential from an isolated frog nerve by threading it through a room temperature, toroidal pick-up coil which was coupled to the sensing coil of a conventional

SQUID magnetometer by a winding around the dewar tail. The system noise was substantially increased, but the improvement in signal sensitivity due to the proximity of the pick-up coil to the source resulted in a signal-to-noise ratio of up to forty after signal averaging; the signal could barely be detected by direct measurement with the SQUID system.

An improvement to this design [104] was to connect the toroidal pick-up coil directly to the SQUID input coil, thus dispensing with the flux transporter. With this modified system, they were able to measure the magnetic field from an action potential in a frog nerve without signal averaging or magnetic shielding. The signal-to-noise ratio has now been further improved with the development of a room temperature amplifier [38].

More speculatively, hybrid systems consisting of pick-up coils made from a liquid nitrogen temperature superconductor and a conventional SQUID [81] and entire high T_c systems [68] have also been proposed. The common feature of all these designs is that they trade an increase in system noise for greater proximity to the source and, under certain circumstances, the overall signal-to-noise ratio can be improved.

The alternative approach is to attempt to modify the standard design of a SQUID magnetometer. In order that the sensing coil remain superconducting, it is generally immersed in liquid helium, and conventional dewar design demands a minimum 4K—300K separation of about 10 mm, unless a sharp increase in the rate of helium consumption is to be tolerated. However, it is possible to modify the shape of the dewar tip to reduce that separation without substantially increasing the rate of heat influx, and such a design was used in the high resolution magnetometer which will be described in the next chapter.

2.3.4 Summary

To conclude this section, I shall summarize the results that have been achieved.

In the first set of simulations (section 2.3.1), I demonstrated that, for a particular configuration of current dipole generators, calculating the field patterns closer to the source *or* with a higher spatial frequency fails to give an accurate visual image of the configuration. However, a visually reasonable pattern is produced when both procedures are carried out simultaneously. The general rule, that to resolve parallel dipoles both the sampling interval and the distance of the measurement must be less than the dipole separation, was stated.

The hazard involved in fitting single current dipoles to dipolar-looking field patterns was demonstrated in two ways. Firstly, I showed that the depth of a set of parallel dipoles could be seriously overestimated by this technique, and then I presented four diverse configurations of dipoles that all appeared to be single dipoles when mapped far away.

In section 2.3.2, I investigated the sensitivity of a coil as a function of spatial frequency and found the amplitude spectrum to be a sinc function. The implication of this result is that a coil is insensitive to spatial frequencies equal to integer multiples of the coil frequency (defined as the reciprocal of its dimension), but that the sensitivity at 'half-coil' frequencies decays quite slowly. The condition that faith should only be placed in those spatial frequencies less than half the coil frequency, was stated, and it was shown that optimum representation of low frequencies is approximated in the same way as the small-angle approximation.

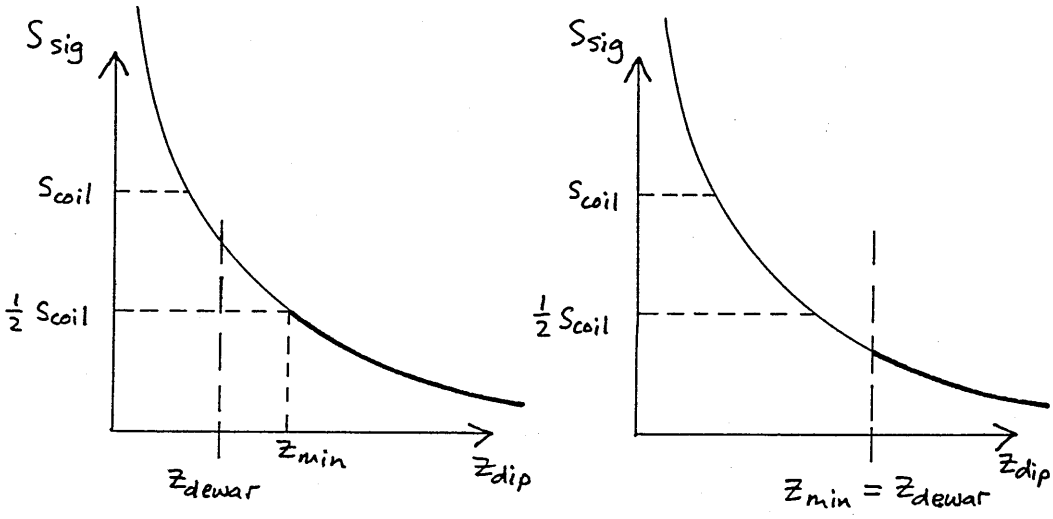

(a) 'Coil-limited' (b) 'Dewar-limited'

Figure 2.17 Resolution limits for measuring a shallow dipole

Finally, consider figure 2.17 [93], which incorporates some of the ideas presented in this section. The graphs show the signal spatial frequency s_{sig} against depth z_{dip} of a single current dipole. The spatial frequency is taken to be the dominant component: ie that corresponding to a wavelength of twice the extrema separation Δ. Thus,

$$s_{sig} = \frac{1}{2\Delta},$$

and combining this with equation 1.4 for the depth of a dipole z_{dip} yields

$$s_{sig} \times z_{dip} = \frac{1}{2\sqrt{2}}. \tag{2.16}$$

This equation defines the rectangular hyperbola of figure 2.17.

There are two physical limits to the shallowness of dipoles which can be reliably measured. The magnetometer in figure 2.17a is 'coil-limited': the minimum dipole depth z_{min} is set by the coil radius as in equation 2.12. In figure 2.17b, on the other hand, the measurement of a shallow dipole is 'dewar-limited' by z_{dewar}, the 4K—300K separation. For a given magnetometer system, one or other of these limits will be dominant.

Chapter 3

SQUIDLET: a high resolution magnetometer

Mr. Nagasyu had got incomprehensibly rich with a very simple idea. He had noticed the huge Japanese success in making things smaller. People seemed to like their high-tech titchy. Determining to take advantage of this curious quirk, he set about making things so small that they kept getting lost. Radios that you had to leave on, or you wouldn't be able to find them again, state of the art speakers and electric toothbrushes that could easily slip down between the cushions on a sofa. As Mr. Nagasyu had guessed, Nagasyu products had constantly to be replaced and he became quite stupidly rich. Ben Elton [29]

In this chapter, I shall describe SQUIDLET, the miniature magnetometer designed and developed at the Open University for the high resolution measurement of biomagnetic fields from small developing and regenerating organisms. Biomagnetism experiments performed with this instrument will be reported in detail in chapter 6. Here, I shall concentrate on its design, development and testing.

For sensitivity to high spatial frequencies, SQUIDLET required both its sensing coil diameter and the distance from the coil to the room temperature environment to be much smaller than in conventional instruments. The latter would be the more difficult to arrange because the thermal efficiency of the dewar was likely to be poor, resulting in increased helium costs. Target parameters were set: a 4 K—300 K dewar tip separation of 5 mm, a sensing coil diameter of 4 mm and a white noise level of 30 $\mathrm{fTHz}^{-\frac{1}{2}}$.

In section 3.1, a discussion of the performance of dewars will lead to a description of the design selected for SQUIDLET. Section 3.2 will be concerned with gradiometers, explaining their generalized function and the specialized design required for high resolution. In this section, I shall also describe a theoretical approach to the problem of 'balancing' a gradiometer that was adopted for SQUIDLET. Section 3.3 will include a summary description of the entire probe, and an account of the initial performance of the instrument in terms of intrinsic and environmental noise, and its ability to resolve close sources. SQUIDLET's first application to biomagnetism (on the giant unicellular alga, *Acetabularia*) will be reported in section 3.4.

3.1 The dewar

Figure 1.2 illustrates the main components of a conventional dewar. Two concentric fibreglass vessels are sealed at the neck and a pump-out port allows evacuation of the space between them. This space contains radiation shields and sheets of highly reflective aluminized mylar, known as 'superinsulation'. The radiation shields are long metal strips which are bonded to the inner vessel at the neck. This arrangement facilitates the conduction of heat from the evacuated region to the neck, where it is received by cold helium vapour evaporating from the interior reservoir.

I wish to concentrate on the dewar tail. A standard magnetometer for MEG and MCG measurements has a coil diameter of about 25 mm. Consequently, the internal diameter of the inner dewar vessel is slightly larger than this. Because of the coil size and the typical depth of MEG and MCG sources, there is little to be gained by reducing the 4 K—300 K separation below about 12 mm. With this separation, the superinsulation and radiation shields can be allowed to extend into the tip, conferring good cryogenic properties: helium is lost from a standard six litre dewar at a rate of about one litre per day. Any substantial reduction of the tip separation would necessitate the removal of thermal shielding from this region, increasing the rates of heat influx and helium loss. The extra running costs that would be incurred have proved to be a strong disincentive to this design modification.

With an adequate vacuum, the primary heat transfer mechanism is radiation, and the rate at which energy crosses the vacuum space is directly proportional to the areas of the tips. Consequently, if the *area* over which the steeper temperature gradient existed were reduced, it ought then to be possible to keep helium consumption to a tolerable level. Because SQUIDLET would have a very much smaller sensing coil than was usual, a significant reduction in surface area at the dewar tip was perfectly feasible, and it was this fact which was the foundation for the design of SQUIDLET's dewar.

Figure 3.1 illustrates the differences between a conventional dewar tail and that designed for SQUIDLET. To minimize the tip separation, the two vessels of the SQUIDLET dewar were designed to touch at the tip when the dewar was at room temperature and, consequently, there was no space in the tip for superinsulation or radiation shields. When filled with helium, the vacuum space tip separation was nothing more than the contraction of the inner vessel. Linear expansivity coefficients of fibreglasses, in cooling from 300 K to 4 K, are around -0.01 and so, in order that the contraction was no more than 3 mm (which, with 1 mm thickness for each vessel, gives the specified 5 mm separation), the maximum depth of helium had to be limited to about 30 cm. As a consequence, the capacity of the dewar was restricted to 2 litres.

With a 4 K—300 K separation of about 5 mm (instead of 12 mm, as in a conventional system) and an absence of insulation, it might be expected that the rate of heat influx in the new design would be intolerably high. However, as mentioned above, SQUIDLET's tiny sensing coil allowed the area over which the helium and room temperature environments were so close, to be as small as a circle of approximate diameter 8 mm, instead of at least 26 mm. In practice, this tenfold reduction in surface area adequately compensates for the

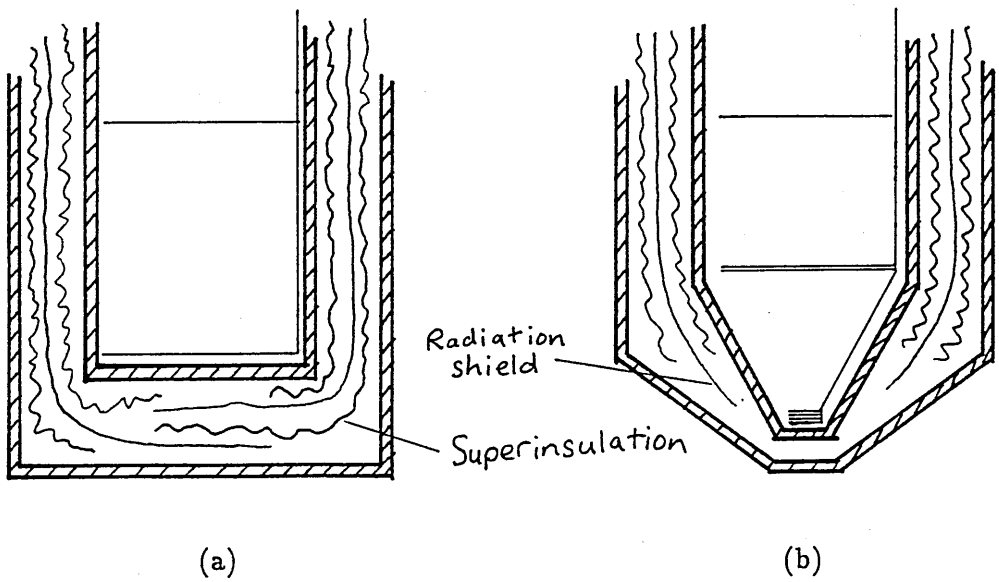

Figure 3.1 Cross-sections of two (helium containing) dewar tails
(a) A conventional instrument for neuromagnetometry and cardiomagnetometry
(b) A miniature instrument for developmental studies (SQUIDLET)

lack of thermal shielding at the tip.

In figure 3.1b, it can be seen that the shapes of the tips of both inner and outer vessels are truncated cones of different vertical angle. This ensures that the separation of the vessels increases rapidly away from the measuring surface, and allows rather better accessibility to small room temperature samples than is provided by a cylindrical tail.

The dewar was manufactured to our specification by a commercial cryogenics supplier[1]. Initial measurements indicated that the tip separation was rather larger than specified, and X-ray photographs confirmed that the two vessels were actually separated by 2 mm at room temperature and that the minimum 4 K—300 K separation was about 7 mm when the system had been cooled down. For a current dipole source (whose field falls off as the square of distance), located close to the dewar surface, this 40 % increase in the source–detector distance represents an attenuation in sensitivity by nearly a factor of two. This was not acceptable and so the dewar was returned to the manufacturer.

After modification, the relative locations of the two vessels were correct and the rate of helium consumption was about 1.5 litres per day: a little higher than it had been previously, but not unreasonable. As the dewar had a capacity of 2 litres, it was necessary to refill from a storage vessel every day.

During transfers and particularly during the initial cooldown, the shape of SQUIDLET's dewar dictated that special care had to be taken to avoid introducing air or leaving any nitrogen inside. A small amount of solidified air forming a layer 1 mm thick on the bottom of a 26 mm diameter cylindical tail would cause no significant problem. Because the tail of SQUIDLET's dewar is so narrow at the tip, however, this same 0.5 cm^3 of solid air would clog up the bottom 5–10 mm. This would be quite unacceptable, since one of SQUIDLET's most

[1]Canadian Thin Film Systems inc, Port Coquitlam, BC, Canada.

important features is the proximity of its sensing coil to the room temperature environment.

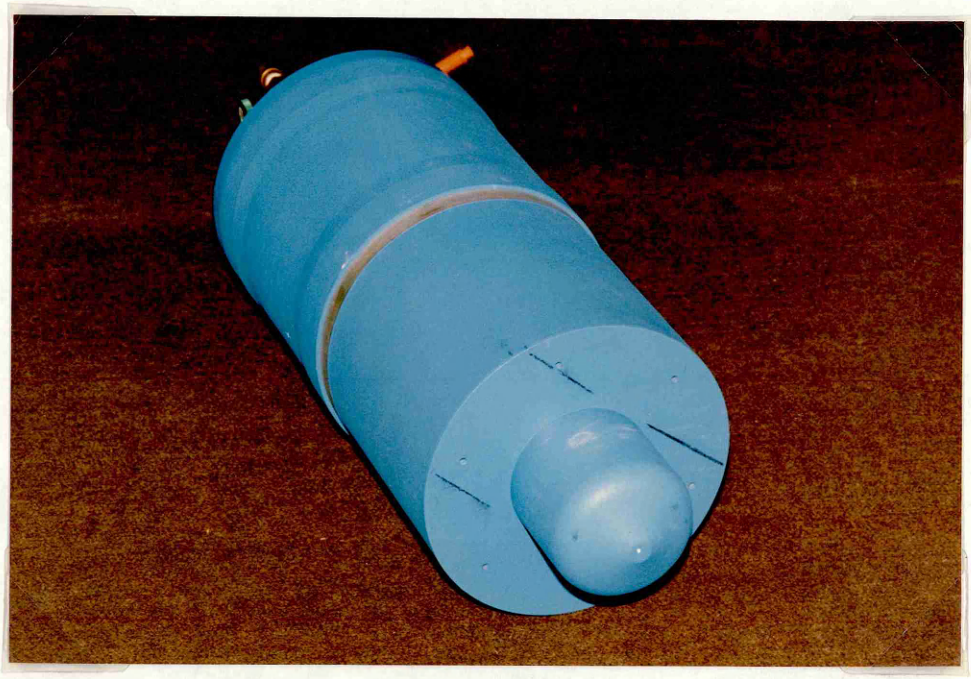

Figure 3.2 Photograph of SQUIDLET's dewar

3.2 Gradiometers

In chapter 2, magnetic field measurement was considered, firstly, at 'points in space' and then, somewhat more realistically, as the integration of the flux density (B) over the area of a single coil. In practice, however, a single coil (known as a 'magnetometer') would be of very little use unless it was operated in a virtually silent magnetic environment. In order to overcome the effect of competitive noise sources, whose fields are often many orders of magnitude stronger than that actually under study, the multi-coil 'gradiometer' has been developed.

In section 3.2.1, I shall describe various types of gradiometer and review work (both theoretical and practical) which has been done on the design and evaluation of gradiometers for particular purposes. When designing a gradiometer, many interacting parameters (such as dewar geometry, SQUID characteristics, desired sensitivity and spatial resolving power, and coil shapes, sizes and separations) have to be taken into account or have values assigned to them. I shall describe this process in section 3.2.2, with reference to the development of a gradiometer design which is specialized for high resolution measurements. Because there are physical limits to the accuracy with which a coil system can be constructed, there is an unavoidable discrepancy between design and reality which, in general, is too great to be acceptable. Section 3.2.3 describes a technique for 'balancing' a gradiometer and includes a derivation which permits rapid assessment of the degree of balancing required in a practical situation.

3.2.1 Discrimination against distant sources

It has been said [96] that there are only two problems for experimentalists in biomagnetism: to make measurements which have a sufficiently high sensitivity to the biomagnetic fields ...and a sufficiently low sensitivity to all the other fields in the neighbourhood. Although a certain amount of work (eg [6], [25] [38]) has been carried out with non-superconducting magnetometers, the first problem was only really solved with the development of the SQUID. There have been a number of approaches to the second problem.

Laboratories have been built in remote settings, well away from human activity, traffic and unnecessary electrical devices and supply lines. Also, shielded rooms have been constructed. These may be made from aluminium (for high frequency eddy current shielding) or high permeability alloys (for creating a region of low flux density) or both, and they are very effective if they are well designed. However, they are extremely expensive. The simplest and cheapest solution, has been to design gradiometers: sensors that discriminate against distant sources, and in favour of local ones.

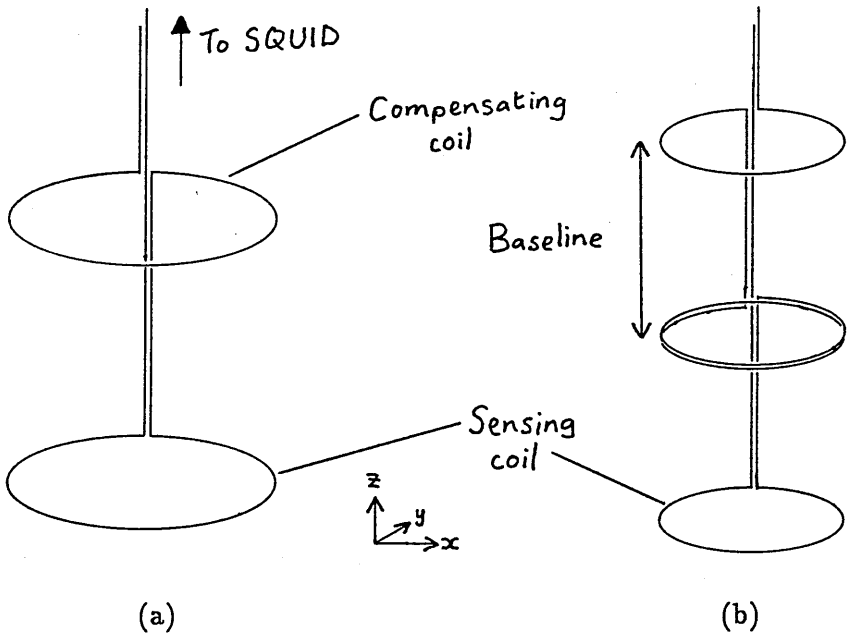

Figure 3.3 Axial gradiometers
(a) First-order gradiometer ($\frac{dB_z}{dz}$)
(b) Second-order gradiometer ($\frac{d^2B_z}{dz^2}$)

Figure 3.3 shows the two commonest types of gradiometer. Because biomagnetic fields fall rapidly in magnitude with distance from the source, a source placed close to the sensing coil in (a) will be detected much more strongly by that coil than by the compensating coil. The separation of the coils is known as the 'baseline'. The compensating coil is wound in the opposite sense and so the contribution it *does* make to the overall signal will be subtracted from that of the sensing coil. A distant noise source, on the other hand, will generate a field which is nearly (spatially) uniform in the region of the detector. Consequently, the flux captured by the two coils will be almost equal and the net signal will be close to zero.

The noise sources under consideration in this section are those generating time-varying fields (such as motors, fans and the mains supply). A static field (as, for example, is produced by a permanent magnet or by the Earth) does not interfere with the measurement directly because it merely shifts the baseline value of the magnetic field[2].

The term 'gradiometer' implies that the device measures the gradient of a magnetic field component, which is not strictly correct. The device is really a 'differential magnetometer' [103], but, in this thesis, I shall stick to the more usual name, 'gradiometer'. A first-order gradiometer *does* measure the field gradient in the special case of a uniform field gradient.

Now, the fact that the gradiometer in figure 3.3a is sensitive to the first-order field gradient ($\frac{dB_z}{dz}$ if the coils lie perpendicular to the z-direction — the usual arrangement) may be inconvenient if a noise source generates a strong (time-varying) field gradient in the region occupied by the gradiometer. In cases where a local noise source is very strong, it is necessary to carry the principle a stage further, rendering the second-order gradiometer (figure 3.3b). Just as a first-order gradiometer comprises two oppositely wound magnetometers, a second-order gradiometer can be regarded as two oppositely wound first-order devices. This configuration is insensitive to uniform fields and uniform field gradients, but will measure second-order gradients.

In principle, third- and even higher-order devices could be used. However, for unshielded systems, the second-order gradiometer has proved to be the most popular. The reasons for this are the extra complexity of accurately fabricating large numbers of coils and the fact that, even in an unshielded laboratory, a balanced (see section 3.2.3) second-order gradiometer provides adequate noise cancellation for most applications. First-order devices are generally used in shielded rooms.

Although the axial symmetric gradiometers illustrated in figure 3.3 are the most common, a wide variety of configurations have been or could be used (see figure 3.4). The shapes and sizes of the coils may be varied and they may contain different numbers of turns. They may be sensitive to other field components or their gradients, and different baselines may be used.

In general, for any given order, a set of equations must be satisfied so that all uniform field gradients up to the required order are rejected. Firstly, if N_i is taken as positive or negative depending on the sense of the ith coil, then the following equation

$$\sum_{i=1}^{n} N_i A_i = 0 \tag{3.1}$$

must be satisfied for uniform field rejection by a $(n-1)$th order device. Restricting the discussion to axial gradiometers, rejection of a uniform field gradient ($B_z(z) = k_1 z + k_0$) is achieved by a second-order device if

$$N_1 A_1 B_z(z_1) + N_3 A_3 B_z(z_3) = N_2 A_2 B_z(z_2),$$

where z_1, z_2, z_3 are the coordinates of coils 1,2,3. However, if equation 3.1 has already been satisfied, this can be simplified. Taking account of the sense of the coils and generalizing to

[2]Static fields do, of course, affect measurements indirectly by magnetizing samples etc, as was described in section 2.2.2.

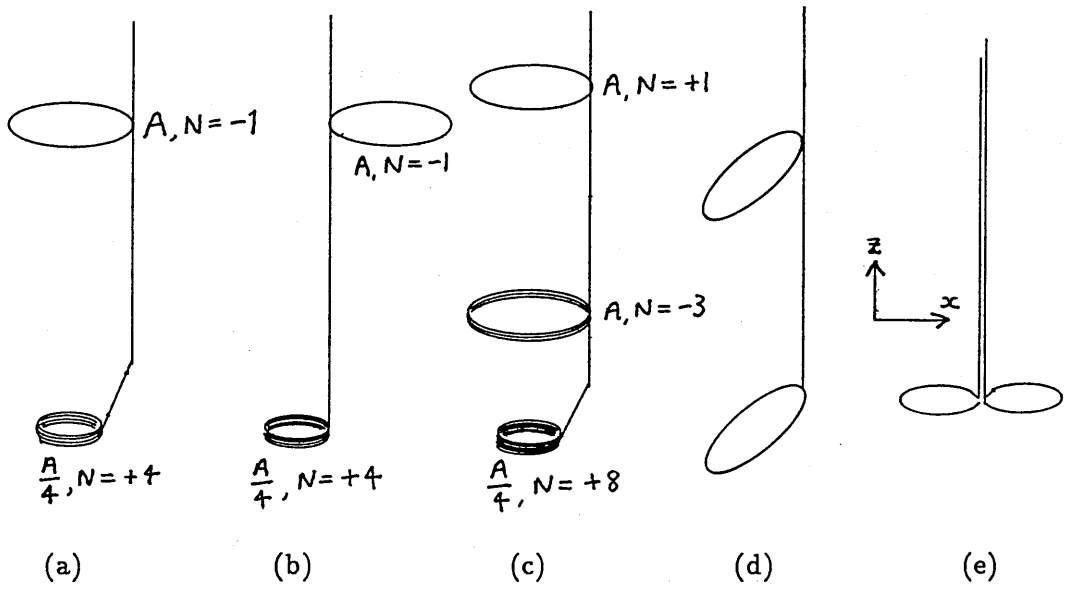

Figure 3.4 A selection of gradiometers
(a) Axial asymmetric first-order
(b) Off-axis asymmetric first-order
(c) Axial asymmetric second-order with unequal baselines
(d) Canted
(e) 'Figure 8' planar ($\frac{dB_z}{dx}$)

n coils, this yields

$$\sum_{i=1}^{n} N_i A_i z_i = 0, \tag{3.2}$$

where z_i now represents the separation of the first and ith coils (ie $z_1 = 0$). Similarly,

$$\sum_{i=1}^{n} N_i A_i z_i^2 = 0 \tag{3.3}$$

defines the general condition for uniform second-order gradient rejection by third- and higher-order devices (assuming uniform field and field gradient rejection).

All these equations hold for axial gradiometers, and, with modifications, can also be applied to off-axis, canted and planar devices (see figure 3.4). In order to satisfy equation 3.1, the small area sensing coils of asymmetric gradiometers must have correspondingly more turns than the larger compensating coils. As will be demonstrated in section 3.2.2, this type of configuration has a particular advantage in terms of overall sensitivity.

This wide range of gradiometer configurations has resulted from the independent development of designs for specific applications in particular locations. The designs are influenced by factors such as the geometry of the proposed source and the ambient noise. The main difficulty with such diversity is the evaluation and comparison of different designs. Gradiometer performance is generally quoted in terms of the measured field noise or sensitivity to particular model sources, but this, of course, depends on the environment and will vary from one laboratory to another.

A number of methods have been proposed to provide an independent assessment.

A technique proposed by Wikswo [103] is to compute the minimum-strength detectable current dipole or magnetic dipole which could be measured by a gradiometer coupled to a

SQUID of a particular sensitivity. An alternative figure of merit, derived by Claassen [20], is source-independent and depends mainly on the efficiency of coupling between the flux transporter and the SQUID. Planar gradiometers are increasingly popular due to their superior accuracy of fabrication (although other difficulties remain), and a theoretical comparison between the dipole localization performances of a planar array and conventional second-order axial gradiometers was carried out by Carelli and Leoni [19].

As reviewed in section 2.3.2, Bruno, Costa Ribeiro and colleagues developed a spatial Fourier technique for characterizing both axial [14] and planar [16] detectors. They also compared second- and third-order gradiometers in terms of their suitability for measuring the magnetocardiogram in a noisy environment [13]. They favoured third-order gradiometers and outlined a 'general design procedure' for such devices, which takes account of the spatial form of the MCG.

In a detailed analysis, which included estimates of the degree of interference due to common noise sources and the effect on performance of predicted construction errors, Vrba *et al* [99] theoretically compared ten designs (including zeroth-, first-, second- and third-order devices). They also varied coil sizes and symmetry, and baseline lengths, characterizing the different configurations in terms of signal-to-noise ratio for a current dipole. They concluded, like Bruno and Costa Ribeiro [13], that third-order gradiometers were the best (although their selection of six third-order devices out of the ten basic designs suggests that they suspected this already). Such was their confidence that they proceeded to construct one and demonstrate it. The fact that, despite these recommendations, only a tiny fraction of the SQUID systems currently in operation utilize third-order gradiometers tends to emphasize the lack of coherent thinking on the subject and the difficulty of the problem.

My own feeling is that a universal formula for selecting a gradiometer, which takes account of all the interacting parameters, is too elusive to be worthwhile. I propose starting with the least flexible feature for the particular application and then putting the design together piece by piece, making compromises where appropriate. The next section describes the design of SQUIDLET's gradiometer [93], for which the least flexible feature was the size of the sensing coil.

3.2.2 A high resolution gradiometer

For SQUIDLET, a sensing coil diameter of about 4 mm was one of the original target parameters and this would not be compromised. As reported in section 3.2.1, second-order gradiometers have been found to reject noise to a satisfactory degree in an unshielded urban laboratory, and so it was decided that SQUIDLET's gradiometer should be of second-order configuration. Another important condition, in order to maximize the overall sensitivity of *any* gradiometer, is to match its inductance with that of the SQUID's input coil. I shall now demonstrate why that is so.

Figure 3.5 illustrates the inductances involved in magnetic field detection by a SQUID system. For SQUIDLET, a commercially produced dc SQUID[3] was purchased and this

[3]Model DBS Dynabias dc SQUID, SHE Corporation (now Biomagnetic Technologies inc), San Diego, CA, USA.

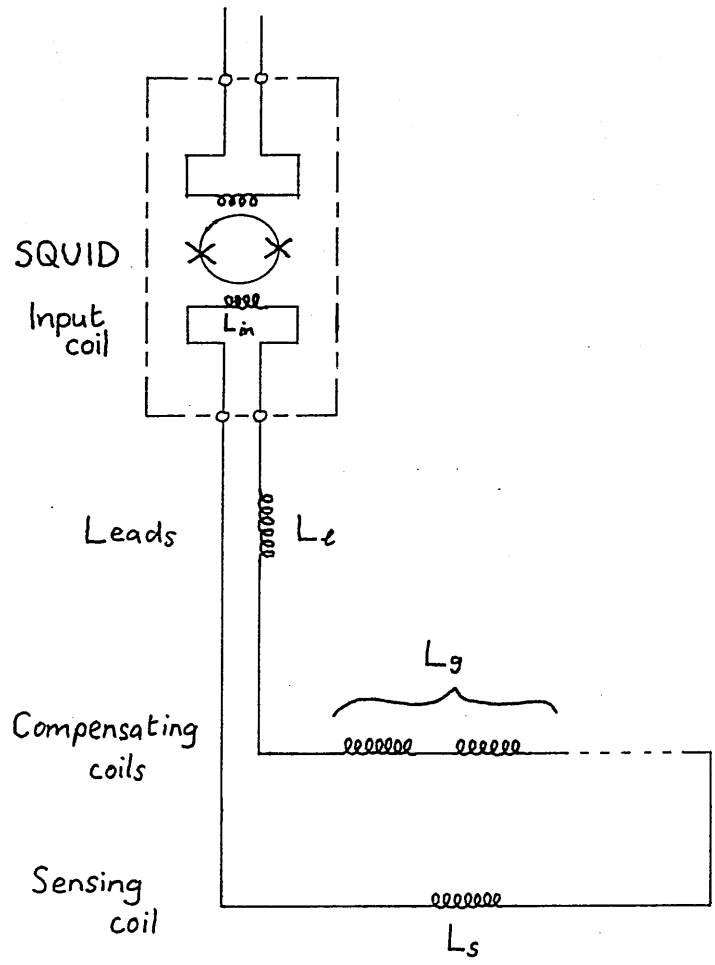

Figure 3.5 Schematic inductance diagram of a SQUID and gradiometer

hermetically sealed unit is indicated by the dashed box. The input inductance L_{in} of the coil which couples to the SQUID is fixed (2 μH) and its value is limited by space and fabrication technology. When connected, it forms part of a closed superconducting circuit (the flux transporter) with the gradiometer, the other inductive components being the leads L_l and the gradiometer coils. The total inductance of the circuit L_T is given by

$$L_T = L_{in} + L_l + L_s + L_g,$$

where L_s is the inductance of the sensing coil and L_g is the sum of contributions from the other coils.

A SQUID can be considered as a linear current-to-voltage amplifier whose transfer function is given by

$$\Delta V_{out} = \alpha \Delta I_{in} = \frac{\alpha \Delta \Phi}{L_T}. \tag{3.4}$$

α is a constant and ΔI_{in} is the change in the flux transporter supercurrent resulting from a net flux change $\Delta\Phi = \sum_i N_i A_i \Delta B_i$ threading the gradiometer, N_i, A_i, ΔB_i being the number of turns, area and change in flux density for each coil. Since we are concerned with the sensitivity of the sensing coil, it is necessary to include only the flux change $\Delta\Phi_s = N_s A_s \Delta B_s$ threading that coil. The inductance of a tightly wound circular coil is

$$L = \mu_0 k N^2 A^{\frac{1}{2}}, \tag{3.5}$$

where

$$k = \pi^{-\frac{1}{2}} \left(\ln \left[\frac{8b}{a} \right] - 2 \right)$$

and a, b are the wire and coil radii [45]. Rearranging equation 3.5 for the sensing coil,

$$N_s = \left(\frac{L_s}{\mu_0 k_s (A_s)^{\frac{1}{2}}} \right)^{\frac{1}{2}}$$

and substituting this into equation 3.4 yields the sensitivity function for the system,

$$\Delta V_{out} = \frac{\alpha N_s A_s B_s}{(L_{in} + L_l + L_g + L_s)} \approx \frac{\alpha (A_s)^{\frac{3}{4}}}{(\mu_0 k_s)^{\frac{1}{2}}} \frac{(L_s)^{\frac{1}{2}}}{(L_{in} + L_s + L_g)} \Delta B_s, \tag{3.6}$$

which should be maximized. L_l is dropped in this equation because the inductance of the leads is negligible when they are twisted together.

Assuming A_s is fixed (a circle of diameter 4 mm for SQUIDLET), this function will be maximized for any particular value of L_s if $L_g \ll L_s$. This condition is clearly not achievable by a symmetric gradiometer (eg figure 3.3). However, the N^2 dependence in equation 3.5 ensures that, for asymmetric gradiometers such as figure 3.4a, b & c, the inductance of the multiple-turn sensing coil can be made much larger than that of the compensating coil(s). The considerable advantage of locating the majority of the gradiometer's inductance in the sensing coil was first pointed out by Zimmerman [110]. He showed that first- and second-order symmetric gradiometers suffered losses in sensitivity by factors of $\sqrt{2}$ and 2 respectively, when compared with a magnetometer with the same coil size. These losses can be reduced to a low level with an asymmetric design.

If L_g is now considered negligible, the sensitivity function is given by

$$\frac{\Delta V_{out}}{\Delta B_s} \propto \frac{(L_s)^{\frac{1}{2}}}{(L_s + L_{in})},$$

which is maximized when

$$L_s = L_{in}.$$

The sensitivity function is not sharply peaked: changing L_s by a factor of 10 causes a reduction of less than 50% in sensitivity. Thus, it is not critical to equate the inductances very accurately. Nevertheless, for asymmetric gradiometers, this condition produces the best performance.

Summarizing the state of the design hitherto, SQUIDLET's gradiometer is second-order and asymmetric with a sensing coil diameter of 4 mm and approximate inductance 2 μH (to match it with the input coil). Using equation 3.5 with wire[4] diameter (excluding insulation) $a \approx 0.05$ mm and coil radius $b = 2$ mm, the inductance of a single turn is 9.5×10^{-3} μH. For reasons of simplicity and symmetry, N_s was chosen to be 16, giving the sensing coil an inductance of 2.42 μH[5].

In order to preserve $L_g \ll L_s$, the central and top compensating coils were made of two and one turns respectively and sixteen times the area of the sensing coil; ie they had radii of

[4] 'Formvar'-insulated niobium-titanium wire, Cryogenics Consultants ltd, London, UK.

[5] In practice, the spatial extent of the cross-section of the sixteen turns reduces the inductance and, although difficult to quantify accurately, the effect may be as large as 30%. However, as has been noted, the matching criterion does not need to be satisfied precisely.

8 mm. Consequently the respective inductances of these coils were about 0.21 μH and 0.05 μH: much smaller than L_s. The only remaining parameter to set was the baseline.

The rationale for baseline selection is to make it as short as possible (so that the gradiometer sensitivity to uniform fields and field gradients is very low), but not so short that the compensating coils capture a significant amount of flux from the source. Clearly, this depends on the depth of postulated sources. SQUIDLET was designed for measurements of superficial sources extremely close to the dewar and so a short baseline of 16 mm was selected.

The flux density at the central coil, due to a current dipole 6 mm below the sensing coil, falls to $(6/22)^2$ of its value at the sensing coil. However, the turns-area is twice as large and so the central coil actually intercepts about 15 % as much flux as the sensing coil (and subtracts it from the signal). This loss is regrettable, but a longer baseline would tend to increase sensitivity to noise sources.

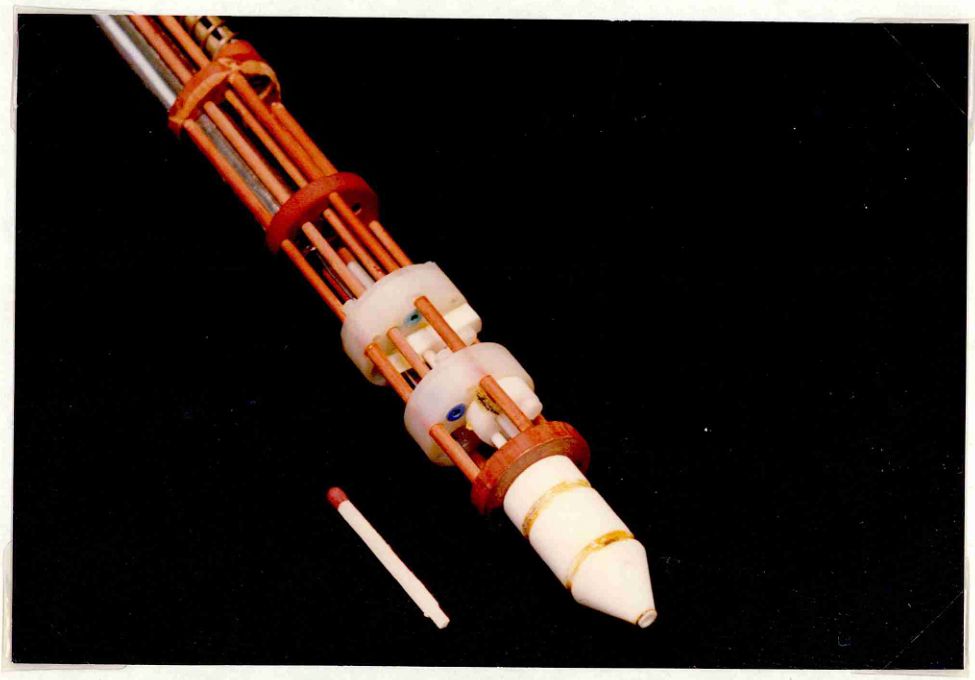

Figure 3.6 Photograph of SQUIDLET's gradiometer

The original gradiometer former was machined from tufnol, a phenolic resin widely used in superconducting magnetometer systems because of its suitable cryogenic properties and absence of contamination. However, repeated thermal cycling (which was unavoidable, initially) degraded the material, making it mechanically unstable, and so it was replaced with one made from Macor[6], a glass ceramic (see figure 3.6). This was much harder and rather brittle, making it difficult to machine, but more stable.

The gradiometer was wound manually, laying the wire into grooves in the former and then fixing it in position with low temperature varnish. The groove for the 16-turn sensing coil was 0.5 mm wide and so the finite diameter of the wire (about 0.08 mm including insulation)

[6] William McGeoch & co ltd, Birmingham, UK.

resulted in a sensing coil with significant radial thickness. Consequently, the average radius of the coil was rather more than 2 mm, and for uniform field rejection with the existing former, it was necessary to reduce the number of turns to fourteen.

3.2.3 Balancing the coils

As has been noted, noise fields in an unshielded laboratory are typically several orders of magnitude greater than biomagnetic fields, and the function of gradiometers is to discriminate in favour of the latter by virtue of their steep gradients. In order to do this satisfactorily, equations 3.1, 3.2, etc must obeyed very accurately and, in general, the accuracy obtained by hand-winding coils (particularly small coils) falls far short of what is required. However, the gradiometer can be 'balanced' after winding, with superconducting 'trim tabs' [2]. This technique will be described below.

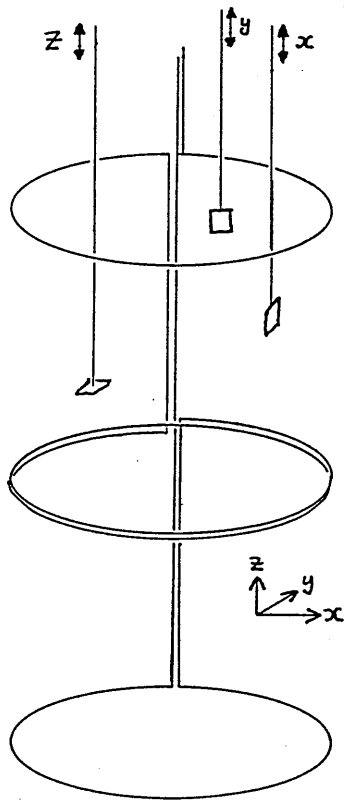

Figure 3.7 Schematic diagram of travelling trim tabs for gradiometer balance

One method involving trim tabs is illustrated in figure 3.7. The tabs themselves are small pieces of superconducting material (usually lead) that deflect magnetic flux. They are either glued to the former or (as in the figure) mounted on rods which can be raised and lowered from outside the dewar. Thus, by judicious positioning of the tabs, the effect of the winding inaccuracies can be negated. Even in the absence of winding errors, it would be advantageous to be able to adjust the degree of unbalance externally because it can drift due to thermal effects. One important detail is to ensure that the tabs are used to alter the flux threading the compensating coils, as placing them close to the sensing coil would severely complicate the interpretation of the signal.

It is not at all intuitively obvious how large the trim tabs should be or where they should be placed, and so their effect was examined analytically. I shall now present a summary of that analysis, concentrating on geometries that were useful for this instrument.

Surface supercurrents induced in a piece of superconductor account for its property of excluding magnetic flux. For a small thin tab placed perpendicular to a magnetic field, the pattern of screening currents produces a field that is, to first order, that of a magnetic dipole. The vector potential A due to a magnetic dipole m is given by

$$\mathbf{A} = \frac{\mu_0}{4\pi r^3}(\mathbf{m} \times \mathbf{r}), \tag{3.7}$$

in which r is the position vector from m to the point at which A is calculated. Integration of this function around a closed circuit C gives the flux which threads C:

$$\Phi_c = \oint_c \mathbf{A}.d\mathbf{l}. \tag{3.8}$$

By solving these general equations within certain helpful constraints, I shall obtain an exact expression for the flux threading a single gradiometer coil, due to a magnetic dipole (equation 3.10). I shall then constrain the problem further, considering the two trim tab geometries which were of practical use, and I shall justify the magnetic dipole approximation.

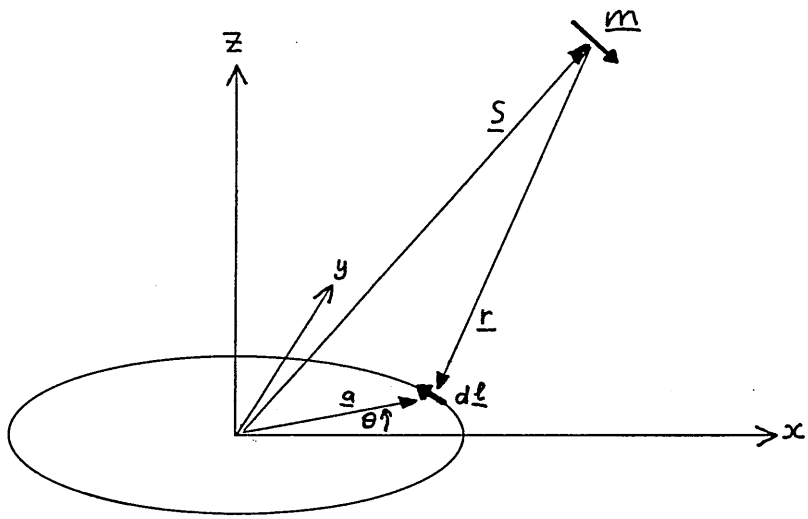

Figure 3.8 Geometrical arrangement

The general arrangement for a single magnetic dipole and a single coil, radius a, is illustrated in figure 3.8. Choosing the centre of the coil to be the coordinate origin, for ease of integration, the magnetic dipole m is then located at s. Each coil element dl is located at a, and so the vector r, which must be used in equation 3.7 is given by

$$\begin{aligned} \mathbf{r} &= \mathbf{a} - \mathbf{s} = (a_x - s_x)\,\mathrm{i} + (a_y - s_y)\,\mathrm{j} + (a_z - s_z)\,\mathrm{k} \\ &= (a\cos\theta - s_x)\,\mathrm{i} + (a\sin\theta)\,\mathrm{j} - s_z\mathrm{k}, \end{aligned}$$

where, in the second formula, a is dropped in favour of polar coordinates a (fixed for the coil) and θ. Furthermore, because of the symmetry of the problem, the coil can be constrained

to the x-y plane and the dipole's location to the x-z plane without losing generality. This implies that $a_z = s_y = 0$. Hence

$$\mathbf{m} \times \mathbf{r} = \left(A'_x \mathbf{i} + A'_y \mathbf{j} + A'_z \mathbf{k}\right),$$

in which

$$A'_x = (-m_y s_z - m_z a \sin\theta)$$

$$A'_y = (m_z \{a\cos\theta - s_x\} + m_x s_z)$$

$$A'_z = (m_x a \sin\theta - m_y \{a\cos\theta - s_x\})$$

and

$$r^{-3} = \left(\{a\cos\theta - s_x\}^2 + \{a\sin\theta\}^2 + \{s_z\}^2\right)^{-\frac{3}{2}} = \left(s_x^2 + s_z^2 + a^2 - 2as_x\cos\theta\right)^{-\frac{3}{2}}.$$

Substitution into equation 3.7 yields

$$\mathrm{A} = \left(\frac{\mu_0}{4\pi}\right)\left(s_x^2 + s_z^2 + a^2 - 2as_x\cos\theta\right)^{-\frac{3}{2}}\left(A'_x\mathbf{i} + A'_y\mathbf{j} + A'_z\mathbf{k}\right) \tag{3.9}$$

for the vector potential.

Now, integrating the vector potential around the coil (remembering that z is non-variable),

$$\oint_c \mathrm{A}.d\mathrm{l} = \oint_c A_x dx + \oint_c A_y dy = a\int_0^{2\pi}(A_y\cos\theta - A_x\sin\theta)\,d\theta,$$

since

$$x = a_x = a\cos\theta \Rightarrow dx = -a\sin\theta d\theta$$

$$y = a_y = a\sin\theta \Rightarrow dy = a\cos\theta d\theta$$

in polar coordinates. Combining this with equations 3.8 and 3.9 yields, on rearrangement,

$$\Phi_c = X\int_0^{2\pi}(Y - Z\cos\theta)^{-\frac{3}{2}}(S + T\cos\theta + V\sin\theta)\,d\theta$$

in which:

$$X = \left(\frac{\mu_0 a}{4\pi}\right)$$

$$Y = \left(s_x^2 + s_z^2 + a^2\right)$$

$$Z = (2as_x)$$

$$S = (am_z)$$

$$T = (m_x s_z - m_z s_x)$$

$$V = (m_y s_z).$$

Expansion of this formula leads to three integrals:

$$\Phi_c = XS\int_0^{2\pi} I_1 d\theta + XT\int_0^{2\pi} I_2 d\theta + XV\int_0^{2\pi} I_3 d\theta,$$

where

$$I_1 = (Y - Z\cos\theta)^{-\frac{3}{2}}$$

$$I_2 = I_1 \cos\theta$$

$$I_3 = I_1 \sin\theta,$$

of which the third is analytically soluble and, as shown below, equal to zero:

$$\int_0^{2\pi} I_3 d\theta = \left[-\frac{2}{Z}(Y - Z\cos\theta)^{-\frac{1}{2}}\right]_0^{2\pi} = 0.$$

Thus, the fully general formula for the magnetic dipole flux intercepted by a coil is given by

$$\begin{aligned}\Phi_c &= \left(\frac{\mu_0 a}{4\pi}\right)\left\{am_z\int_0^{2\pi}\left(s_x^2 + s_z^2 + a^2 - 2as_x\cos\theta\right)^{-\frac{3}{2}}d\theta\right. \\ &\left. + (m_x s_z - m_z s_x)\int_0^{2\pi}\left(s_x^2 + s_z^2 + a^2 - 2as_x\cos\theta\right)^{-\frac{3}{2}}\cos\theta d\theta\right\}. \quad (3.10)\end{aligned}$$

There are two positions where it is relatively simple to analyze the effect of a trim tab, and which would afford engineering convenience. These are on the gradiometer axis (for a tab perpendicular to the vertical/axial field component) and on the surface of the former (for tabs perpendicular to horizontal/radial components). I shall, hereinafter, refer to these two genera as 'vertical' and 'horizontal' tabs, respectively. Each of these special cases has friendly symmetry, allowing considerable simplification of the formula for the flux captured (equation 3.10). I shall analyze them separately and then discuss the results in the context of practical experience.

(i) For a vertical tab on axis, $m_x = m_y = 0, m_z \neq 0$, and $s_x = s_y = 0, s_z \neq 0$. Entering this information into equation 3.10 and integrating yields

$$\Phi_v = \frac{\mu_0 a^2 m_z}{2\left(s_z^2 + a^2\right)^{\frac{3}{2}}}. \quad (3.11)$$

For reasons of symmetry, it is sensible to use a circular tab. Actually, of course, I mean a thin disc: a limiting case of a flattened (oblate) spheroid. For a given axis i of any spheroid placed in a uniform external magnetic field H_{ext}, the internal and external fields (H_{int} and H_{ext}) are related by [97]

$$H_{int,i} = H_{ext,i} - D_i M_i,$$

in which M_i is the magnetization along that axis and D_i is the 'demagnetization factor'. This latter parameter is shape-dependent and, for an oblate spheroid in a magnetic field oriented parallel to the polar axis (which I shall call z), is given approximately by

$$D_z = 1 - \frac{\pi p}{2q},$$

where p and q are the polar and equatorial semiaxes respectively, as shown in figure 3.9.

Considering just z-components, inside the disc

$$\frac{B_{int}}{\mu_0} = H_{int} + M = H_{ext} - DM + M,$$

which is zero for a superconductor (a perfect diamagnet), and therefore

$$M = -\frac{H_{ext}}{1 - D} = -\frac{2qH_{ext}}{\pi p} = -\frac{2qB_{ext}}{\pi p \mu_0},$$

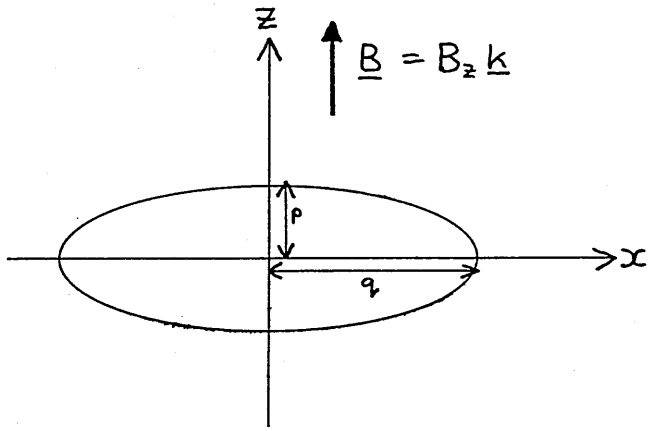

Figure 3.9 Cross section showing magnetization inside an oblate spheroid

using the formulae above. The magnetic dipole moment due to this piece of magnetized material is given by

$$m_z = M_z V$$

provided that the volume $V = 2p\pi q^2$ is small. In practice, this means that it must be small compared with the dimensions over which its effect will be considered (in this case, the area of a coil). If this condition is satisfied, the dipole moment of a superconducting disc opposing an external field B_{ext} is given by

$$m_z = \frac{4q^3 B_{ext}}{\mu_0}$$

and so substitution into equation 3.11 gives the flux in the coil due to the tab:

$$\Phi_{vtab} = \frac{2q^3 B_{ext} a^2}{(s_z^2 + a^2)^{\frac{3}{2}}}.$$

This can be compared with the flux intercepted by the *sensing* coil (turns-area $N_s A_s$) directly due to B_{ext}, and in the absence of the tab:

$$\Phi_{ext} = N_s A_s B_{ext},$$

$$\frac{\Phi_{vtab}}{\Phi_{ext}} = \frac{2q^3 a^2}{N_s A_s (s_z^2 + a^2)^{\frac{3}{2}}}. \tag{3.12}$$

Thus, equation 3.12 gives the degree of unbalance which can be introduced by a circular superconducting trim tab on axis (to compensate for the winding unbalance). I shall discuss this result in the light of practical experience after considering horizontal tabs.

(ii) <u>For a horizontal tab at a fixed radius</u> with its plane oriented tangentially, $m_y = m_z = 0, m_x \neq 0$, and $s_y = 0, s_x \neq 0, s_z \neq 0$, since, as was stated earlier, it can be constrained to the x-z plane (say) without losing generality. Substitution of this information into equation 3.10 yields

$$\Phi_h = m_x s_z X \int_0^{2\pi} (Y - Z\cos\theta)^{-\frac{3}{2}} \cos\theta d\theta, \tag{3.13}$$

in which X, Y, Z are abbreviations for the same functions as before and are repeated here:

$$X = \left(\frac{\mu_0 a}{4\pi}\right)$$

$$Y = \left(s_x^2 + s_z^2 + a^2\right)$$
$$Z = (2as_x).$$

Now, the function

$$(Y - Z\cos\theta)^{-\frac{3}{2}} = Y^{-\frac{3}{2}}\left(1 - \frac{Z}{Y}\cos\theta\right)^{-\frac{3}{2}}$$

can be approximated by a binomial expansion if $\left|\frac{Z}{Y}\cos\theta\right| < 1$. Clearly $|\cos\theta| \leq 1$, and so it is required that $Y > Z$, ie that

$$s_x^2 + s_z^2 + a^2 > 2as_x \Rightarrow (s_x - a)^2 + s_z^2 > 0,$$

which is also clearly true.

Setting $P = \frac{Z}{Y}$, the expansion is

$$\begin{aligned}(1 - P\cos\theta)^{-\frac{3}{2}} &= 1 + \left(-\frac{3}{2}\right)(-P\cos\theta) + \frac{\left(-\frac{3}{2}\right)\left(-\frac{5}{2}\right)(-P\cos\theta)^2}{2!} \\ &\quad + \frac{\left(-\frac{3}{2}\right)\left(-\frac{5}{2}\right)\left(-\frac{7}{2}\right)(-P\cos\theta)^3}{3!} \\ &\quad + \frac{\left(-\frac{3}{2}\right)\left(-\frac{5}{2}\right)\left(-\frac{7}{2}\right)\left(-\frac{9}{2}\right)(-P\cos\theta)^4}{4!} + \ldots\end{aligned}$$

and all the terms are positive. This series can be generalized and substituted into equation 3.13 to give

$$\Phi_h = m_x s_z X Y^{-\frac{3}{2}} \int_0^{2\pi} \left(\sum_{i=0}^{\infty} P^i \left\{\frac{(2i+1)!!}{2^i . i!}\right\} \cos^{i+1}\theta\right) d\theta \qquad (3.14)$$

in which the notation "$n!!$" means $n \times (n-2) \times (n-4) \times \ldots$ terminating with unity or two (whichever is encountered). Note also, that 0!! is defined to be unity. Using the standard result that

$$\begin{aligned}J_\lambda = \int_0^{2\pi} \cos^\lambda\theta d\theta &= 2\pi\frac{(\lambda-1)!!}{\lambda!!} \qquad (\lambda \text{ even}) \\ &= 0 \qquad (\lambda \text{ odd}),\end{aligned}$$

it can be seen that the function in equation 3.14 is zero for $i = 0$ and all even values. Thus, the formula can be simplified with a change of counter: $j = \frac{1}{2}(i+1)$, yielding, after simplification and resubstitution for abbreviations P, X, Y:

$$\Phi_h = \frac{\mu_0 a}{2}\left(s_x^2 + s_z^2 + a^2\right)^{-\frac{3}{2}} m_x s_z \sum_{j=1}^{\infty}\left(\frac{as_x}{s_x^2 + s_z^2 + a^2}\right)^{2j-1} \frac{(4j-1)!!}{(2j)!!\,(2j-2)!!}. \qquad (3.15)$$

Using the observation that adjacent terms in this summation are related by

$$T_j = T_{j-1}\left[\left(\frac{as_x}{s_x^2 + s_z^2 + a^2}\right)^2 \frac{(4j-1)(4j-3)}{2j\,(2j-2)}\right],$$

where T_j is the jth term and T_{j-1} the previous one, a computer program was written to calculate solutions to equation 3.15. The series was terminated after calculating the j_{max}th term when the following condition was satisfied:

$$\frac{\sum_{j=j_{max}+1}^{\infty} T_j}{\sum_{j=0}^{j_{max}} T_j + \sum_{j=j_{max}+1}^{\infty} T_j} < 0.01.$$

At that point in the calculation, the sum of terms was $\sum_{j=0}^{j_{max}} T_j$. The sum of the remaining terms was estimated by making the approximation that, for large j,

$$\frac{(4j-1)(4j-3)}{2j(2j-2)} \approx 4$$

and using the sum of terms in a geometrical series:

$$\sum_{j=j_{max}+1}^{\infty} T_j = WT_{j_{max}} + W^2T_{j_{max}} + W^3T_{j_{max}} + \ldots = \frac{T_{j_{max}}}{(1-W)},$$

where

$$W = 4\left(\frac{as_x}{s_x^2 + s_z^2 + a^2}\right)^2.$$

The magnetic dipole moment m_x of a circular horizontal trim tab was calculated in exactly the same way as described for the vertical tab. Substitution of this formula into equation 3.15 yields the flux Φ_{htab} coupled by a coil due to a horizontal trim tab in an external field. Dividing this by the flux Φ_{ext} which *would* be intercepted by the sensing coil, if it were oriented perpendicular to B_{ext}, gives the degree of unbalance which can be introduced. The program was extended to carry out these calculations[7].

Practical application of the trim tab analysis

I shall now digress briefly, to consider how gradiometer unbalance actually arises and how trim tabs remedy the problem. In practice, the total turns-area vector will not be zero, as designed, and placement of a vertical tab within the plane of that coil which is slightly larger than the others will deflect some flux outside of it and reduce its effective area. Generally, a position between coil levels will be found to satisfy the balance condition.

Horizontal unbalance, on the other hand, is caused by tilting of the coil planes and its relationship with the position of the trim tab is more complicated. The horizontal tabs are most effective if they travel on a fairly large radius, close to the wire, whereas a central position is optimal for the vertical tab [78].

SQUIDLET's gradiometer former was designed to accommodate three control rods, each of which would carry a trim tab. As illustrated in figure 3.10, three vertical holes were drilled in the former: the central one for vertical field balancing and the two peripheral ones, centred on mutually perpendicular radii of 6 mm, for horizontal field balancing. The nylon rods were controlled by a gear box located above the gradiometer, and the lead foil tabs were glued to the rods: a lead circle of radius 1 mm for vertical balance and lead squares of side 2 mm for horizontal balance. The mechanism was adjusted so that the tabs' range of vertical travel was from a few millimetres above the upper coil to a few millimetres below the central coil.

Equation 3.12, which is reprinted below, was used to calculate the balancing range that the vertical tab would provide.

$$\frac{\Phi_{vtab}}{\Phi_{ext}} = \frac{2q^3a^2}{N_sA_s(s_z^2 + a^2)^{\frac{3}{2}}}$$

With the tab in the plane of the upper coil, $q = 1$ mm, $a = 8$ mm, $N_sA_s = 16 \times \pi\,(2)^2$ mm^2 and $s_z = 0$ mm, yielding an unbalance of about 1,200 ppm. The modulus of the theoretical

[7] An alternative approach to this analysis could have utilized the reciprocity theorem [32].

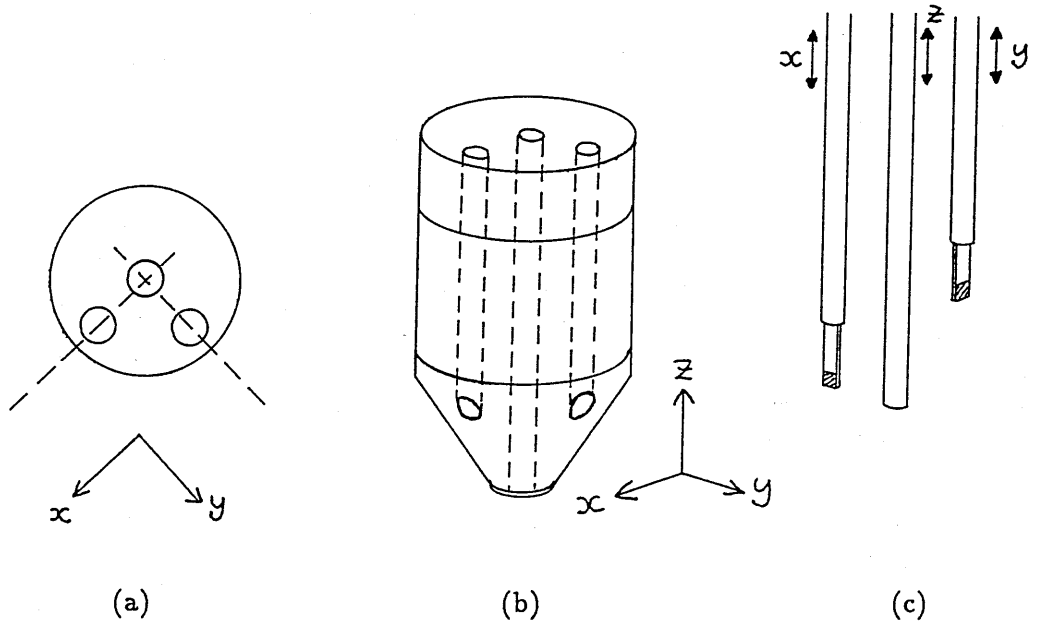

Figure 3.10 Practical arrangement for balancing uniform fields
(a) Plan view of gradiometer former
(b) Perspective view without control rods
(c) Control rods

value at the other extreme (tab in the plane of the central coil) is twice as much because there are two turns instead of one. The balancing range, then, was expected to be about 3,600 ppm: rather less, because the antagonistic effect on the other coils, in each case, had been neglected. A more difficult calculation (a programmed algorithm developed from equation 3.15) predicted that the horizontal balancing range would be about 2,000 ppm.

There is no contingency in the designs illustrated in figures 3.7 and 3.10 for affecting the response to uniform field gradients. This is a considerably more difficult engineering problem requiring, as it does, adjustment of the baseline [3]. Because of SQUIDLET's short baseline, a mechanism for gradient balancing was deemed unnecessary: indeed, it would have been highly impractical, given the shortage of available space. It seems likely, in retrospect, that SQUIDLET's ultimate noise performance, although satisfactory, was limited by noise gradients.

In order to determine the degree of unbalance experimentally, a time-varying and spatially uniform magnetic field is required, and this may be generated by Helmholtz coils. The set of coils in the Open University laboratory consists of a pair of vertical coils (ie generating a uniform vertical field) with common radius and separation of 0.95 m and a pair of horizontal coils for which the same dimension is 1.04 m. With this arrangement, the axial field homogeneity over the volume of SQUIDLET's gradiometer, if it is placed at the centre of the coils, is better than 2 ppm.

Once wound, SQUIDLET's gradiometer was connected to the SQUID, inserted into the dewar and positioned at the centre of the Helmholtz coil set. By energizing the coils with a low frequency ($\approx$ 30 Hz) alternating current and by monitoring the SQUID output, it was clear that the gradiometer was badly out of balance.

As explained during the derivation of equation 3.12, the degree of unbalance (to horizontal

and vertical field components) is usually quoted as a fraction: the measured output for a given field sweep divided by that calculated for the same field sweep, assuming the detector consisted solely of the sensing coil placed perpendicular to the field. In order to reduce noise levels in an urban environment sufficiently to make biomagnetic measurements, the unbalance usually needs to be less than 10 ppm. In practice, SQUIDLET's gradiometer could be balanced to a precision of better than 6 ppm to vertical fields, and better than 2 ppm to horizontal fields, ie about the same precision as the field homogeneity.

However, SQUIDLET's initial unbalance was about 30,000 ppm for the vertical field (corresponding to half a turn on the sensing coil) and about 5,000 ppm for horizontal fields[8]. The balancing ranges of the travelling trim tabs were measured and found to be 3,000 ppm and 2,000 ppm respectively (in good agreement with the predicted values). These results confirmed the necessity of *fixed* trim tabs: to bring the unbalance within the range of action of the travelling tabs.

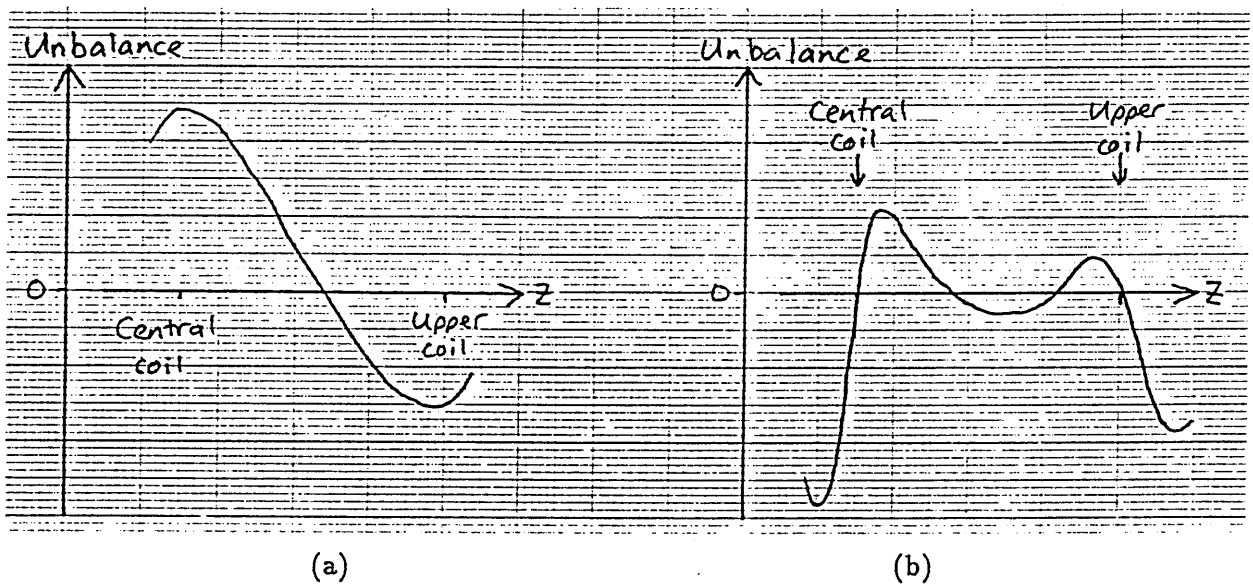

Figure 3.11 Gradiometer unbalance to uniform fields
(a) Vertical field
(b) A horizontal field component

Figure 3.11 shows the measured degree of unbalance as a function of trim tab position for the vertical field (a) and for one horizontal field component (b). The effect of adding or removing fixed tabs is to move these curves up and down the ordinate axis. The figures show optimal situations with the zero unbalance point approximately central in the range, and (in b) on a relatively shallow part of the curve (so that the degree of unbalance introduced by small changes in the tab position is minimized).

Equation 3.12 and its analogue for the horizontal balance sensitivity were utilized in the design of the fixed trim tabs.

The vertical unbalance (30,000 ppm) was about as bad as it could be without actually

[8]The horizontal field coils are positioned to generate a uniform field parallel with a magnetic meridian (for geomagnetic field cancellation purposes), but by rotating the dewar through 90° the unbalance along both x- and y-axes (see figure 3.7) could be measured.

requiring an extra turn on the sensing coil, and a fixed tab in the central coil, say, needed to have about twelve times more effect than the travelling one, in order to rectify this. For practical reasons, it was obviously not possible to place the fixed tab on the gradiometer axis; indeed, the available space was limited and irregular in shape. Consequently, equation 3.12 had to be used as a semi-empirical guide. As illustrated in figure 3.12a,b, the vertical tabs (circle sectors with upper and lower radius limits) were inserted into horizontal saw cuts in the gradiometer former close to the upper and central coils. It turned out that the magnetic dipole moment was weakly dependent on shape and strongly dependent on the size of the tab, particularly when s_z was small.

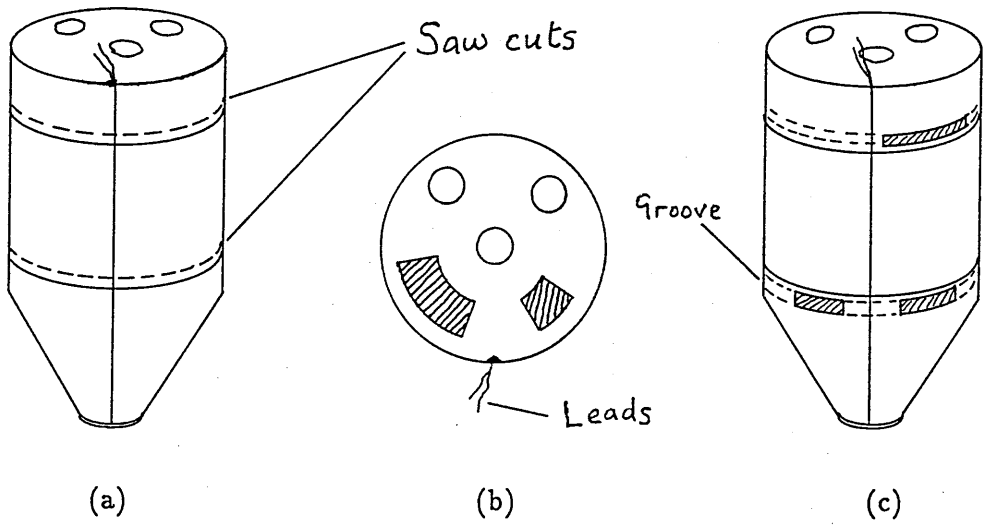

Figure 3.12 Shape and positioning of the fixed trim tabs
(a) Saw cuts for vertical tabs
(b) Plan view of vertical tabs
(c) Perspective view of horizontal tabs

For the horizontal tab, experimentation with the algorithm that had been developed from equation 3.15 produced the following result. A flat rectangular tab, 5 mm long × 1 mm high, centred 1 mm above or below the central coil changes the unbalance by about 4,500 ppm: of the same order as a typical winding error unbalance to horizontal fields. The flat tab is a good approximation to a realistic situation in which the tab curves around the gradiometer former. If necessary, the tabs could be made somewhat longer than this, and the effect could be doubled by placing a tab just above the coil on one side of the former and another just below it, on the other side. Additionally, the upper coil could be used.

To facilitate positioning these tabs, 1 mm high shallow grooves were machined in the gradiometer former. They were centred 1 mm above and below the upper and central coils. After measuring the unbalance, it was possible to predict, quite accurately, the size of horizontal trim tab which was required to bring the unbalance into the range of the travelling tabs (see figure 3.12c). Clearly, two independent horizontal field components can be decoupled and so, with each thermal cycle, the unbalance to each of two perpendicular horizontal uniform field components was measured, and the two were corrected separately.

The vertical unbalance was also corrected independently.

The use of the analysis outlined in this section, although only approximately correct, for analytical and engineering convenience, undoubtedly saved a considerable amount of time when balancing for uniform fields. This was verified by the fact that on most occasions, when the gradiometer was rewound, no more than two thermal cycles were required to bring both the vertical and horizontal unbalance into the range of the travelling tabs. Fine balancing with the travelling trim tabs could then improve the unbalance to 6 ppm for vertical fields and 2 ppm for horizontal fields.

A similar analysis of balancing procedures has been developed independently by Guy *et al* [48].

3.3 The operating SQUIDLET probe

Figure 3.13 is an overall view of the probe. I have already described the gradiometer in great detail. The leads are twisted together and threaded through a narrow lead tube which shields the signal from interference. The tube is fixed relative to the gradiometer, and relative to the SQUID, but there is some flexibility to allow for changes in the length of the probe. This was expected as a normal consequence of thermal cycling, but, in any case, variability in the probe length was built into the design to ensure that the gradiometer sensing coil would rest on the tip of the dewar. To achieve this, a spring was incorporated.

For clarity, the tufnol upper sections of the trim tab control rods are not shown in figure 3.13. These extend through the top plate, where they are operated, and provide multiple-turn angular drive to the worm gears driving the nylon rods, on which the trim tabs are mounted. Two 470 Ω Allen Bradley carbon resistors are bonded to the fill tube at positions corresponding to the bottom and top of the broad helium reservoir and serve as depth gauges.

In the remainder of the section, I shall describe the testing and characterization of the instrument. Section 3.3.1 is concerned with the detection of unwanted signals and the attempts to attenuate the noise in the system to a satisfactory level. Then, in section 3.3.2, I shall describe a curious pathology that was observed whilst the gradiometer was being balanced. Finally, SQUIDLET's high resolution performance will be reviewed when I report two model experiments in section 3.3.3.

3.3.1 Noise

Because the exact processes of noise production are various and often incompletely understood, it has become conventional to quote noise performance in terms of *equivalent* noise; ie the noise due to a well-defined process that is equivalent to that measured. The most oft-quoted figure in magnetometry is the equivalent field noise at the sensing coil, which has units of tesla per root hertz ($\mathrm{THz}^{-\frac{1}{2}}$). This is derived from the field spectral density, $S_B(f)$: the mean square field within a 1 Hz bandwidth centred at frequency f. Noise is often almost independent of frequency (white) over large bandwidths and so, in these circumstances, $S_B(f)$ is constant. Expressing the noise in terms of the root spectral density is

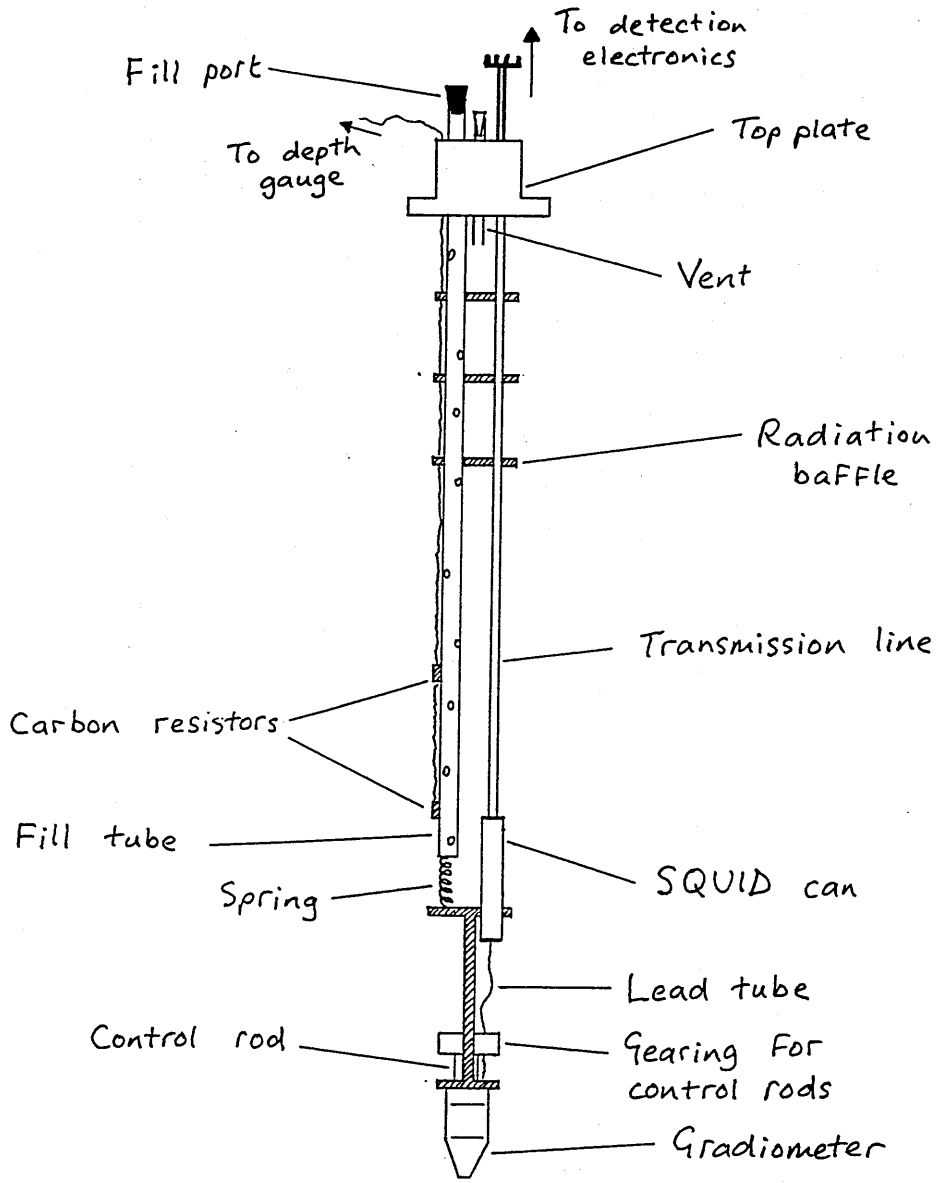

Figure 3.13 Diagram of the entire SQUIDLET probe

convenient, as it allows a direct comparison with typical signal fields. Related parameters are the equivalent current noise and equivalent energy noise in the input coil.

Noise in a SQUID magnetometer system may be categorized as originating in three distinct ways: there are sources intrinsic to the measurement system, sources extrinsic to the experiment and subject-related sources. I shall concentrate on the first two of these.

Intrinsic noise arises due to thermal processes in the Josephson junction(s) in the SQUID or in associated circuitry, such as the radio frequency tank circuit used to bias an rf SQUID. The equivalent input coil current noise in the SQUID that was built into SQUIDLET's probe, was quoted by the manufacturer to be 1.37×10^{-12} AHz$^{-\frac{1}{2}}$. The equivalent field noise is the rms field per root bandwidth at the sensing coil which would produce this quoted current noise in the flux transporter. Now,

$$B_s = \frac{\Phi}{N_s A_s} = \frac{L_T I_{in}}{N_s A_s},$$

where $L_T = 4\mu$H is the total inductance of the flux transporter and $N_s A_s = 16\pi(2 \times 10^{-3})^2$ m^2 is the turns-area of the sensing coil. Thus, the equivalent field noise due to intrinsic sources should be about 27 fT Hz$^{-\frac{1}{2}}$. However, other sources were dominant.

In theory, a SQUID can be isolated from the environment, by superconductively shorting the terminals to the input coil. In this state and in spite of the SQUID's shield, however, SQUIDLET's SQUID was still sensitive to movements of a small permanent magnet a metre away, and the measured white noise was too high by a factor of three. It was quite possible, therefore, that ambient field fluctuations could also couple directly to the SQUID, despite the shield.

Numerous measurements of the noise in various bandwidths and under many different conditions were made, in an attempt to locate the source of the extra noise: eddy current noise in the dewar, normal metal injection of Johnson noise and noise due to vibrations or helium bubbling were eliminated. An additional shield, of thick soldered lead foil, was constructed around the existing one and, after several refinements, a small but definite improvement in performance was observed. The greatest improvement (a reduction in the shorted noise of about 40%) was achieved by replacing the locking nut at the upper end of the fitted shield with a nylon one. It turned out that the original nut was made of highly magnetic steel and that the shield, itself, was covered with a ferromagnetic alloy, conetic. I shall return to a further effect of the conetic in section 3.3.2.

The intrinsic noise performance which was eventually achieved was about 40 fT Hz$^{-\frac{1}{2}}$ in a 0–40 Hz bandwidth. There was less than 20% variation in this figure across the SQUID's operating spectrum from dc to 10 kHz.

However, with the gradiometer reconnected to the SQUID, the measured noise was considerably greater than this. The second type of noise encountered in sensitive magnetometry is that originating extrinsically. Examples are radio frequency communication signals, mains frequency (50 Hz) fields and moving magnetic objects such as fans, tea trolleys or motor vehicles. In SQUIDLET's case, rf interference was a significant problem.

SQUIDLET's SQUID can operate in either of two modes which have different slew rates (the maximum rate of change of current in the input coil which can be tracked). If a signal from the biomagnetic source or a noise source exceeds the limiting frequency (which, itself, is a function of signal intensity) then the SQUID will admit one or more flux quanta and 'break lock'. Thus, the SQUID is more likely to remain flux-locked in the faster slew rate mode (which may be necessary in noisy conditions), but will be more sensitive to high frequency noise. Strong radio transmissions can stop the instrument functioning altogether, if they exceed the fastest slew rate of the instrument. The most common point of entry of the interference is the gradiometer, and a shunt resistor, placed across the input coil terminals can greatly attenuate rf signals without degrading the low frequency signal of interest.

The effect is to divide the current between the resistor and the input coil, and the proportion in each arm is a function of frequency. Referring to figure 3.14,

$$I_T = I_{in} + I_{sh}$$

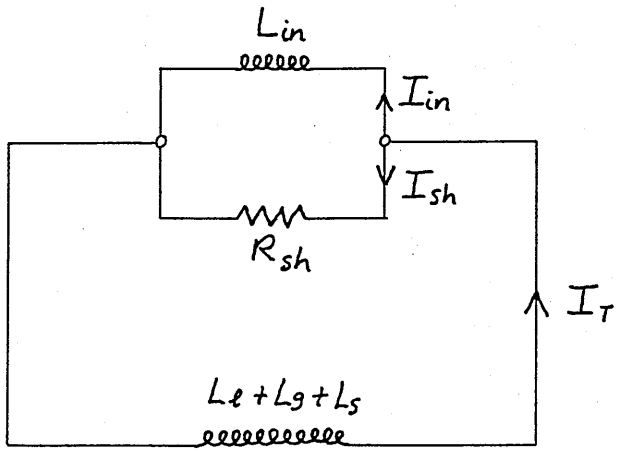

Figure 3.14 The rf shunt

and, for 50% attenuation, the impedances must be matched:

$$\omega L_{in} = R_{sh}.$$

The lower the resistor, the lower is the cutoff frequency and the greater is the effective shielding against rf interference. However, the resistor is also a source of thermal (Johnson) noise, and if the bandwidth is too small, this can become a limiting noise source. A compromise must be struck. A 10 Ω carbon resistor was used to shunt SQUIDLET's terminals. The resistance of this device at 4.2 K was 70 Ω and so 50% rejection (the −3 dB point) was at a frequency of 5.6 MHz. For biomagnetic signals of, say, $f = 10$ Hz, the resistor takes only 1.8 ppm of the signal. This modification improved the rf rejection enormously, while injecting negligible thermal noise, and the system was operable most of the time.

However, a shunt is effective against differential mode interference only. If rf is being picked up by both sides of the circuit (common mode), a different form of screening is required.

A high conductivity screened room or a Faraday cage provide the greatest protection, but they have disadvantages of cost and bulkiness. For SQUIDLET's dewar, a close-fitting jacket, consisting of six sections of aluminium foil, was designed. Adjacent sections had to overlap tightly, although eddy current paths which could couple flux into the gradiometer had to be avoided, and so strips of insulation were required at the overlaps. Furthermore, all of the shield had to be electrically connected and earthed at one point. In fact, four concentric shields were fitted.

The rf shield appeared, surprisingly, to increase the noise and it turned out that this was due to Johnson noise in the part of the shield covering the tip of the dewar. Here, the shield was only 5 mm away from the sensing coil, and a great reduction in the low frequency noise was observed, while sustaining the further improvement in rf rejection, when this section was removed. To give a feeling for the seriousness of rf shield Johnson noise, I shall present a rough calculation of the noise due to the remaining shield.

According to Sarwinski [85], the field noise in gauss per root hertz at the centre of an

open-ended cylinder whose length and diameter are similar, is given by

$$B_{rms} = 8\left(\frac{\pi kT\delta \times 10^{-9}}{2lr\rho}\right)^{-\frac{1}{2}}, \tag{3.16}$$

where all the quantities are in cgs units. Considering merely the shield section around the tail of the dewar (the rest being distant from the gradiometer and not making a significant contribution), with radius $r = 5.9$ cm, length $l = 11.8$ cm, thickness $\delta = 0.008$ cm (four sheets of 20 μm aluminium) and resistivity $\rho = 2.5 \times 10^{-6}$ Ωcm, the field noise is 44 fT $Hz^{-\frac{1}{2}}$ at 298 K.

Although this is greater than the intrinsic noise, it would not limit performance, because much of this noise field would be rejected by the gradiometer configuration, and, in any case, the lowest achievable noise was still as high as 65 fT $Hz^{-\frac{1}{2}}$, when the gradiometer was precisely balanced. However, the noise from four aluminium sheets across the tip, just 5 mm from the sensing coil was much greater than this.

It was observed that precise balancing was not really necessary, as the 'best performance' could be maintained over a range of balance conditions. I believe that the rejection of extrinsic noise was limited by field gradients, against which discrimination was very poor. The vertical gradient unbalance was measured, by passing opposite currents through the two Helmholtz coils. When this was compared with the calculated unbalance of a first-order gradiometer (same coil size and baseline as SQUIDLET's), the fractional unbalance was found to be about 8%. This is poor: Barbanera *et al* [3] reported a significant improvement in unshielded low frequency performance when they reduced the gradient unbalance to about 100 ppm.

Nothing could be done to improve the gradient unbalance and so field noise of 65 fT $Hz^{-\frac{1}{2}}$ was accepted. This corresponded to a noise floor of about 400 fT when measuring with a 40 Hz bandwidth.

3.3.2 Hysteretic behaviour

In this section, I shall describe a mysterious phenomenon which was observed during balancing.

Assuming field homogeneity over the volume of the gradiometer (see section 3.2.3) application of a low frequency signal to the Helmholtz coils should elicit an in-phase response from the gradiometer when it is unbalanced and zero response when it is balanced. Figure 3.15 shows the SQUID output as a function of applied field as the trim tab is moved through its balance position. In (a) and (c), the gradiometer is unbalanced with opposite polarities, and in (b) it is balanced.

Traces like these were obtained when the amplitude of the uniform applied field was small; the usual protocol was to apply a 10 mA peak-to-peak current to the coils, which produced a peak-to-peak field of about 700 nT at the centre. However, when a larger field was applied, the traces developed a hysteresis, as shown in figure 3.16. When the gradiometer was unbalanced, the difference between the 'field-increasing' and 'field-decreasing' paths was

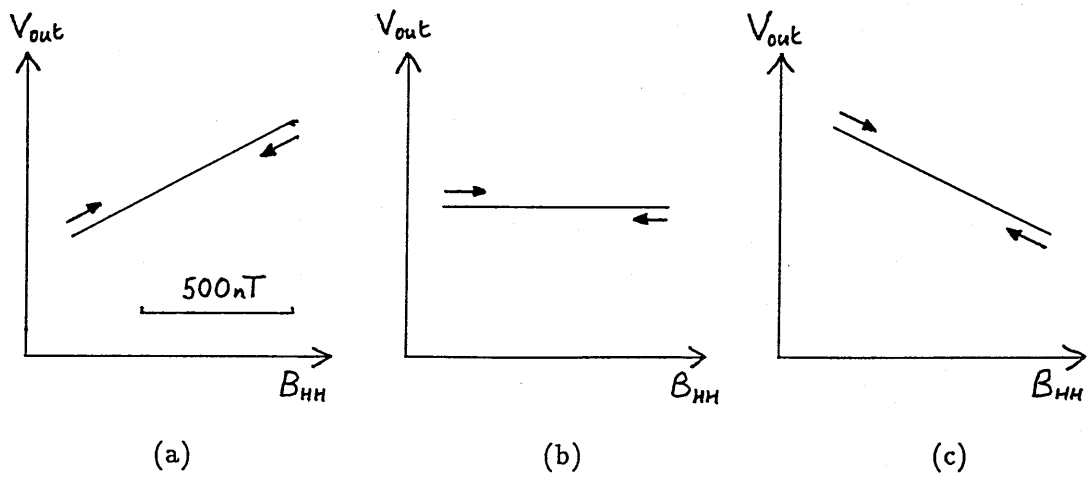

Figure 3.15 SQUID output during balancing ($B_{pp} \approx 700$nT)
(a) Positive unbalance
(b) Zero unbalance
(c) Negative unbalance

barely perceptible, but as the balance point was approached, it became more apparent, although the enclosed area appeared to be the same.

Although a balance point could still be found (meaning a tab position at which the SQUID output was identical at either end of a 7 μT field sweep), it was different from the balance point obtained with a 700 nT field sweep. Thus, the balance point was a function of the amplitude of the applied field.

After many checks of possible mechanisms, it was inferred that the ferromagnetic conetic shield on the SQUID was responsible. This conclusion remained somewhat tentative, however, because the effect was not amenable to precise calculation and the shield could not be removed.

A possible mechanism might be that the gradiometer experienced both the applied Helmholtz field and an additional contribution from the nearby conetic shield. This additional field would be non-linearly dependent on the Helmholtz field because of the hysteretic nature of ferromagnets. The situation was probably aggravated by the adjacency of the niobium shield, a large superconductor, and further complications would be introduced if the relaxation time of conetic, in a constant field, is short.

This analysis was not pursued any further and, on the assumption that noise fields would be smaller than 700 nT, this amplitude was used for balancing. Since, with an applied field of this magnitude, the gradiometer could be balanced to the most precise degree provided by the SQUID, it was deduced that the error in the balance point was too small to be of concern. In any case, the field noise was not dependent on small changes in the level of unbalance, and minimizing the field noise is, after all, the purpose of balancing!

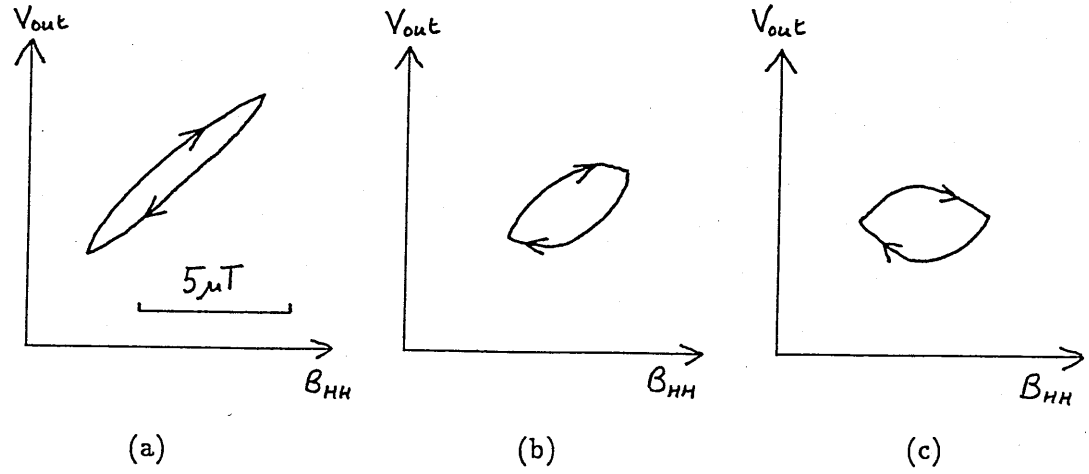

(a) (b) (c)

Figure 3.16 SQUID output for $B_{pp} \approx 7\mu$T
(a) Poorly 'balanced'
(b) Almost 'balanced'
(c) 'Balanced'

3.3.3 High resolution performance of SQUIDLET

This section is concerned with SQUIDLET's ability to resolve close current sources. I shall describe briefly two experiments, present some of the data and draw conclusions about the resolution of the instrument. A detailed account of the standard post-SQUID data processing and experimental software will appear in chapter 6 with reference to the chick egg measurements. The arrangements for these experiments were very similar. The presentation in this chapter is intended to be a simple demonstration of SQUIDLET's performance.

The first experiment was designed to determine SQUIDLET's response to close parallel and antiparallel line currents. The results of these measurements are important because they indicate the reliability of high resolution data in which the sources are not known.

A 3 m computer ribbon cable, consisting of 50 insulated wires separated by 1.27 mm, was used. Each measurement consisted of a single 120 mm scan in the x-direction, performed as described in section 2.2.1, across the centre of the cable which lay parallel to the y-axis. Magnetic field data and position data were simultaneously recorded and the field data are presented as scans with increments of 0.94 mm. For each scan, two wires were simultaneously energized with 1 mA currents, and the measurements were repeated at several different depths below SQUIDLET's dewar. The signal-to-noise ratio was always greater than 100.

Figure 3.17 shows some of the recorded scans. For each set of five scans, the wire separations were as follows (from top to bottom in the figures): 6.3 mm, 8.9 mm, 12.7 mm, 19.0 mm, 25.3 mm. The scans in (a) were recorded with the ribbon grazing the dewar tip, corresponding to a depth $d = 6$ mm below the sensing coil, for those in (b) and (c), $d = 9$ mm and 16 mm respectively. The horizontal extent of each scan is 120 mm, and the vertical axes (measured field) are individually normalized.

The closest separation of wires that can be visually resolved is given by the second scan when the depth $d = 6$ mm, the third with $d = 9$ mm and and the fourth with $d = 16$ mm.

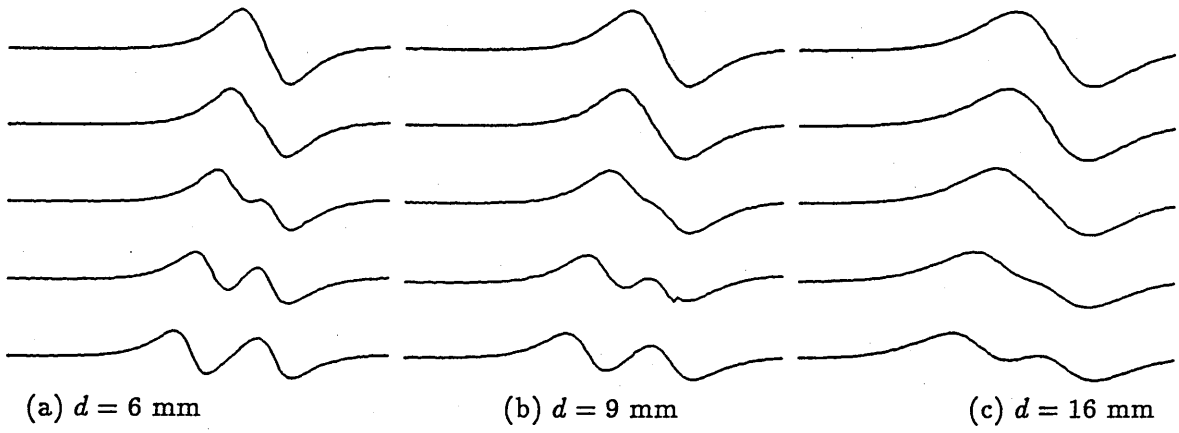

Figure 3.17 Three sets of scans over parallel line currents

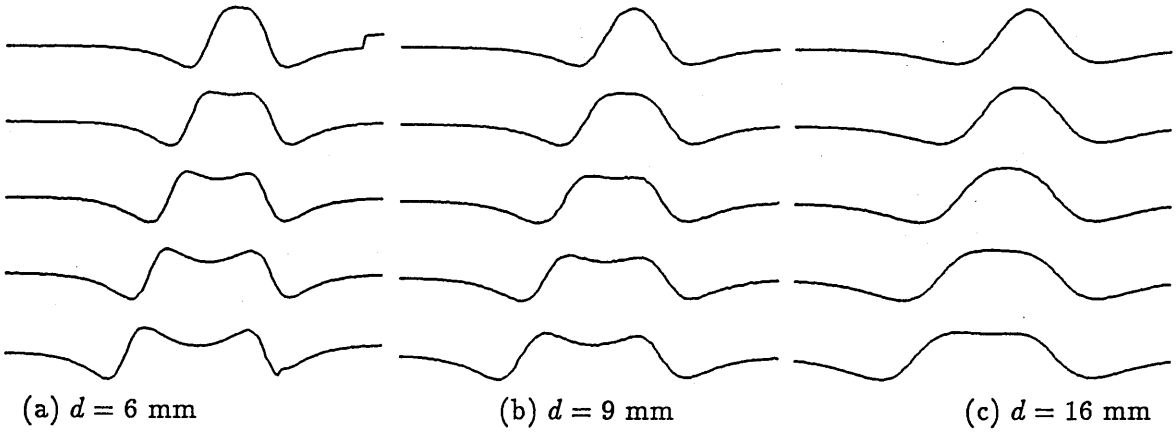

Figure 3.18 Three sets of scans over antiparallel line currents

Figure 3.18 illustrates that the visual separation of antiparallel line currents is more difficult, because the magnetic field traces tend to merge into a single peak (superficially similar to a magnetic dipole) more quickly than traces due to the parallel currents merge into a single bipolar pattern. In these figures, the wire separations (from top to bottom) are: 19.0 mm, 25.3 mm, 31.6 mm, 38.0 mm, 44.3 mm.

d/mm	Parallel Δ_{min}/mm	Antiparallel Δ_{min}/mm
6	9	25
9	13	32
16	19	38
26	25	53
46	38	> 62

Table 3.1 Minimum separation of line current sources for visual discrimination

The results of a visual interpretation of these and other traces are summarized in table 3.1. The error bars on these measurements are about $\pm$ 3 mm.

In section 2.3.1, I deduced that, with an ideal point detector, it was not possible to resolve parallel sources (in that case, I considered current dipoles, but the difference is not profound) which are closer together than their depth below the measurement area. Additionally, in

section 2.3.2, I demonstrated that the sensitivity of a finite coil to a sinusoidal signal is zero if the wavelength is equal to the coil dimension and attenuated for shorter waves, but greatest when the wavelength is somewhat greater than the coil dimension. Thus, it is entirely consistent that, for shallow depths, SQUIDLET's limit of resolution should be equal to the depth *plus* a small correction of the same approximate size as the sensing coil diameter. At greater depths, parallel sources closer to each other than the depth can be resolved. This is probably due to the effect of the compensating coils which cannot be ignored at large depths. Antiparallel currents are discriminated for separations about two to three times greater than is required for parallel currents at the same depth.

An automated approach to the determination of whether two sources can be discriminated could utilize the local gradient. This technique for comparing the resolution of different instruments would take into account both spatial discrimination and noise performance. The range over which the gradient is calculated would need to be large enough to be insensitive to the noise. For two parallel currents, the algorithm could search for a point of inflexion between the extrema, and for antiparallel currents, three (as opposed to one) extrema would define separate sources.

I shall now present, without analysis, the results of scanning a more complex two-dimensional current distribution. The source was a thin-film niobium pattern, low-pressure sputtered onto a silicon wafer [88]. The pattern was configured as a planar second-order gradiometer $\left(\frac{\partial^2 B_z}{\partial y^2}\right)$ with three rectangular coils. The outside coils have four turns and measure 18 mm × 5 mm, and the central one has two turns with dimensions 18 mm × 20 mm. The baseline length is 22.5 mm.

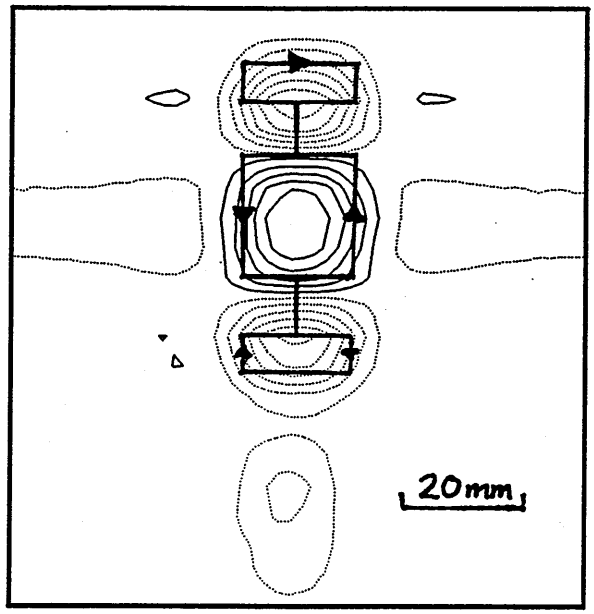

Figure 3.19 Isofield contour map recorded above the patterned silicon wafer

Figure 3.19 shows the isofield contour map recorded 10 mm above the wafer when 1 mA was passed through the circuit. The large-scale current path is also shown and this pattern has been easily resolved by the measurement. SQUIDLET could not, however, resolve the individual 'wires' in the film. They are 50 μm wide and separated by 50 μm. However, the map correctly shows that the field in the outside coils is larger than that in the central one,

but the depth of the source and finite size of the sensing coil has smeared the pattern, so that the field generated by the outside coils is not represented as being twice as large, as it should be. Higher resolution measurements of an almost identical source have been reported [107], at a much shallower depth with another instrument (see chapter 7). Such measurements, if improved, could serve as the basis of a method of investigation of electronic components without the need for direct electrical or mechanical coupling with the detector.

3.4 Measurements of ionic currents from *Acetabularia*

In this section, I shall describe SQUIDLET's first measurements of a biomagnetic source. The experiment was, primarily, a simple demonstration of the instrument in action, but it also provided new information about the conformation of ionic currents close to a particular living cell.

Acetabularia acetabulum or *Acetabularia mediterranea* as it was formerly known, is a species of giant unicellular alga. The plant grows naturally in the Mediterranean Sea and has become a very popular experimental subject for developmental biologists by virtue of several unusual properties.

It's great size (a few centimetres long and about half a millimetre in diameter when mature) makes *Acetabularia* an ideal single cell to study. In addition, it is easily cultured and harvested, and is extremely hardy, requiring little more care than an approximate sea water environment at room temperature. Particularly interesting are the transmembrane quasi-static ionic currents which accompany growth, and the ability of the cell to regenerate even after removal of the nucleus.

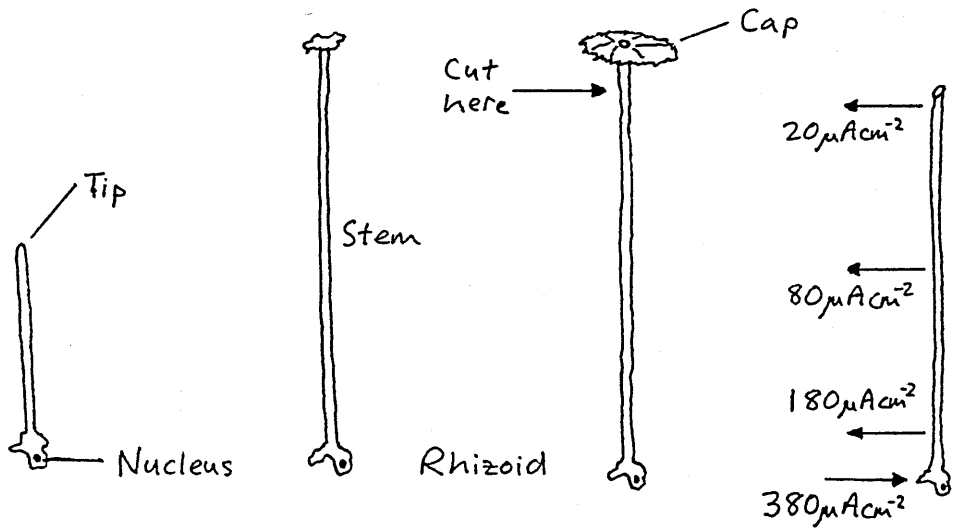

(a) Elongation (b) Morphogenesis (c) Cap removal (d) Regeneration

Figure 3.20 Development and regeneration in *Acetabularia acetabulum*

The main features of the plant are shown in figure 3.20. The nucleus is located in the irregular rhizoid region at the basal end of the stalk and the growing tip is at the apical end. Growth occurs by elongation of the stalk tip away from the rhizoid, and then by the formation of a cap. Small pieces of the nucleus migrate up the stalk, becoming surrounded by cytoplasm *en route* and forming cysts when they reach the cap. The cap degenerates, releasing the cysts which unite in pairs to give rise to new individuals. If, however, the cap is cut off prior to cyst formation, the stalk will elongate further before forming another cap, and this regeneration still occurs even if the rhizoid containing the nucleus has been removed.

Using the vibrating electrode technique of Jaffe and Nuccitelli [61] (which will be described in section 5.1), extracellular ionic currents have been measured around *Acetabularia* during both normal development and regeneration [76]. Briefly, an oscillating electrode records the electric field in the electrolyte around the cell and, from a knowledge of the resistivity of the medium, the current density is inferred.

As shown in figure 3.20d, during regeneration, positive current is directed outwards from the tip and stalk and inwards at the rhizoid, where current densities as high as 380 μA cm^{-2} have been recorded: larger than from any other single cell. By performing ion replacement experiments, these have been shown to be due mainly to the passage of chloride ions in the opposite sense to that indicated above. The rate of chloride influx along the stalk is very inhomogeneous, varying from 20 μA cm^{-2} at the tip to 180 μA cm^{-2} near the basal end. Calcium ions have been shown [41], [42] to play an imporant morphogenetic role despite making only a very small contribution to the measured currents. If the calcium concentration at the tip is not within a fairly narrow range, both elongation and morphogenesis are arrested. The currents are also dependent on the intensity and frequency of illumination [11].

By virtue of its size and the extracellular direct currents, which can be evoked, *Acetabularia* was an amenable system for study by SQUIDLET. The experiments were not pursued in any depth, but preliminary work yielded interesting results.

The plants are easily stored at room temperature in an artificial sea water (ASW). They can be removed for short periods for experimentation but should not be allowed to dry out. Death of the cell is indicated when it becomes blotchy and translucent in parts.

Intact specimens were laid on filter paper soaked in ASW and linearly scanned in a horizontal plane. From the vibrating electrode measurements [76], two current loops were expected, creating peak magnetic fields of order 1–10 pT. This should have been easily detectable, but no magnetic signal was observed. This might be because the extracellular current flows back very close to the membrane (the electrode measurements do not extend to large separations), or it might indicate that the assumed conductivity in the electrode experiment was too high.

To coerce the developmental current into generating more flux so that the magnetometer could 'see' it, a specimen was laid across a 1 mm insulated gap in a loop of filter paper (see figure 3.21a). The basal end extended just beyond the gap so that chloride ions leaving the rhizoid had to travel around the 20 mm diameter loop in order to reach higher regions of membrane.

With this arrangement (now just a single conducting loop) a signal was detected from

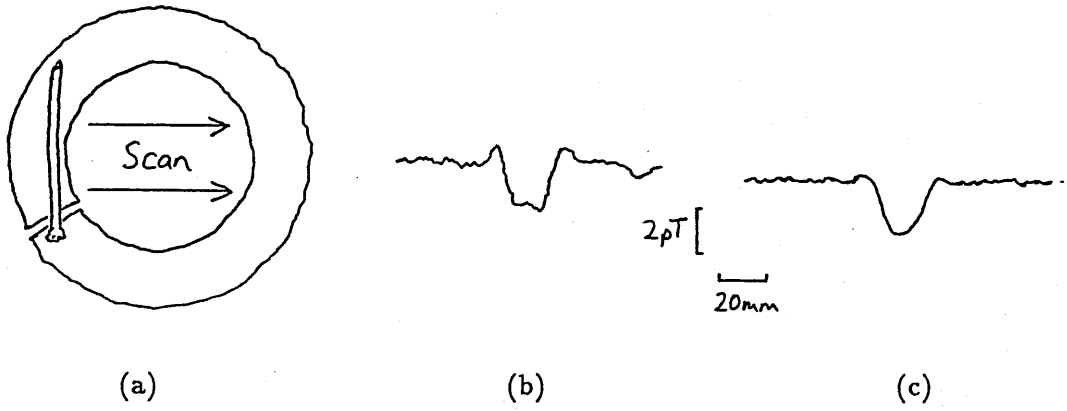

Figure 3.21 Magnetic field from *Acetabularia*
(a) Experimental arrangement
(b) Linear scan by SQUIDLET
(c) Linear scan across metal loop

the specimen (see figure 3.21b). The polarity of the field was correctly predicted by the chloride model for ionic current flow and the magnitude of the current was deduced to be about 0.3 μA by passing known currents through a lead loop of equal size (see figure 3.21c). This current is much smaller than those measured with the vibrating electrode, probably because of the reduced conductivity of ASW-soaked filter paper as compared with ASW.

This first study was not followed up, but the discovery that the extracellular currents lie so close to the organism indicated a possible inadequacy in relying entirely on one technique (electrode measurements). The combination of magnetic field and electric current measurements could provide substantially more information than either of them alone, in, for instance, mapping the conductivity distribution in an extracellular medium. This knowledge is of vital importance in the modelling of electrophysiological data.

Chapter 4

Modelling discrete and extended sources

In this chapter, I shall discuss the modelling of biomagnetic data.

After introducing the topic in section 4.1, I shall be concerned in section 4.2 with solving the inverse problem for discrete sources. This will only be a brief review because most of the modelling used later in this thesis will relate to extended continuous sources. In section 4.3, I shall describe a probabilistic approach to this more difficult problem. I shall also, in this section, summarize the mathematical framework behind the extended source algorithm that has been implemented at the Open University. This algorithm will be utilized in the analysis of magnetic field data from chick eggs in chapters 6 and 7.

4.1 Introduction

Stated most simply, the biomagnetic forward problem is the calculation of the magnetic field $\mathrm{B}(\mathrm{r})$ from the electric current density $\mathrm{J}(\mathrm{r}')$ and it can, in principle, be solved exactly by applying the Biot-Savart law (equation 1.2)

$$\mathrm{B}(\mathrm{r}) = \frac{\mu_0}{4\pi} \int_{v'} \left(\frac{\mathrm{J}(\mathrm{r}') \times (\mathrm{r} - \mathrm{r}')}{|\mathrm{r} - \mathrm{r}'|^3} \right) dv'$$

over the volume v' of the source. However, there is a complication. In any real situation, the volume within which the biomagnetic source is embedded is a conducting space, and so return currents are set up in v'. Return currents constitute the ohmic current distribution in a conductor caused by an impressed source. Hence $\mathrm{J}(\mathrm{r}')$, the total current density, is given by

$$\mathrm{J}(\mathrm{r}') = \mathrm{J}(\mathrm{r}')_p + \mathrm{J}(\mathrm{r}')_v, \tag{4.1}$$

where $\mathrm{J}(\mathrm{r}')_p$ is the primary current density and $\mathrm{J}(\mathrm{r}')_v$ is the volume current density. Thus, it is more practically meaningful to regard the forward problem as the calculation of $\mathrm{B}(\mathrm{r})$ from $\mathrm{J}(\mathrm{r}')_p$.

To assist in understanding the external magnetic fields generated by the heart and brain, Grynszpan and Geselowitz [47], in 1973, solved this forward problem and derived a general expression, in the form of a polynomial expansion, for the magnetic field outside a conducting volume containing an arbitrary impressed current distribution.

They showed that the external field vanishes in cases of axial symmetry and that, if the conducting space is spherical, the external field is independent of the sphere radius.

The inverse problem is the calculation of $\mathbf{J}(\mathbf{r}')_p$ from $\mathbf{B}(\mathbf{r})$. The solution is non-unique — this is obvious in the light of the result that certain non-zero total current distributions produce zero external field. Even if the total current could be calculated exactly, its division into the primary source, which is of interest for practical purposes, and the return current is also non-unique. If the hypothetical source is parameterized, however, it is possible to define a 'best fit' solution within the variation of those parameters, and a unique solution can emerge. For this, a source model is required.

4.2 Discrete source models

Because of the complexity of Grynszpan and Geselowitz's formula for the field due to an arbitrary current distribution in an arbitrarily shaped conducting volume, it has been usual for biomagnetic models to be framed in simpler terms, ie current dipoles in conducting volumes of simple geometry such as infinite half spaces and spheres.

As described in section 1.2.3, the current dipole is an infinitesimal current element which can be fully described by six parameters: the orientation (two parameters) and magnitude of its dipole moment $\mathbf{Q}$, and its position vector $\mathbf{r}'$ (three parameters). The magnetic field of the 'bare' dipole (ie a dipole within an infinite volume containing no spatial conductivity gradients) $\mathbf{B}(\mathbf{r})$ is given by equation 1.3,

$$\mathbf{B}(\mathbf{r}) = \left(\frac{\mu_0}{4\pi}\right) \frac{\mathbf{Q} \times (\mathbf{r} - \mathbf{r}')}{|\mathbf{r} - \mathbf{r}'|^3}.$$

For a dipole lying parallel to the x-y plane in an infinite homogeneously conducting half space ($z < 0$), the z-component B_z of the field depends on the source dipole alone. The separation Δ, in the plane $z = 0$, of the normal component field extrema (see figure 1.5) is related to the depth d of the dipole below that plane by equation 1.4,

$$\Delta = d\sqrt{2}.$$

This model and this equation have been used in the analysis of signals from the heart [46].

Evoked magnetic field maps recorded from the brain are often very similar to dipole fields and so, Cuffin and Cohen [26] investigated the field of a current dipole in a conducting sphere. They showed that radially oriented dipoles produce no external field and that, for tangential dipoles, the radial component of the field was independent of the return currents. Consequently, if the brain's electrical activity can be modelled in terms of a current dipole in a conducting sphere, measurements of the radial field lead directly to the primary source, without the complication of return currents.

The acceptability of the dipole in a sphere model for the interpretation of human brain measurements depends not only on the adequacy of the dipole approximation, but also on the adequacy of the sphere approximation to the head's geometry. The latter was investigated by Janday and Swithenby [65], who found that artificial dipoles in a gel-filled skull could be located with an accuracy of a few millimetres in the parietal and occipital areas of the brain. However, in areas of more rapidly changing skull curvature, the modelling and dipole location accuracy was far less robust: typical errors rose to over one centimetre. Moreover,

the quality of fitting of the data, as exemplified by a least-squares residual parameter, was insensitive to the accuracy of the dipole prediction. Thus, the parameter that was designed to indicate the reliability of the model could give misleading information.

The leading term in the description of any field map is almost always dipolar [89] and so the current dipole model can be extremely seductive. A suitable algorithm will fit a dipole (often with a very high correlation with the data) but its predictions may, nevertheless, bear little similarity to the actual source current. It's tractability is so alluring[1] that there is a tendency to overlook the gross assumptions inherent in the model and to describe dynamic physiological processes in the brain as the movement of a single current dipole.

Nevertheless, empirically and subject to the caveats described above, the current dipole model is very helpful and has been used extensively in MEG analysis.

4.3 Extended sources

For full generality, biomagnetic sources should be described by primary current density distributions. Fewer assumptions are inherent in modelling sources as a vector field $\mathbf{j}(\mathbf{r}')$, although, in algorithms to date, significant simplifications in the conductivity distributions are still necessary.

Although the problem is still non-unique [84], it can be treated probabilistically [50] by considering all the possible current density functions $\mathbf{j}(\mathbf{r}')$, and selecting the one that, in a defined sense, has the greatest probability of being correct. Clarke and Janday [23] used an argument based on statistical entropy to construct a probability distribution over the set of all current configurations and then calculated the current which corresponded to the expectation value ($< \mathbf{j}(\mathbf{r}') >$) of the probability distribution. This procedure is equivalent to maximizing the statistical entropy. The method has been refined by Clarke [22], and has been used by Ioannides and colleagues in the development of a sophisticated and general algorithm for solving the biomagnetic inverse problem that accommodates discrete and continuous sources (consisting of either or both ionic currents and magnetizations) in a wide range of experimental geometries [21], [56]. The method will be summarized below.

4.3.1 Mathematical framework

A set of s basis functions (the 'lead fields' or 'phi functions') is defined. Each of these $\Phi_i(\mathbf{r}')$ is chosen to be the vector field that defines the sensitivity to current sources of the ith field detector,

$$m_i = \int_{v'} \Phi_i(\mathbf{r}') \cdot \mathbf{j}(\mathbf{r}') dv'. \tag{4.2}$$

This equation is simply the general solution of the forward problem where $\mathbf{j}(\mathbf{r}')$ is the current density function in the space v', and m_i is the measurement made by the ith detector. By replacing $\mathbf{j}(\mathbf{r}')$ with a simple model source (a delta function), the lead fields can be readily

[1] A drunkard, crawling around on his hands and knees beneath a lamppost, is approached by a policeman, who enquires after his welfare. The drunkard replies that he has lost his door key. After searching for some time the policeman asks where, exactly, he dropped the key. "Back in those bushes" answers the drunkard. "Then, why are you looking for it here?" "Because it's so dark over there that I'd have *no* chance of finding it!"

calculated. This is equivalent to the alternative definition of a lead field, whereby the field over the source space due to unit current in the detector is calculated. The expectation value of the source $< \mathbf{j}(\mathbf{r}') >$ could be written as a linear combination of any basis set, but the choice of the lead fields ensures that the computed current density function contains no contribution from magnetically silent sources (about which the real detectors can have no information). The general result for $< \mathbf{j}(\mathbf{r}') >$ has been shown [23] to be

$$< \mathbf{j}(\mathbf{r}') >= \sum_{k=1}^{s} A_k \Phi_k(\mathbf{r}') w(\mathbf{r}'), \tag{4.3}$$

where A_k are the set of coefficients that must be calculated and $w(\mathbf{r}')$ is an *a priori* probability weight which must be specified. In the simplest case, this function is set to be unity throughout v', but it may, alternatively, be used to incorporate physiological information about the sources. In order to calculate the coefficients A_k, equations 4.2 and 4.3 are combined, yielding the set of equations

$$m_i = \sum_{k=1}^{s} P_{ik} A_k, \tag{4.4}$$

in which the 'P-matrix' is defined by

$$P_{ik} = \int_{v'} \Phi_i(\mathbf{r}') \Phi_k(\mathbf{r}') w(\mathbf{r}') dv'.$$

The coefficients A_k, and hence the expected current density $\mathbf{j}(\mathbf{r}')$, can then be obtained by inverting equation 4.4.

A problem arises when s is very large (ie there are a large number of closely spaced detectors) because some of the phi functions Φ_i are then very nearly linear combinations of other ones. Consequently, the P-matrix is nearly singular and its inversion is numerically difficult: small errors (such as the finite precision of the computer) are rapidly magnified. This could be avoided by ignoring some of the measurements. There would then be fewer phi functions, making the inversion less ill-conditioned. However, in this approach, potentially valuable information is jettisoned. Alternatively, a new set of basis functions could be used [50], but then the advantage of needing to calculate the set of phi functions once only, for a given experimental geometry, would be lost.

Instead, the method adopted at the Open University is to impose a finite standard deviation β on the expectation value $< \mathbf{j}(\mathbf{r}') >$. This is not unreasonable since its effect is to bias the expected current density against very large currents, which are, in any case, implausible on physiological grounds. The procedure also makes it impossible to fit the data exactly, but this is not a disadvantage in the presence of noise, since there is nothing to be gained by fitting the data more accurately than its own standard deviation σ.

The fact that P_{ik} is nearly singular can then be turned to advantage, because the Φ_ks that are most nearly linear combinations of others can be discarded, without discarding the equivalent measurements and without significantly affecting the accuracy of the inversion. This has the effect of reducing the amount of computation required. The expected current distribution $< \mathbf{j}(\mathbf{r}') >$ is then expanded in terms of the smaller subset ($t \leq s$) of basis

functions, so that equation 4.3 is replaced by

$$< \mathrm{j}(\mathrm{r}') >= \sum_{k=1}^{t} A_k \Phi_k(\mathrm{r}') w(\mathrm{r}'). \tag{4.5}$$

It is important that the Φ_ks are reordered so that the least significant ones are at the end of the matrix [22]. The reduced equation that has to be inverted (replacing equation 4.4), is

$$\tilde{m}_i = \sum_{k=1}^{t} \tilde{P}_{ik} A_k \qquad (i = 1 \ldots t), \tag{4.6}$$

in which there are now only t 'measurements' $\tilde{m}_i$. However, each one contains information from the original set of s measurements:

$$\tilde{m}_i = \sum_{k=1}^{s} P_{ik} m_k \qquad (i = 1 \ldots t),$$

and the reduced P-matrix is given by

$$\tilde{P}_{ik} = \sum_{j=1}^{s} P_{ij} P_{jk} + \zeta P_{ik} \qquad (i = 1 \ldots t, \quad k = 1 \ldots t),$$

where $\zeta = \sigma^2/\beta^2$.

This process is called 'regularization' and the regularization parameter ζ is a measure of the amount of smoothing applied. It can be chosen so that the amount of 'noise' in the reconstructed current distribution is equivalent to the amount of noise in the data.

4.3.2 Implementation

The original implementation of the method consisted of FORTRAN routines which ran on a mainframe computer[2]. However, for many purposes, this has now been superseded by a version written in OCCAM2 and running on a transputer array[3] comprising thirty processors [57].

The nature of the inversion method makes it particularly amenable to parallel processing. Because calculations involving a given region of the source space v' are independent of those relating to other regions, v' is divided between the separate processors, which each perform similar operations on their own portion and then return their results to the master transputer after similar periods of time. The overall saving in time is enormous: some computations that took several hours on the mainframe can be performed in a few minutes by the transputer array.

The general procedure is substantially the same for both implementations. The primary source space v' is specified (as a disc, for instance) and the relative geometry of the detector (ie the full gradiometer coil set) at each measurement site is input to the program. The phi functions $\Phi(\mathrm{r}')$ are then calculated. Once this has been done, inversions take relatively little time. This feature is extremely advantageous if (as is frequently the case) many experiments have been performed with the same geometrical arrangement. The scheme also allows for

[2]VAXcluster (2 × VAX 8800, 1 × VAX 11/785), Digital Equipment Corporation, Maynard, MA, USA.
[3]Inmos ltd, Bristol, UK.

experimentation with *a priori* information $w(\mathbf{r}')$ about the source, which can be entered after computation of the phi functions.

In addition to modelling 'free space' or total current distributions, it is possible to account for the return currents generated when the primary source is embedded in a conducting volume such as a sphere. In order to do this, a different set of phi functions is calculated. These include contributions from the return currents as well as the impressed current itself.

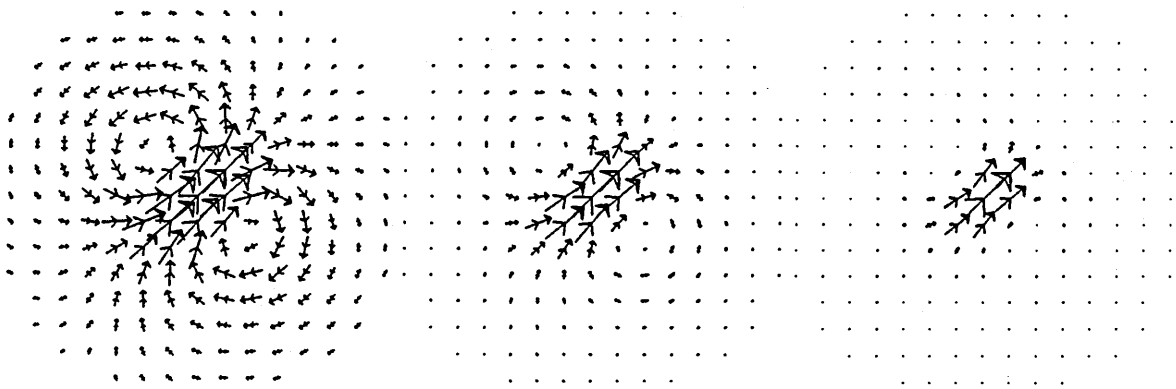

(a) A localized current dipole source

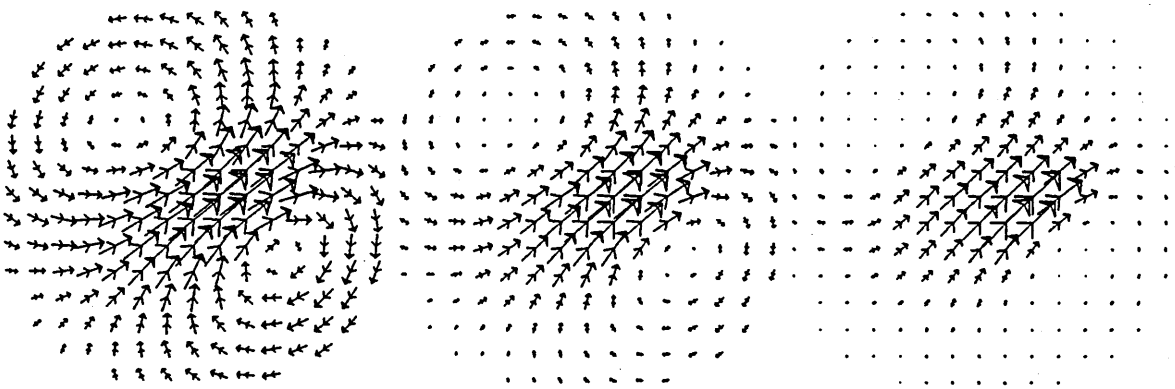

(b) A 'distributed' source

Figure 4.1 Solutions after zero, one and three (left to right) iterations for two sources

The method is clearly very suitable for distributed sources, but it can also perform well in situations where the true source is highly localized. An iterative inversion scheme can be used, in which the *a priori* probability weight $w(\mathbf{r}')$ for each iteration is defined in terms of the computed current $< \mathbf{j}(\mathbf{r}') >$ for the previous result. Figure 4.1 illustrates this technique. The model source in (a) is a single current dipole oriented at 45° to the axes and located at the centre of the circular source space (40 mm diameter and 8 mm below the plane containing the sensing coil of SQUIDLET's gradiometer). The source in (b), on the other hand, imitates an extended source, consisting of thirty dipoles with the same common orientation distributed within a circle of diameter 10 mm at the centre of the source space.

The two first solutions (zero iterations) are very similar, but after three iterations, the solution in the current dipole example has collapsed to a localized region of the source space, whereas the solution to the distributed source field remains distributed and does not collapse further with more iterations. Furthermore, the correlation between the original model data and the field of each solution improves with each successive iteration in the

current dipole example. After the first iteration, this correlation progressively deteriorates for the distributed source model. These properties of the algorithm are of great significance in that they allow localized and distributed sources to be differentiated.

With the original implementation (on the Open University VAXcluster), it is only feasible, without extremely long run times, to compute current densities in a two-dimensional space. However, depth information can still be recovered by allowing the depth of the source space to vary and comparing the field due to the computed solution with the original data. A strong correlation indicates that the correct depth has been found [56]. Full 3D inversions are easily within the capability of the transputer implementation.

Many examples of the various modelling schemes outlined above are to be found in references [21], [57], [56] & [58].

In summary, the distributed source model has many advantages over localized source models. In particular, it is appropriate for data that are obviously non-dipolar. Moreover, it is implicit in the theory that, of all the possible solutions, those about which the detectors have most information are favoured. Finally, with 'time-evolving' data (such as the evoked MEG), the model can produce a dynamic three-dimensional image of the most probable current sources, of the type required for medical applications.

Chapter 5

Electrophysiology of developing systems

"Wonderful as are the laws and phenomena of electricity when made evident to us in inorganic or dead matter, their interest can bear scarcely any comparison with that which attaches to the same force when connected with the nervous system and with life." Michael Faraday [31]

The remaining chapters of this thesis will be concerned primarily with the electrophysiology of one particular biological system: the embryo, and associated *in ovo* structures, of the chicken, *Gallus domesticus*. For several reasons, the chick embryo has been the organism selected for intensive study by developmental biologists for well over a century. Fertile eggs are cheap and easy to obtain, and they can be successfully hatched using artificial incubators *in loco parentis*. During this period, the detailed development of the embryo can be followed by microscopic examination of stained sections at different stages. The great convenience for study afforded by the chick has made it the most popular model system of embryonic development.

Normal structural development has been characterized in great detail in this way — an extremely painstaking process, exemplified by the tremendous detail of standard texts, eg Romanoff [83]. Much recent research has concentrated on electrical properties of the tissues, such as transmembrane potentials and ionic fluxes. The significance of the ionic currents, in particular, is not well understood, but their presence can be demonstrated in a number of ways, including magnetometry.

In section 5.1, I shall present a brief and general review of electrophysiology, referring to studies of various species. Section 5.2 is a synopsis of chick development during the first few days of incubation and, in section 5.3, I shall discuss some of the electrophysiology experiments concerning the *in ovo* chick. Finally, in section 5.4, I shall describe the first magnetic field measurements from chick eggs, which were performed at the Open University. At the end of this chapter, section 5.4.3 will detail the improvements in experimental and analytical procedure which were indicated by the first magnetometry experiments (the most important of which was a move to higher resolution), in order to make a better interpretation of the magnetic fields. Chapters 6 and 7 will be concerned with the high resolution measurements.

5.1 Introduction to electrophysiology

That the phenomena of electricity are intimately linked with living processes has been appreciated for almost as long as electrical effects have been observed. At the end of the eighteenth century, Galvani demonstrated both the special sensitivity of some biological tissue to an artificial electrical stimulus and, unwittingly, the existence of injury currents [37]. More than two millenia earlier, the ancient Greeks and Egyptians were aware of the shocks that could be delivered by electric fish.

Endogenous bioelectric effects are now known to be involved in all metabolic function, and a familiar example is the action potential, whereby communication along nerve fibres is achieved. A resting potential (interior negative) is maintained across the membrane of a nerve cell by the balance between ion pumps and leakage channels, and if this potential is reduced sufficiently, the membrane properties are radically altered, resulting in a voltage pulse being transmitted along the axon. Electrophysiological studies have deduced the mechanisms for the maintenance of the resting potential and for the initiation and propagation of an action potential. However, such a thorough explanation has still to be found for many bioelectric phenomena.

For instance, if a cell membrane, which is supporting a resting potential, is ruptured, there is no barrier to ionic flow into and out of the cell. Experiments have suggested that the resulting 'injury current' may be necessary if the cell (or, if the damage is widespread, the tissue) is to repair itself, but definite causality is very difficult to establish. However, ionic currents have been observed to accompany the macroscopic repair of bone fractures and the regeneration of entire limbs in certain species.

The processes of development, healing and regeneration typically occur over timescales of days or longer, and so the associated electric fields and currents are quasi-static. Consequently, both electrical and magnetic measurements suffer from difficulties of drift and low frequency noise (see section 2.2.1). This probably accounts for the lack of progress in studying these low frequency effects compared with the relative success with understanding the action potential, which is very much an ac phenomenon.

A breakthrough in the study of quasi-static currents came in 1974, when Jaffe and Nuccitelli perfected their vibrating probe electrode [61]. The idea of artificially increasing the measuring frequency by introducing relative motion between sensor and system is identical to that described in section 2.2.1 for magnetometry. Thus, instead of making dc voltage measurements, the technique involves vibrating a small spherical electrode tip at a low audio frequency and with an amplitude of a few tens of microns. The tip potential is measured by a lock-in amplifier and the current density J can then be calculated from the output V of the amplifier using Ohm's law,

$$J = \frac{V}{\rho l}, \tag{5.1}$$

where l is the amplitude of the vibration and ρ is the resistivity of the medium, which must be measured separately. The instrument has a resolution of 1–2 nV, corresponding to 10–20 nA cm^{-2} in sea water, and is appropriate for making measurements close to an organism or cell in an aqueous environment.

Use of the probe to study currents, associated with the repair and regeneration of tissue, will be the subject of section 5.1.1. I shall also review some of the attempts to influence tissue repair by enhancing or opposing the endogenous electrical activity. Then, in section 5.1.2, I shall discuss bioelectric effects which have been observed in young organisms undergoing normal morphological development, and present some of the theories about the relationship between bioelectricity, cell migration and growth. It is this relationship which is of most relevance to the following studies of the chick embryo.

5.1.1 Bioelectricity and regeneration

An early experiment with the vibrating probe electrode by Borgens *et al* [9] demonstrated current densities of 10–100 μA cm^{-2} leaving the cut end of a limb stump of the red-spotted newt and much smaller current densities over a larger area entering the intact skin close to the site of amputation. This species, like many amphibians, naturally regenerates amputated limbs over a period of weeks and the currents were measured during the first 5–10 days of this process. By controlling ion concentrations in the external medium and by selectively blocking the skin's ion pumps, they established that the circuit was driven by the skin's sodium 'battery', the observed currents being the leakage back into the medium.

In a related experiment [8], the same team initiated some limb regeneration in adult frogs, which do not normally regenerate, by supplying a similar magnitude of current to the core of the stump for several weeks. The severed bones extended, and new muscle, ligament and cartilage developed as well as "extraordinarily large amounts" of nervous tissue. Moreover, reversing the polarity caused extensive *de*generation. It may be relevant that amphibians which do not naturally regenerate limbs, such as adult frogs, have highly conducting subdermal lymph spaces, which shunt current around the central tissues unless it is supplied directly to them. Borgens suggests [10] that exposure of the central stump region to currents may be required for regeneration.

A rare human study [54], which utilized a larger, more robust version of Jaffe and Nuccitelli's probe [4], reported currents of 10–30 μA cm^{-2} leaving the amputated fingertips of children (aged 1–15). The significance of these currents is strongly indicated by the observation that, if the point of amputation is distal to the last joint, a perfect replica fingertip grows back in most cases, provided the stump currents are not prevented. If the cut surface is sutured or given a skin graft, regeneration does not occur.

The endogenous stump currents described above are quite different from cellular injury currents. The former are driven by active physiological processes whereas the latter result from the migration of ions down an electrochemical gradient due to the rupture of a membrane. However, injury currents are also believed to promote regeneration in smaller (particularly single cell) preparations and the mechanism may be the same.

Borgens [10] reports that extremely large current densities (500–800 μA cm^{-2}) enter the cut face of the spinal cord of larval lamprey immediately after sectioning. The current density profile over the cut surface showed marked peaks corresponding to the centres of individual giant axons in the cord. Over 1–2 days, the currents fell to a steady value of about 4 μA cm^{-2}. Ion replacement tests identified sodium and calcium as the main current

carriers.

In a second experiment, electrodes were implanted close to the point of sectioning and an electric field, with a polarity reinforcing the injury currents described above, was applied. Unequivocal enhanced axonal regeneration was reported, in comparison with sham experiments, where electrodes were implanted but not energized.

The electrical stimulation of the healing of soft tissue wounds in mammals has been reviewed by Weiss *et al* [102]. They concluded that exogenous electric fields often accelerated healing and produced better repair tissue, particularly in skin wounds. Although the mechanism is unknown, there is strong evidence that tissue repair is favorably affected by the proximity of the negative electrode and adversely affected by the positive electrode.

Electric fields are also important in mammalian bones. Standing potential differences develop naturally in stressed bone, regions of tension becoming relatively positive and regions of compression becoming relatively negative [109]. These are probably 'streaming potentials' — the separation of charges caused by forcing an ionic fluid through a channel which preferentially binds ions of one polarity. Although this is a mechanical process that is not dependent on the viability of the bone, the effect may still play a role in the ability of living bone to remodel itself in response to applied stress (known as Wolff's law).

More interesting are the quasi-static, stress-independent bioelectric potentials which were shown by Friedenberg and Brighton [35] to affect normal growth, remodelling and fracture repair. Relative negativity has again been observed in areas of normal bone growth and at the site of fractures, although the latter effect may be due to injury currents in the bony tissue and adjacent soft tissue.

These observations have led to attempts to stimulate bone growth and fracture repair with applied electric and magnetic fields. In clinical trials, direct current stimulation has enhanced the rate of healing of bone nonunion [12] and also initiated new bone formation within the medullary canal [30], [36]. However, a detailed review of the influence of pulsed magnetic fields on tissue growth and repair [5] concluded that, while there were indications of some success, considerably more trials were required to establish the effects of varying field amplitude, homogeneity, frequency and waveform shape.

In summary, there is good evidence that currents and potentials generated endogenously in the neighbourhood of damaged tissue are important in the healing process, and that applied electrical stimuli can enhance the effect. A recurring observation is that regions of natural tissue growth often develop a negative potential and that repair and regeneration can often be enhanced close to a negative electrode. Despite the volume of literature on the subject, there is still considerable confusion about the mechanism and about the optimum clinical treatment of all types of tissue damage.

Finally, as far as I know, there have been no magnetometric studies of these regenerative processes. In 1980, a project to investigate the magnetic fields associated with naturally healing fractures in the lower leg was planned [43]. However, strong quasi-static magnetic field patterns, which depended on the state of relaxation of the musculature, were measured close to all healthy, non-fractured legs. Consequently, attention was switched to this phenomenon, and these normal fields were stereotyped. Inverse problem analysis of the data

[44] implied the existence of loops of current (of about 10 μA) in the leg muscles.

5.1.2 Developmental bioelectric effects

This section concerns endogenous bioelectric activity accompanying normal growth and development (as opposed to that associated with the repair and regeneration of damaged tissue).

The first application of the vibrating probe (which constituted a minor part of Jaffe and Nuccitelli's paper containing details of the instrument [61]), demonstrated a phenomenon, not previously observed. They recorded orientation-specific current pulses in the sea water around one-day embryos of the fucoid alga *Pelvetia*. The embryo (just two cells at this stage) already exhibited its characteristic structural polarity: one of the cells develops a sharp tip while the other remains hemispherical. Polarity was also evident in *Pelvetia*'s electrophysiology. Strong pulses were observed to enter the embryo at the tip, and by vibrating the probe perpendicular to the surface distant from the tip, it was possible to measure weaker pulses leaving the embryo. Systematic measurements with the probe around the embryo led to the construction of a self-consistent current density field during the pulses.

There have been many electrophysiological studies of *Acetabularia*. A summary of the interesting physiology of this plant appears in section 3.4, where it was stated that ionic currents are associated with both normal development and regeneration. The discovery that the cell can grow a new cap after transection, even if the nucleus has been removed, was a surprising result and it was later shown [72] that the cell membrane plays an important role in this regenerative capacity. Goodwin and colleagues [41], [42] succeeded in preventing morphogenesis (cap regeneration), but not stalk elongation, by disturbing the membrane's specific permeability to calcium and magnesium with an ionophore. The effect was greatest at the growing tip. Despite the importance of the presence of these divalent cations, it has been established [76] that the main constituent of the current (both during elongation and morphogenesis) is the chloride anion. The pattern of inward and outward current density is illustrated in figure 3.20d.

Patterns of ionic current have also been observed in animal embryos. Overall and Jaffe have reported [77] that *Drosophila* (fruit fly) follicles drive steady currents through themselves in two distinct stages of development. During its main period of growth, the follicle can be distinguished as a number of prominent 'nurse cells', which are similar to the growing tips of *Pelvetia*, and the larger 'oocyte'. Peak current densities of 3–30 μA cm^{-2} enter the nurse cell caps, forming a current loop which passes through the bridges to the oocyte before returning to the medium. Most of the current is due to sodium ions, and the authors speculate that the source of the electric field generating this current may be a 'battery' located in the syncytium between the nurse cells and oocyte, and that its function may be to control the movement of charged species (particularly sodium) in order to establish a factor, favouring the development of the head, in the oocyte.

Later, during development of the chorion (the outer embryonic membrane), the overall current pattern appears to be reversed, with new foci of inward current appearing at the opposite end of the follicle. Furthermore, these foci are located in regions of relatively intense

chorion secretion. In this case, the authors suggest that the purpose of the currents is to resorb water from newly deposited chorionic materials, thereby concentrating them.

There exist similar reports of transcellular ion currents preceding and predicting particular aspects of morphogenetic development in a variety of other developing organisms. These have been reviewed by Harold [52] who discusses experimental evidence relating to a number of other questions which have been posed. Is growth encouraged at sites of high transcellular current densities? Are cytoplasmic ion concentration gradients related to transcellular currents? Under what circumstances can polarity be imposed upon tip-growing organisms with applied electric fields? Finally, do transcellular ion currents *have* to have a function? It is generally assumed that the answer to this last question is 'yes', and yet, the currents may be non-causal consequences of functions such as the spatial segregation of transport mechanisms.

There has long been considerable debate over which factors influence growth, morphogenesis and development. I shall now review some of the general essays on this subject, concentrating on those hypotheses involving ionic currents.

In what he saw as a dangerous tendency to overapply the principles of molecular genetics, ultimately to account for the entire development process, Lionel Jaffe published, in 1969, an article [59] in which he strongly advanced the "centripetal", as opposed to the "centrifugal", course of development. With this choice of language, he stressed the importance of the cell membrane, rather than the nucleus, for initiating development. Citing examples as diverse as the developmental sensitivity of certain cells to polarized light and the interaction of a sperm with an ovum, he argued that, in most types of intercellular communication (which underpins development), the functions of signal generator, transmission line and target are all performed by the cell's surface.

Eggs of the *Fucus* alga serve as a paradigm of the developmental phenomenon of localization, whereby one of the two cells into which the zygote initially divides, develops a growing tip, thus determining the polarity of the plant. The species is closely related to *Pelvetia*, mentioned earlier. In the same article [59], Jaffe discussed the possible mechanisms by which this example of morphogenesis originates at a particular site, acts back to augment its own differentiation and inhibits the same process from being initiated elsewhere. He considered it likely that an endogenous electric current that was driven through the organism at about this stage was involved, but instrumentation with which to measure it reliably was not, at that time, available. However, by stringing together hundreds of aligned eggs in a capillary, he succeeded in measuring a small voltage across the chain length and deduced that each egg generated about 10 μA cm^{-2} through its growing tip. Randomly oriented eggs produced no voltage.

The current was clearly linked with the phenomenon of localization, but was it the cause? Jaffe believed it was and speculated about possible mechanisms such as the 'popped balloon hypothesis' and electrophoresis. The former accounts for the inhibition of secondary sites due to a lowered transmembrane potential, by analogy with the improbability, due to the reduced internal pressure, that a popped balloon will develop a second hole. The latter mechanism is the movement of charged macromolecules (which may be involved in organizing new tissue)

in an electric field generated by the passage of ions. In order to test these hypotheses more thoroughly, the currents had to be measured with greater spatial and temporal resolution, and it was these requirements that led to the development of the vibrating probe.

In a later article [62] (1977, after the probe's introduction), Jaffe and Nuccitelli reviewed progress in the field of developmental biology. They concluded that, instead of there being a few isolated examples of links between electrophysiology and development, it was a general rule that developing systems drive steady ion currents through themselves and generate substantial voltage gradients across themselves. In addition to the very primitive (mostly single-celled) organisms described already, they reviewed measurements of potential differences across various types of embryonic epithelia, including the chick chorioallantoic membrane (see section 5.2 for an account of chick embryo anatomy).

Two further reviews by Jaffe [60] and Stern [90] cover much of the same ground. There are examples of endogenous developmental ionic currents in a wider variety of species, and examples of the influence on development of applied electric fields or polarized light. Explanatory models, based mainly on electrophoresis, are proposed.

One new experiment was the seed of the chick magnetometry project at the Open University. Jaffe and Stern [63] measured strong currents (extrapolated to be about 100 μA cm^{-2}) leaving the primitive streak of the embryo, during its first day of incubation, in all directions. The primitive streak is a 1–2 mm long groove in the epithelial bilayer, through which cells from the upper layer (the epiblast) migrate *en route* to forming the internal tissue of the embryo (see section 5.2). I shall discuss this experiment in more detail after describing the embryology of the chick.

5.2 Chick embryology

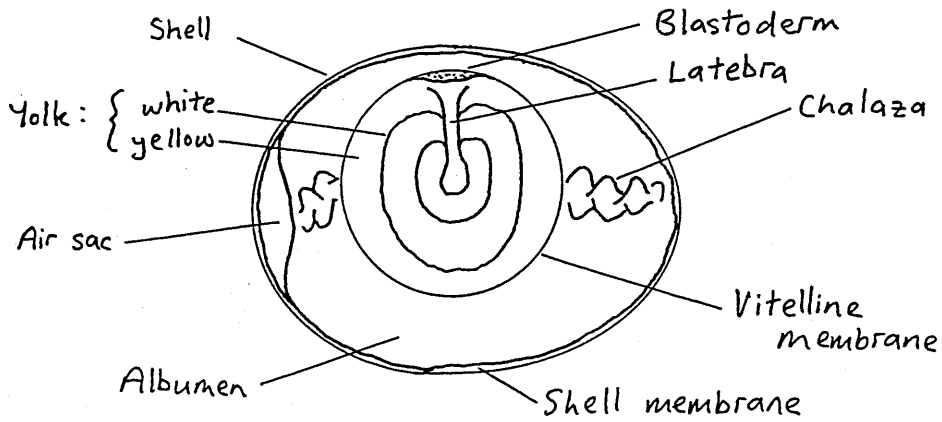

Figure 5.1 Structure of the fertilized chick egg at laying

When it is laid, a fertilized chick egg is a relatively simple system on the macroscopic scale (see figure 5.1). It consists of a roughly spherical yolk encased in its vitelline membrane, floating in a reservoir of albumen. Both components contain proteins, vitamins and carbohydrates, but virtually all of the egg's lipids are in the yolk (which explains its lower density) while

the aqueous content of the albumen is much the greater. The virtually undifferentiated cluster of cells that ultimately gives rise to the embryo constitute a pale disc, about 3 mm in diameter, called the blastoderm, which floats on top of the yolk. Helical strands of viscous albumen, the chalaza, link the yolk to the ends of the egg to provide some protection against mechanical shock. The whole structure is contained within the brittle porous shell, which is lined by two membranes which separate only at the blunt end to create the air sac.

If the egg is provided with an environment of appropriate temperature, humidity and atmospheric oxygen, normal development will proceed, yielding after 21 days a baby chick, complete with brain, beak and feathers! To ensure successful hatching, the egg should also be rotated several times per day during the first two weeks. It is generally believed that this is necessary to prevent adhesion of the embryo's tissues to the shell membrane, but an alternative theory, that it is necessary to stir the subembryonic fluid, has been proposed by Deeming *et al* [28].

Clearly, the structural changes occurring inside the egg are highly complex and there are a number of ways of studying them. One could simply record the structure of the embryo etc, as a function of time, observing when particular tissues or organs appear. However, this yields no information about the internal organization, and so a standard technique is to cut slices and study them with a microscope (see, for instance, Freeman & Bracegirdle [34]). To do this properly, sectioning should be carried out in several different orientations throughout the embryo at each stage of development. Alternatively, the progress of each organ, or region of interest in the baby chick, could be followed from the first appearance of the primitive structure, observing how its development interrelates with that of other ones.

In practice, all of these approaches are useful and complementary. Consequently, in standard textbooks such as Lillie [51], Romanoff [83] and Patten [79], they tend to be applied in parallel. An important point is that the development cannot be compartmentalized: it is contiguous, both spatially and temporally. Although various series of 'developmental stages' have been defined, each stage is merely representative of the current state of a continuous process, and has been selected more or less arbitrarily. The staging system referred to in this thesis will be that of Lillie [51].

One segregation that I shall apply is between the embryo and the extra-embryonic membranes. The latter arise from the embryo at various stages, but are then spatially and functionally fairly distinct from it. They will be the subject of section 5.2.2, which will follow a consideration of the embryo's development in section 5.2.1.

5.2.1 The embryo

The first visible evidence of development after laying is the appearance of two contrasting regions of the blastoderm. The central, translucent *area pellucida* develops into the tissues of the embryo, and the peripheral, opaque *area opaca* ultimately gives rise to the extra-embryonic membranes (see figure 5.2a). At around the same time, the cells of the *area pellucida* differentiate vertically to form the three germ layers. In this process (termed gastrulation), the blastoderm initially divides into two layers: an upper epiblast and a lower hypoblast. Cells from the epiblast then migrate into the cavity between these layers to form

the mesodermal tissue from which all the internal tissues and organs arise (see figure 5.2b,c).

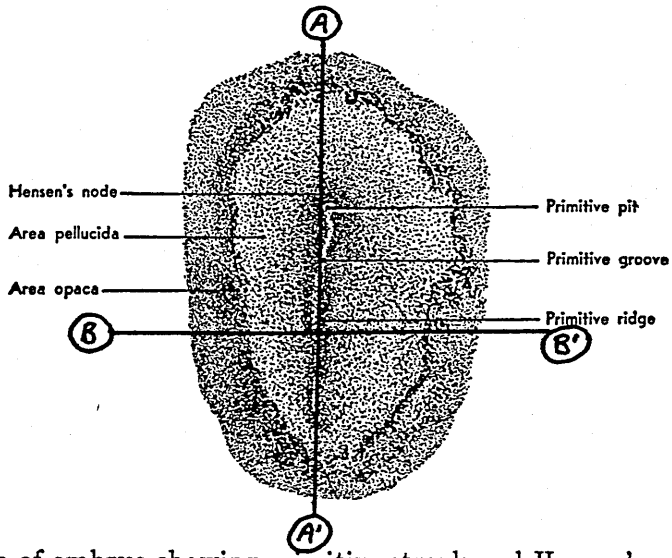

(a) Plan of embryo showing primitive streak and Hensen's node (×14)

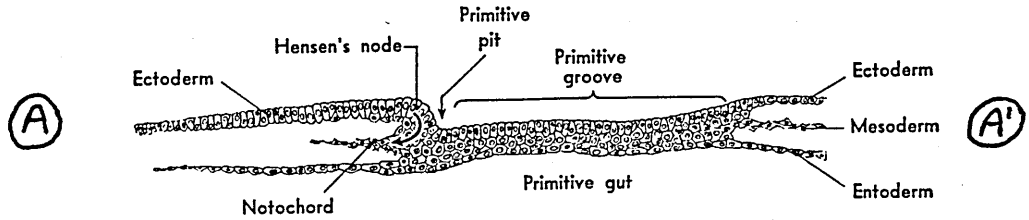

(b) Longitudinal section A–A′ (×56)

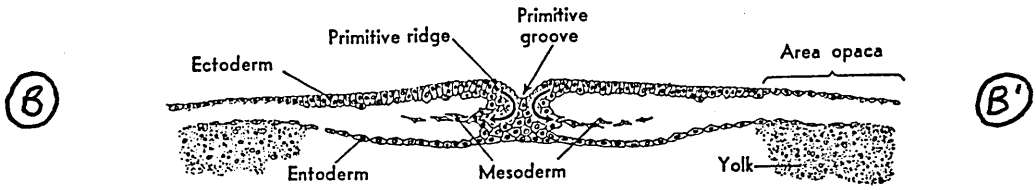

(c) Transverse section B–B′ (×56)

Figure 5.2 Formation of the gastrula
(after Patten [79])

Migration is preceded by the appearance in the epiblast of the primitive streak, a furrow flanked by two thickened ridges, with a prominent local thickening, Hensen's node, at one end (the cephalic end). This establishes the polarity of the embryo, and in about two-thirds of cases, the streak is perpendicular (±45°) to the egg axis with Hensen's node away from the observer if the blunt end of the egg is to the left [51]. Epiblast cells continue to proliferate from the margin of the *area pellucida*. This results in a mass centripetal migration of cells towards and into the streak, and finally into the space between the original two germ layers to form the third, the mesoblast or mesoderm (see the arrows in figure 5.2b,c). This is a critical stage in development (after about 12–20 hours of incubation) and corresponds to the latency at which strong currents were observed to pass out of the streak into the albumen above Jaffe and Stern's preparation [63].

Subsequent cellular organization continues with the appearance of the notochord anterior to Hensen's node, leaving the primitive streak as a relic of an earlier phase. More anteriorly,

the crescent shaped head fold develops, causing a flap of tissue (the head!) to protrude slightly above the plane of the epiblast (see figure 5.3b). This is the first definition of the bodily extent of the embryo. Later, the lateral body folds start to undercut the embryo and the head fold progresses posteriorly to meet them. In the region of the notochord, the neural plate (the first appearance of nervous tissue) also starts folding to form the neural groove, which eventually closes along most of its length yielding the neural tube.

Between the neural tube and the disappearing primitive streak, the mesoderm begins to be organized into laterally paired blocks of cells called somites. These dark squares are easily visible through a microscope and provide a convenient yardstick by which to stage development between about 20 and 80 hours of incubation, appearing at a roughly uniform rate of one pair every 1–1$\frac{1}{2}$ hours. Figure 5.3 shows the embryo at about 24 hours, after the complete formation of three pairs of somites.

Meanwhile, the distal region of the *area pellucida* and the proximal region of the *area opaca* have taken on a dark mottled appearance due to the formation of blood islands. Arising from the mesoderm, these aggregate into vessels and ultimately into an elaborate and beautiful capillary network, whose border, the *sinus terminalis*, marks the extent of the vitelline vascularization. The heart first appears as a transparent longitudinal tube beneath the neural tube with a fork marking the proximal segment of the omphalomesenteric veins, which later connect with the vitelline circulation. Even at this stage, the essential pulsatility of the cardiac tissue is made evident by spontaneous and random contractions. By 36 hours (13 somites), the heart has started pumping blood around both the vitelline system and the internal vessels which have developed, particularly in the cephalic region.

The next major developments are the flexures of the head, which result in torsion of the upper body, initially at the level of the anterior somites, and progressing posteriorly. The embryo ends up lying with its left side against the yolk and, after about 40 hours (16 somites), the lens is visible in its right eye. It is no longer nourished by direct diffusion of nutrients, but from the yolk sac via the vitelline circulation, heart and internal circulation.

After 4 days of incubation, undercutting by the body folds has virtually closed the ventral surface of the embryo, so that it lies completely on its left side, remaining attached to the yolk sac by the slender yolk stalk. Wing- and leg-buds are now evident, and development of both the central nervous system and the digestive system is in progress. From this stage until hatching, there is a general enlargement of the animal as the yolk sac becomes depleted, and further development of the internal organs and limbs. After hatching, the lungs, and digestive system take over the roles performed in the egg by the allantois and yolk sac membrane, and the amnion, which has been providing mechanical protection, is dispensed with. I shall describe these extra-embryonic structures in the following section.

5.2.2 The extra-embryonic membranes

The undercutting effect of the cephalic, lateral and caudal body folds, on the second and third days of incubation, allows an unambiguous distinction to be drawn between embryonic and extra-embryonic tissue, which was not previously possible. The extra-embryonic tissue includes four important membranes: the yolk sac, chorion, amnion and allantois. I shall

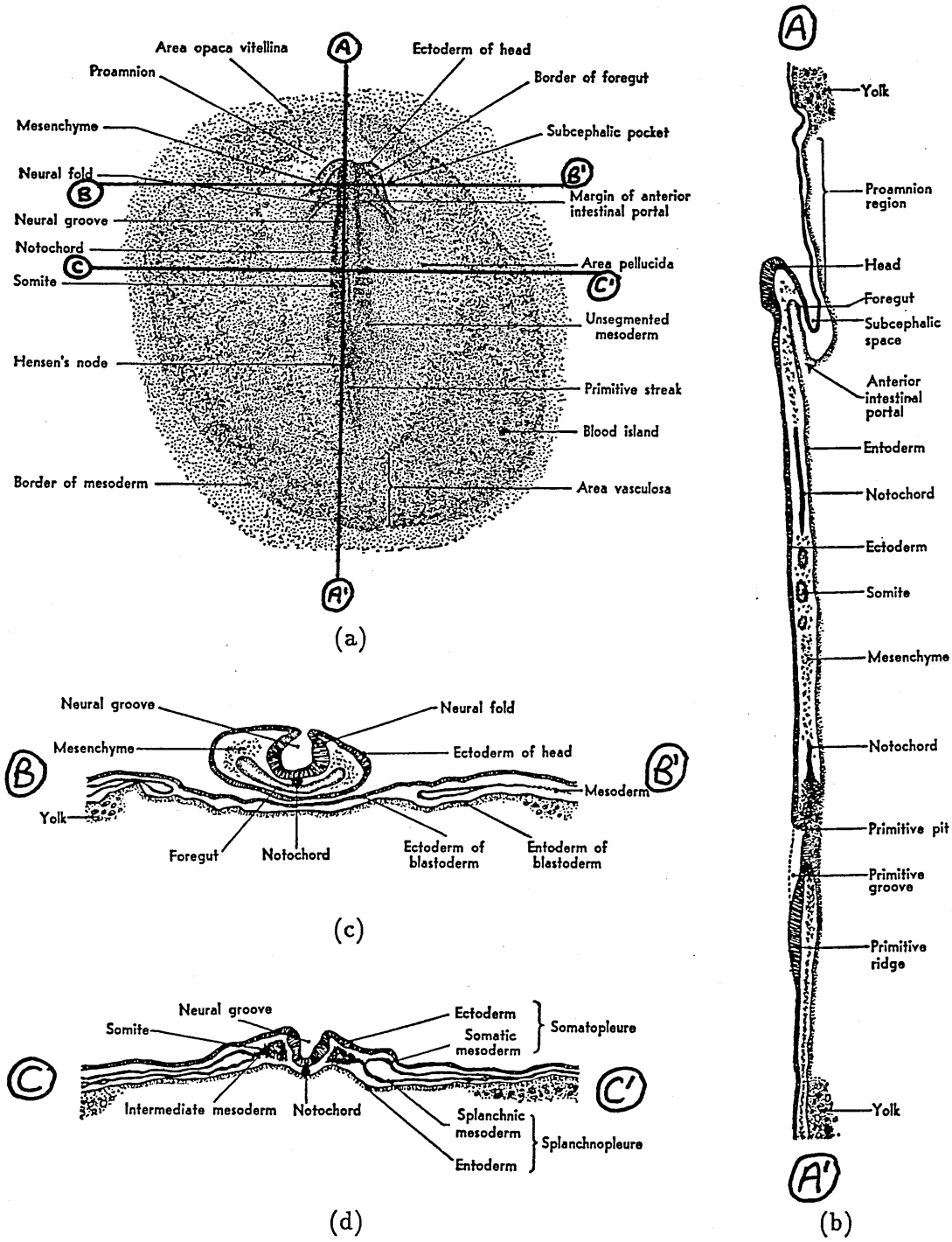

Figure 5.3 Structure of the chick at about 24 hours
(a) Plan view showing three complete pairs of somites (×16)
(b) Longitudinal section A–A′ showing protruding head (×64)
(c) Transverse section B–B′ through head (×64)
(d) Transverse section C–C′ through somites (×64)
(after Patten [79])

discuss them separately.

The topology and three dimensional interrelationships of these structures is rather complicated. Furthermore, they are extremely dynamic (for instance, the allantois initially increases its surface at a rate of about 20–30 $mm^2\ day^{-1}$), so that during the incubation period, several different relative configurations are adopted. Figures 5.4 and 5.5 represent an attempt to help visualize the changes. Figure 5.4 shows a vertical longitudinal section through the egg (ie perpendicular to the embryo axis) at four latencies, and figure 5.5 illustrates the yolk sac, amnion and allantois in perspective after $5\frac{1}{2}$ days, with the shell, albumen and chorion removed.

After gastrulation, the central of the three layers (the mesoderm) starts aggregating to form the internal tissues, beneath the blastoderm. More peripherally, however, it divides into two layers, the upper one combining with the epiblast to form the somatopleure while the lower one combines with the hypoblast to form the splanchnopleure. On the second day, the splanchnopleure, which is now called the yolk sac, starts to extend around the yolk, by increasing its surface area, until on the fifth day it encloses it except for a small region antipodean to the embryo. The vitelline membrane, which had previously enclosed the yolk, recedes. It is within the yolk sac that the observed blood islands and vitelline circulation arise. The omphalomesenteric vessels connecting this system to the heart pass through the yolk stalk.

This is the route that nutrients from the yolk take to reach the embryo, rather than directly via the yolk stalk. As the yolk sac enlarges its surface, the yolk with which it comes into contact is acted upon by enzymes in the membrane, liquefying it so that it is in a form which may be absorbed into the vitelline circulation, whereafter it is called the sub-embryonic fluid. As the embryo occupies more and more of the space inside the egg, the albumen is transferred into the yolk, the yolk into the sub-embryonic fluid and then into the embryo.

Also on the second day, the somatopleure develops folds which grow around the head and tail of the embryo, and from now on, it is considered as two separate membranes. The amnion is the portion which lies close to the embryo while the chorion extends around the yolk, adjacent to the yolk sac.

The folds of the somatopleure converge above the embryo after three days, so that the transparent amnion completely encloses the embryo. It is filled with a watery fluid which provides shock protection. The fluid is gently fanned by amniotic fibres, so that the embryo is subjected to a continuous, slow rocking motion which, presumably, assists its development by keeping growing parts free from each other. The chorion, meanwhile, extends around the yolk at the same rate as the yolk sac: in fact, the mesodermal components of the two membranes remain partially fused at their periphery.

Later, at the end of the third day, the allantois emerges from the ventral wall of the embryo, near its tail (splanchnopleure). Consequently, it is located outside the amnion, in the space between the yolk sac and the chorion. Fluid accumulates inside the allantois, so that it inflates rapidly and comes into contact with the inner surface of the chorion, pushing it against the shell. The mesoderms of these two membranes fuse, and the allantois continues

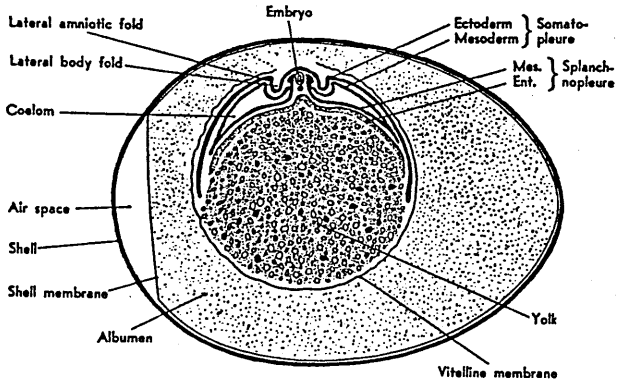

(a) After 2 days incubation

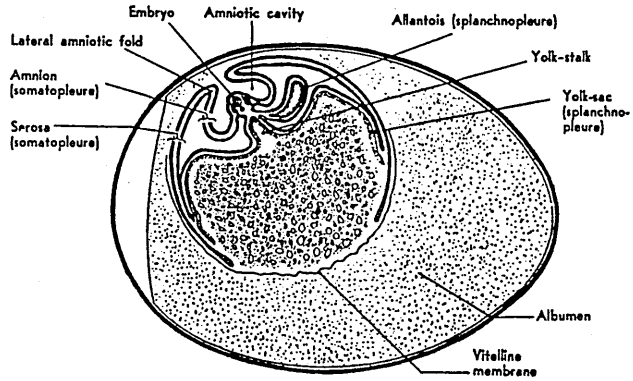

(b) After 3 days incubation

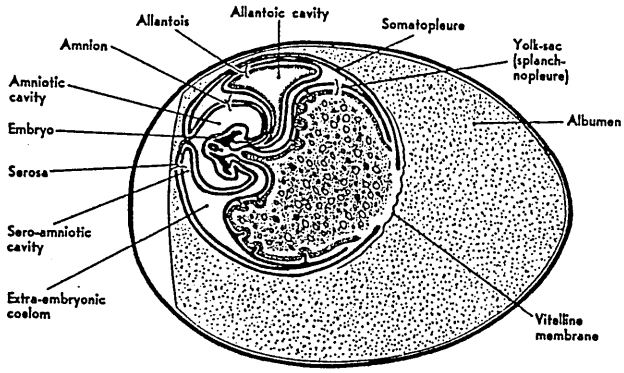

(c) After 5 days incubation

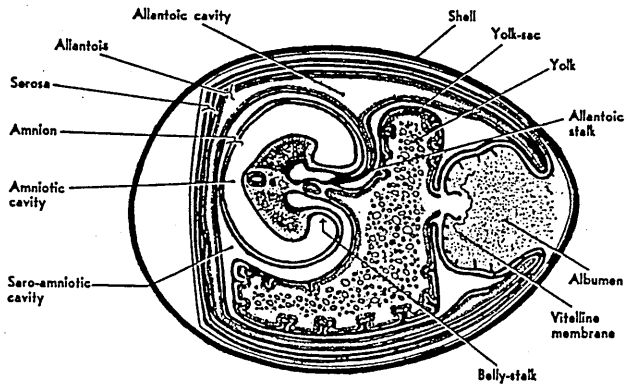

(d) After 14 days incubation

Figure 5.4 Section highlighting interrelationships of the extra-embryonic membranes (after Patten [79])

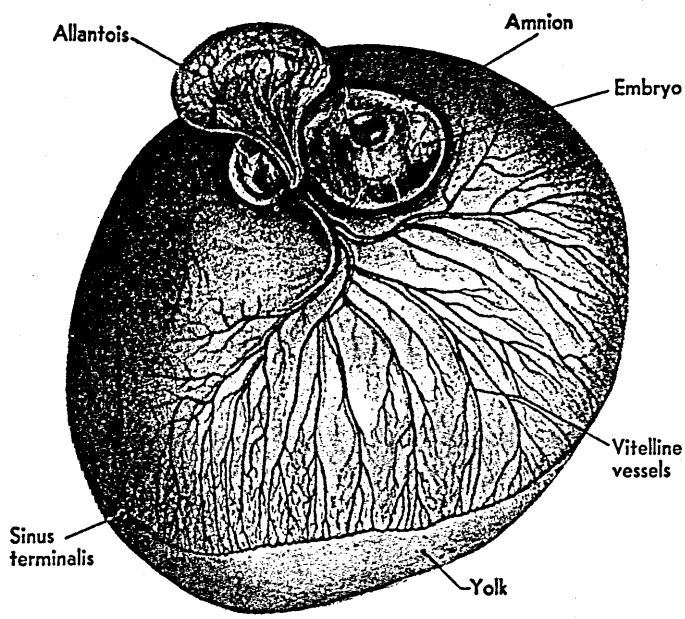

Figure 5.5 Perspective drawing of some of the extra-embryonic membranes after $5\frac{1}{2}$ days (after Patten [79])

expanding until the compound structure has spread over most of the inner surface of the shell.

The chorioallantoic membrane, as it is hereafter known, becomes richly vascularized, constituting the third circulatory system in the egg (the others being the vitelline and internal systems). The primary function of the chorioallantoic circulation is the supply of oxygen and disposal of carbon dioxide by gaseous diffusion through the porous shell. Additionally, it removes metabolic waste products from the embryo. Both urea and uric acid are toxic and, because they cannot be expelled from the shell, they require safe storage, distant from the embryo. Thus, the allantois also acts as a waste dump, the shrivelled membrane adhering to the broken shell after hatching serving as its legacy.

5.3 Electrophysiology of the egg

In this section, I shall review some of the electrophysiology experiments which have been carried out on chick eggs. My purpose here is to give a flavour of this work, and mention a few specific findings that will be relevant to the magnetometry experiments.

Vorontsov and Emchenko [98] elegantly demonstrated that fertilized chick eggs generated electric fields. They designed a holder for an egg, that was fitted with two electrodes and that could be rotated through 180°. An egg was placed in the holder, so that the upper electrode made contact with the shell immediately above the embryo while the lower electrode contacted the opposite surface, and a potential difference was measured. When the holder, including the electrodes and the egg, was inverted, the existing potential difference changed to a new value over a period of a few tens of seconds, as the embryo and its associated structures slowly moved back to the upper part of the egg by gravity. The technique eliminated difficulties caused by the shell's large resistance and the contact potentials. They showed

that, during the first five days, the embryo was positive with respect to the albumen by 1–10 mV. This potential difference attained a peak on the fourth day and then declined.

Kyriakides and Simkiss [70] have studied the chorioallantoic membrane later in incubation (between 10 days and hatching) and measured potential differences of order 10 mV, interior negative, across it. They determined that most of the voltage is developed across the outer chorion and that it is very sensitive to chloride ion concentration. The function of this transmembrane potential may be to control later development by polarizing the distribution of certain charged membrane components. Simkiss [87] later described the water and ionic fluxes in the egg in terms of interfaces between the sub-embryonic fluid, amnion and allantois. The considerable changes in relative sizes and configurations undergone by these fluid-filled compartments are an integral part of the development process, and are controlled by electrochemical and osmotic gradients.

Between days 3 and 7, the yolk sac membrane has been shown to support a potential difference of several millivolts, which is sodium dependent. It has been proposed [28] that this causes a sodium flux from the albumen into the sub-embryonic fluid, at the periphery of the yolk sac. Such a flux would also be important in controlling osmotic pressures and in determining the development of the various compartments in the egg.

Within the embryo itself, Gillespie and McHanwell [39] have measured a pH gradient of 0.5 units between the neural tube and the primitive streak, in the period 24–48 hours. They suggested that, through the effect of cell adhesion, this gradient may play a role in determining the important cell migrations taking place at that time.

Finally, I come to Jaffe and Stern's experiment [63], first referred to in section 5.1.2. Using the vibrating probe, they measured peak current densities of 10–20 μA cm^{-2} in a plane 0.2 mm above the epiblast, oriented away from the primitive streak in all directions. The greatest current densities were recorded leaving Hensen's node (see figure 5.2b), the local thickening of the epiblast at the anterior end of the streak. Its significance is that the epiblast cells ingressing at this point differentiate to form the notochord: the precursor of the chick's spinal cord. The strength of the measured currents in such a confined space (estimated to be about 100 μA cm^{-2} and directed upwards) could generate fields that are sufficiently large to cause electrophoresis within the ingressing cells. This would redistribute charged macromolecules and thus alter the properties of the membranes of these cells. Since apparently identical epiblast cells differentiate to form the observed variety of tissue types after passing through the streak, could the spatial and temporal variation of streak currents account for this differentiation?

It was decided to use SQUID magnetometry to try to image this current distribution. The results of the early measurements are summarized in a review by Swithenby [92], and they will be the subject of the next section.

5.4 Low resolution measurements

In this section, I shall review the relatively uncharted subject area of chick magnetometry. Prior to this thesis, just two studies have been carried out, by Lennard [71] and Janday

[64]. Both projects utilized the same magnetometer system[1] consisting of a second-order gradiometer (coil diameter 24 mm, 4 K—300 K separation 12 mm) connected to an rf SQUID. Section 5.4.1 contains a description of the *in ovo* experimental procedure and some typical results. The experiments discussed in section 5.4.2 are more diverse, and were designed to try to elucidate the source of the signals. Finally in section 5.4.3, as a springboard to the last two chapters, I shall list the modifications to both the experimental and analytical techniques that I saw as a requirement for obtaining an improved understanding of this phenomenon.

5.4.1 Procedure and typical results

The standard protocol in these experiments was as follows. Eggs from a commercial hatchery were incubated in the laboratory at about 38°C and 60% humidity, and were rotated several times per day to ensure normal development. Before a measurement could be performed, it was necessary to cancel the Earth's field in the measurement region. The diamagnetic signal due to an egg (effectively about 50–100 cm^3 of water) can be estimated by comparison with the calculation in section 2.2.2, and is considerable. The egg was then placed on a non-magnetic support and passed backwards and forwards beneath the detector while simultaneously recording its position and the SQUID output.

The usual arrangement was to align the egg's axis with the laboratory y-axis and then make parallel sweeps (typically separated by 14 mm) in the x-direction. The distance of closest approach to the sensing coil was also 14 mm. Spatial signal averaging was usually employed to improve the signal-to-noise ratio. Measurements were made at intervals of 6 or 12 hours on several dozen eggs. Most eggs were only monitored for the first 5–7 days, although a few were monitored regularly until they hatched. Normal, healthy chicks emerged after 21 days, confirming that the experiments did not adversely affect development.

Approximately 20% of the eggs scanned produced no measurable signals whatsoever. However, it was easily shown that such eggs had not been fertilized. The development of the magnetic field patterns due to the remaining eggs followed a broadly similar trend.

The first unambiguous evidence of a signal above the noise level ($\approx$ 0.2 pT) was after about 18–24 hours. The signal increased steadily in magnitude over the following 2–3 days, maintaining a roughly bipolar field pattern and reaching a maximum peak to peak amplitude of 4–40 pT on, or close to, the fourth day. After this time, the strength of the field pattern subsided, sometimes dramatically, the characteristic bipolarity giving way to a noisy, complex configuration. All inter-egg consistency was lost at this stage and low magnitude complex patterns then persisted until hatching.

Ferromagnetic contamination was eliminated as a potential source of the signals.

Figure 5.6 shows a sequence of contour plots recorded during the period of signal growth of one typical egg.

The initial polarity of the pattern for all eggs was fairly similar. If the source had been modelled as a single current dipole, its orientation, in most eggs, would have been found to be parallel (within 45°) to the egg's axis and towards the sharp end. However, during the

[1]Model 330X rf SQUID, SHE Corporation (now Biomagnetic Technologies inc), San Diego, CA, USA.

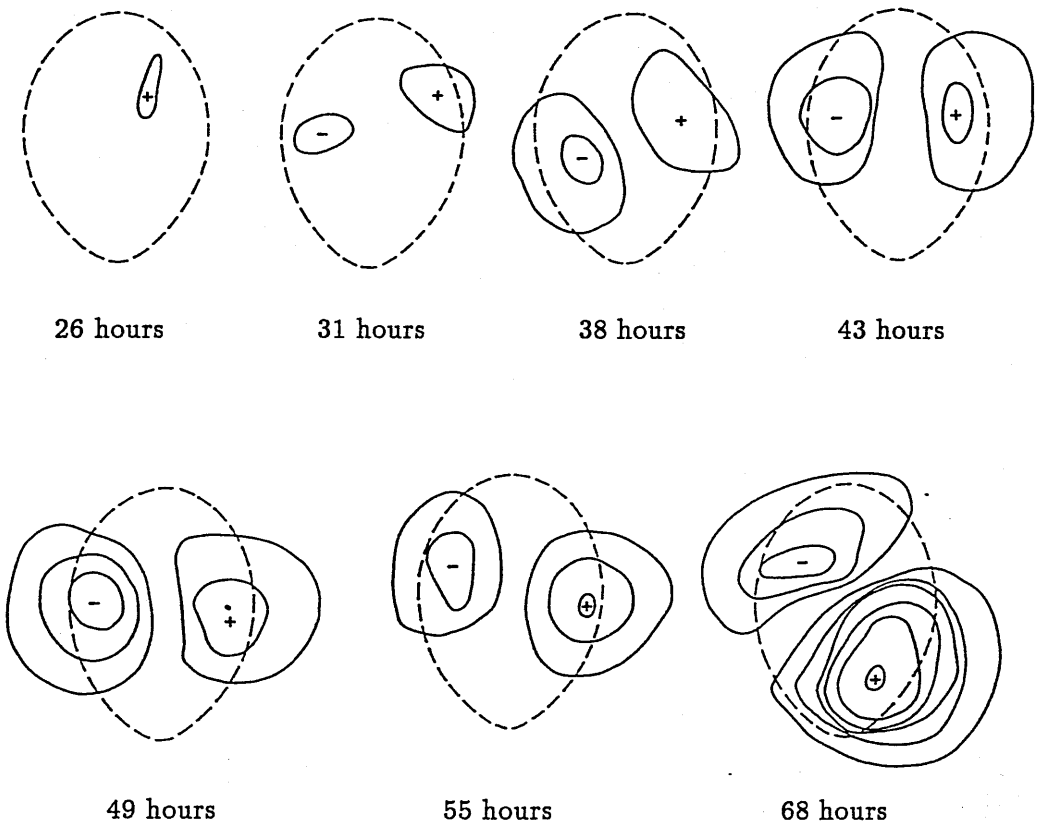

Figure 5.6 Signal variation with incubation time for a typical egg
Contour separation = 1 pT, after Janday [64]

period of signal growth, the orientation of the field polarity varied, in some cases reversing completely, so that there was very little inter-egg consistency by the time of the strongest field pattern.

The source was modelled as a single current dipole. For both a bare dipole and a dipole in a conducting sphere, the predicted depths were improbably large. The equivalent dipole was consistently found to be 5–15 mm below the shell, within the yolk. This is too deep to be associated with the embryo and a localized source somewhere in the yolk is highly unlikely. The conclusion was that the model was not suitable, and that the real current configuration is more distributed.

5.4.2 Auxiliary experiments

Refrigeration for an hour caused the signal to disappear entirely, but it returned if the egg was replaced in the incubator, and reattained its prior magnitude after about two hours. It was also established that removal from the incubator and exposure to the laboratory temperature for up to ten minutes (a period in excess of the total scanning time) did not cause a significant attenuation of the signal.

In an attempt to correlate the early (bipolar) field pattern with the orientation of the embryo, several eggs were 'windowed'. By carefully scoring the shell, it was possible to remove a small section along with the underlying opaque shell membranes. This allowed

observation of the embryo. If the window was covered and sealed with transparent film, to prevent infection or desiccation of the embryo, apparently normal development proceeded and apparently normal magnetic field patterns were obtained. There was no obvious correlation between the orientation of the embryo and that of the equivalent current dipole.

A series of invasive measurements on chick embryos of three and four days incubation by Janday [64] indicated that the embryo was not the source of the observed signals. With windowed eggs, it was observed that, if the embryo in its amnion was carefully dissected away without disturbing the underlying tissue, the magnetic field pattern was altered but not eliminated. When the egg contents were transferred from the shell to a dish containing saline soaked cotton wool, the signals were distorted (presumably due to the altered geometry), but of the same approximate magnitude as they were before transfer. The empty shells, meanwhile, gave no signal. Finally, removal of the embryo from the shell-less system also had an ambiguous effect on the signals, disturbing them but not removing them.

It was concluded that at least part of the signal was generated in the extra-embryonic membranes.

Using specific metabolic inhibitors, Janday attempted to establish which ions were in motion. With one exception, all of the poisons killed the embryo fairly quickly (the heart stopped beating), without having any effect on the magnetic signals for up to half an hour. However, injection of a detergent beneath the embryo immediately arrested the signal.

5.4.3 Improvements to the experiment

A major objection to the early experiments, described above, was the poor spatial resolution with which the fields were measured. The sensing coil had a diameter of 24 mm and was located more than 14 mm from the source. It is not surprising that bipolar field patterns were obtained, since the dipole contribution to any current distribution dominates at distances large compared with the scale of the source.

Thus, considerably more information was potentially available, by repeating the measurements with SQUIDLET. Despite SQUIDLET's noise floor being higher than that of the conventional magnetometer, it was expected that the overall signal-to-noise ratio would be improved, because the much closer approach would more than compensate. This might obviate the necessity to signal average as well as allowing earlier identification of the signal. It was anticipated that field maps, containing much more detail than previously, would be obtained.

The primary objective was to closely relate the lateral location and orientation of the embryo and the extra-embryonic membranes, with the vertical field component measured a few millimetres above the egg. Thus, eggs with large ($\approx$ 20 mm diameter) windows would be required, together with an apparatus for the accurate ($\approx$ 1 mm) localization of the important anatomical features immediately prior to, or following, scanning. In this way, it was hoped that a correspondence between features of the magnetic field map and anatomical landmarks would be found.

Finally, with the implementation of an algorithm capable of solving the inverse problem for extended current density distributions [56], and the indication that the source was dis-

tributed in the extra-embryonic membranes, came the possibility of highly realistic modelling of the currents within the developing system.

Chapter 6

High resolution measurements of chick eggs

Measurements of chick eggs with SQUIDLET were carried out over a period of about eighteen months during which time, as was the case with the earlier studies, dozens of eggs were scanned. However, it was only towards the end of that period, that adequate protocols had been established and that the magnetometer performance had been optimized. Consequently, this chapter is devoted mainly to those later experiments in which the important results were obtained.

I shall report three different types of experiments: serial measurements of intact eggs, serial measurements of windowed eggs and 'snapshot' measurements of windowed eggs. The logical progression from the previous experiments was to accurately relate the observed fields to the location, orientation and stage of development of the embryo and extra-embryonic membranes as incubation proceeded, and these measurements will be described in section 6.3. Prior to that, measurements of intact eggs, as a function of incubation period, will be reported (section 6.2), to investigate the higher resolution field patterns without the complications of windowing. Certain other advantages were afforded by making single 'snapshot' measurements of windowed eggs, and these will be discussed in section 6.4. Section 6.5 contains the results of modelling the sources as current density distributions. Finally, in section 6.6, I shall discuss the results and comment on the occasional appearance of a highly localized feature on the field maps, which would require a considerable further improvement in spatial resolution, to image adequately.

I shall start, in section 6.1, by describing the techniques and apparatus that were common to all the experiments.

6.1 General protocols

6.1.1 Treatment of the eggs

All eggs used in these experiments were obtained from a local commercial hatchery. They had been refrigerated at 8°C immediately after laying and were delivered via refrigerated transport no more than three days later. It was recommended that they be left to stand for at least another twenty-four hours before commencing incubation, and so, eggs had probably been chilled for about 4–5 days before the experiment was started. According to Patten [79], refrigeration prior to incubation retards development slightly and developmental stages occur about 3–4 hours later in these eggs than in ones that have not been chilled. This

observation is important when assessing whether embryo development after a certain period of incubation is 'normal'.

Chick hatcheries and some large-scale research facilities use automatic incubators, in which the eggs are gently rocked backwards and forwards through about 45°. No such machine was available in the laboratory, and so a simple box with a thermostatically controlled heater and water tray sufficed. This is the kind of incubator used commercially during the last few days before hatching, when rotation of the egg is not necessary. The advantage of the static incubator was that eggs had been stationary for some hours prior to scanning, and so any transients due to rotation could be neglected. The disadvantage was that they had to be physically turned about four times per day. Eggs were always stored, incubated and scanned with the long axis horizontal.

The eggs were wiped clean with de-ionized water, to remove any ferromagnetic contamination, individually labelled and then incubated at 38°C and 60% humidity. They were rotated by 45° for twenty minutes and then returned to their normal orientation, at least four times per day. This was usually done immediately after scanning.

6.1.2 Data acquisition software

Figures 6.1 and 6.2 synopsize the computer program used for data acquisition, in the form of flowcharts. Rectangular boxes represent calculations and operations performed by the program and elliptical boxes represent points at which user input from the keyboard was required before the program would continue.

The laboratory microcomputer[1] ran an MS-DOS operating system[2] and the program was written in the scientific programming language ASYST2.0[3].

Figure 6.1 shows the logic for the overall program. I shall discuss some significant features. There were two input channels to the computer. One was from the filtered SQUID output and the other was from a potentiometer connected to the stage, whose output varied linearly with displacement during a scan. The potentiometer calibration procedure involved positioning the stage at the two extremes of motion and giving a keyboard signal each time.

The laboratory coordinate system was defined as follows. Each egg measurement consisted of a number of parallel scans in the x-direction (perpendicular to the egg's axis), at different y-positions, while the z-component of the field (vertical) was measured at a fixed point in the laboratory frame. The number of scans, the number of databins (contiguous sections of the scan within each of which a single datum was ultimately recorded) and the range (the total scan length over which data would be collected) were selected. From the range and number of databins, the program calculated the potentiometer values corresponding to the boundaries between the bins, and the egg's position was then calibrated with respect to the x-coordinate along the scan. Having set the scan number to one, the program waited until the egg had been moved out of the x-axis measuring range, and then it was ready.

After one keystroke, an entire map was recorded without further input from the keyboard,

[1] Zenith Data Systems, St Joseph, MI, USA.
[2] Microsoft Corporation, whereabouts unknown.
[3] Macmillan Software Company, New York, NY, USA.

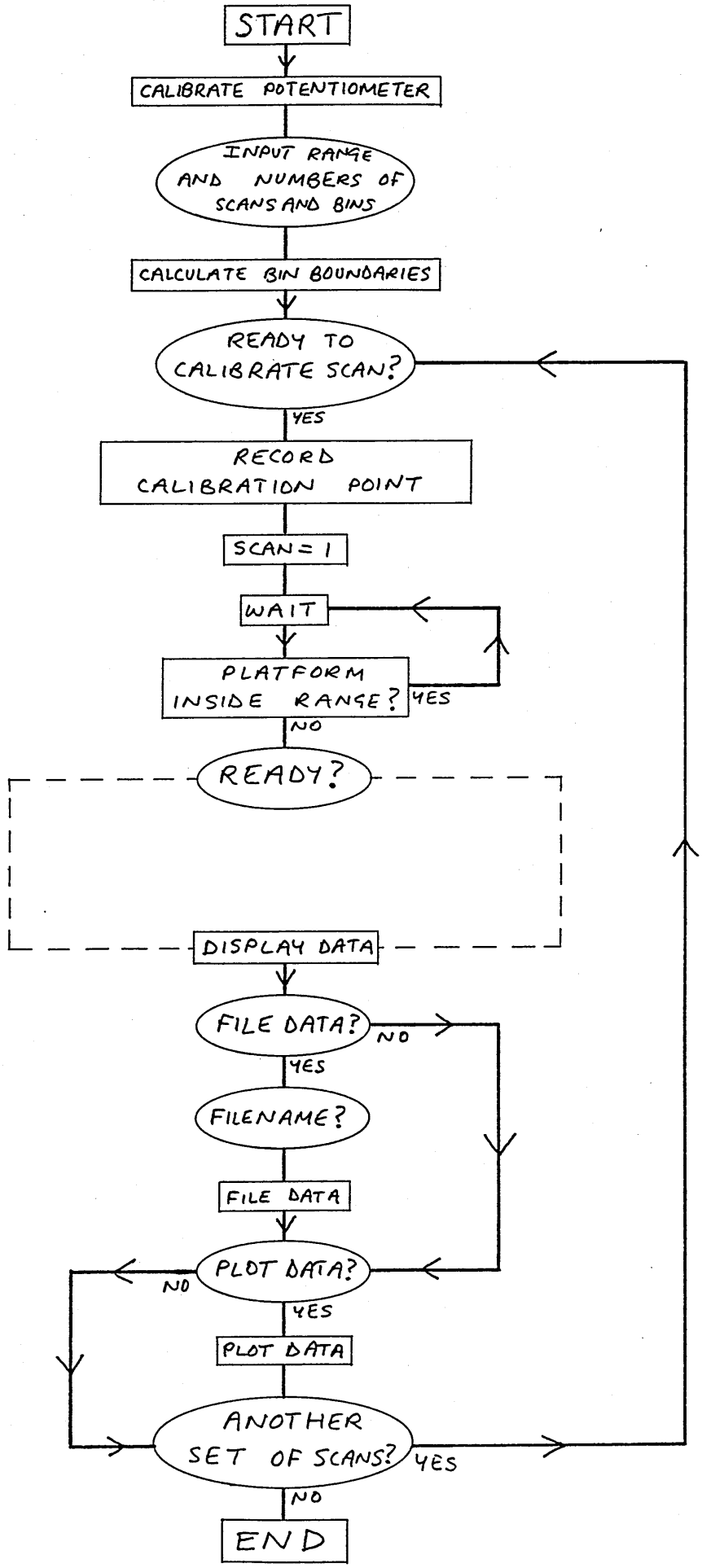

Figure 6.1 Flowchart of the data acquisition program

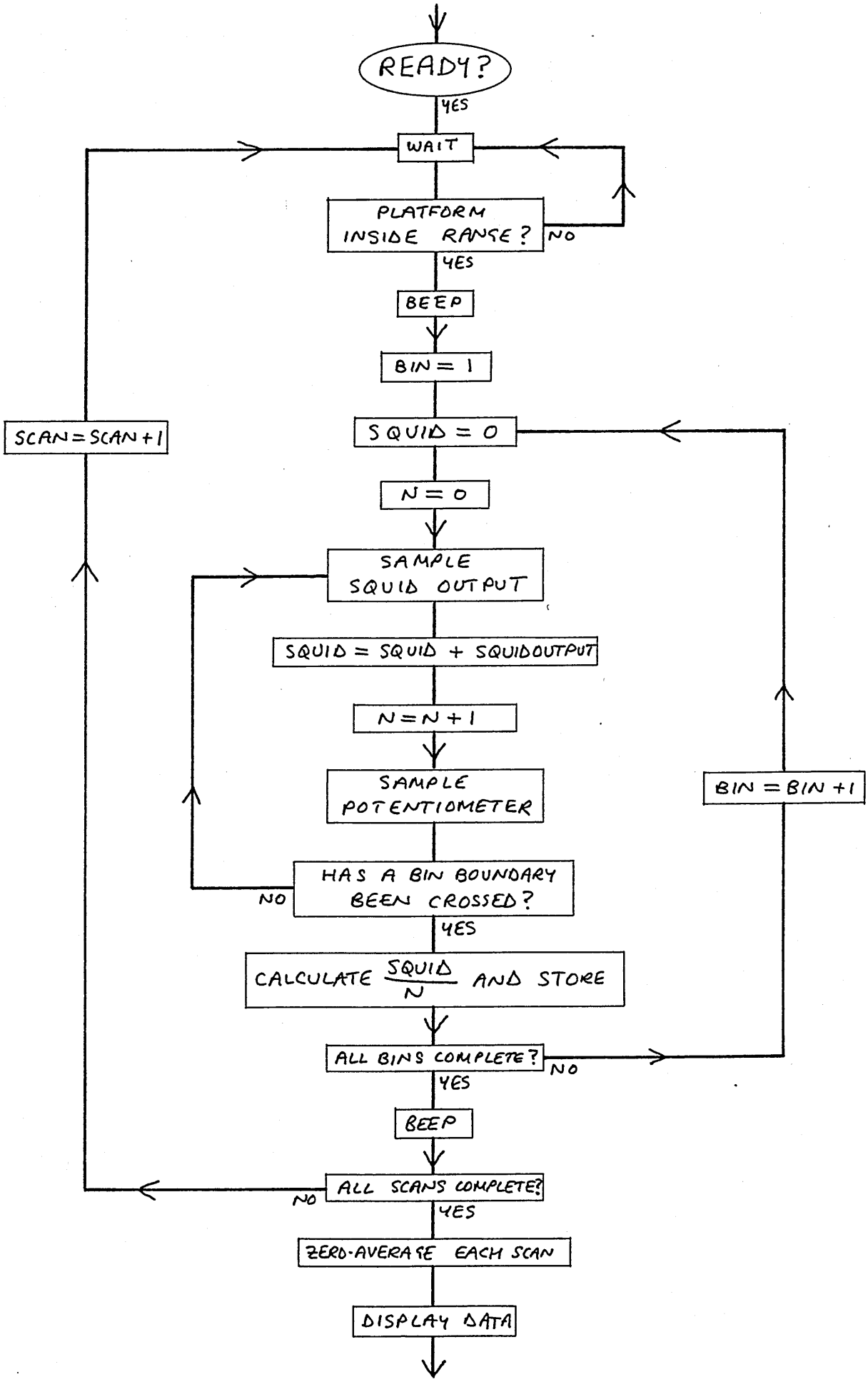

Figure 6.2 Expanded flowchart of the scanning part of the program

while the egg was swept manually backwards and forwards. The software dealing with this part of the experiment is shown in figure 6.2 and is represented by the dashed box in figure 6.1. Data collection commenced when the potentiometer output indicated that the egg had been moved into the measuring range. The SQUID output and potentiometer voltages were then sampled alternately at the computer's maximum sampling frequency (a few kilohertz), whilst keeping a record of the cumulative SQUID voltage and the number of measurements. When the egg moved out of the first databin, the average SQUID reading was calculated and stored in an array with the x-coordinate of the centre of that bin. This procedure was repeated until the egg had passed through all the bins (ie the scan was complete). The stage was manually moved until the egg was at the next y-position while the program waited for the potentiometer output to come once again into range. When this happened, the recording of another scan was initiated. At the end of the entire map, each scan was individually zero-averaged to remove any dc shift. The scans were then displayed consecutively on the screen and the user could file and/or plot them.

There were additional error-checking routines to warn the user if the egg was within range before data collection had started, and to interpolate data if any bins were empty. However, this was unlikely because the sampling frequency was usually about two orders of magnitude greater than the average bin frequency. For the same reason, the digitizing error introduced when a single SQUID reading was erroneously allocated to the subsequent bin was negligibly small.

6.1.3 Experimental procedure

The laboratory Helmholtz coils were used to balance the Earth's field with a precision of about 5 nT (120 ppm and 260 ppm for the vertical and horizontal components respectively). The field balance at the dewar tip was checked several times per day (prior to scanning) and the coil currents were adjusted if the net field was greater than about 20 nT in any direction.

When a measurement was made, the egg was removed from the incubator and placed on the scanning platform in its normal orientation and with its sharp end pointing in the +y-direction. The scanning platform consisted of a wooden stand with vertical adjustment and a three-point support for the egg (see figure 6.3). The stage, upon which it was mounted, could be manually moved in the laboratory x-direction (during the scans) and y-direction (between the scans), as in figure 2.1. The egg was iteratively oriented about three axes with a reproducibility that was better than $\pm 5°$ and the height of the platform was set, with the aid of a feeler gauge, so that the highest point on the egg was 0.5 mm below the dewar tip.

Scanning took about five minutes. Twenty-five scans, each separated by $\delta y = 5$ mm, were made, so the total measurement area overlapped each end of the egg by about 3 cm. Each scan was of $\Delta x = 25$ cm, which ensured that the egg-related signal fell to a negligible level at the extremes (thus conferring baseline knowledge), and data for each scan were averaged into 128 bins (ie $\delta x_{bin} \approx 2$ mm). In order that distortion of the signal due to low-pass filtering (as described in section 2.2.3) would be insignificant, the scanning was performed slowly, taking about ten seconds per scan (the measuring bandwidth was 0–40 Hz). Between scans, the stage was manually set to the new y-position.

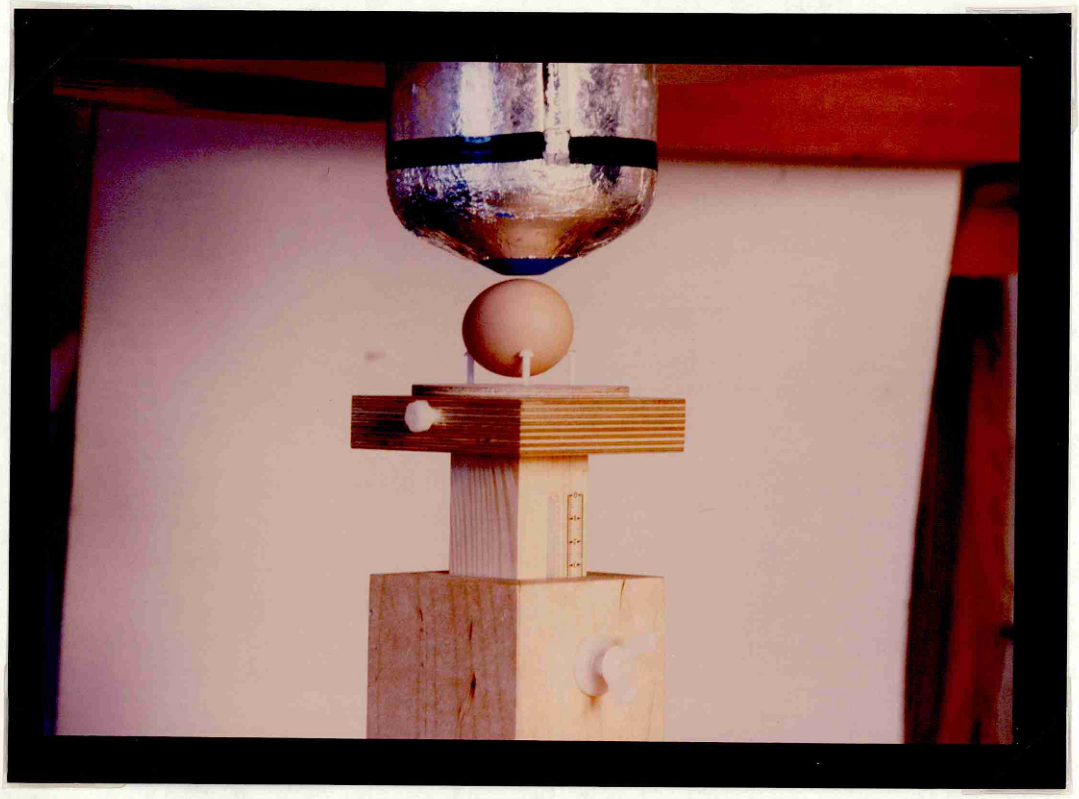

Figure 6.3 Photograph showing scan of an intact egg

After completing the scans, the egg was replaced in the incubator in a different orientation for about twenty minutes as described in section 6.1.1.

6.1.4 Preprocessing the data

Figure 6.4 illustrates schematically the data acquisition electronics.

The Dynabias/feedback and dc SQUID control units[4] were both included in the commercial SQUID package. The dc offset unit was a simple home-made device, containing a single operational amplifier, which allowed a fixed offset to be added to or subtracted from the signal. This was necessary in order to properly utilize the $\pm$ 10 V range and 12 bit sensitivity of the computer's input channel. The filter/amplifier[5] contained two serial low-pass filters. The -3 dB points were usually set at 40 Hz, to remove mains-frequency interference.

As described earlier, the stage potentiometer was connected to the computer via a second input channel.

6.2 Measurements of intact eggs

6.2.1 The effect of cooling

Since the egg would have to spend several minutes out of the incubator for each measurement, it was clearly important to know what effect this had on the signals. Janday's experiments [64] demonstrated that the amplitude of the field pattern was attenuated by refrigerating

[4] Models 400 and 40, respectively, SHE Corporation (now Biomagnetic Technologies inc), San Diego, CA, USA.

[5] Variable filter model VBF/4, Kemo ltd, Beckenham, Kent, UK.

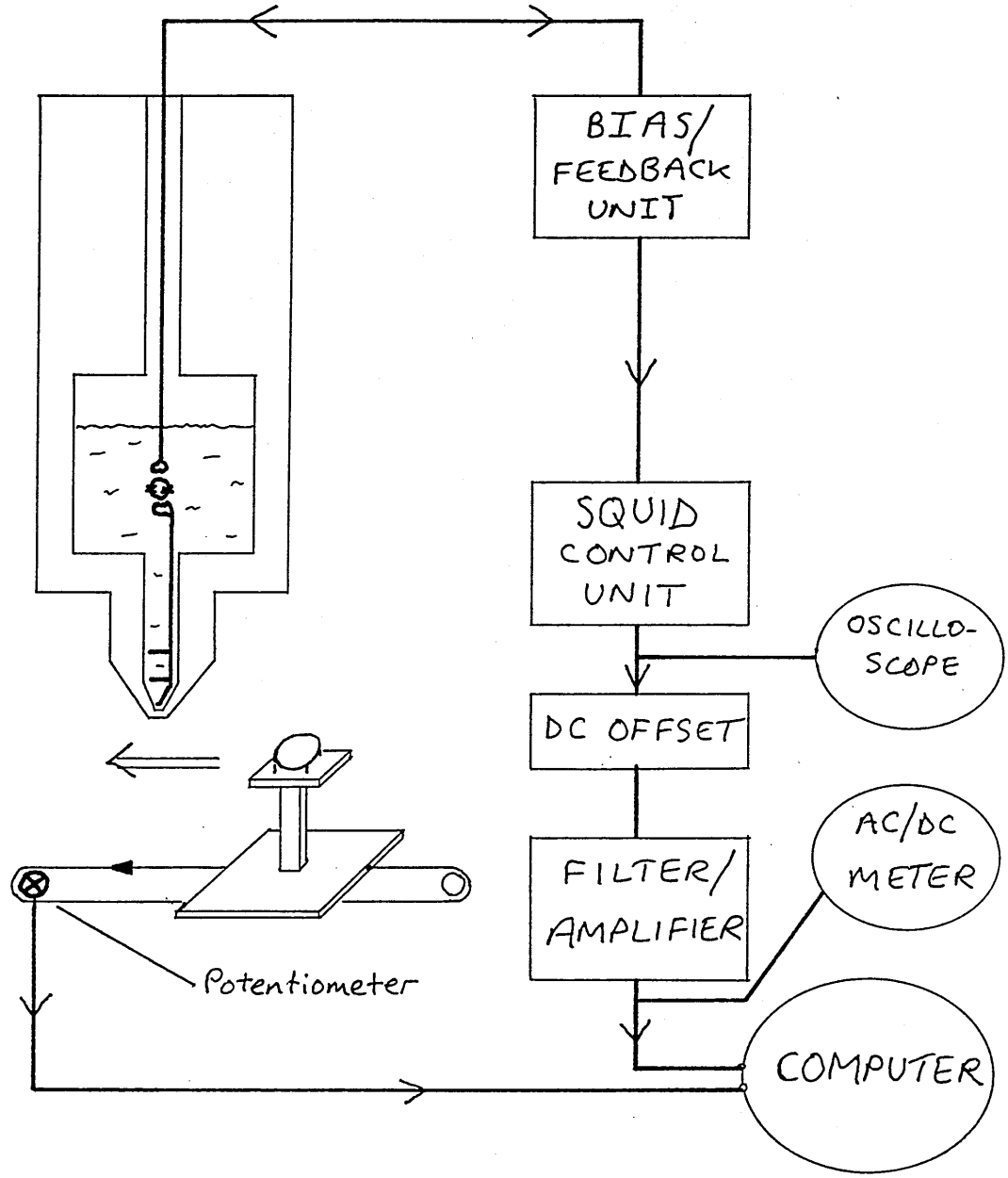

Figure 6.4 Schematic diagram of the signal channels

the egg — but what about keeping the egg at laboratory temperature? If the signal declined sharply, there would be difficulties with recording an entire magnetic field contour map.

On investigation, it was discovered that the effect of the temperature change was negligibly small over the time taken to record a full field map. Figure 6.5 shows the peak to peak signal value for four different scan positions on the same unwindowed egg (after 71 hours of incubation) as a function of time. The four scans were taken over the central region of the egg. All remained bipolar and of essentially the same shapes for a period of one hour at laboratory temperature, but decreased in amplitude.

The amplitude fell, at a roughly uniform rate, by 30–35% in an hour. This corresponds to an attenuation of less than 3% during the five or so minutes required to record a complete map. During a full mapping, only a few scans over the centre of the egg give strong signals, and so this variation would certainly not distort the field map to any significant extent.

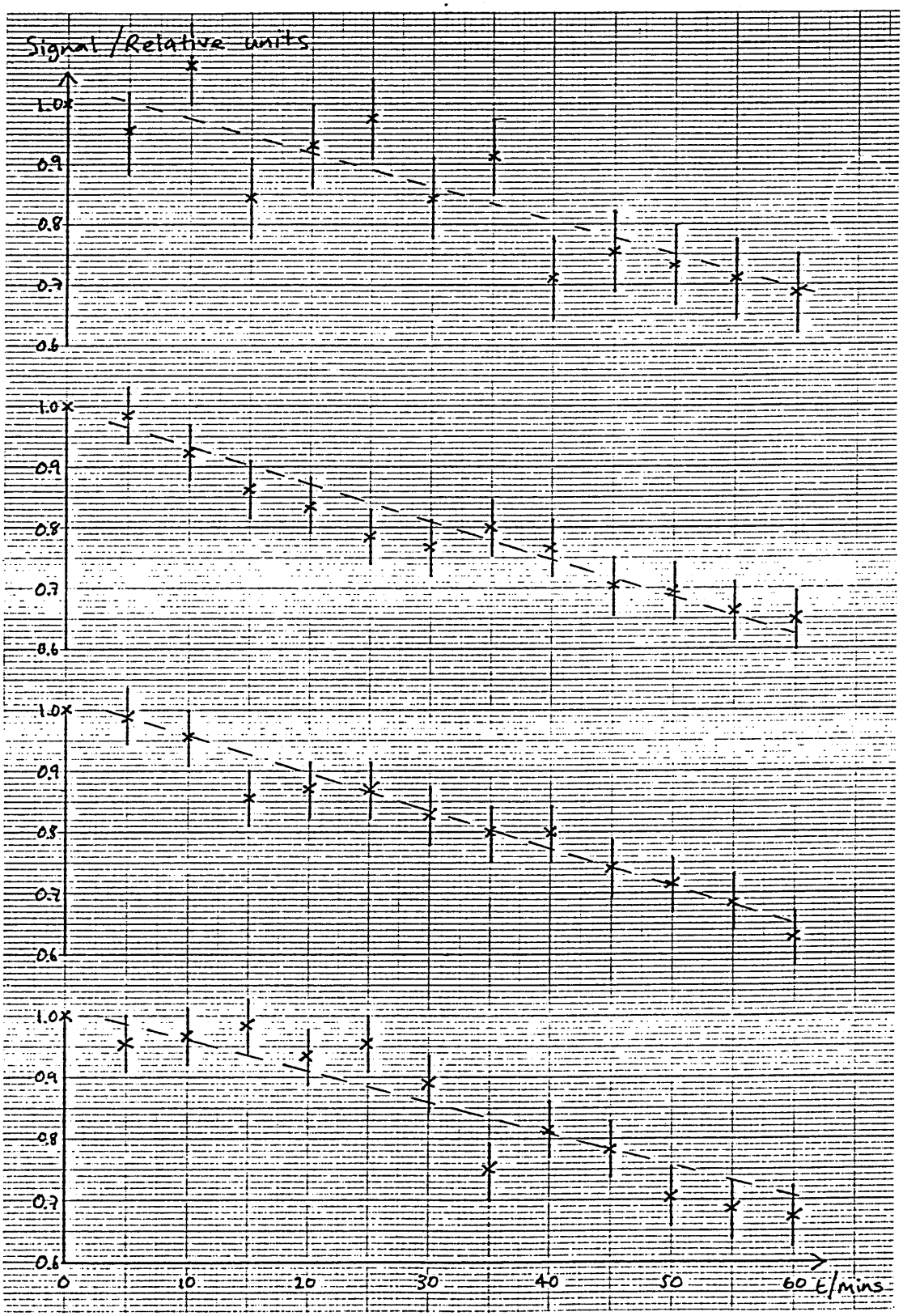

Figure 6.5 Decrease of signal amplitude with time at laboratory temperature

6.2.2 Serial measurements

Magnetic field maps were recorded from approximately thirty unwindowed eggs during their first week of incubation. The results of these experiments are not amenable to a presentation of detailed statistics because both the experimental protocol and the data acquisition software were being developed at this time. In any case, the objective was to confirm the results of previous experiments and to deduce whether any extra information might be forthcoming by measuring with higher resolution. The general conclusions were similar to those obtained by Lennard and by Janday. However, a greater complexity in the field patterns was revealed, and at some stage of development, almost all of the eggs generated a pattern that *could not possibly* be modelled as a single current dipole.

Four eggs were allowed to proceed to full term and they hatched into normal, healthy chicks, verifying that the treatment of the eggs did not have an adverse effect on their development. Eggs which gave no signal were found to be unfertilized.

I shall summarize the preliminary results obtained from intact eggs by SQUIDLET. The typical features were as follows:

- Signals appeared on the second day of incubation.
- The signals attained their maximum amplitude after about four days; this 'strongest' field pattern was usually bipolar with an effective current dipole that would be located within the yolk.
- By the fifth day, the overall signal strength was falling, and it was often apparent that there were several independent, competing sources.
- Development of the field pattern between consecutive measurements (separated by about 6 or 12 hours) was sometimes smooth and sometimes very abrupt.
- Some of the field patterns obtained were quite complex, and there was frequently a quadrupolar pattern.

I shall present data for one egg which epitomizes these general observations. Figure 6.6 shows a sequence of magnetic field contour maps recorded from an unwindowed egg on the third, fourth and fifth days of incubation. The outline of the shell has been overlaid. In these and all subsequent maps in this thesis, solid lines represent positive contours (ie $B_z > 0$) and broken lines represent negative ones. The data have not been smoothed (except by the spatial averaging into bins during data acquisition).

A small signal was just evident on a scan recorded after 42 hours of incubation (not shown), and twelve hours later, a clear bipolar field pattern had emerged. This developed into a more complex map after 65 hours, consisting of one positive and two negative poles. After 89 hours, a strong quadrupolar field pattern appeared. The strongest field was measured after 99 hours, at which time the pattern had reverted to two extended poles with a separation of about 30 mm and a peak to peak signal of about 32 pT. Thereafter, the signal declined rapidly, becoming fragmented and noisy. It is clear that, for extended periods, a single current dipole could not 'explain' these data.

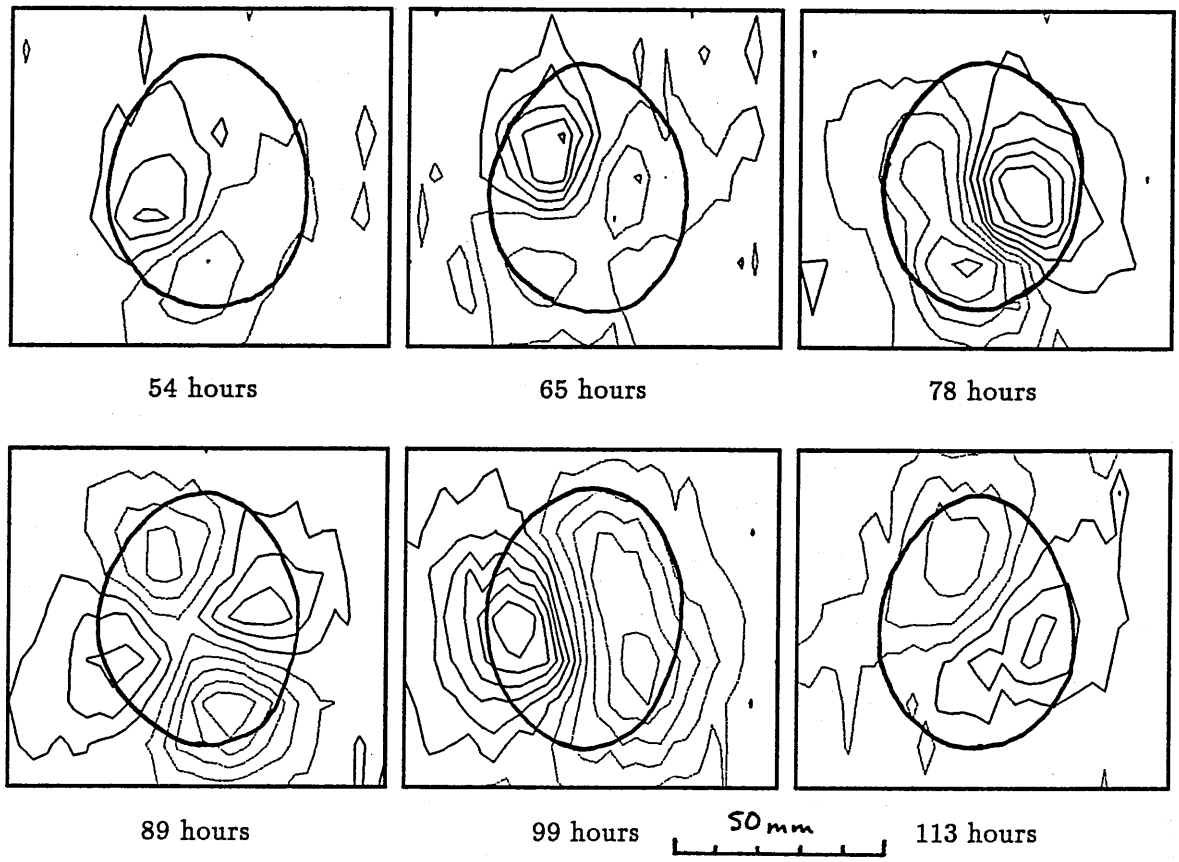

Figure 6.6 Sequence of field maps recorded from a typical intact egg
Contour separation = 2.9 pT

Although these experiments do not permit precise judgments about the generators of the magnetic fields, the miniature magnetometer has succeeded in imaging them in much greater detail than was previously possible. SQUIDLET operated with a noise-limited field sensitivity only about half as good as that of the commercial system used in earlier studies, and yet, by making measurements closer to the source, it yielded much more information. Proximity to the source and high resolution have demonstrated the naivety of the single current dipole model in this case.

6.3 Serial measurements of windowed eggs

The purpose of these experiments was to relate the developing field maps to the chick's developing anatomy during the first few days of incubation. Consequently, the eggs had to be windowed and a technique for accurately recording the lateral layout of the anatomy was required. These issues are addressed in section 6.3.1 and the results of the experiments are presented in section 6.3.2.

6.3.1 Protocol for windowed eggs

Typical problems which were encountered during windowing were with contamination, infection and desiccation. After several refinements, a successful technique was developed.

The use of steel scalpels was risky because, quite often, a tiny piece of the blade would break off and adhere to the cut edge of the shell, giving a strong ferromagnetic signal. After experimenting with various tools, the only reliable one was found to be a diamond stylus. This was not as sharp as the scalpels, and so cutting the window was more difficult.

The shell and underlying opaque shell membranes were removed with the stylus and plastic tweezers. The window area was usually about 2 cm^2, approximately rectangular and cut in the upper surface, with respect to the egg's resting orientation prior to incubation. In most cases, the blastoderm lay centrally beneath the window, so that the embryo developed in full view.

There was an unacceptably high mortality rate when the windowing was carried out in the laboratory, probably due to infection of the embryo. This was avoided by performing the operation with sterilized tools in a class 2 microbiological safety cabinet. To guard against infection during incubation and to avoid desiccation of the egg contents, a sterilized piece of transparent film was laid over the window. With a few drops of de-ionized water, it adhered to the surrounding shell. By taking these precautions, most windowed eggs developed normally for, at least, the first seven days. They were all terminated at about this stage.

The experimental protocol for windowed eggs was an extension of that detailed in section 6.1.3 for intact eggs. I shall now describe the additional apparatus and procedures employed for windowed eggs.

After the egg had been correctly positioned on the three-point support, a wooden box with an adjustable transparent roof was fitted above it on the platform. Drawn on the roof was a millimetre Cartesian grid and, by sliding the roof in the x- and y-directions, the grid origin was brought to lie directly over the sharp end of the egg. By viewing vertically downwards, the 'anatomical geography' (ie the lateral layout of the embryo, visible internal structures, extra-embryonic membranes and blood vessels) could be drawn onto millimetre graph paper, relating it to the grid coordinate system.

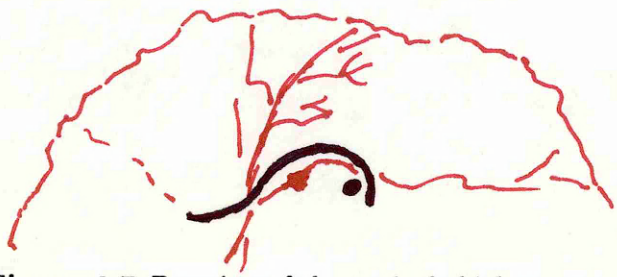

Figure 6.7 Drawing of the typical chick anatomy after 80 hours

Figure 6.7 is presented as a guide to the structures drawn on the overlays that relate to the various field maps and current density maps in this chapter and the next. The figure shows the development after about 80 hours of incubation. The black hook-shaped line is the embryo's body, and the curved end is cephalic, representing the head flexures described in section 5.2.1. It will be noted that, in most cases, the embryo turns onto its left side, although there are a few exceptions. In some drawings, the amnion was particularly obvious and so the embryo has 'thickness', but in most cases, the strongest feature was the line

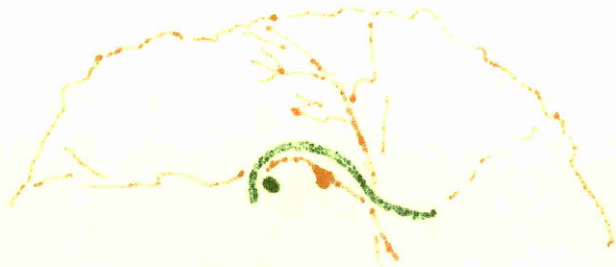

of somites. The red region, 'inside' the hook, is the heart, and the remaining red lines are the extra-embryonic blood vessels. Two particular parts of the vasculature were often quite obvious: the omphalomesenteric vessels, which connect directly with the heart and usually lie at about 60° to the body axis and the circumferential *sinus terminalis*. In earlier preparations ($\lesssim$ 60 hours), the black boundary is the unvascularized yolk sac margin, which extends around the yolk ahead of the *sinus terminalis*, and in the later ones ($\gtrsim$ 90 hours), the eye appears as a black dot. It should be noted that this kind of anatomical drawing is not a precise art, and that the embryo *in ovo* is very much less clear than when it is mounted on a microscope slide.

After completing the drawing, the grid coordinates were related to the x,y laboratory coordinates by moving the stage along x and y until a peg, fixed in the grid coordinates, was coincident with a fixed point in the laboratory system[6]. Finally, the depth of the embryo below the highest point on the cut shell was measured and recorded, and the height of the platform was set, with the aid of a feeler gauge, so that that highest point was 0.5 mm below the dewar tip.

In order to validate both the comparison of anatomical and magnetic field data from a single measurement and the comparison of data from thirty or forty measurements recorded over several days of incubation of the same egg, this tedious relocation and calibration procedure had to be performed carefully. However, it was also important to set the measurement up quickly, because (as demonstrated in section 6.2.1) the signals are attenuated with time when the egg is out of the incubator. With practice, it was possible to carry out this protocol, including the drawing, in about two minutes. The amplitude of signals from windowed eggs did not decline substantially more rapidly than those from intact eggs: scans recorded immediately after removal from the incubator and repeated after mapping again showed an attenuation of only a few percent.

The protocols for scanning and the data preprocessing scheme were the same as described for intact eggs.

At the end of the entire experiment (ie after 5–7 days of incubation), each embryo was excised from its egg, mounted on a microscope slide and studied under dark-field illumination. By counting somites and examining the development of other regions such as the brain, the allantois and the lens of the eye, the embryo was staged according to Lillie's system [51].

6.3.2 Results

The magnetic fields from approximately fifty windowed eggs were measured. Some of these were windowed after a few days of incubation, before which time they had been scanned as intact eggs. A large number of the embryos died during the development of a successful windowing protocol. For these reasons, it is not meaningful to present global statistics. I shall consider just one series of measurements carried out on six eggs at a time when the experimental protocol had been fully developed and SQUIDLET was operating reliably.

[6]The x-coordinates of these two reference frames were related to each other by recording the output of the position potentiometer with the software, as described in section 6.1.2, whereas the y-coordinate of the laboratory frame was defined at this time.

One egg was not windowed, as a control, and produced 'normal' (as described in section 6.2.2) signals, and one egg was infertile, producing no signals. One further egg became infected and the embryo died after four days of incubation. Of the remaining three eggs, the blastoderm in one, D5, was located approximately 60° from the upper surface, about the egg's axis. Consequently, the anatomical information, recorded as described in section 6.3.1 was sparse, and its lateral layout could not be related to the field maps.

Sequences of isofield maps relating to the other two eggs, D1 and D3, are shown in figures 6.8 and 6.9 respectively. The overlays contain drawings of the embryo and extra-embryonic vasculature at each stage, as viewed through the shell window. Using the apparatus and protocols described earlier, the precision with which the anatomical information was recorded and related to the field maps is better than ±2 mm. Each frame represents an area 10 cm × 10 cm.

At the end of the experiment, the embryos were excised from the egg and staged. In both cases, the actual incubation time was about 5 hours longer than that predicted by Lillie for that stage, and the allowance for chilling the eggs prior to incubation accounts for the discrepancy. Both embryos were healthy and normal, and their hearts were beating strongly until the moment of excision.

Analysis of the information contained in figures 6.8 and 6.9 yielded no consistent correlation between the position and orientation of the embryo and the field pattern. This was also true of the many other field/anatomical map pairs recorded from all the eggs not reported here.

The position of viable embryos was usually close to the centre of the field pattern. One hypothesis, prior to the experiment, was that there might be a consistent correlation between the embryo's orientation and the polarity of the field. For instance, the head might always point towards a region of negative magnetic field B_z. However, this was found not to be the case: once the embryo's orientation in the egg had been established, it varied by no more than a few degrees during the periods investigated, whereas the pattern's polarity changed considerably and often reversed at least once. In most eggs, including the two illustrated, complicated multipolar patterns were obtained at some stage. Another indication of the absence of a direct relationship between the fields and the embryo was the persistence of fields after embryo death. This observation was also made by Lennard [71].

An interesting development, which was observed with some eggs is exemplified by the maps recorded after 69, 75 and 81 hours from D1 and after 87, 91 and 93 hours from D3. In both these short sequences, the field pattern undergoes a radical change. It appears that one dominant current configuration takes over from another, and the intermediate map, which is mainly quadrupolar, captures contributions from both. I shall return to these data when I analyze the computed current density maps in section 6.6.1.

The field maps can additionally be used to illustrate the timescale of the electrophysiological activity during incubation. Figure 6.10 shows the variation of total recorded signal power as a function of time for the same two eggs (D1 and D3), including data recorded at latencies for which field maps are not shown. The period of strongest signals, 50–100 hours, coincides closely with the extension around the yolk and vascularization of the yolk

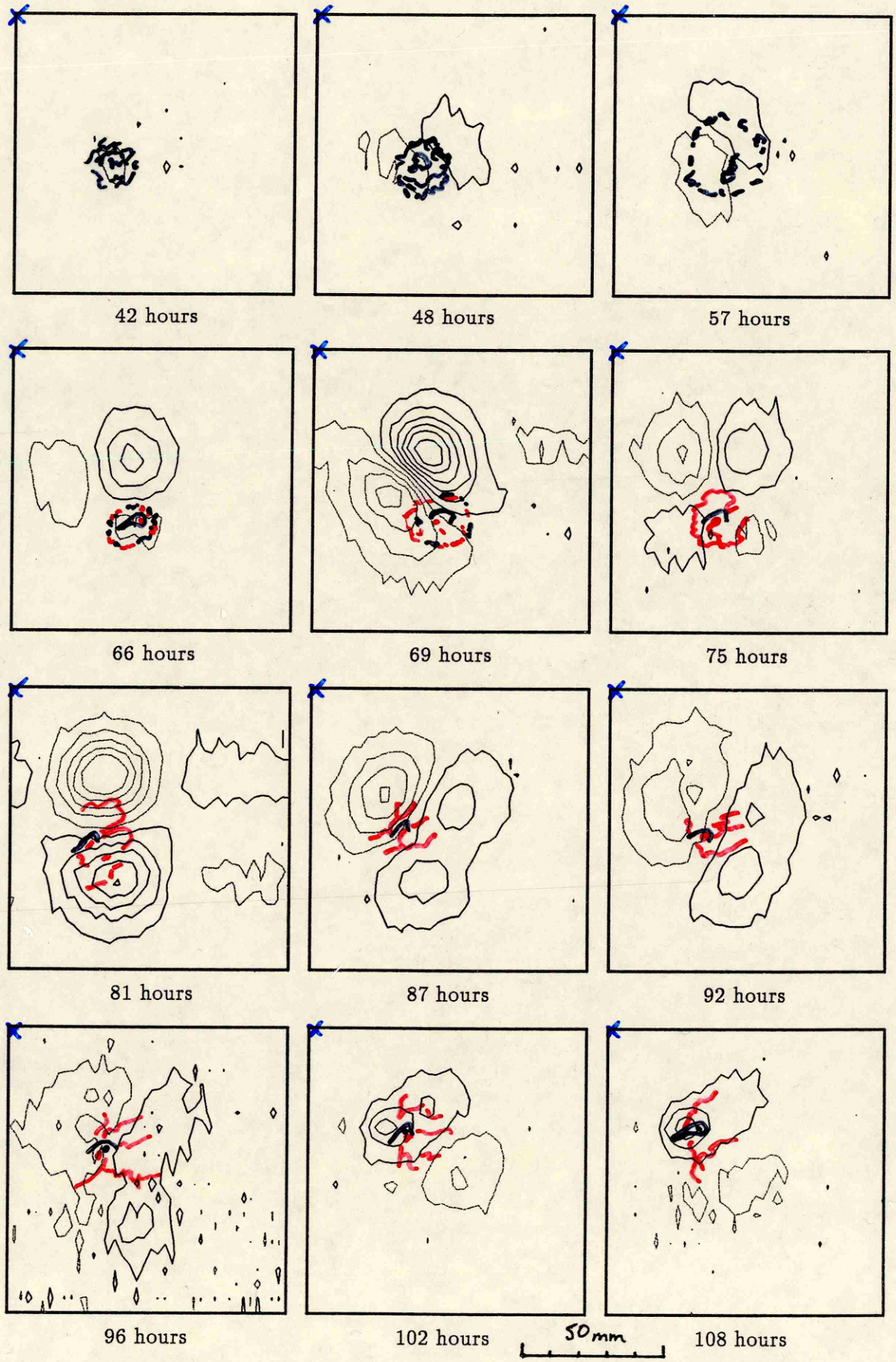

Figure 6.8 Field maps and anatomical geography for windowed egg D1
Contour separation = 5.7 pT (66–92 hours), 4.5 pT (remainder)

p102

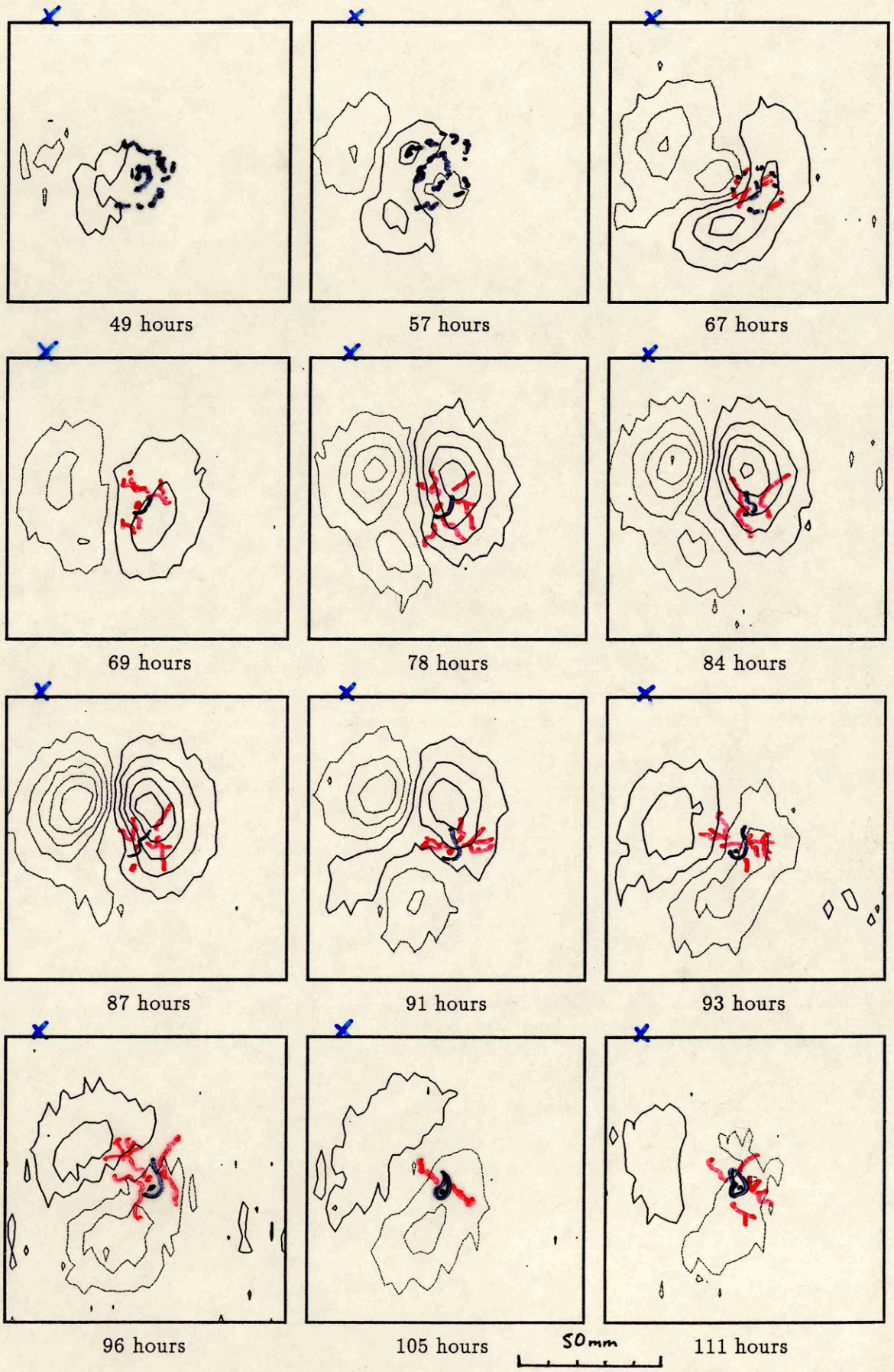

Figure 6.9 Field maps and anatomical geography for windowed egg D3
Contour separation = 4.1 pT

p. 103

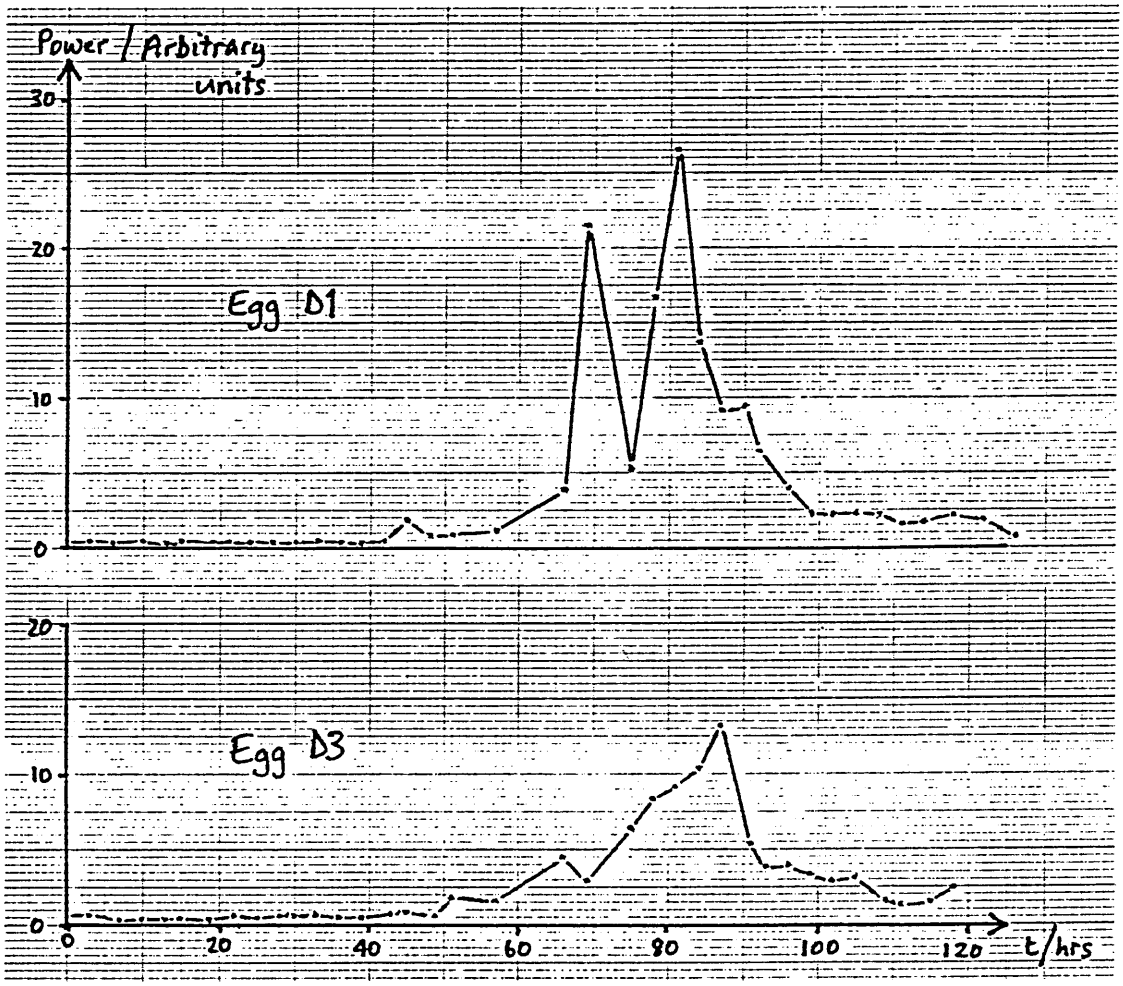

Figure 6.10 Signal power as a function of incubation time for eggs D1 and D3
Instrument noise $\approx$ 0.5 units

sac. The amnion first appears after 45 hours and has enclosed the embryo by 70 hours, and the period of rapid allantois expansion is from 75 to 100 hours. This evidence suggests that these extra-embryonic membranes are associated with the fields.

6.4 The 'snapshot' measurements

With the strategy of assimilating more information for less effort, 'snapshot' measurements of a further eleven eggs were made. In these experiments, eggs which had already spent a few days in an automatic incubator were obtained from a local ($\approx$ 1 minute's walk away) research unit. They were placed in the laboratory incubator for a few hours, to eliminate any rotational transients, and then windowed, scanned once and staged in much the same way as described for the serial studies. One important difference was that rather than simply cutting a window, the upper part of the shell was broken away in small pieces until the remaining shell was just large enough to contain the fluid contents. This allowed the dewar tip to pass within a millimetre of the embryo itself.

The anatomical and magnetic field maps for these eleven eggs are illustrated in figure 6.11. Nine of these eggs had been incubated for between 67 and 99 hours when they were

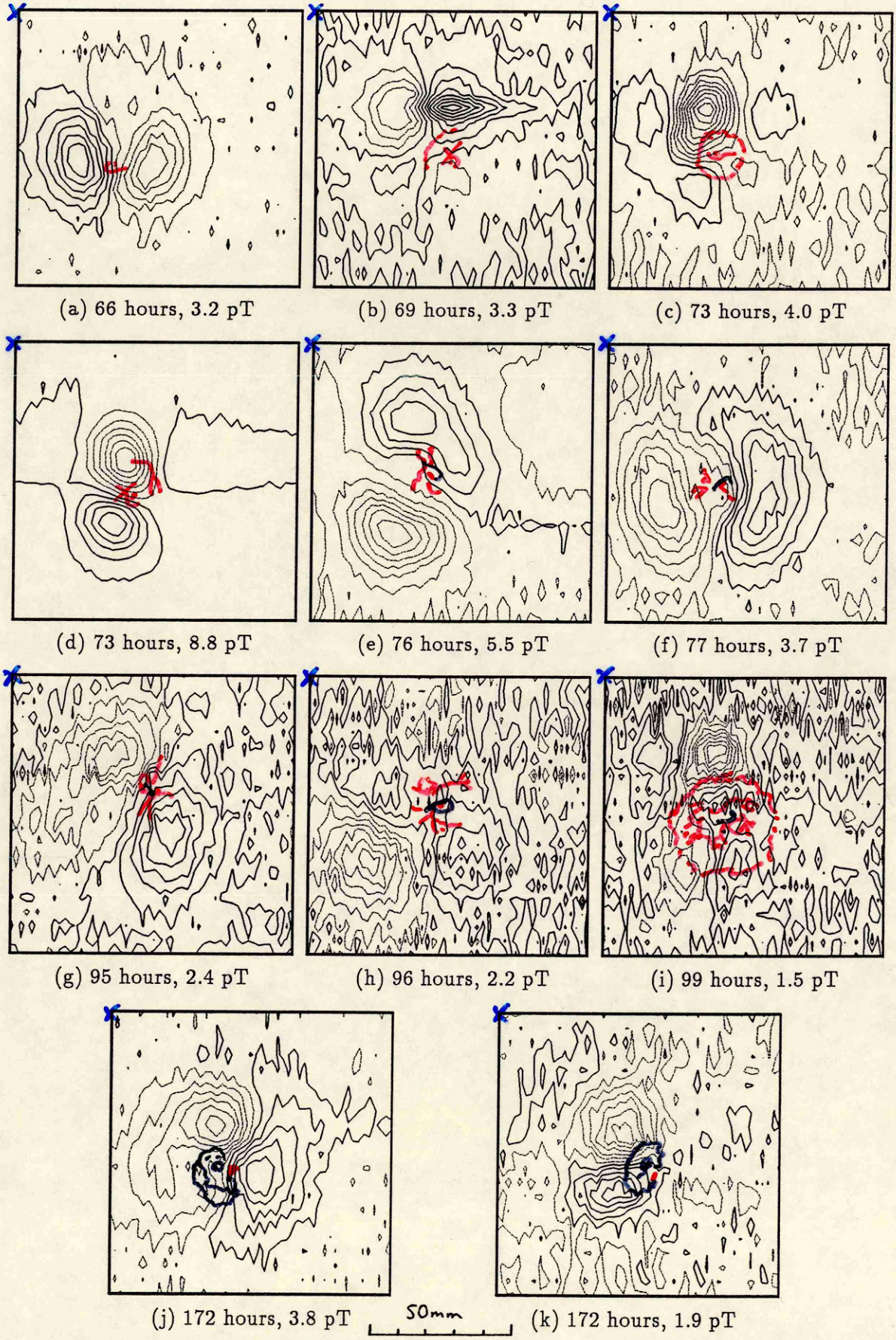

(a) 66 hours, 3.2 pT (b) 69 hours, 3.3 pT (c) 73 hours, 4.0 pT

(d) 73 hours, 8.8 pT (e) 76 hours, 5.5 pT (f) 77 hours, 3.7 pT

(g) 95 hours, 2.4 pT (h) 96 hours, 2.2 pT (i) 99 hours, 1.5 pT

(j) 172 hours, 3.8 pT (k) 172 hours, 1.9 pT

Figure 6.11 Field maps and anatomical geography for snapshot eggs

scanned: the period at which the strongest signals had been seen in developmental studies. The other two were about a week old. After scanning, microscopic examination of the excised embryos showed that development was normal in all eleven eggs. Again, the gross signal morphology was uncorrelated with the position and orientation of the embryo.

However, two of the magnetic field maps (figure 6.11e,f) showed some evidence of a localized feature or, at least, a distortion of the large-scale pattern at the location of the embryo. In both cases, the background bipolar pattern is clearly disrupted at the site of the embryo. I shall discuss these data again in section 6.6.2.

Two other short experiments were carried out on some of these eggs. Two eggs were rescanned after the embryo (with amnion and allantois) had been carefully excised. In both cases, the overall signal strength was substantially unaltered, although the pattern became somewhat distorted. When the composite membrane consisting of the vascularized yolk sac and the chorion was then removed from the yolk, however, the signals disappeared entirely.

Three eggs were used to try to detect the heartbeat. This was the only experiment, reported in this thesis, to measure a dynamic field and so the eggs were not scanned. A different data acquisition program was used, which collected 1024 data over a set period (usually a few seconds), performed a fast Fourier transform and calculated the signal power spectrum. The windowed eggs were placed so that the beating hearts were as close as possible to the dewar tip (several slightly different positions were used) and the spectra obtained were compared with ones recorded with no egg present. The visually observed heart rates were between 1.5 and 2.0 Hz, but no significant signal at this frequency (which was not also present in the corresponding noise spectrum) could be found.

6.5 Modelling the source as a distributed current density

This section concerns the modelling of the data reported in section 6.3.2. The primary currents generating the large-scale field patterns that were observed to be associated with all fertilized eggs were modelled as two-dimensional current density distributions.

In section 6.5.1, I shall review the observations that have been made and discuss what ionic processes might be giving rise to the fields. Section 6.5.2 describes how the method for modelling distributed sources, which was described in section 4.3, was applied to the measurements and in section 6.5.3, I shall present the results.

6.5.1 A physiological model

There are several reasons to suppose that the ionic processes responsible for the generation of the large-scale magnetic fields occur in the extra-embryonic membranes, most probably in the yolk sac or chorion.

Firstly, the fields are probably metabolic in origin. This was strongly indicated by the cooling experiments (section 6.2.1) and by the application of poisons [64]. Also, infertile eggs produce no fields when they are incubated. From this evidence, it seems overwhelmingly likely that the sources are located in the embryo or the extra-embryonic membranes.

There is *some* structural differentiation in the yolk of a fertile egg, but it is difficult to see how this could account for the observed external magnetic fields. At laying, there exist two types of yolk, white and yellow, distinguished by the size of the granules they contain. The most significant region of white yolk is the latebra (see figure 5.1), a vertical channel extending downwards from the blastoderm to the centre of the yolk. Longitudinal currents in the latebra would not be detected by a vertically axial gradiometer because their associated magnetic field would have no vertical component. The remaining white yolk lies in thin concentric shells within the predominant yellow yolk and the differentiation is believed to have no functional significance, existing merely as a relic of the daily accumulation of yolk during egg formation.

Secondly, the current patterns are not localized. Evidence for this comes from the highly complicated configurations of many of the field maps and from failed early attempts to model the data as a single current dipole. This procedure yielded improbably high dipole moments in a region of the egg (the centre of the yolk) where there is no known physiological activity. This observation tends to argue in favour of the yolk sac and chorion, which both extend over relatively large areas at time of the appearance of the fields, and against the embryo, amnion and allantois, which could be classed as 'localized' hypothetical sources in the existing context.

Thirdly, fertile eggs in which the embryo dies after only two days continue to generate magnetic fields. This evidence also favours the yolk sac and chorion, as they are the most active structures (in terms of growth) prior to this stage.

Fourthly, and most crucially, independent removal of (i) the shell, (ii) the albumen, (iii) the embryo and (iv) the embryo, amnion and allantois (in a more advanced specimen) does not result in the disappearance of the magnetic fields. Removing the yolk sac/chorion extinguishes them completely. Nevertheless, it is not possible to be certain that the embryo, amnion and allantois do not contribute, because their removal *alters* the measured field pattern.

Assuming, for the time being, that the source is located somewhere in the extra-embryonic membranes, the most likely mechanism by which the currents are propagated and sustained involves ion pumps. There are many examples [10], [54], [72] of ion pumps in epithelial tissue in various species driving substantial ionic currents in circumstances where there is some nearby tissue damage. Any distribution of pumps has this potential ability, which it can realize only when local ionic leaks in the tissue allow a circuit to be completed.

A mechanism based on a distribution of pumps and leaks in the extra-embryonic membranes could account very well for the observed currents. The germ layers, which differentiate on the first day of incubation, contain large numbers of ion pumps, and the membrane potential across the yolk sac has been shown [28] to be dependent on sodium concentration. Experiments to estimate the density of ion pumps in membranes [69] indicate that they are, in general, inhomogeneously distributed. This implies that when they are operating, they generate electric fields both outside and inside the epithelium, which act on the ions to generate ionic currents. The yolk sac has also been shown [28] to be leaky to sodium ions, particularly at its circular periphery.

Such a complex, inhomogeneous distribution of pumps and leaks would, undoubtedly, drive a similarly complex pattern of ionic currents. This, I believe, is the origin of the large-scale magnetic field patterns that have been observed.

6.5.2 Using the distributed source model

In this section, I shall describe attempts to model the observed currents using a distributed source algorithm [56]. My central assumption will be that the source distribution is confined to a partial spherical shell that approximately includes the region of metabolically active epithelia. Within this region, I shall make no assumptions about the sources.

There is a subtlety with the modelling. The model to be applied is framed in terms of a homogeneously conducting sphere and consequently, radial sources are invisible [26]. However, in reality, the egg includes regions of differing conductivities, and, in particular, there will be conductivity changes at the epithelia. This leads to a breakdown of the invisible radial source result.

Within the model, additional sources appear at the conductivity boundaries so that a radial primary source will be detected as a set of apparent tangential sources. This relationship is difficult to quantify in the absence of reliable knowledge of the conductivity distribution, but these 'secondary' sources will appear in the regions where the conductivity changes. It is, therefore, reasonable to choose a spherical shell as the source space, and the solution is likely to contain representation from both the tangential and radial components.

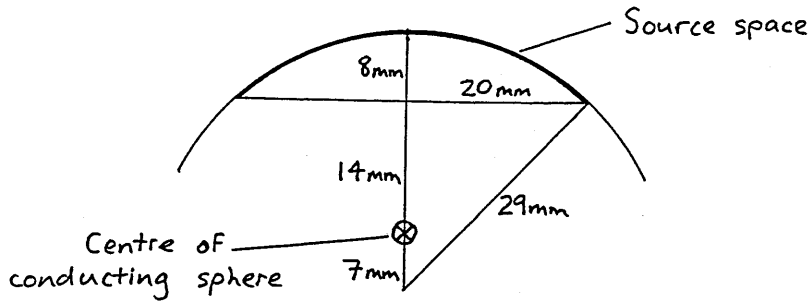

Figure 6.12 Geometry of the source space and conducting sphere

The parameters input to the model were as follows. The source space (see figure 6.12) was a single, two-dimensional spherical surface with a radius (when projected onto the x-y plane) of 20 mm. The curvature was defined by a solid angle of 0.55π steradians on a sphere of radius 29 mm.

The primary currents were constrained to flow within this space, which included all of the active physiology in the egg (viz the embryo and extra-embryonic membranes). The source space was positioned inside a conducting sphere whose centre was 22 mm below the apex of the source space. Specification of the centre of the conducting sphere (the space for return currents) makes the analysis fully general: varying the radius makes no difference to the solution [47].

For each map, a subset consisting of 81 datapoints mutually separated by 2 mm was

selected. Using the full data set slowed the algorithm, but caused no significant change in its predictions. It was desirable that the source space should relate to the embryo in a consistent way, and so the subset was always centred on the site of the embryo's heart. This ensured a consistent geometric relationship between the field data, the anatomy and the source space.

Finally, the depth of the source space below the detector had to be selected. As a trial, this parameter was allowed to vary while solutions were computed, for several of the field maps. On each solution (a current density distribution), the forward problem was carried out and the magnetic field obtained was compared with the original data. By calculating the correlation coefficient between these two data sets, it was possible to grade the fit of the data. The best estimate of the depth of the vertex of the source space was 8 ± 1 mm below the sensing coil. This was reassuringly close to the depth predicted on physiological grounds. It was 5.5 mm from the centre of SQUIDLET's sensing coil to the outer surface of the dewar, a further 0.5 mm to the highest point on the windowed shell and the depth below this point of the embryo (and hence, also, the highest part of the membranes) was about 1–3 mm. Having selected the data and all the required parameters, the inverse calculation was carried out.

6.5.3 Results

Data from the two series of egg measurements, whose isofield contour maps were illustrated in figures 6.8 and 6.9, were input to the model and the current density distributions obtained comprise figures 6.13 and 6.14 respectively. The scale of the maps is indicated by the scale bar. Arrow length is directly proportional to the computed current density at the centre of the arrow's shaft, and normalization has been carried out independently over each entire sequence of time slices. However, the renormalization procedure used in the probabilistic approach to the inverse problem inevitably loses information about absolute current density magnitude, and so the plots cannot be calibrated.

6.6 Discussion and implications

In this section, I shall consider firstly (section 6.6.1) the modelling of the distributed source. I shall then conclude the chapter by considering localized features that were present on a few of the field maps (section 6.6.2).

6.6.1 The distributed source

The current density images in figures 6.13 and 6.14 all fit the magnetic field data with correlation coefficients of 85–98%. There are also some general similarities with the magnetic field maps from which they were computed. The signal power follows the same profile, the current density distributions usually change smoothly from one latency to the next, but occasionally do so abruptly, and there is no consistent relationship between the orientation of the current density vectors and the orientation of the embryo. This truth of this last fact is again made evident by the constant embryo orientation compared with the variable direction of both the local and the overall current density.

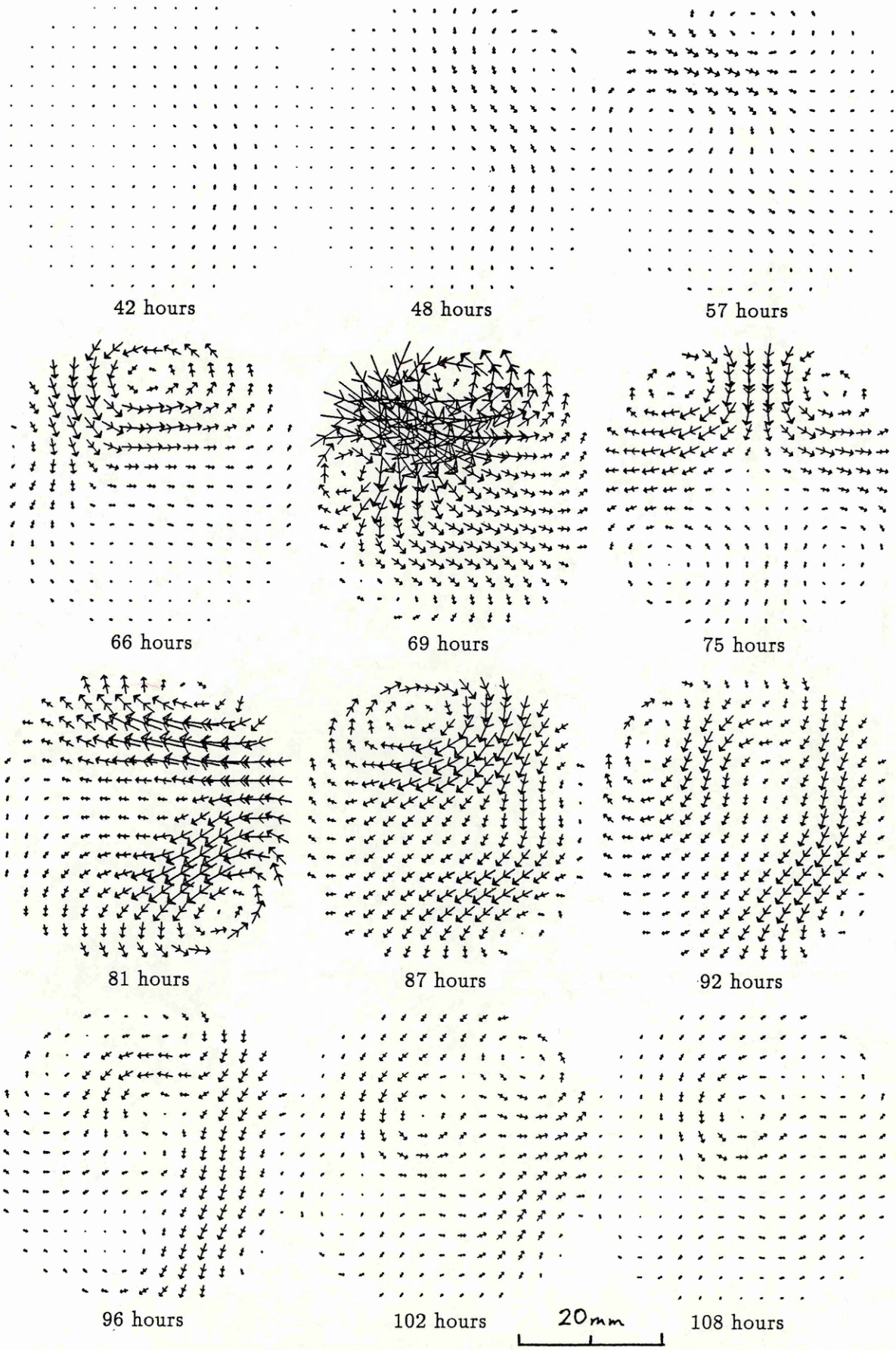

Figure 6.13 Current density distributions and anatomical geography for egg D1

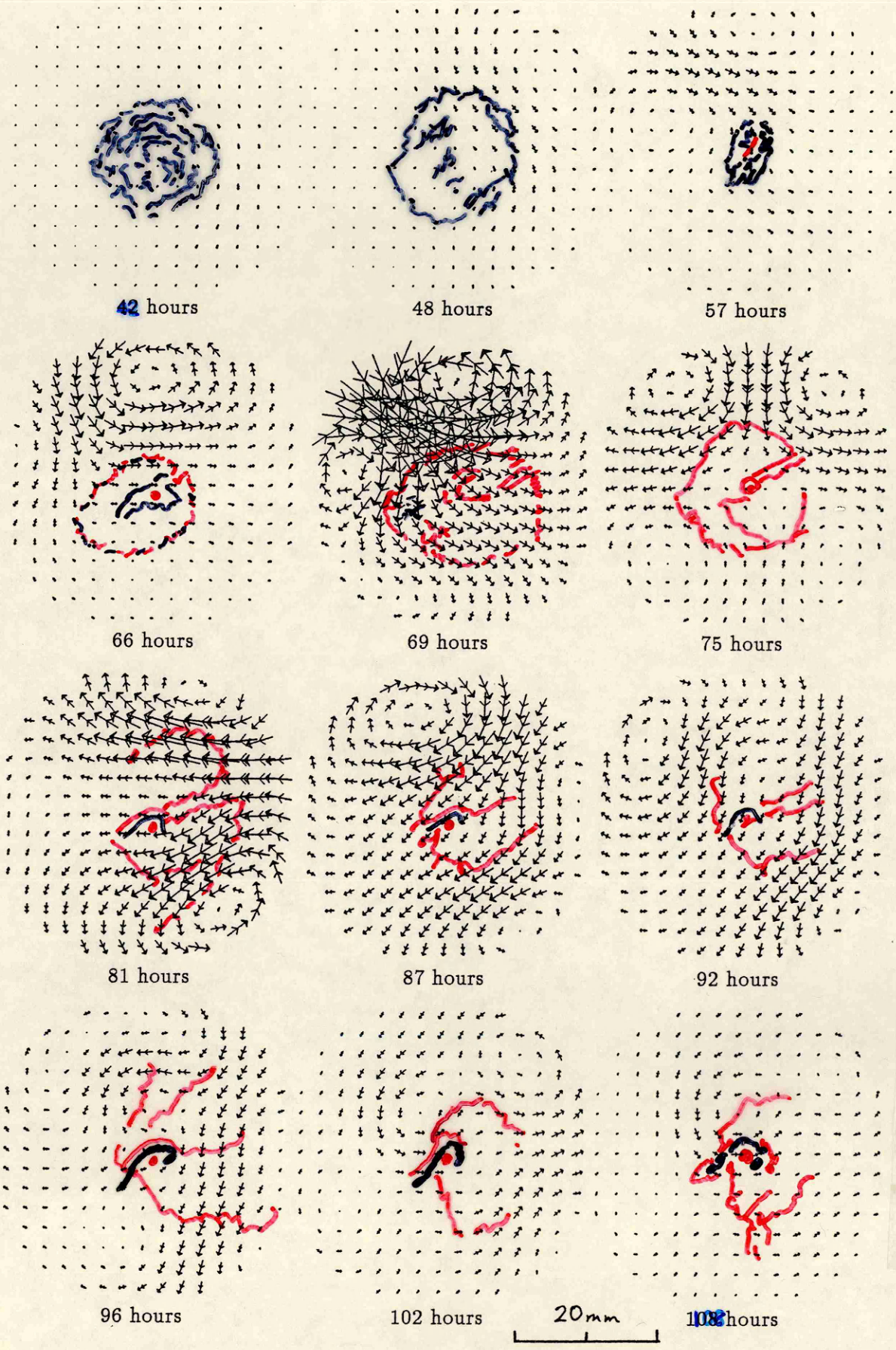

Figure 6.13 Current density distributions and anatomical geography for egg D1

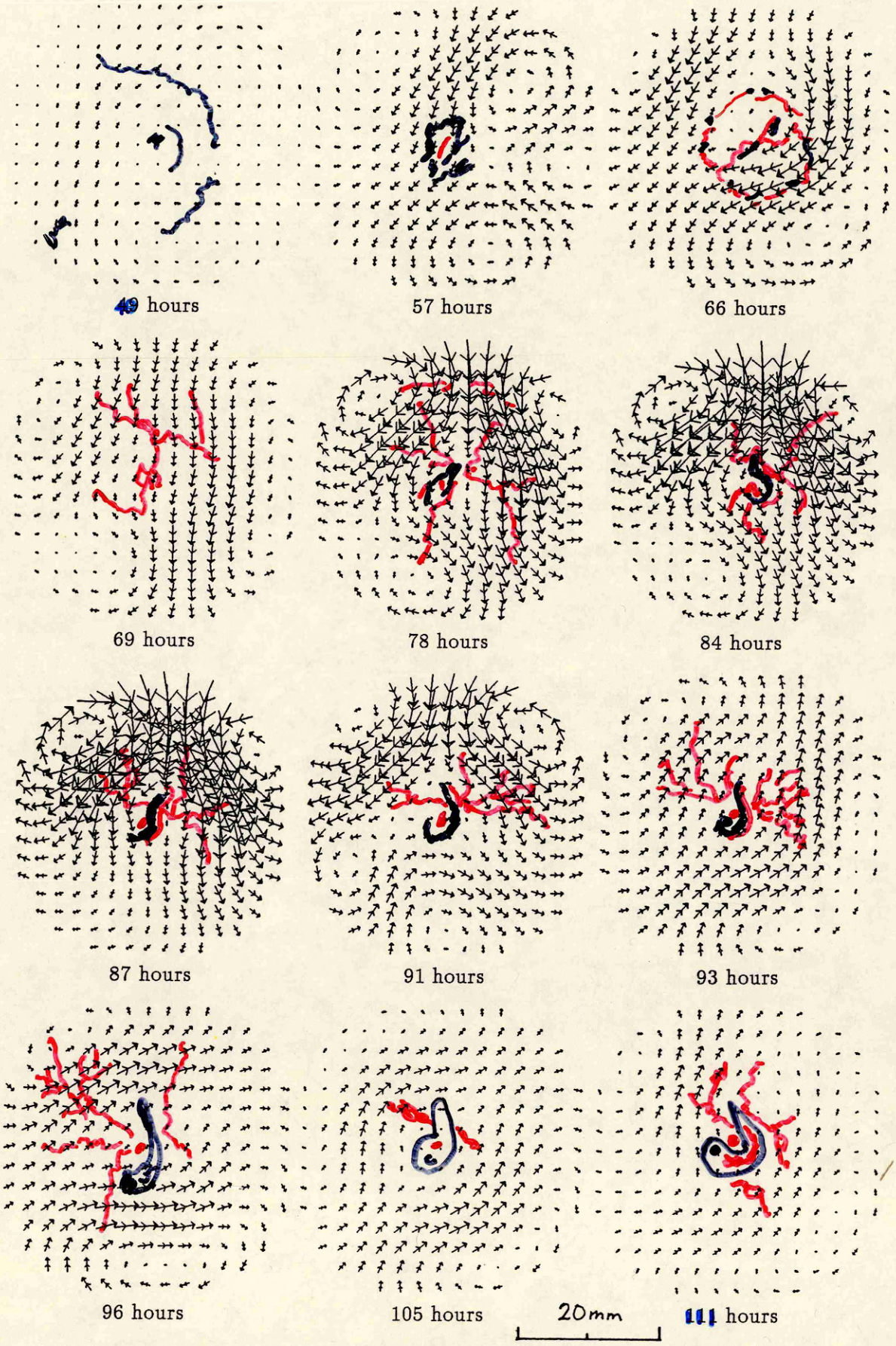

Figure 6.14 Current density distributions and anatomical geography for egg D3

p. 111

I wish to draw attention, once more, to one short sequence from each egg. Consider the current density maps corresponding to 69, 75 and 81 hours of incubation of D1, and those corresponding to 87, 91 and 93 for D3. These sequences contain the most abrupt changes in current density distribution. In both cases, the overall direction of the currents changes between the first and third maps with the second map containing contributions from both. A hypothesis that presents itself is that, at any one time, the observed current pattern is dictated by a particular configuration of currents or a region of activity, and occasionally an alternative process becomes dominant. When this happens, there is a 'transfer of power' that takes several hours.

Another interesting feature is that, on most of the maps, the current density is very low at the location of the embryo. In some cases, the main flow of current appears to bifurcate in order to avoid it. If the current flow is initiated in the extra-embryonic membranes, it is not unreasonable that, at the site of the embryo, the computed current density should be very low. This information is not obvious from the field maps.

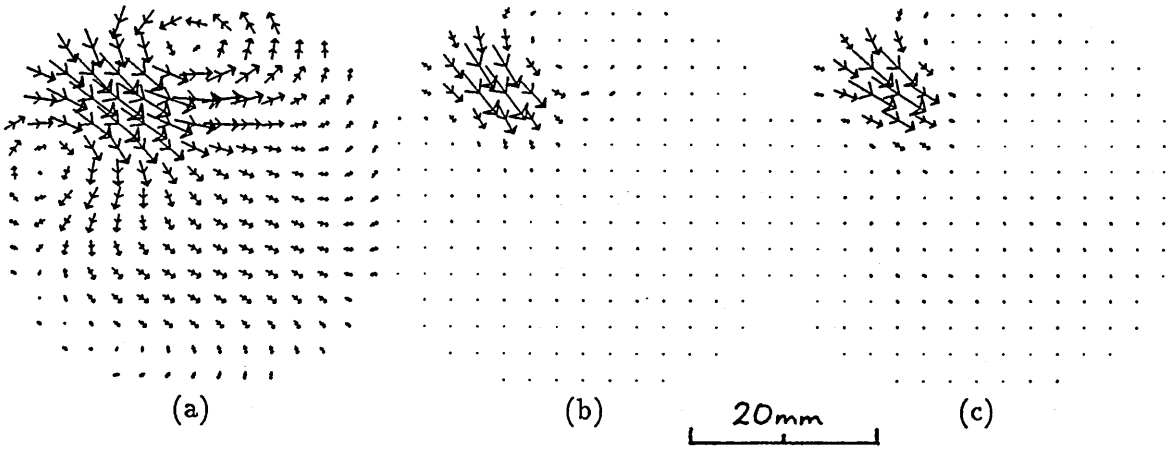

Figure 6.15 Solutions after zero (a), one (b) and three (c) iterations for egg D1 (69 hours)

Finally, consider figure 6.15 which shows the zeroth, first and third iterated solutions to the data recorded from egg D1 after 69 hours. These current density images were derived from the field map containing the greatest magnetic field amplitude of all those presented. The solution fails to become any more spatially localized after one iteration, and the correlation with the field measurements deteriorates with further iterations (data not shown). This behaviour contrasts with the result for a model current dipole field (see figure 4.1a), when the solution continued to converge to a more localized source, and the correlation with the data continued to improve. It is much more similar to that for the model 'distributed' source field (see figure 4.1b). This result strongly endorses the view that the source is distributed and not localized, and justifies the use of the distributed model described above.

I conclude that an inhomogeneous distribution of ionic pumps in the extra-embryonic membranes (probably the composite yolk sac/chorion) is balanced by leaks, probably through the peripheral membrane regions. The process is not initiated in an infertile egg, because the membranes do not develop. However, if the membranes are present, this ionic flow continues whether or not the embryo survives. As the number of pumps increases and the membranes grow in size, the field amplitude initially increases, but then cancelling effects cause the

pattern to become complex and reduce the overall amplitude.

There are two possibilities concerning the developmental significance of the current density patterns to the chick embryo. It may be that the magnetic field patterns, which have been observed, are entirely fortuitous, resulting from the ionic currents described above but not causally connected to the development of the chick. Alternatively, the relationship may be hidden deeper. Just as repeating the experiments with SQUIDLET demonstrated the inadequacy of the large detector, it may be that by looking even more closely at the magnetic fields, with a smaller coils and a smaller separation, an important correlation will become clear.

6.6.2 A localized source?

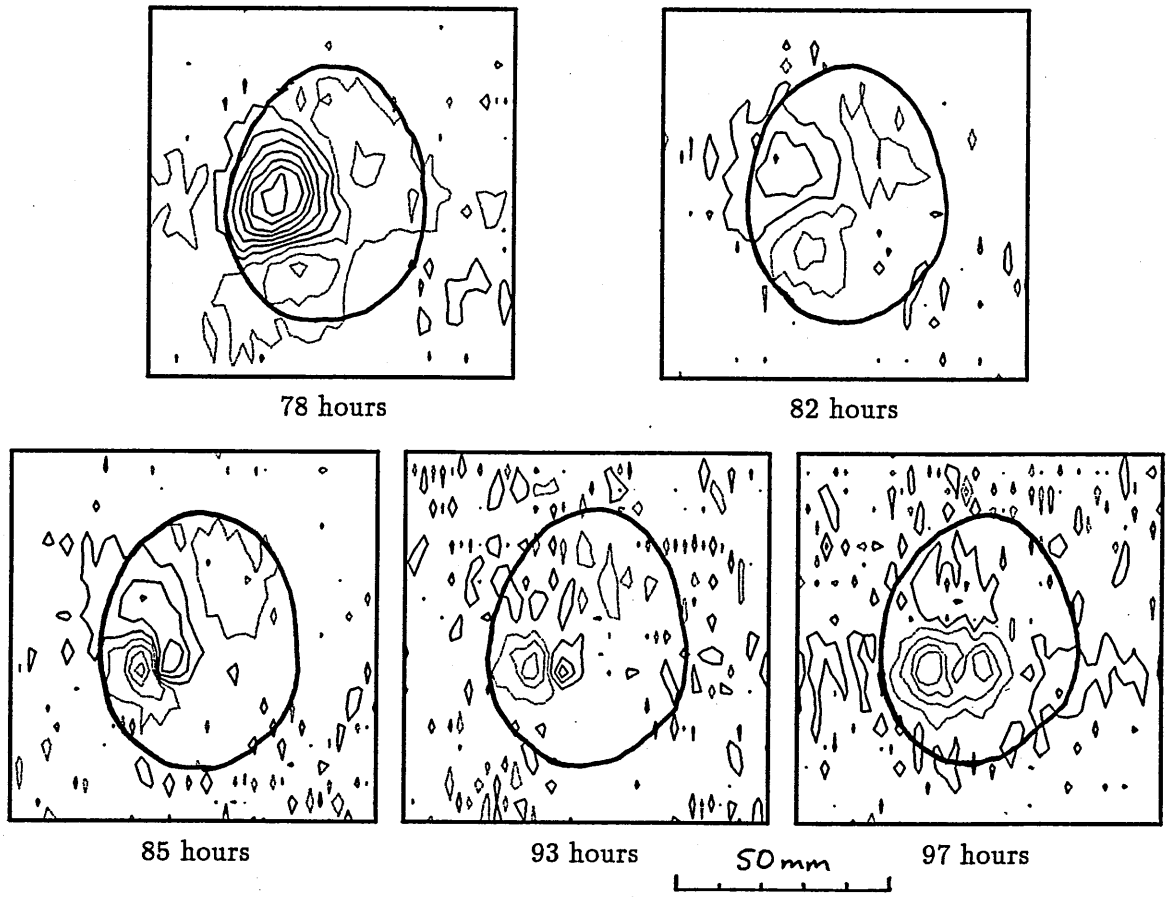

Figure 6.16 Sequence of field maps recorded from an unusual intact egg
Contour separation = 2.1 pT

I wish, finally, to present a particularly interesting sequence of field maps recorded from one intact egg (see figure 6.16). The first two maps show the decline of a complex, large-scale pattern, similar to those measured from other eggs, but somewhat earlier than has generally been observed. There then appears a highly localized bipolar feature. The extrema are separated by about 10 mm and so the generator must be very superficial. Perhaps this signal is generated by the embryo.

This appears to be similar to the localized signal recorded in two of the snapshot experiments (figures 6.11e,f). In those two cases, the localized perturbation to the background

field coincided with the location of the embryo very closely. A possible explanation for the rarity of the appearance of this signal is that it is usually masked by the stronger large-scale field pattern and that, only when the large-scale field is particularly weak, can the localized signal be seen.

With a further improvement in instrumental spatial resolution, it may be possible to image this feature. This will be the subject of chapter 7.

Chapter 7

Very high resolution measurements

In this chapter, I shall describe a further series of egg measurements that were carried out in the Department of Physics and Astronomy at Vanderbilt University, Nashville, USA. These experiments were made possible by the kind invitation of Professor John Wikswo.

The main purpose of these experiments was to obtain more detailed information about the localized source which was observed close to the embryo in a number of eggs investigated with SQUIDLET. To achieve this, it was necessary to improve the spatial resolution further. It was possible that this might also reveal an underlying pattern to the current distribution in the extra-embryonic membranes.

As stated in chapter 3, SQUIDLET had a smaller sensing coil and shorter 4 K—300 K separation than any other SQUID magnetometer when it was first operated in 1987. In 1989, however, it was superseded in both aspects by a new instrument, MicroSQUID[1] [17], which was installed at Vanderbilt University. After outlining the design of MicroSQUID in the next section, I shall describe the apparatus and software used in the experiment and the protocol adopted. In section 7.2 I shall present an analysis of the magnetic field data and, in section 7.3, I shall describe the modelling procedures that were applied. Section 7.4 is a discussion of the results of these experiments. Finally, in section 7.5, I shall review the subject of chick egg magnetometry.

7.1 Acquiring the data

7.1.1 MicroSQUID: a very high resolution magnetometer

SQUIDLET is close to being the highest possible resolution SQUID magnetometer of conventional design. Its resolution is limited by its 4 K–300 K distance which is defined by the thickness of the two fibreglass dewar walls and the vacuum space. Because the walls are in contact at the tip when the cryostat is warm, their separation is minimized. It is difficult to imagine how any significant improvement could be achieved without a radically new design.

A radically new design was precisely what was proposed in 1988 by Wikswo [105]. By thermally coupling the coils to a helium reservoir, but actually placing them in the vacuum, he removed from the equation giving the stand-off distance, one dewar wall thickness and most of the vacuum space. Figure 7.1a is a schematic illustration of this technique.

[1] Model 640 μSQUID^{TM}, Biomagnetic Technologies inc, San Diego, CA, USA.

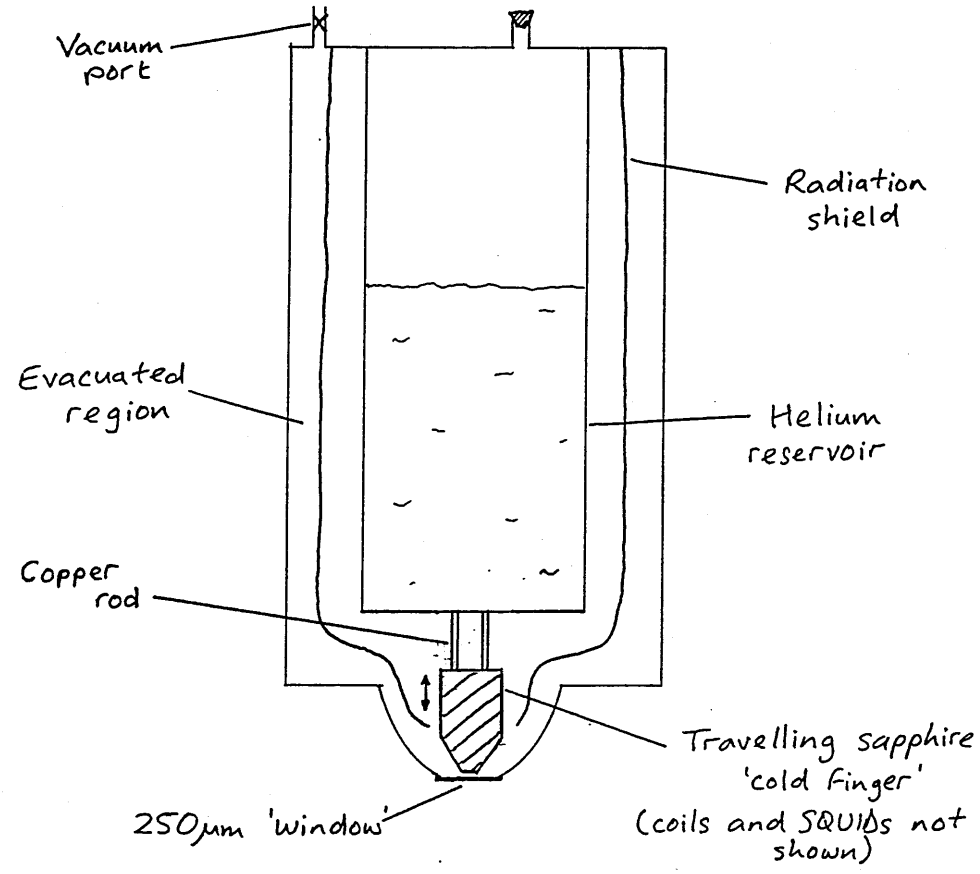

(a) Schematic diagram of MicroSQUID

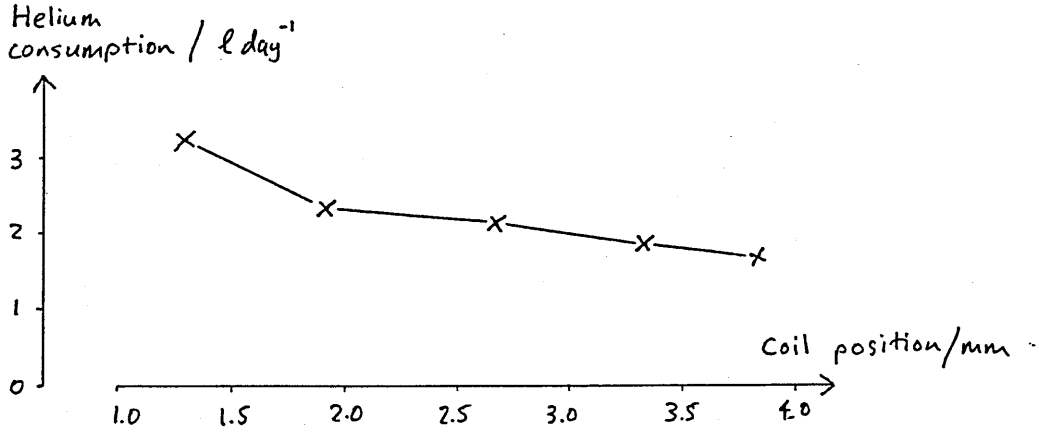

(b) MicroSQUID's helium consumption

Figure 7.1 A novel cryogenic arrangement

MicroSQUID's coils are mounted on a 'cold finger' machined from sapphire, which is thermally coupled to the helium reservoir, and is of sufficiently high thermal conductivity that the coils can be maintained in the superconducting state. The cold finger travels vertically over a distance of 4 mm relative to the reservoir, actuated from outside the dewar by a screw. When the instrument is not in use, the coils can be backed off to their highest position to reduce helium losses. Figure 7.1b shows how helium consumption varies with the position of the coils.

In order to achieve the minimum stand-off distance of about 1.4 mm, the cold finger is lowered until the sensing coil rests on the 250 μm thick fibreglass/epoxy 'window' which forms the tip of the dewar. Heat influx makes the coils go normal, but when they are backed off fractionally they once again become superconducting, as can be verified by observing the SQUID transfer function.

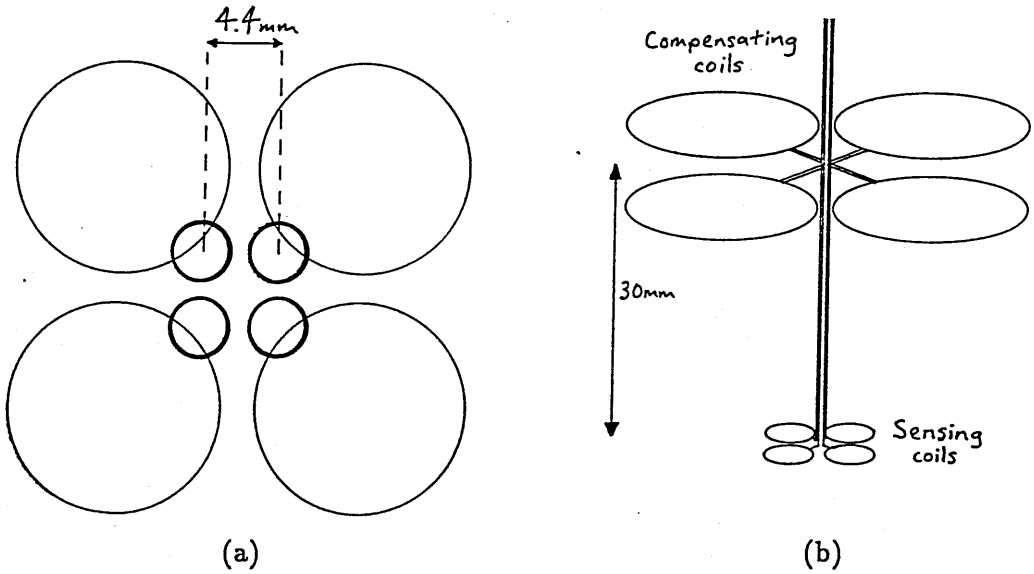

Figure 7.2 Plan (a) and isometric drawing (b) of MicroSQUID's gradiometers

MicroSQUID is actually a four channel instrument (see figure 7.2), incorporating standard BTi dc SQUIDs. Each 16-turn 3 mm sensing coil is balanced by a single 12 mm compensating coil and the baseline is 30 mm. For each channel, the axes of the sensing coil and the compensating coil are parallel but not colinear. This absence of common gradiometer axes produces some interesting variations between the channel outputs when simple model sources are scanned, as will be seen in section 7.1.3.

The first order gradiometer has a short baseline, but would still be unacceptably sensitive to external noise were the entire system not mounted in a shielded room (see figure 7.3). The external dimensions of the shield are approximately 0.9 m $\times$ 1.5 m and it is about 1.8 m high. The walls consist of (from the outside inwards) half-inch aluminium, sixteenth-inch μmetal, six inches of sand (to damp vibrations), half-inch aluminium, sixteenth-inch μmetal. A removable door, about 40 cm $\times$ 30 cm allows access from the front.

Figure 7.3 The Vanderbilt University shielded room

7.1.2 Auxiliary apparatus

In this section, I shall describe the scanning mechanism, the adjustable platform for supporting the egg inside the shield, and the apparatus for recording anatomical information and relating it to the magnetic field data.

About 50 cm below the dewar tip is an x-y stage. The stage can be manoeuvred within a 50 mm × 50 mm square area by two orthogonally mounted motors[2]. The motors can be operated interactively or under computer control: they move the stage uniformly at approximately 2 mm s^{-1} with negligible ramping time or backlash. After initializing the system, any desired pattern of x-y movement can be programmed, and the motors are then switched on and off according to the program and the stage position. This software runs on a microcomputer[3] located outside the shield, which also controls the recording of data from the four channels of the magnetometer.

Several different programs of stage movement/data collection were used. The two main ones, both of which covered the entire available area, were called 'snake6' and 'snake51'.

[2]Model 7000 Inchworm™ motor controller, Burleigh, Fishers, NY, USA.
[3]Zenith Data Systems, St Joseph, MI, USA.

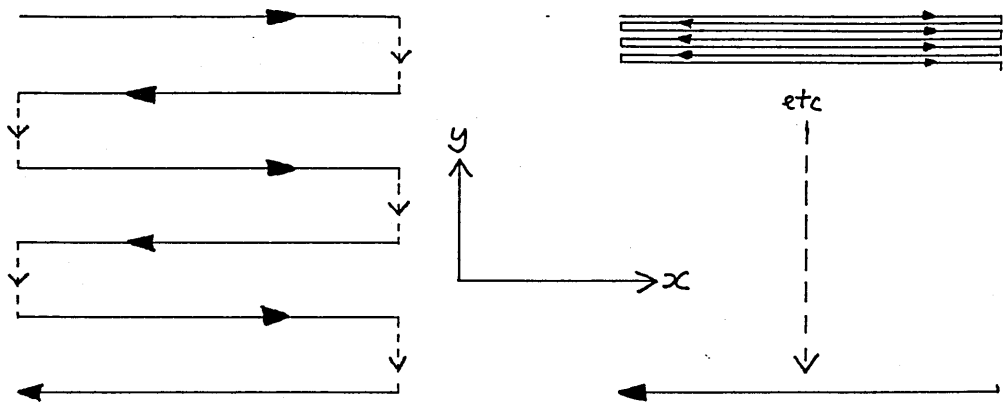

(a) 'Snake6' (b)'Snake51'

Figure 7.4 Scanning programs

The former, consisting of six scans parallel to x and mutually separated by $\delta y = 1$ cm, was suitable for noise runs and quick checks, while 'snake51', with fifty-one scans separated by $\delta y = 1$ mm, was used for collecting the high resolution data for analysis (see figure 7.4). Although, in reality, the stage was moving and the magnetometer stationary, these diagrams show the motion of the magnetometer in the stage's reference frame, as is conventional for ease of interpretation. In both programs, travel in the $\pm$ x-direction and data collection were triggered simultaneously and 1024 values were then recorded at a sampling frequency of 40 Hz. To avoid aliasing and remove high frequency noise, a 20 Hz low-pass filter was used. No data were recorded while the y-motor stepped to the next scan position and then the x-motor and data collection were once again triggered.

In order to maximize the advantage of MicroSQUID's short stand-off distance, it was desirable to position the egg as close as possible to the dewar tip and so, a variable-height platform was constructed from cherry wood, incorporating a plastic jack (see figure 7.5a). This was bolted to the stage and the platform could be raised or lowered with the jack. Once the height had been set, locking nuts were used to secure the whole structure rigidly.

The egg support consisted of three 15 cm vertical glass rods glued into a block of wood which located in a dovetail holder on the top of the platform. This facilitated easy removal and replacement and so, several such supports were made and the eggs were glued to the tops of the rods during the experiment (see figure 7.5a). All components were checked for contamination. Because of their distance from the sensor, any contamination sources in the wood or jack would produce signals with a very low spatial frequency.

The central objective of the experiment was to relate the magnetic field pattern from the egg to the position and orientation of the embryo. To facilitate this location process, a replica of the dovetail holder was fitted into a frame on the benchtop. This frame incorporated an adjustable transparent sheet on which was drawn a millimetre grid. With the windowed egg on its support in *this* holder, and the grid position calibrated, a camera on a tripod recorded the position and orientation of the embryo in relation to the grid (see figure 7.5b). I shall explain how the grid position was calibrated in section 7.1.3.

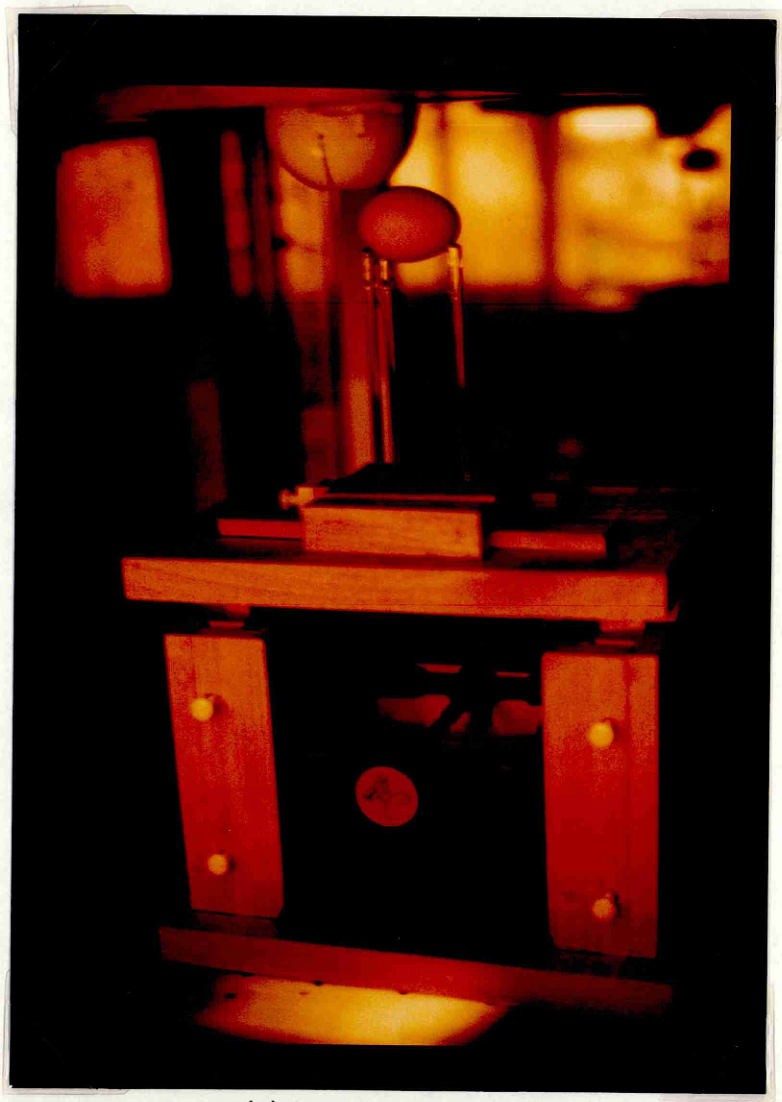

(a) Scanning apparatus

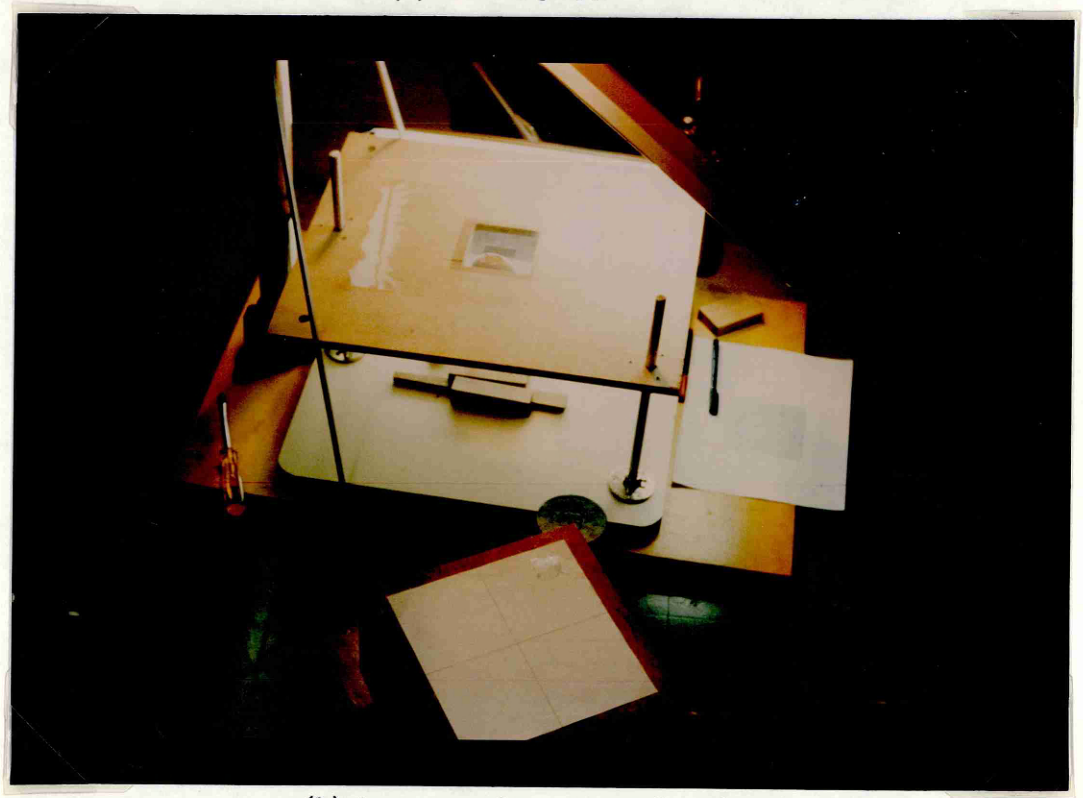

(b) Apparatus for anatomy location

Figure 7.5 Experimental arrangement

120

7.1.3 Experimental protocol

Eggs were obtained from a commercial hatchery and were refrigerated at 8°C until the start of incubation. They were incubated at 38°C and 60% humidity and were rotated by 45° every 6 hours up to the time they were scanned. Ten eggs were used for preliminary scans to permit familiarization with the instrumentation, design of new apparatus and the development of a valid protocol. Twelve eggs, whose incubation periods varied between 61 and 104 hours, were then scanned intensively. The results for these eggs will be presented in section 7.2.5.

The normal protocol was as follows. An unused support, consisting of a dovetail block and three glass rods, was scanned using the program 'snake6' to check for contamination. The selected egg was then glued with a fast-bonding epoxy adhesive to the tops of the rods in the same orientation as that in which it had been resting. The egg, on its support, was then returned to the incubator for five minutes. There was no evidence of any adverse developmental effect due to the glue.

When the glue had set, the egg support was placed in the holder inside the shield and securely fixed with a dovetail wedge. Using a plastic feeler gauge, the height of the platform was adjusted so that the highest point of the eggshell was 0.5 mm below the tip of the dewar. The locking nuts were then tightened, making the whole structure rigid. The lateral position of the platform had already been set so that the area of measurement was approximately centred on the egg. The shield door was fitted, the Burleigh motors and SQUIDs were reset and the 'snake51' program was started.

Each scan at a single y-position took about 25 seconds, and then a similar period was required to allow the data to be filed and for the stage to move to the start of the next scan. Consequently, the total time for the mapping was about forty minutes. As reported in section 6.2.1, the signal amplitude was reduced by a significant degree (about 20–25%) if the egg was kept outside the incubator for such a long time in the Open University laboratory. This was attributable to the slow-down of metabolism at the lower temperature. However, the confined space of the shielded room would allow very little air movement and had a higher ambient temperature, and so we supposed that the problem might not be so serious in the Vanderbilt University laboratory. According to Patten [79], development and metabolism continue, albeit at a slower rate, at temperatures below the optimum 38°C, but all processes cease below about 21°C. The temperature was always greater than this.

Clearly, the possibility that the signals changed significantly during the 40 minutes mapping time had to be investigated and so another scanning program, 'midscan' was run after each mapping. This consisted of a single repeat of scan 26, the central one, where the signal was expected to be strongest. As will be shown in section 7.2.2, the signal attenuation, while just noticeable in most cases, was not significant.

When the magnetic field had been recorded, the egg was removed from the shield and (still glued to the support) windowed. The position and orientation of the embryo and blood vessels do not vary as long as the egg is handled carefully and its orientation with respect to gravity is maintained[4]. The windowed egg was then photographed with the calibrated

[4] As a departure from the normal protocol, two eggs were windowed prior to scanning, and it was confirmed that the anatomical arrangement did not vary during the scanning procedure.

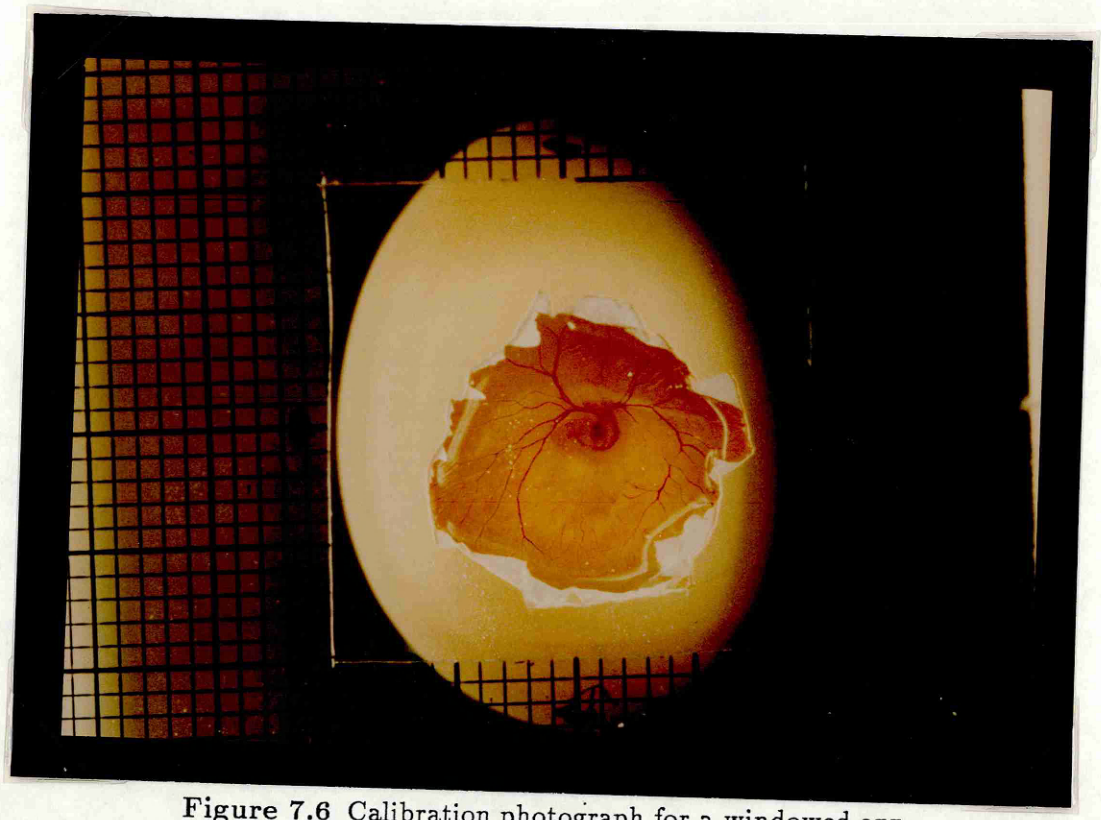

Figure 7.6 Calibration photograph for a windowed egg

grid transparency superposed. The important anatomical details were also drawn on graph paper with the aid of the grid. Figure 7.6 shows an example of a photograph of one egg. For clarity, a grid in which the central region had been removed was used for the photographs, whereas an intact grid was required for the drawings.

The embryo was then excised from the egg and studied microscopically under dark field illumination. Its development was staged according to Lillie's system [51].

In order that the photographs and drawings of the embryo could be related to its magnetic field map, a box carrying a pair of mutually perpendicular cross-wires was mounted on an identical dovetail block to those used in the egg supports. At the start of the series of experiments, the position of the grid transparency was calibrated by fixing this box in the benchtop apparatus and viewing from above. Then, after each egg had been scanned, the box was fixed in the holder beneath the magnetometer *without unlocking the platform* and a 5 Hz, 0.5 mA peak to peak sinusoidal current was passed to each wire in turn. When the wire parallel to the x-axis was energized (program 'wirey'), data were recorded during two scans in the y-direction, and vice-versa for the other program, 'wirex' (see figure 7.7a).

The magnetometer output was sampled at 80 Hz and by integrating over each half-cycle of the current waveform, the signal modulus was derived as a function of scan position. The point at which this function fell to zero, corresponded to the point at which the energized wire lay beneath the coil.

Figure 7.7b shows the form of these functions. An interesting feature was the asymmetry observed for channels 2 and 4 with 'wirex' and for channel 3 with 'wirey'. The lack of a common gradiometer axis accounted for this effect.

An infinite line current fitting procedure [94], which took full account of gradiometer

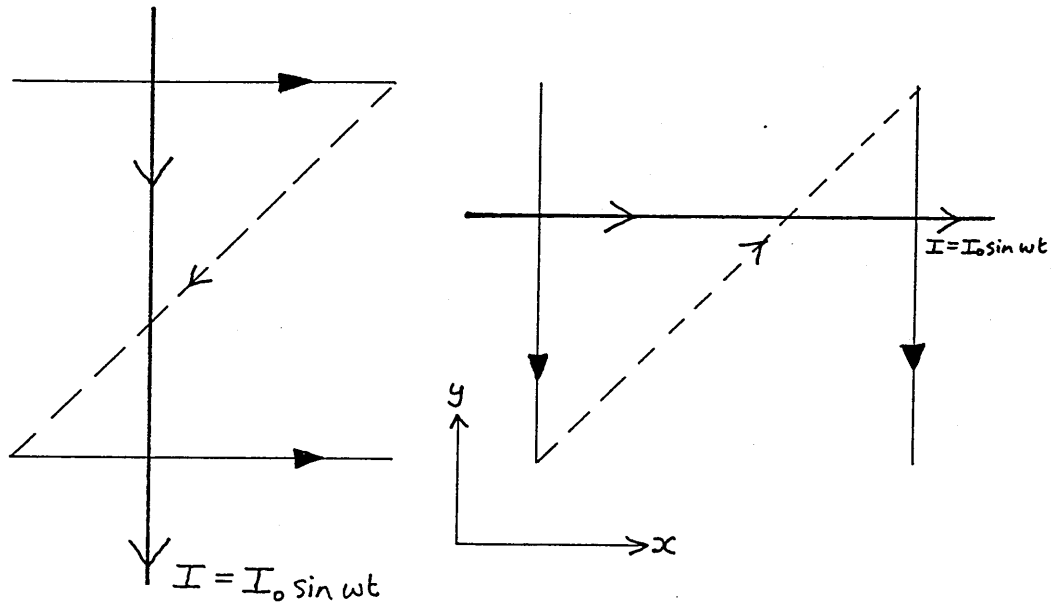

'Wirey' 'Wirex'

(a) Scanning programs for calibration

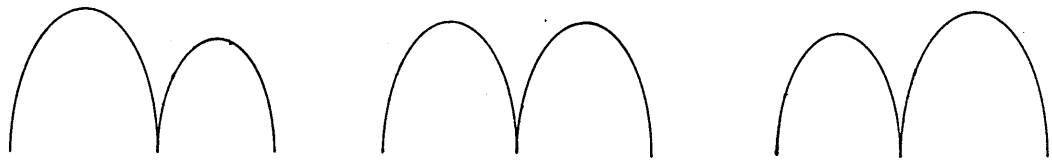

Channel 2 Channel 3 Channel 4

(b) Modulus functions recorded with 'wirex'

Figure 7.7 The calibration procedure

configurations was applied to the data to deduce the lateral location and depth of the wires. Taking care with the transformation of reference frames, it was then possible to relate the field map to the anatomical map. None of the potential sources of error introduced an uncertainty greater than 0.5 mm and the entire procedure was accurate to better than 1 mm.

The results of this procedure indicated that the coils of channel 4 were slightly lower than the other coil sets. The discrepancy was typically 0.05 mm suggesting that the gradiometer system was tilted with respect to the scanning plane by about 0.5°.

7.2 Analyzing the data

In this section, I shall make a preliminary analysis of the data and describe various procedures that were carried out to ensure accuracy and remove artefacts. I shall then present and interpret the corrected magnetic field data.

Although MicroSQUID is a four-channel instrument, the SQUID for channel 1 did not

remain in flux-locked mode, making measurements impossible. This may have been due to a fault in the feedback circuit or to the gradiometer being badly out of balance. Figure 7.8 shows the arrangement of the three functioning channels in the laboratory co-ordinate system.

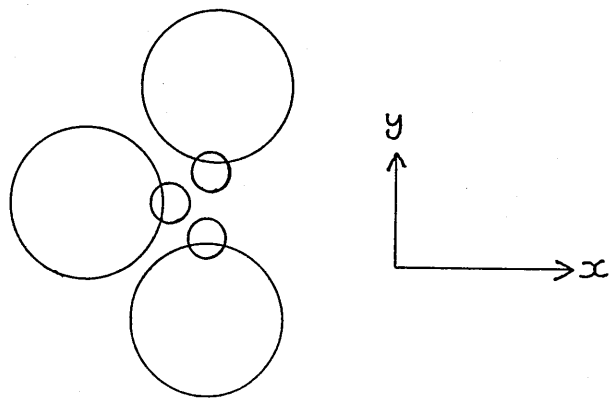

Figure 7.8 Plan view of the three functioning channels

7.2.1 Noise and initial measurements

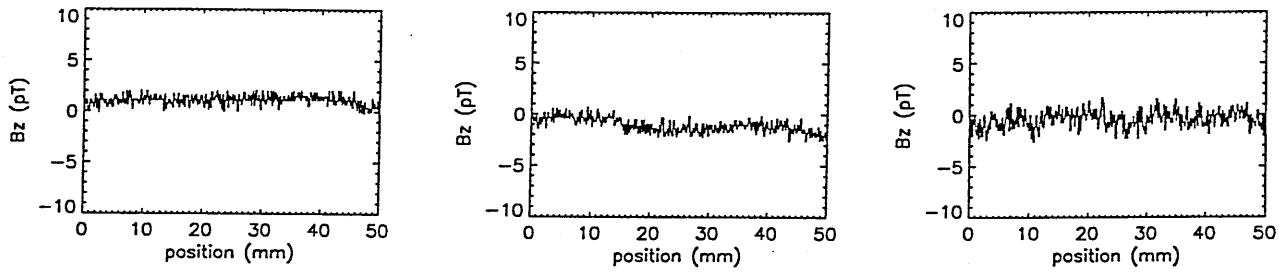

(a) 10 mm below dewar; door open

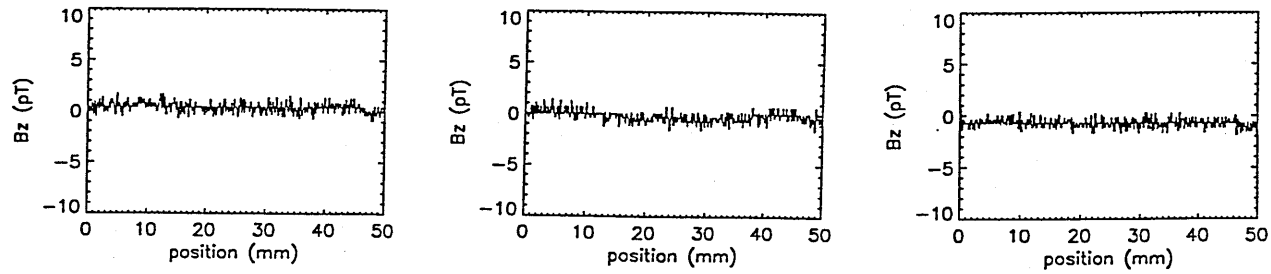

(b) 30 mm below dewar; door closed

Figure 7.9 Contamination scans (B_z against x)

The wideband noise of the system was measured and found to be approximately 0.1 pT $Hz^{-1/2}$, with a slight improvement when the shield door was fitted. The performance of

channels 2 and 3 was usually a little better than that of channel 4. This field noise was about one and a half times worse than SQUIDLET's, but a rough calculation[5] indicated that the overall signal-to-noise ratio for a typical egg would be better for MicroSQUID.

All the components of the adjustable-height platform and the egg supports were checked for contamination. Figure 7.9a is a scan across the centre of one support with the tips of the glass rods passing about 10 mm below the dewar tail. Although the surface had been thoroughly cleaned, there was still some evidence of a little contamination in the glass. In an actual experiment the rods would be expected to be at least 30 mm below the dewar and figure 7.9b shows the same scan, but with the rods lowered to this depth and with the shield door fitted. This level of noise and contamination was considered satisfactory.

Figures 7.10a,b show scans recorded from an egg that had been incubated for 75 hours. The first set (a) was recorded within a few minutes of removal from the incubator and the second set (b) (over the same position on the egg) about forty minutes later. The scans show an enormous improvement over SQUIDLET in the signal-to-noise ratio and also demonstrate the value of a multi-channel instrument: there is a clear difference between the field profiles measured along parallel scans about 3.1 mm (one sensing coil diameter) apart. Furthermore, the attenuation of the signal over a period roughly equivalent to a full mapping was only about 10% and there was no change in the signal shape. Most significantly, though, the scan picked out, with great clarity, a highly localized feature superimposed on a background pattern. This is precisely what was suggested by some of SQUIDLET's data from embryos of the same approximate age.

The metabolic origin of the signals was demonstrated with another egg after 88 hours of incubation. Figure 7.10c is a scan across a central part of the egg shortly after removal from the incubator and figure 7.10d is a repeat of the same scan after the egg had been refrigerated at 8°C for fifty minutes. At this lower temperature, the signal attenuation is 75%. If the egg had been refrigerated for long enough for it to cool completely to 8°C, no activity would have been expected.

7.2.2 Constancy of the source

Using the data recorded with 'midscan', it was possible to compare, on all eggs, two field profiles at position 26, recorded about twenty minutes apart. Figure 7.11 shows typical examples for three of the eggs. The lower trace is the original scan and the upper trace is the 'midscan' repeat. As had been predicted from the preliminary experiments, there was a slight decrease in signal amplitude, but in all eggs except one[6], the overall shape of the signal was unaltered and the change in amplitude was less than 10%.

Features of the field maps will be represented slightly more strongly at the top of the map than at the bottom, but not to a significant extent.

[5] Assuming a dipolar source 2 mm below the surface of the shell, MicroSQUID's coils would be 4 mm away as opposed to 8 mm, giving a fourfold increase in field strength. Sensitivity is further enhanced by having 16 instead of 14 turns, but the coil area is reduced by a factor of 9/16. Combining all these factors indicates that the flux signal strength for the dipole would be increased by about two or three times.

[6] The results from this anomalous egg will be discussed separately in section 7.2.5.

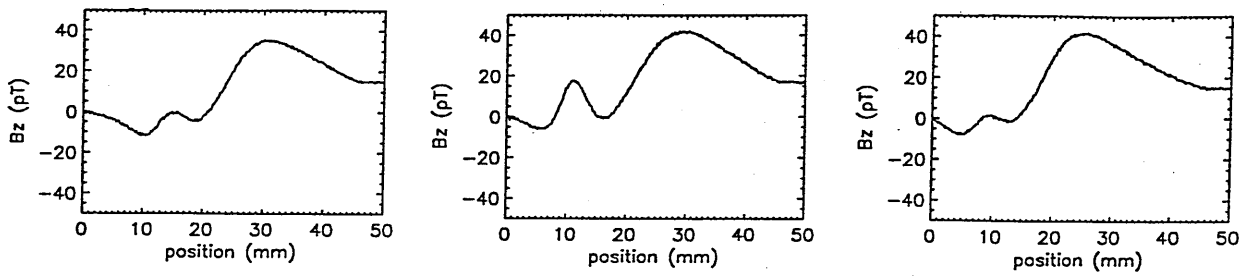

(a) EGGV2: On removal from incubator

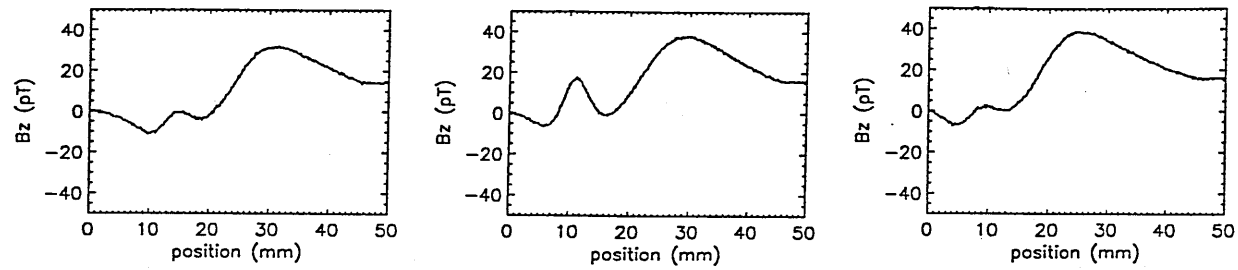

(b) EGGV2: Forty minutes later

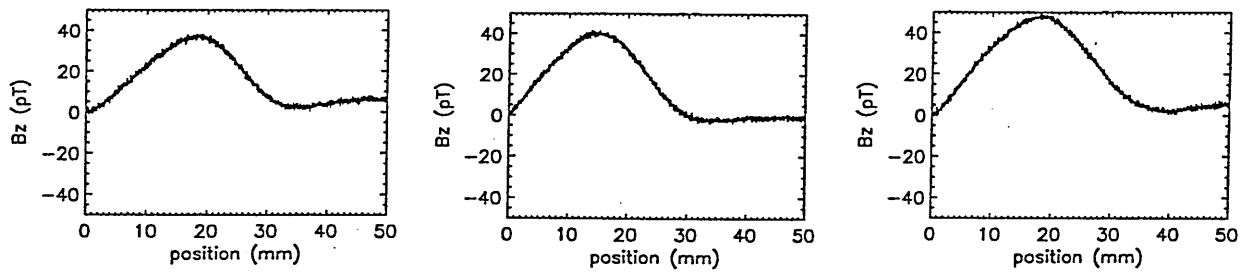

(c) EGGV5: On removal from incubator

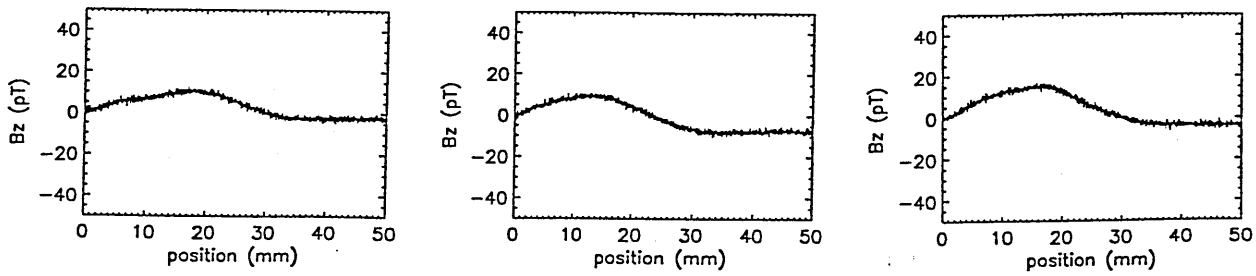

(d) EGGV5: After fifty minutes refrigeration

Figure 7.10 Examples of egg scans (B_z against x)

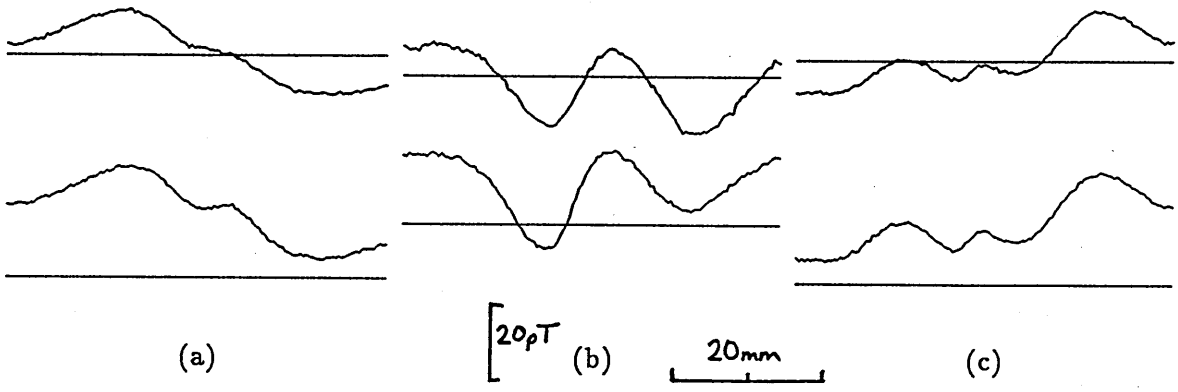

Figure 7.11 Three examples of the repeated 'midscan'

7.2.3 Isofield contour plots

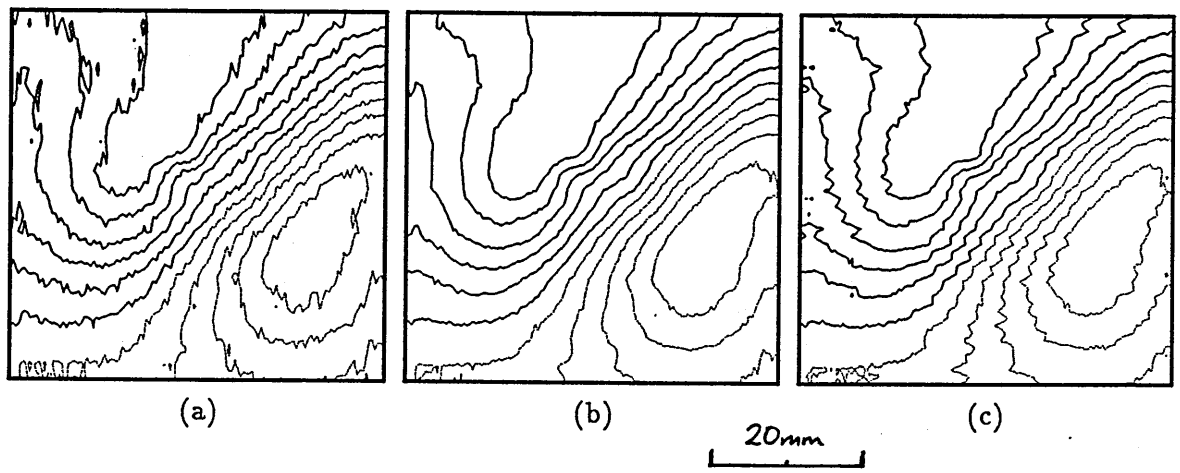

Figure 7.12 Presentation of the data
(a) Individual data selection (26 scans)
(b) Spatial averaging (26 scans)
(c) Spatial averaging (51 scans)

Data from the eggs were then plotted as magnetic field contour maps. Because of limitations of computational speed and capacity in the graphics programs, it was not possible to include all of the data. In figure 7.12a, every eighth data point was selected and plotted, whereas in 7.12b, each scan was spatially averaged in groups of eight data. The effect of spatial averaging is to smooth the signal (in this case over a range of about 0.4 mm) and this method was adopted for presentation purposes. However, raw data were used for modelling (section 7.3).

In figures 7.12a,b and subsequent contour maps, only the 26 odd-numbered scans were used (ie those involving magnetometer movement in the + x-direction). This use of a subset of the data was necessary because of a slight discrepancy ($\approx 1\%$) between the period of data collection and the time taken by the motor to traverse a scan. This introduced an offset between the computed x-positions in the odd and even scans. The effect of using all 51 scans is illustrated in figure 7.12c.

7.2.4 Baseline corrections

The peak to peak signal amplitudes of the thirty-six field maps (three channels for each of twelve eggs) varied between 26 pT and 110 pT. In the weaker maps (eg figure 7.13a), a slowly changing background field was very apparent, with the egg-related signal superimposed. The form of this background signal was a roughly uniform gradient in the z-component of the field of about 500 $\mathrm{pT\,m^{-1}}$. The gradient was directed from the bottom to the top of the map. Its source may have been deep magnetic contamination, on the moving stage for instance, or drift in the SQUID electronics (since the magnetometer moved from top to bottom during mapping). Re-examination of the midscan data reinforced the latter theory, for, in almost all cases, there was a substantial negative baseline shift of 10–20 pT between these maps (see figure 7.11).

From a pragmatic point of view, it did not really matter what was the cause as long as it could be adequately modelled and eliminated. Using a least squares iterative perturbative fitting algorithm [55], the source of the background drift/contamination signal on the map associated with EGV23 was modelled as a magnetic dipole with components in the x-y plane only, deep below the detector. The dipole was initially placed at a depth of 30 cm below the centre of the measurement plane and oriented parallel with the positive y-axis. Twelve peripheral data points were selected, avoiding the (presumably) egg-related feature in the centre (figure 7.13a). After three iterations, the model converged and a good fit was obtained. The procedure was repeated, including an additional twelve points from the periphery of the same map. As a final check, twenty-four points from another map (EGGV8) in which the egg-related signal was also weak, were used. In all three cases, a very similar result for the 'best fit' position, orientation and strength of the magnetic dipole was achieved, in the range 30–35 cm below the measurement plane and within its 5 cm × 5 cm area. Consequently, the possibility that the signal was due to contamination on the apparatus could not be ruled out.

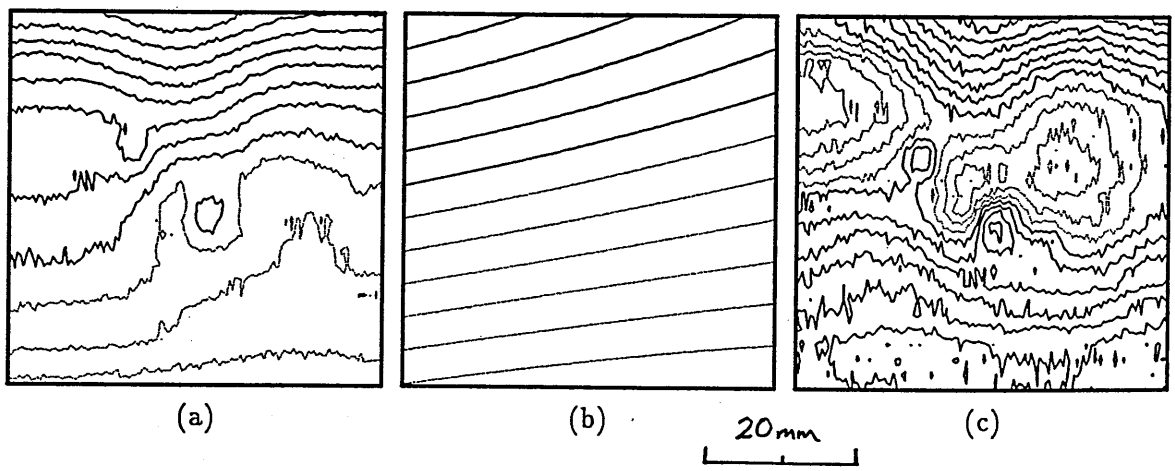

Figure 7.13 Removal of the background drift
(a) The original data (contour separation = 2.6 pT)
(b) Reconstructed field map of the best-fit source (2.8 pT)
(c) Clean data (1.3 pT)

The field due to this equivalent magnetic dipole was then computed at *all* the measure-

ment sites (figure 7.13b) and subtracted from the original data to give the map shown in figure 7.13c. Although this appears to be considerably more noisy (because of the auto-scaling of the contours), the localized egg-related features have in fact been enhanced. The background field was then subtracted from maps of all the eggs, taking care to sample the field at the correct locations for the different channels. This use of a background signal identified from just two maps, in the data from all the eggs is justified by the observed similarity of the drift and the probability that the contamination (if present) was the same in every case. As expected, there was little visible effect on the maps containing strong egg-related signals, but as has been demonstrated, the drift in absolute field between the top and bottom of the weaker maps was largely removed.

The final operation performed on the data was to zero-average the maps. When SQUIDLET was used to map the eggs, the scans were so wide (30 cm) that the signal due to the egg could safely be assumed to have fallen to zero at the edges. Data at both ends of the scan were then set to zero, and a linear correction term was added to all the values in-between. It was quite clear from the MicroSQUID maps that the signal of interest did not fall to zero at the edges, and so the baseline level was unknown. In particular, some maps consisted entirely of negative values, simply because of the states of the SQUID outputs at the start of scanning.

It was assumed that the net flux over the measurement area was really zero and all the maps were baseline-shifted to satisfy this condition. While not fully justifiable, this approach was the best that could be done. Unfortunately, baseline information was an item that had been traded for the great improvement in spatial resolution. The effect of this ignorance on the modelling is not profound; it will be investigated in section 7.3.1.

Figure 7.14 illustrates that the only significant difference between the field maps recorded by the three channels from the same egg is a simple translation of coordinates corresponding to the precise locations of the gradiometers with respect to the specimen. A close examination of the numerical data revealed that the peak to peak amplitudes in the maps recorded by channel 4 were consistently the highest by a few percent providing further support for the hypothesis that the plane of the gradiometer sensing coils is slightly tilted.

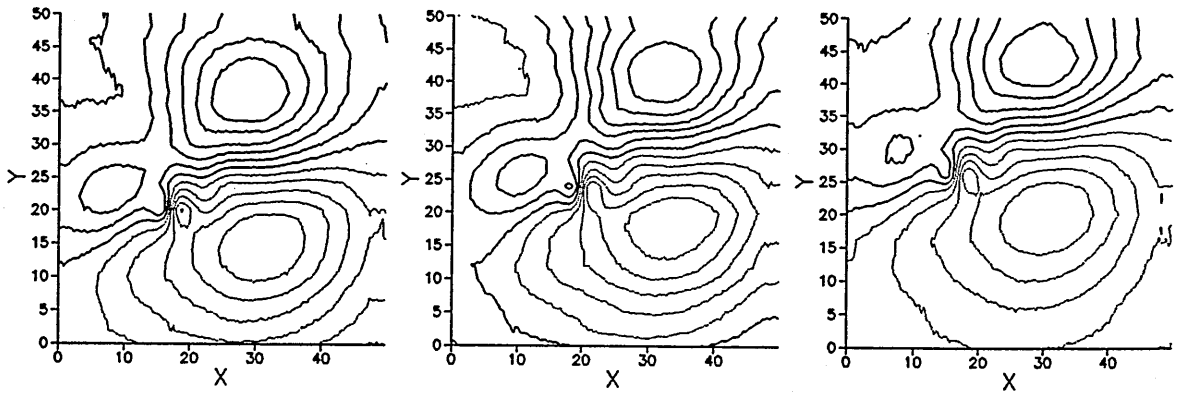

(a) Channel 2 (b) Channel 3 (c) Channel 4

Figure 7.14 Comparison of field maps recorded by each channel

7.2.5 Summary of results

In this section, I shall present and analyze the corrected magnetic field data. One map recorded from each egg is displayed in figure 7.15 which has an overlay containing the anatomical information. All eggs were oriented with the sharp end pointing to the right. In each case, the channel with the lowest noise was selected for presentation.

Normal development was verified in all except two of the eggs: EGV19 and EGV20. EGV19 probably developed normally but was not windowed, and in EGV20 no embryo was visible. Nine of the ten embryos exposed lay on their left side and in six, the antero-posterior axis lay transversely ($\pm$ 45°) with the head pointing away when the sharp end of the egg was to the right. This agrees well with reported statistics (eg Lillie [51]). Staging of the embryos was also consistent with normal development, having allowed a few hours for the fact that the eggs were refrigerated prior to incubation.

Sample	Incubation period/hrs	Stage (Lillie)	Uppermost eye	Embryo orientation	Large-scale field	Small-scale field
EGGV7	94	22	R	−45°	dipolar	yes (?)
EGGV8	97	22–23	R	−45°	dipolar	yes
EGV13	74	18	R	0°	dipolar	yes (?)
EGV16	76	17–18	L	0°	quadrupolar	yes (?)
EGV17	89	19	R	+90°	contamination	-
EGV18	90	19–20	R	180°	quadrupolar	no
EGV19	95	-	not windowed		complex	yes
EGV20	94	-	no embryo		complex	no
EGV21	99	20	R	+45°	dipolar	yes (?)
EGV22	102	20	R	−90°	dipolar	yes
EGV23	104	25	R	0°	complex	yes
EGV29	61	15	R	−135°	complex	yes

Table 7.1 Summary of anatomical and magnetic field data

Table 7.1 summarizes the main observations. The embryo orientation is given relative to the most common situation and 'yes (?)' indicates that while there was no clear small-scale feature, a localized perturbation to the large-scale field coincided with the embryo. I shall now describe the main observations from each map.

EGGV7: The main feature is a fairly strong dipolar field with extrema separated by 30 mm. There is a perturbation in the region of the embryo.

EGGV8: Subtraction of the background drift revealed a very clear highly localized feature corresponding precisely with the embryo location. The large-scale field is weak and roughly dipolar.

EGV13: A very strong dipolar pattern is very slightly distorted at the embryo's location.

EGV16: This egg was windowed prior to scanning. The overall pattern is a quadrupolar field, and the contours are again distorted in the region of the embryo.

EGV17: This was the other egg that was windowed before scanning and the map contains a very unusual feature whose location corresponds with one edge of the window. Although a diamond stylus was used for windowing, it seems likely that a piece of magnetic contamination (possibly dust) adhered to the cut edge. The repeat midscan showed a markedly

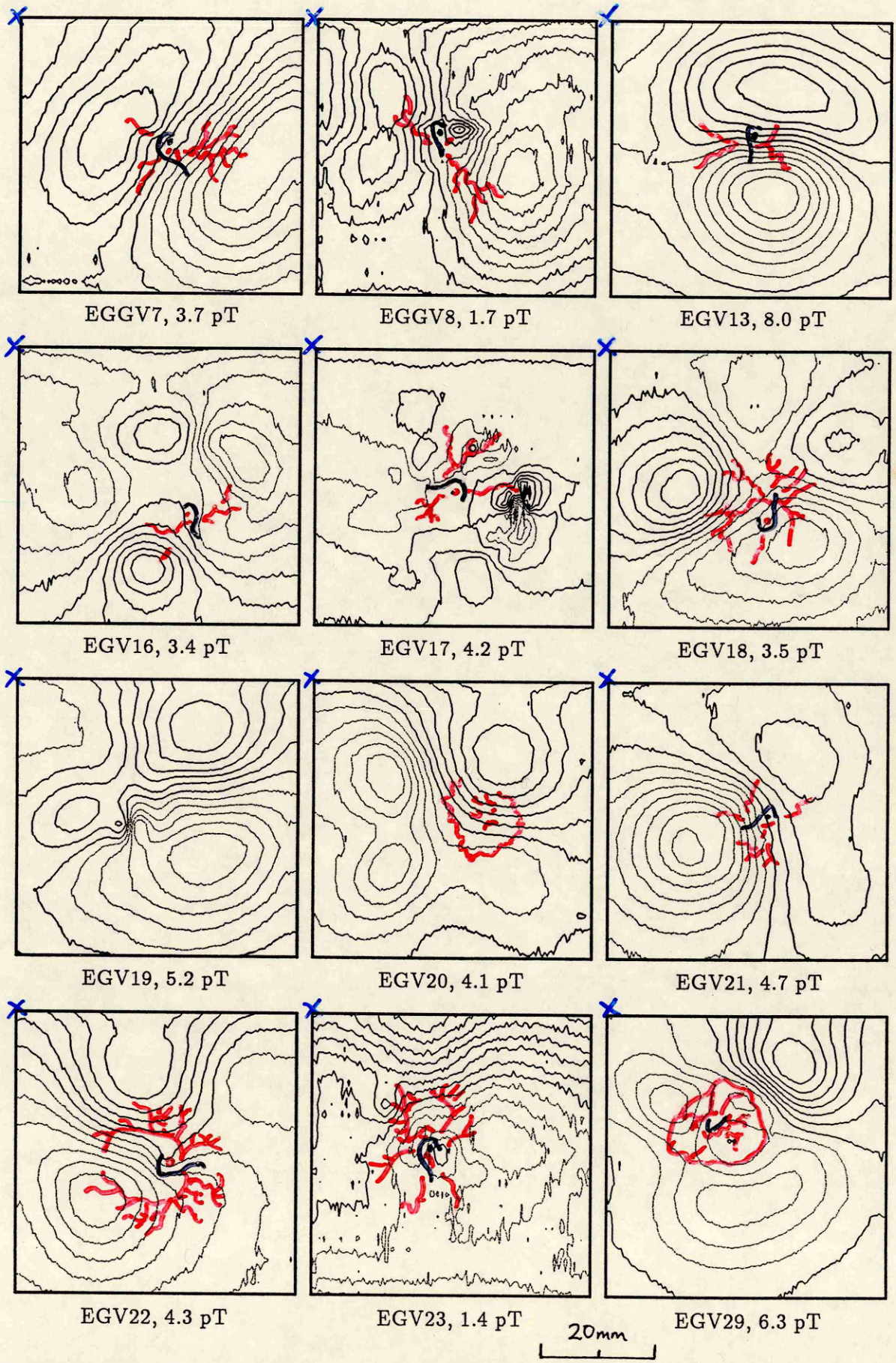

Figure 7.15 Field maps and anatomical geography for the 12 eggs
Egg code and contour separation are given with each map.

different field profile, suggesting very strongly that the source was not of physiological origin. This data was not analyzed further.

EGV18: This map consists of a quadrupolar field pattern with no real evidence of a localized feature.

EGV19: Here is a very beautiful small-scale feature superimposed on a complicated pattern. Unfortunately, this egg was never windowed and so it cannot be confirmed that the embryo's position coincided with the feature. However, the equivalent dipole would be located about 1 mm below the shell.

EGV20: When this egg was windowed, it was apparent that the embryo had died recently. The *sinus terminalis* had attained a diameter of about 15 mm and the embryo had sunk into the yolk. Again there is still a large-scale field pattern which, clearly, cannot be embryo-related. However, since normal development had not proceeded, this egg was disregarded in further analysis.

EGV21: A fairly strong large-scale dipolar pattern in this map is slightly distorted in the region of the embryo.

EGV22: Superimposed on this large-scale roughly dipolar pattern, there is an obvious localized distortion of the contours close to the embryo.

EGV23: This was the weakest field map, but as with EGGV8, subtraction of the background drift revealed a relatively strong and highly localized signal. The source appears to be coincident with the embryo and the equivalent dipole is about 1 mm below the shell. There is a second localized feature nearby.

EGV29: This young specimen produced a fairly complex field pattern containing a localized signal coincident with the developing tissues. However, the scale of this feature is about the same as the size of the membranes and its origin is probably the membranes.

7.2.6 An interpretation

Disregarding the contaminated sample (EGV17) and the abnormally developed egg (EGV20), there are clear, highly localized features in four out of ten eggs. In three of these (EGGV8, EGV22 and EGV23), the position of this feature corresponds very closely with that of the embryo; there is no anatomical information about the other one (EGV19). In four other eggs (EGGV7, EGV13, EGV16 and EGV21), the large-scale field pattern is visibly distorted at the embryo's location. The small-scale field pattern in EGV29, which is the least developed system, is probably not embryo-related and there was no discernible localized feature in EGV18.

From these results, I propose that two entirely independent mechanisms are responsible for the observed field patterns.

The large-scale field patterns are generated by current flow in the extra-embryonic membranes as described in section 6.6.1.

The small-scale fields, on the other hand, are generated within the embryo itself or in its immediate neighbourhood. They are difficult to see for two reasons. Firstly, they require extremely high resolution measurement and secondly, they can be easily swamped by the

large-scale field. It is probably significant that two of the three really clear localized signals (EGGV8 and EGV23) were seen on the two maps with the weakest overall pattern.

The model I propose for the current distribution, then, is a localized generator at the site of the embryo and an extended current density source in the yolk sac (as described in section 6.6.1).

7.3 Modelling the data

The experiments involving MicroSQUID were designed and performed with the primary objective of investigating highly localized sources. The large-scale field patterns measured with SQUIDLET were thoroughly analyzed and their sources were successfully modelled as distributed currents in the extra-embryonic membranes in section 6.6.1. The same procedure was carried out on the MicroSQUID data and this verified that the origin of these signals had a very similar overall form. I shall summarize the results of the distributed source modelling and the effect of adding a constant baseline shift in section 7.3.1.

I shall then concentrate, for the remainder of this section on the localized sources, of which there was evidence, on nine of the field maps. By smoothing the data over various different scale ranges and then applying a vector transformation, I shall demonstrate how the localized feature can be enhanced, and these results will be discussed in section 7.3.2. Finally, in section 7.3.3, I shall describe an alternative technique for highlighting the feature of interest, in which the large-scale field is modelled as a simple source and *its* field pattern is then subtracted from the composite map.

7.3.1 The distributed current source

In all of the following calculations, a subset (99 points) of the corrected field data were used and, except for inversions to study the effect of a baseline shift, the subset was zero-averaged. Before the inversion could be carried out, suitable values for the size and geometry of both the source space and the conducting space had to be chosen. In chapter 6, the source space adopted was a portion of a spherical shell, to model the shape of the extra-embryonic membranes surrounding the yolk. Because the distributed current source is not the main focus of this chapter, a simplified and slightly less realistic model, consisting of a flat disc, was used.

To choose an appropriate depth for the disc, the signals from two eggs were inverted for several different depths and source space radii, both in free space and within a conducting sphere. The depth which gave the best correlation between the original signal and the reconstructed field (about 99%) was 6.0 $\pm$ 0.5 mm. This was rather deeper than expected (about 3 mm below the inner surface of the shell), but it probably represents an average depth of the real source space, the error being introduced by the flat disc approximation.

The main concern, during modelling of the MicroSQUID data was the effect of ignorance of the field baseline. Figure 7.16 shows the current distributions computed at a depth of 6 mm for a uniform field (the magnitude of the field made no difference to the pattern). In (a), the source disc had a radius of 5 cm and in (b), it was 2 cm; the 99 measurement sites

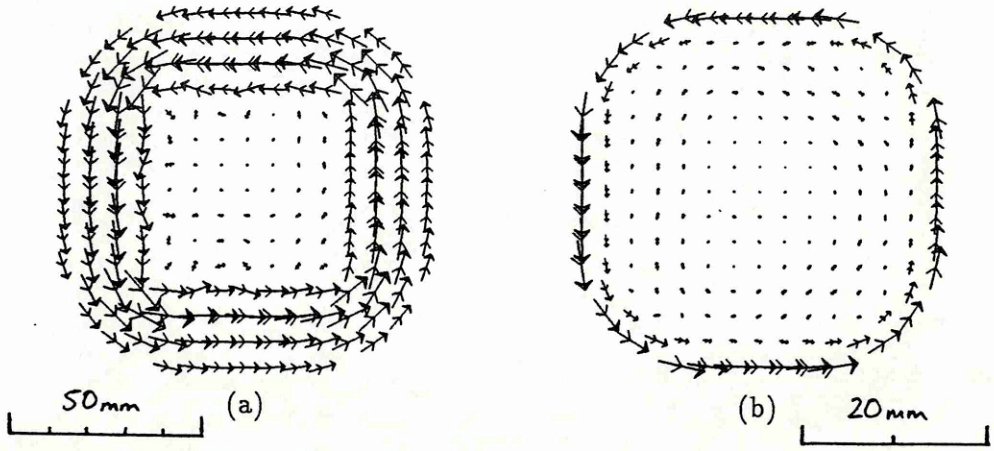

Figure 7.16 Current distribution for a uniform field
(a) 5 cm radius source disc
(b) 2 cm radius source disc

occupied the 5 cm × 5 cm square grid. The figures show that the currents due to an unknown baseline circulate in the region outside the measurement area or, if the source space is too small, are confined to its periphery.

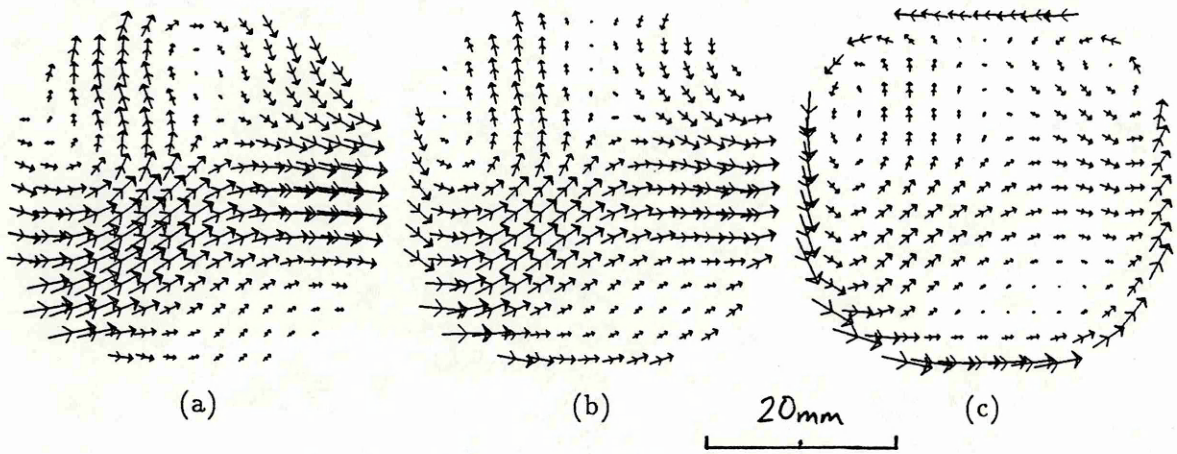

Figure 7.17 The effect of adding a uniform baseline
(a) Zero-averaged signal
(b) 5 pT baseline added
(c) 25 pT baseline added

Figure 7.17 shows the effect of adding a constant baseline to actual data. In (a), the zero-averaged data were used, while in (b) and (c), baselines of 5 pT and 25 pT respectively were added; in all cases the source space radius was 2 cm. The circulating current tends to dominate the map if the baseline is very large, but even in (c), the pattern of egg-related sources is well-represented, if the peripheral few millimetres are ignored. In view of this result, a disc radius of 3 cm was adopted for the inversions, even though this is not anatomically correct. The baseline error is unlikely to be greater than about 25 pT and therefore I have confidence that the error does not lead to serious source misinterpretation. Nevertheless, the interpretation of the current distribution in the peripheral region of the maps should be tentative.

As a further check on modelling assumptions, I have investigated the effect of a conducting

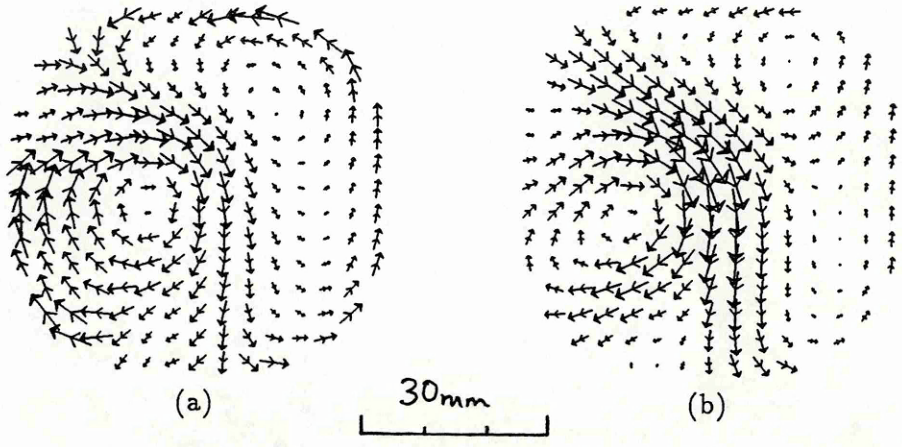

Figure 7.18 The effect of a conducting sphere
(a) Current distribution computed allowing for a conducting sphere
(b) Current distribution computed for the primary source alone

volume in which the primary source distribution may be embedded. Figure 7.18 shows a comparison between current density maps produced assuming that the source disc exists (a) within a conducting sphere and (b) in a non-conducting medium. In (a), the volume currents due to the computed source distribution also contribute to the fitted magnetic field data, whereas in (b), the fitted field pattern is due to the primary currents alone. It can be seen that if the entire egg is modelled as a conducting sphere centred 25 mm below the measurement plane, the current density is more dispersed, and this more plausible model was adopted. It is worthy of note that the relative current densities in the central region of the maps are very similar, and that the assumption is not critical.

In figure 7.19, which shows current density maps for nine of the eggs investigated with MicroSQUID, the primary source space was a disc of radius 3 cm centred 6 mm below the measurement plane within a conducting sphere centred 25 mm below. The overlay shows the anatomical information. I shall now make some general observations about these results and then briefly discuss two cases.

General observations: The three eggs which were omitted from this analysis were EGGV8 and EGV23 (these eggs had relatively small distributed signals and will be analyzed in the following section), and EGV17 (contaminated). It is clear that this technique is not sensitive to the highly localized features which are visible on the field maps (see the current distribution for EGV19, in particular). This is not surprising since a subset of data with a relatively low spatial frequency was used. Comparison of these current distributions with figures 6.13 and 6.14 indicates that the large-scale features are broadly similar to those recorded with SQUIDLET, but with rather more detail.

EGV20: This was the egg in which the embryo had recently died. The metabolism had not completely broken down because a large-scale distributed current was still evident. If the egg is maintained at incubation temperature, magnetic fields can be detected for several hours after embryo death.

EGV29: This egg contained a young (61 hours incubation) embryo and the current distribution is similar to all the others. The distributed signal appears very much earlier

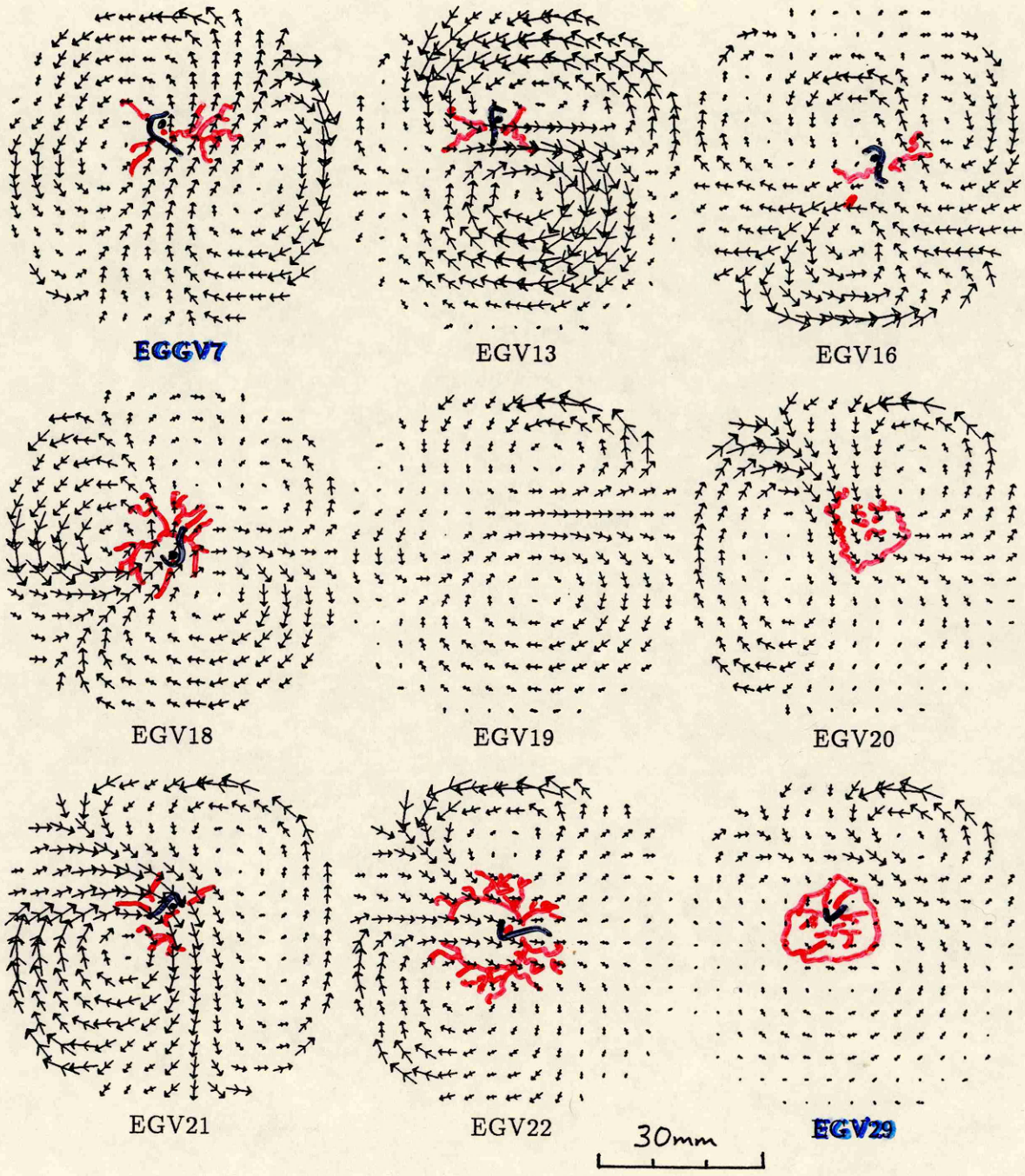

Figure 7.19 Current density maps and anatomical geography for 9 of the eggs

than the embryo-related signal.

7.3.2 The smoothed V3 transformation

I shall now concentrate on the localized signal visible on many of the MicroSQUID maps. In this section, I shall apply a vector transformation, the 'V3 transformation' [58] to smoothed data from the three eggs that showed the most prominent localized features (EGGV8, EGV23 and EGV19). In the first two of these cases, I shall compare the results with the position and orientation of the embryo.

The V3 transformation is a two-dimensional vector transformation of the magnetic field normal to the plane of measurement: it produces a vector field (the V3 map) which is a good estimate of the inferred current distribution close to the measurement plane. The local gradient of the normal field component is calculated over the measurement area and this vector is then rotated through 90° clockwise at all points. The result is a vector field which has a large magnitude in regions where the field gradient is high and a direction perpendicular to the maximum gradient; the choice of clockwise rotation ensures that the relationship of the V3 vector with the field map which generated it is consistent with the relationship between positive electric current and magnetic field.

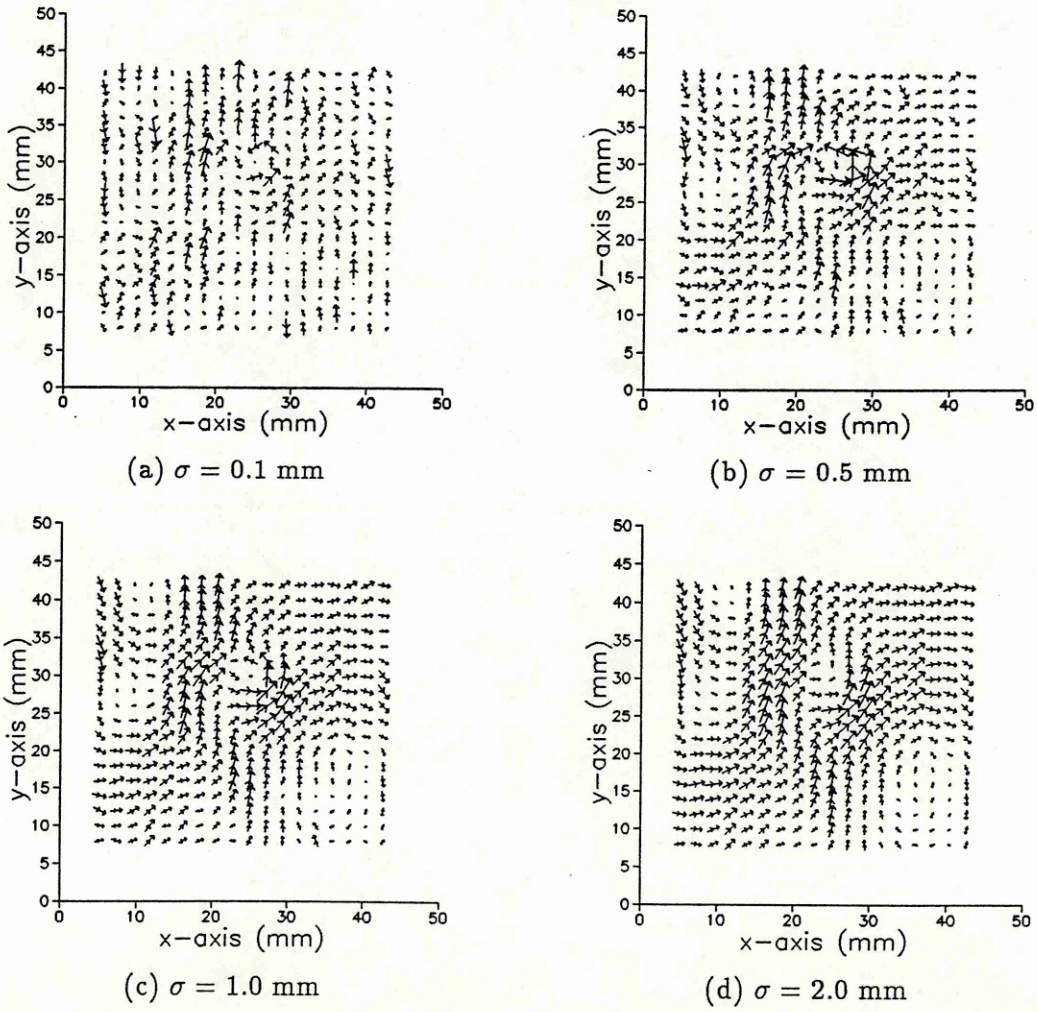

(a) $\sigma = 0.1$ mm

(b) $\sigma = 0.5$ mm

(c) $\sigma = 1.0$ mm

(d) $\sigma = 2.0$ mm

Figure 7.20 The V3 transformation with various levels of smoothing

Initially, selected raw data (after removal of the background drift and overall zero averaging) were used, but because of the V3's sensitivity to noise, smoothing became necessary. The frequency of data along x was much higher than that along y, and so noise in the signal produced high spatial gradients in the x-direction. Consequently, the V3 vector always had a much stronger y-component. To remove this bias, a two-dimensional Gaussian spatial filter $G(x_0, y_0)$ was applied to the original signal $S(x_0, y_0)$ at each data point x_0, y_0 and integrated over the measurement space to produce the smoothed signal,

$$S_{smoothed}(x_0, y_0) = \iint S(x_0, y_0) G(x_0, y_0) dx dy, \tag{7.1}$$

where

$$G(x_0, y_0) = \frac{1}{2\pi\sigma^2} \exp\left\{ \frac{-\left[(x - x_0)^2 + (y - y_0)^2\right]}{2\sigma^2} \right\}. \tag{7.2}$$

The scale parameter σ was used to define the level of smoothing: the larger the value of σ, the greater the smoothing, and $\sigma = 0$ reproduced the unsmoothed signal. To select an appropriate value, the V3 transformation was performed on data from EGGV8 which had been smoothed with four different scale parameters (see figure 7.20).

In figure 7.20a, the smoothing is insufficient because the y-component of the vector clearly dominates (rather like the case of no smoothing, not shown). The situation is improved in (b) and again in (c), but the effect of increasing the scale parameter from 1 mm to 2 mm is merely to equalize the magnitudes of the vector over the map rather than eliminate the spurious x-y bias. Consequently, $\sigma = 1.0$ mm was selected and used for all subsequent plots. This was a reasonable value because it was the same order as the step between data in the y-direction (2 mm) and much greater than the step in the x-direction (0.05 mm).

Figure 7.21 shows the result of applying the V3 transformation to three data sets recorded from eggs and the overlay contains the anatomical information where available. This procedure highlights the localized signals from all three eggs. The localized features in EGGV8 and EGV23 are enhanced and, in both cases, their locations in the x-y plane are shown to correspond closely with that of the embryo. However, the most impressive illustration of the ability of the V3 to emphasize localized sources is the map of EGV19, in which the magnitude of the V3 vector in a very small region of the map is several times greater than anywhere else. Unfortunately, it is not possible to confirm that the embryo's position corresponds with this location.

The high density data recorded with MicroSQUID is ideally suited to analysis by the V3 method. It has been used here to demonstrate the strength of the technique for locating highly localized sources. Application of the V3 transformation to the egg data has emphasized localized signals and shown these to correspond with the embryo position where this is known.

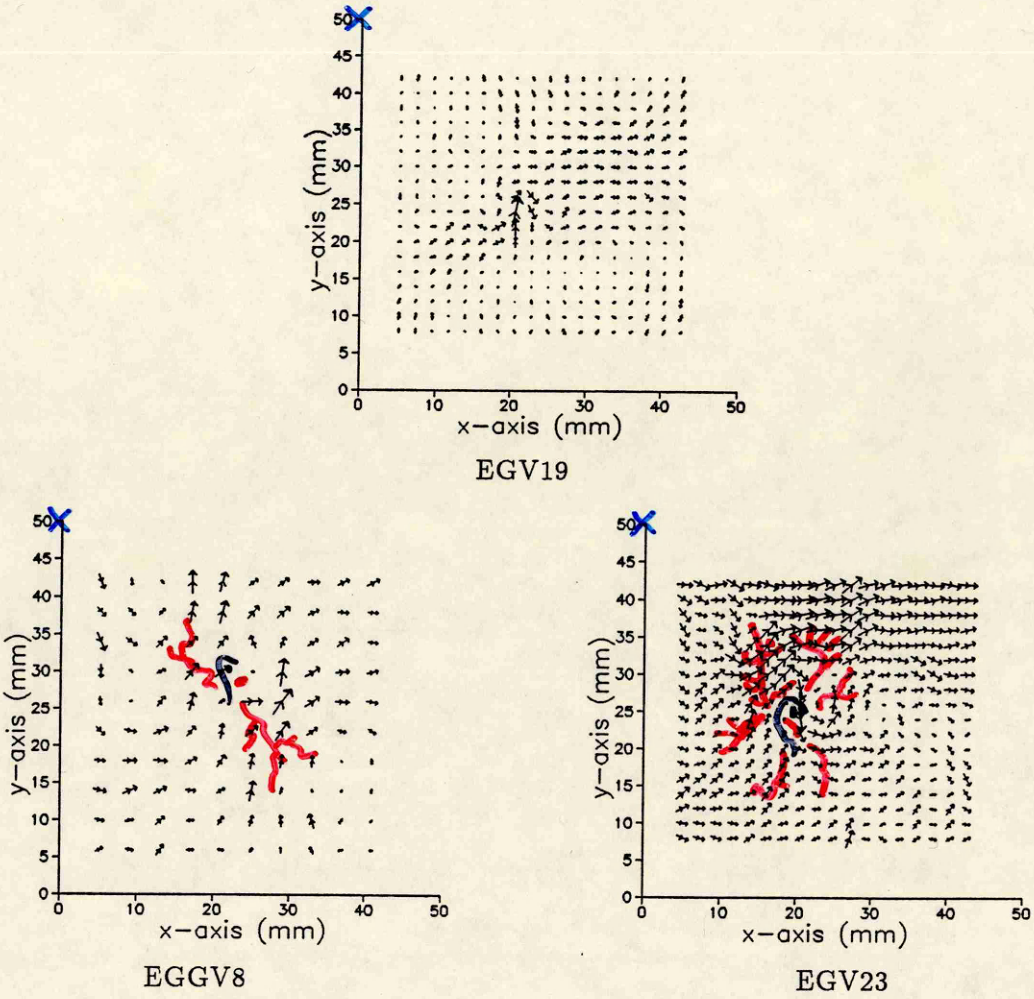

Figure 7.21 V3 vector maps for three eggs

7.3.3 Subtraction of the large-scale field

In this section, I shall demonstrate an alternative method to highlight the localized feature, with two other eggs. Referring to figure 7.15, the field maps recorded from EGGV7 and EGV13 both have a small perturbation in the region of the embryo, superimposed on a roughly dipolar background field. By considering a subset of data points which avoid the perturbation, the background field from each of these two eggs was modelled as a current dipole. The field due to this equivalent dipole was then subtracted from the original data at *all* points to emphasize the non-dipolar contribution.

For each egg, a regular square grid of forty-nine points was selected. Figure 7.22a shows the original field maps for the two eggs, with this grid superimposed. Corrected field data were then input to an iterative point source fitting algorithm [55], taking full account of gradiometer coil geometry. The starting point for the current dipole was chosen to be halfway between the field extrema, and at a depth given approximately by $d = \Delta/\sqrt{2}$.

A 'bare' dipole was modelled and after several iterations, the solution had converged and a good fit was obtained for both eggs. The field due to this current dipole, which would be measured by the appropriate MicroSQUID gradiometer, was then computed at all the actual measurement sites (see figure 7.22b). Finally, this dipolar field was subtracted

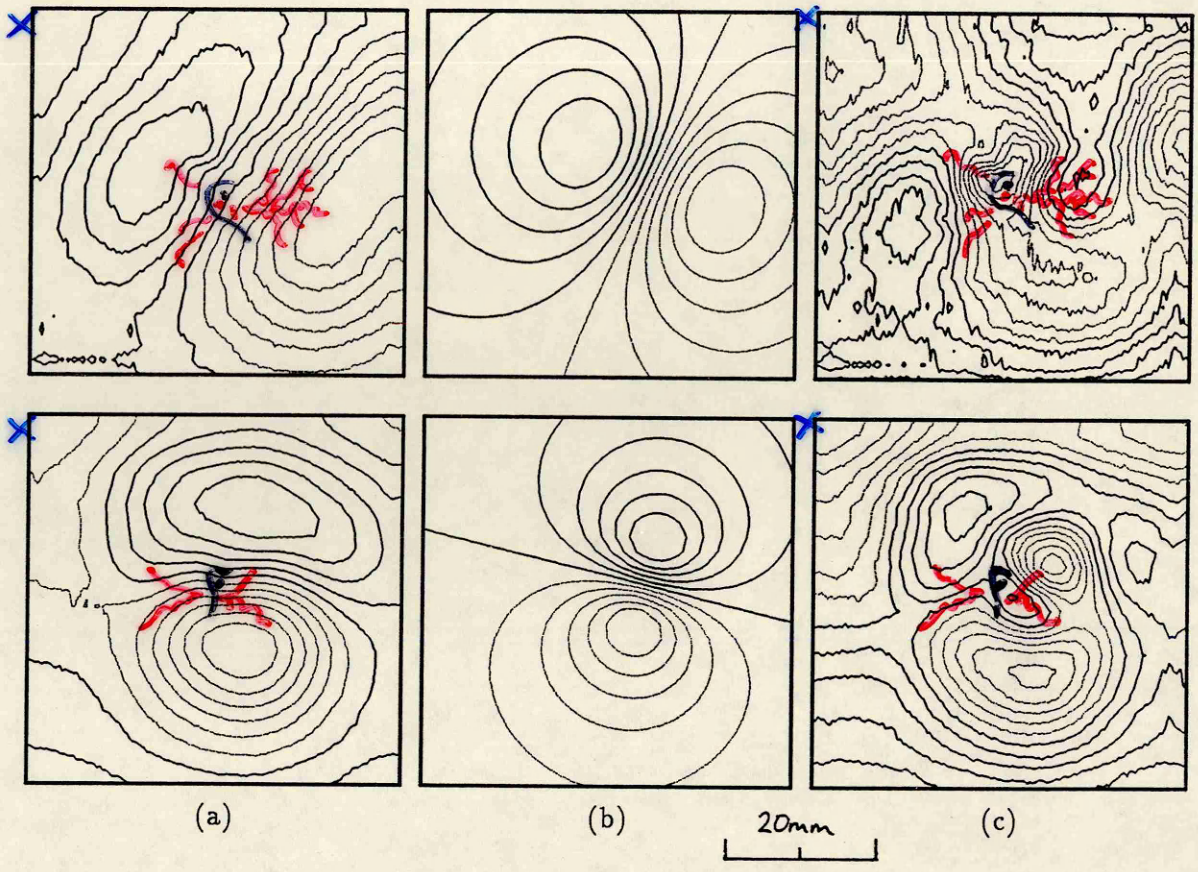

Figure 7.22 Subtracting a current dipole (upper set: EGGV7, lower set: EGV13)
(a) Original data with selected points
(b) Field due to effective dipole
(c) Residual field after subtraction

from the original data to reveal the patterns shown in figure 7.22c. In both cases, a strong localized feature coincident with the embryo has appeared, where previously, there was very little evidence of activity.

7.4 Discussion

I set out, at the start of this chapter, to "obtain more detailed information about the localized source which was observed close to the embryo in a number {three, one without anatomical information, out of about one hundred} of eggs investigated with SQUIDLET". This has been achieved in five, one without anatomical information , out of twelve eggs investigated with MicroSQUID. Considerable data manipulation has been necessary to extract this information, and it is very worthwhile to review the statistics of the experiment.

Of the twelve eggs studied intensively, one (EGV17) was highly contaminated so that the data could not be usefully analyzed and in one (EGV20) the embryo had recently died, although the extra-embryonic membranes were still active and producing fields[7]. Clearly distinguishable localized features were visible in the field maps for three others (EGGV8, EGV19 and EGV23) and these were emphasized by applying the V3 vector transformation. In two of these cases the localized area of activity was very close to the embryo and in the

[7]It is also very likely that the process of membrane autolysis contributed to the measured field.

third (EGV19) no anatomical information was available. The field maps for five further eggs showed evidence of similarly highly localized source very close to the embryo, and in two of these (EGGV7 and EGV13) the subtraction of a simple model for the background (membrane-related) field powerfully highlighted these features. Of the two viable eggs where no embryo-related feature was apparent, one (EGV29) was very young.

In this relatively limited data set, it is not possible to claim a systematic correlation between the orientations of the current and the embryo. This would be a very well-defined objective for a future experiment. However, in EGV23, the V3 vector (representing the current) is directed caudally within the embryo and in EGGV7 and EGV13, subtraction of the background field revealed a localized area of positivity in front of the embryo, which would be consistent with the same current.

It is premature to speculate about the physiological source of this feature, which has been observed in embryos of latencies between 74 and 104 hours. However, I shall note that Gillespie and McHanwell [39] measured significant pH gradients in much younger embryos (24–48 hours) These mediate development and morphogenesis by determining the behaviour of proteins in cellular membranes and epithelia and consequently, controlling the mutual adhesion of cell.

7.5 The state of chick egg magnetometry

In this conclusive section, I shall summarize the achievements of the thesis and review the current state of chick egg magnetometry.

Significant advances have been made in three 'techniques' areas: one physical, one biological and one mathematical. I shall consider them separately.

Within the context of physics, the aspect of high resolution magnetic field measurement was addressed. A new instrument was designed, built and developed to a state wherein it was capable of measuring biomagnetic fields with a previously unsurpassed spatial resolution. The 4 mm diameter sensing coil has a minimum separation from the biomagnetic source of less than 6 mm. I presented theoretical arguments that such a modification would yield considerable new information about superficial sources in small biological systems, and then demonstrated that this was true in the case of the chick embryo, the most widely studied model system of developmental biology. Finally, I utilized a different magnetometer with 3 mm diameter coils which could be placed only 2 mm from the source. This technique could be usefully applied to other developing and regenerating biological systems such as worms, axolotls or jellyfish!

The biological technique that was advanced was the preparation and successful incubation of windowed chick eggs. A method was developed that permitted simultaneous recording of the anatomical and magnetic field development from the chick. A potential improvement in this area would be to use shellless cultures to eliminate the existing difficulties of recording the anatomical information.

Mathematically, a novel algorithm for calculating distributed current sources from magnetic field data was used to image the two-dimensional ionic currents flowing in the extra-

embryonic membranes (probably the yolk sac) of the 1–5 day old chick embryo. A further improvement in this area, which is already in progress, is the three-dimensional imaging of such currents. Two other analytical techniques provided compelling evidence of a localized current generator which is very closely associated with the embryo. The future objectives of chick egg magnetometry would appear to lie with this source rather than the apparently uncorrelated distributed source.

The working hypothesis concerning this source is that it is generated within the embryo and may be related to pH gradients that have been measured with other techniques. Alternatively, it may be generated within the allantois or amnion, two other extra-embryonic membranes, which are very small at the relevant incubation latency, and which are involved in vital developmental functions.

What is required now, to further study this signal, is a systematic time sequence survey that provides good morphological data on the embryo scale in conjunction with very high resolution magnetic field data. These measurements would have to be made by MicroSQUID or an instrument with even smaller coils placed even closer to the source. The possibility of using a hybrid device containing high T_c coils coupled to a conventional SQUID and placed less than 100 μm from the source, is already under investigation.

Bibliography

[1] Atsumi K, Kotani M, Ueno S, Katila T & Williamson SJ, eds, 'Biomagnetism '87' (Proceedings of the sixth international conference on biomagnetism, Tokyo, Japan, August 1987), Tokyo Denki University Press, Tokyo, Japan, 1988.

[2] Attoniemi K, Karp PJ, Katila T & Kuusela ML, 'On balancing superconducting gradiometric magnetometers', J Phys (Paris) 39:1223–25, 1978.

[3] Barbanera S, Carelli P, Fenici R, Leoni R, Modena I & Romani G-L, 'Use of superconducting instrumentation for biomagnetic measurements performed in a hospital', IEEE Trans Mag MAG-17(1):849–52, 1981.

[4] Barker AT, 'Measurement of direct currents in biological fluids', Med & Biol Eng & Comput 19:507–08, 1981.

[5] Barker AT & Lunt MJ, 'The effects of pulsed magnetic fields of the type used in the stimulation of bone fracture healing', Clin Phys Physiol Meas 4(1):1–27, 1983.

[6] Baule GM & McFee R, 'Detection of the magnetic field of the heart', Am Heart J 66:95–96, 1963.

[7] Biomagnetic Technologies inc, San Diego, CA, USA. Announced at the seventh international conference on biomagnetism, New York, NY, USA, 1989.

[8] Borgens RB, Vanable JW & Jaffe LF, 'Bioelectricty and regeneration: initiation of frog limb regeneration by minute currents', J Exp Zool 200:403–16, 1977.

[9] Borgens RB, Vanable JW & Jaffe LF, 'Bioelectricity and regeneration: large currents leave the stumps of regenerating newt limbs', Proc Acad Natl Sci USA 74(10):4528–32, 1977.

[10] Borgens RB, 'What is the role of naturally produced electric currents in vertebrate regeneration and healing?', Int Rev Cytol 76:245–300, 1982.

[11] Bowles EA & Allen NS, 'Steady currents go through *Acetabularia crenulata*: a vibrating probe analysis', Biol Bull 167:501–41, 1984.

[12] Brighton CT, Black J, Friedenberg ZB, Esterhai JL, Day LJ & Connolly JF, 'A multicenter study of the treatment of nonunion with constant direct current', J Bone Joint Surg [Am] 63:2–13, 1981.

[13] Bruno AC & Costa Ribeiro P, 'A symmetric third order gradiometer without external balancing for magnetocardiography', Cryogenics 23:324–326, 1983.

[14] Bruno AC, Costa Ribeiro P, von der Weid, JP & Symko OG, 'Discrete spatial filtering with SQUID gradiometers in biomagnetism', J Appl Phys 59(7):2584–89, 1986.

[15] Bruno AC, Dolce CS, Soares SD & Costa Ribeiro P, 'Spatial Fourier technique for calibrating gradiometers' in [108].

[16] Bruno AC, Guida AV & Costa Ribeiro P, 'Planar gradiometer input recovery using a Fourier technique' in [1].

[17] Buchanan DS, Crum DB, Cox D & Wikswo JP, 'MicroSQUID: A closely spaced four channel magnetometer', in [108].

[18] Bures, Petran & Zachar, 'Electrophysiological methods in biological research', Academic Press, New York, NY, USA, 1967.

[19] Carelli P & Leoni R, 'Localization of biological sources with arrays of superconducting gradiometers', J Appl Phys 59(2):645–50, 1986.

[20] Claassen JH, 'Coupling considerations for SQUID devices', J Appl Phys 46(5):2268–75, 1975.

[21] Clarke CJS, Ioannides AA & Bolton JPR, 'Localized and distributed source solutions for the biomagnetic inverse problem', in [108].

[22] Clarke CJS, 'Probabilistic methods in a biomagnetic inverse problem', Inverse Problems 5:999–1012, 1989.

[23] Clarke CJS & Janday BS, 'The solution of the biomagnetic inverse problem by maximum statistical entropy', Inverse Problems 5:483–500, 1989.

[24] Clarke J, 'Superconducting quantum interference devices for low frequency measurements', in [86].

[25] Cohen D, 'Magnetoencephalography: evidence of magnetic fields produced by alpha-rhythm currents', Science 161:784–86, 1968.

[26] Cuffin BN & Cohen D, 'Magnetic fields of a dipole in special volume conductor shapes', IEEE Trans Biomed Eng 24(4):372–81, 1977.

[27] Cuffin BN & Cohen D, 'Effects of detector coil size and configuration on measurements of the magnetoencephalogram', J Appl Phys 54(6):3589–94, 1983.

[28] Deeming DC, Rowlett K & Simkiss K, 'Physical influences of embryo development', Journal of Experimental Zoology Supplement 1:341–45, 1987.

[29] Elton B, 'Stark', Sphere, London, UK, 1989.

[30] Esterhai JL, Friedenberg ZB, Brighton CT & Black J, 'Temporal course of bone formation in response to constant direct current stimulation', J Orthop Res 3:137–39, 1985.

[31] Faraday M, 'Experimental Researches in Electricity', Bernard Quaritch, London, UK, 1839.

[32] Farrell DE, Tripp JH, Brittenham GM, Danish EH, Harris JW & Tracht AE, 'A clinical system for accurate assessment of tissue iron concentration', in [82].

[33] Feynman RP, 'Lectures on Physics I', Addison-Wesley Publishing Company, Reading, MA, USA, 1963.

[34] Freeman WH & Bracegirdle B, 'An atlas of embryology', Heinemann, London, UK, 1967.

[35] Friedenberg ZB & Brighton CT, 'Bioelectric potentials in bone', J Bone Joint Surg [Am] 48:915–53, 1966.

[36] Friedenberg ZB, Zemsky LM, Pollis RP & Brighton CT, 'The response of nontraumatized bone to direct current', J Bone Joint Surg [Am] 56A:1023–1030, 1974.

[37] Geddes LA & Hoff HE, 'The discovery of bioelectricity and current electricity', IEEE Spectrum 8(12):38–46, 1971.

[38] Gielen FLH, Roth BJ & Wikswo JP, 'Capabilities of a toroid-amplifier system for magnetic measurement of current in biological tissue', IEEE Trans Biomed Eng BME-33(10):910–21, 1986.

[39] Gillespie JI & McHanwell S, 'Measurement of the intra-embryonic pH during the early stages of development in the chick embryo', Cell Tissue Res 247:445–51, 1987.

[40] Gmitro AF, Idell PS & Lahaie IJ, eds, 'Digital Image Synthesis and Inverse Optics' (SPIE proceedings vol 1351), 1990.

[41] Goodwin BC & Pateromichelakis S, 'The role of electrical fields, ions and the cortex in the morphogenesis of acetabularia', Planta 145:427–35, 1979.

[42] Goodwin BC, Skelton JL & Kirk-Bell SM, 'Control of regeneration and morphogenesis by divalent cations in *Acetabularia mediterranea*', Planta 157:1–7, 1983.

[43] Grimes DIF, 'Two methods of modelling electric current systems by analysis of magnetic field data, with particular reference to the quasi-dc magnetic field of the human leg', PhD thesis, Open University, Milton Keynes, UK, 1989.

[44] Grimes DIF, Lennard RF & Swithenby SJ, 'Macroscopic ionic currents within the human leg', Phys Med Biol 30(10):1101–12, 1985.

[45] Grover FW, 'Inductance Calculations', Dover Publications inc., New York, NY, USA, 1946.

[46] Grynszpan F, 'Relationship between the surface electromagnetic fields and the electrical activity of the heart', PhD dissertation, University of Pennsylvania, Philadelphia Eagles, PA, USA, 1971.

[47] Grynszpan F & Geselowitz DB, 'Model studies of the magnetocardiogram', Biophysical Journal 13:911–25, 1973.

[48] Guy CN, Cayliss A & Walker S, 'An analysis of gradiometer balancing procedures', Phys Med Biol 35(6):741–53, 1990.

[49] Hahlbohm HD & Lübbig H, eds, 'SQUID '85, Superconducting Quantum Interference Devices and their Applications' (Proceedings of the third international conference on superconducting quantum devices, West Berlin, Germany, June 1985), Walter de Gruyter, Berlin, Germany, 1985.

[50] Hämäläinen MS & Ilmoniemi RS, 'Interpreting measured magnetic fields of the brain: estimates of current distributions', preprint TKK-F-A559, Helsinki University of Technology, Finland, 1984.

[51] Hamilton HL (revised), 'Lillie's Development of the Chick' 3rd ed, Holt, 1952.

[52] Harold FM, 'Transcellular ion currents in tip-growing organisms: where are they taking us?' in [73].

[53] Hoenig HE, Daalmans G, Folberth W, Reichenberger H, Schneider S & Seifert H, 'Biomagnetic multichannel system with integrated SQUIDs and first order gradiometers operating in a shielded room', Cryogenics 29:809–13, 1989.

[54] Illingworth CM & Barker AT, 'Measurement of electrical currents emerging during the regeneration of amputated finger tips in children', Clin Phys Physiol Meas 1(1):87–89, 1980.

[55] Ioannides AA, personal communication, 1990.

[56] Ioannides AA, Bolton JPR & Clarke CJS, 'Continuous probabilistic solutions to the biomagnetic inverse problem', Inverse Problems 6:1–20, 1990.

[57] Ioannides AA, Bolton JPR, Hasson R & Clarke CJS, 'Localized and distributed source solutions for the biomagnetic inverse problem II', in [108].

[58] Ioannides AA, Hasson R & Miseldine GJ, 'Model-dependent noise elimination and distributed source solutions for the biomagnetic inverse problem', in [40].

[59] Jaffe LF, 'On the centripetal course of development in the *Fucus* egg, and self-electrophoresis', Developmental Biology Supplement 3:83–111, 1969.

[60] Jaffe LF, 'The role of ionic currents in establishing developmental pattern', Phil Trans R Soc Lond B 295:553–66, 1981.

[61] Jaffe LF & Nuccitelli R, 'An ultrasensitive vibrating probe for measuring steady extracellular currents', J Cell Biol 63:614–28, 1974.

[62] Jaffe LF & Nuccitelli R, 'Electrical controls of development', Ann Rev Biophys Bioeng 6:445–76, 1977.

[63] Jaffe LF & Stern CD, 'Strong electrical currents leave the primitive streak of chick embryos', Science 206:569–71, 1979.

[64] Janday BS, 'Biomagnetic field measurements and their interpretation using the dipole in a sphere model', PhD thesis, Open University, Milton Keynes, UK, 1987.

[65] Janday BS & Swithenby SJ, 'Analysis of magnetoencephalographic data using the homogenous sphere model: empirical tests', Phys Med Biol 32(1):105–13, 1987.

[66] Jones MH, 'A Practical Introduction to Electronic Circuits', Cambridge University Press, Cambridge, UK, 1977.

[67] Kaufman L & Williamson SJ, eds, 'Conference Digest: Seventh International Conference on Biomagnetism' (Conference digest for [108]).

[68] Koch RH, Gallagher WJ, Foglietti V, Oh B, Laibowitz RB, Koren G, Gupta A & Lee WY, 'Present staus and future of dc SQUIDs made from high T_c superconductors ' in [108].

[69] Kuffler SW, Nicholls JG & Martin AR, 'From Neuron to Brain' 2nd edn, Sinauer Associates inc, Sunderland, MA, USA, 1984.

[70] Kyriakides CPM & Simkiss K, 'Transmembrane potential differences across the chorioallantois', Comp Biochem Physiol 51A:875–79, 1975.

[71] Lennard RF, 'The measurement of small ionic currents in living organisms by means of sensitive magnetometry', PhD thesis, Open University, Milton Keynes, UK, 1984.

[72] Novak B & Bentrup FN, 'An electrophysiological study of regeneration in *Acetabularia mediterranea*', Planta 108:227–44, 1972.

[73] Nuccitelli R, ed, 'Ionic Currents in Development', Alan R Liss, New York, NY, USA, 1985.

[74] Okada YC, 'Discrimination of localized and distributed current dipole sources and localized single and multiple sources' in [100].

[75] Okada YC, Lauritzen M & Nicholson C, 'Magnetic field associated with spreading depression: a model for the detection of migraine', Brain Research 442(1):185–90, 1988.

[76] O'Shea PS, Goodwin BC & Ridge I, 'A vibrating electrode analysis of extracellular currents in *Acetabularia acetabulum*', to appear in J Cell Science.

[77] Overall R & Jaffe LF, 'Patterns of ionic current through *Drosophila* follicles and eggs', Developmental Biology 108:102–19, 1985.

[78] Overweg JA & Walter-Peters MJ, 'The design of a system of adjustable superconducting plates for balancing a gradiometer', Cryogenics 18(9):529–34, 1978.

[79] Patten BM, 'Early Embryology of the Chick', McGraw-Hill, USA, 1971.

[80] Rassi D, Blott BH, Al-Sewaidan H, Davies S & Ni C, '*In vivo* SQUID measurements of the magnetized human thorax', in [108].

[81] Romani G-L, 'The use of SQUIDs in the study of biomagnetic fields' in [101].

[82] Romani G-L & Williamson SJ, eds, 'Il Nuovo Cimento della Società Italiana di Fisica' (Proceedings of the fourth international workshop on biomagnetism, Rome, Italy, September, 1982), Editrice Compositori, Bologna, Italy, 1983.

[83] Romanoff AL, 'The Avian Embryo', Macmillan, New York, NY, USA, 1960.

[84] Sarvas J, 'Basic mathematical and electromagnetic concepts of the biomagnetic inverse problem', Phys Med Biol 32(1):11–22, 1987.

[85] Sarwinski RE, 'Superconducting instruments', Cryogenics 17(12):671–79, 1977.

[86] Schwartz BB & Foner S, eds, 'Superconductor Applications: SQUIDs and Machines', (Proceedings of the NATO advanced study institute on small scale applications of superconductivity, Gardone Riviera, Italy, September 1976), Plenum Press, New York, NY, USA, 1977.

[87] Simkiss K, 'Water and ionic fluxes inside the egg', Amer Zool 20:385–93, 1980.

[88] Singh KD, personal communication, 1990.

[89] Smith TB, 'Best-fit multipole expansions for fields from static currents', Inverse Problems 1:173–79, 1985.

[90] Stern CD, 'A simple model for early morphogenesis', J Theor Biol 107:229–42, 1984.

[91] Swithenby SJ, 'SQUIDs and their applications in the measurement of weak magnetic fields', J Phys E Sci Instrum 13: 801–13, 1980.

[92] Swithenby SJ, 'Non-invasive monitoring of ionic current flow during development by SQUID magnetometry', Experientia 44:673–78, 1988.

[93] Swithenby SJ, personal communication, 1990.

[94] Tan Shaofen, personal communication, 1990.

[95] Tan Shaofen, Roth BJ & Wikswo JP, 'The magnetic field of cortical current sources: the application of a spatial filtering model to the forward and inverse problems', Electroencephalography and Clinical Neurophysiology 76:73–85, 1990.

[96] Thomas IM, 'High resolution measurements of quasi-static biomagnetic fields', PhD thesis, Open University, Milton Keynes, UK, 1990.

[97] Van Duzer T & Turner CW, 'Principles of Superconducting Devices and Circuits' p 262, Edward Arnold, London, UK, 1981.

[98] Vorontsov DS & Emchenko AU, (cited in [18]), Nauchnye Zapiski 2(2):101, 1947.

[99] Vrba J, Fife AA, Burbank MB, Weinberg H & Brickett PA, 'Spatial discrimination in SQUID gradiometers and 3rd order gradiometer performance', Can J Phys 60:1060–73, 1982.

[100] Weinberg H, Stroink G & Katila TE, eds, 'Biomagnetism: Applications & Theory' (Proceedings of the fifth international conference on biomagnetism, Vancouver, Canada, August 1984), Pergamon Press inc, Oxford, UK, 1985.

[101] Weinstock H & Nisenoff M, eds, 'Superconducting Electronics' (Proceedings of the NATO advanced study institute on superconducting electronics, Il Ciocco, Italy, June–July 1988), Springer-Verlag, Berlin & Heidelberg, Germany, 1989.

[102] Weiss DS, Kirsner R & Eaglstein WH, 'Electrical stimulation and wound healing', Arch Dermatol 126:222–25, 1990.

[103] Wikswo JP, 'Optimization of SQUID differential magnetometers', AIP Conference Proc 44:145–49, 1978.

[104] Wikswo JP, 'Improved instrumentation for measuring the magnetic field of cellular action currents', Rev Sci Instrum 53(12):1846–50, 1982.

[105] Wikswo JP, 'High resolution measurements of biomagnetic fields', Advances in Cryogenic Engineering 33:107–116, 1988.

[106] Wikswo JP, Barach JP & Freeman JA, 'Magnetic field of a nerve impulse: first measurements', Science 208:53–55, 1980.

[107] Wikswo JP, van Egeraat JM, Ma YP, Sepulveda NG, Staton DJ, Tan S & Wijesingh RS, 'Instrumentation and techniques for high-resolution magnetic imaging', in [40].

[108] Williamson SJ, Hoke M, Stroink G & Kotani M, eds, 'Advances in Biomagnetism' (Proceedings of the seventh international conference on biomagnetism, New York, August 1989), Plenum Press, New York, NY, USA, 1989.

[109] Yasuda I, 'Fundamental aspects of fracture treatment', J Kyoto Med Soc 4:392, 1953.

[110] Zimmerman JE, 'SQUID instruments and shielding for low-level magnetic measurements', J Appl Phys 48(2):702–10, 1977.